

Electrochemical studies of barrier films on structural materials of nuclear power plants

By

SUMATHI SURESH

Enrolment No. CHEM01201104031

BHABHA ATOMIC RESEARCH CENTRE, MUMBAI

A thesis submitted to the

Board of Studies in Chemical Sciences

In partial fulfillment of requirements

for the Degree of

DOCTOR OF PHILOSOPHY

of

HOMI BHABHA NATIONAL INSTITUTE



AUGUST 2017

Homi Bhabha National Institute

Recommendations of the Viva Voce Committee

As members of the Viva Voce Committee, we certify that we have read the dissertation prepared by Sumathi Suresh entitled “Electrochemical studies of barrier films on structural materials of nuclear power plants” and recommend that it may be accepted as fulfilling the thesis requirement for the award of Degree of Doctor of Philosophy.

Chairman - Dr. S. Velmurugan Date:23/02/2018

Guide / Convener - Dr. S. Rangarajan Date:23/02/2018

Examiner - Dr. Jyotsna Dutta Majumdar Date:23/02/2018

Member 1- Dr. Sitaram Dash Date:23/02/2018

Member 2- Dr. N. Sivaraman Date:23/02/2018

Final approval and acceptance of this thesis is contingent upon the candidate's submission of the final copies of the thesis to HBNI.

I hereby certify that I/we have read this thesis prepared under my direction and recommend that it may be accepted as fulfilling the thesis requirement.

Date:

Place:

Guide

STATEMENT BY AUTHOR

This dissertation has been submitted in partial fulfillment of requirements for an advanced degree at Homi Bhabha National Institute (HBNI) and is deposited in the Library to be made available to borrowers under rules of the HBNI.

Brief quotations from this dissertation are allowable without special permission, provided that accurate acknowledgement of source is made. Requests for permission for extended quotation from or reproduction of this manuscript in whole or in part may be granted by the Competent Authority of HBNI when in his or her judgment the proposed use of the material is in the interests of scholarship. In all other instances, however, permission must be obtained from the author.

Sumathi Suresh

DECLARATION

I, hereby declare that the investigation presented in the thesis entitled “Electrochemical studies of barrier films on structural materials of nuclear power plants” submitted to Homi Bhabha National Institute, Mumbai, India for the award of Doctor of Philosophy in Chemical Sciences has been carried out by me under the guidance of Dr. S. Rangarajan. The work is original and has not been submitted earlier as a whole or in part for a degree / diploma at this or any other Institution / University.

Sumathi Suresh

List of Publications arising from the thesis

Journal

1. "Electrochemical characterization of nano zinc ferrite coating on carbon steel by pulsed laser deposition", **Sumathi Suresh**, S. Rangarajan, Santanu Bera, R. Krishnan, S. Kalavathi and S. Velmurugan, Thin Solid Films, **2016**, 612, 250–258.
2. "Evaluation of corrosion resistance of bi-layer coatings of nano spinel oxide on carbon steel", **Sumathi Suresh**, S. Rangarajan, Santanu Bera, R. Krishnan, S. Amirthapandian, M. Sivakumar and S. Velmurugan, Thin Solid Films, **2018**, 645, 77-86.
3. Effect of nickel ion substitution in magnetite film of carbon steel on its corrosion by electrochemical measurements, **Sumathi Suresh**, S. Rangarajan, P. Chandramohan, Santanu Bera, P. Magudapathy and S. Velmurugan (to be communicated).
4. Electrochemical corrosion studies of magnesium ferrite coating on carbon steel by pulsed laser deposition and hydrothermal method, **Sumathi Suresh**, S. Rangarajan, Santanu Bera, R. Krishnan, R. Ramaseshan and S. Velmurugan (to be communicated).

Conferences

1. Surface and electrochemical Characterization of nano zinc ferrite coating on carbon steel, **Sumathi Suresh**, S. Rangarajan and S. Velmurugan,

Symposium on Water Chemistry and Corrosion in Nuclear Power Plants in Asia – 2015, September 2-4, 2015, Anupuram, India.

2. Effect of nickel ferrite coating on corrosion resistance of Carbon Steel, **Sumathi Suresh**, S. Rangarajan and S. Velmurugan, 20th International Conference on Water Chemistry of Nuclear Reactor Systems, The Grand Brighton, Brighton, UK, 2-7 October 2016.
3. Corrosion studies of nano magnesium ferrite coating on carbon steel, **Sumathi Suresh**, S. Rangarajan and S. Velmurugan, Twelfth ISEAC Discussion Meet in Electrochemistry, The Acres Club, Chembur, Mumbai, India, December 7-8, 2016.

Sumathi Suresh

DEDICATED
To
My loving Parents

ACKNOWLEDGEMENTS

The present work was carried out at Water and Steam Chemistry Division of Bhabha Atomic Research Centre Facilities, Kalpakkam under the guidance of **Prof. Dr. S. Rangarajan** (Head, Surface Characterization and Mass Transport Studies Section, WSCD). I would like to express my deep sense of gratitude for his tremendous support in carrying out my research work. I am thankful to him for his constant motivation, guidance and useful suggestions. Thanks are due to him for giving me the full freedom to do the work and providing me the required infrastructure and resources to accomplish my research work.

My sincere thanks are to **Prof. Dr. P. D. Naik**, Director, Chemistry Group, BARC for his constant support and encouragement. My heartfelt thanks to Doctoral Committee members **Dr. S. Velmurugan** (Chairman and Head, Water and Steam Chemistry Division (WSCD)), **Dr. S. V. Narasimhan** (Former Chairman and Former Head, Water and Steam Chemistry Division (WSCD)), **Dr. Sitaram Dash** (Member) and **Dr. N. Sivaraman** (Member) for their useful suggestions and constant support throughout my research work. I would like to thank chemistry discipline faculties during my course work in teaching me the important topics which has helped me a lot in carrying out my work in an organized manner.

I am extremely thankful to **Dr. Santanu Bera** for XPS characterization and for his constant support in my entire research work by giving his invaluable scientific suggestions. I would also wish to express my thanks to **Dr. P. Chandramohan** for Raman and for his scientific approach in carrying out my work.

I would like to express my gratitude to **Dr. M. Kamruddin** and **Dr. R. Pandian** for FESEM characterization, **Mr. M. Sivakumar** and **Dr. Arup Dasgupta** for HRSEM, **Dr. R. Krishnan** for PLD, **Mrs. Sunitha Rajkumari** and **Dr. S. Ilango** for GI-XRD, **Mr. P. Magudapathy** and **Dr. S. Kalavathi** for XRD, **Mr. Ashok Bahuguna** for profilometry, **Dr. K. Saravanan** for RBS, **Dr. R. Ramaseshan** for scratch test and **Dr. S. Amirthapandian** for HRTEM.

A very special mention of my friends **Padma, Pushpa, Veena** and **Vanitha** for their encouraging words and friendly advices.

I would also wish to acknowledge all the staffs of WSCD and my special thanks for **Raja** who has helped me in the autoclave work.

I am speechless in expressing my gratitude to my dear Husband, **K. Suresh** who always stood by me whenever his support was needed. His constant encouragement and unconditional love helped me in carrying out my Ph.D work.

Last but not the least I would like to express my thanks to my sons **S.S. Siddharth** and **S.S. Sushil** for sparing their valuable time throughout my Ph.D tenure. Finally, I would like to thank each and everyone who have helped me directly or indirectly for the successful completion of my thesis.

CONTENTS

S. No.	Title	Page No.
I	Synopsis	xv
II	List of Figures	xxv
III	List of Tables	xxx
IV	List of Abbreviations	xxxii

CHAPTER 1

INTRODUCTION

1	Introduction	1
1.1	Types of Reactors	2
1.1.1	Pressurised Water Reactor (PWR)	2
1.1.2	Boiling Water Reactor (BWR)	2
1.1.3	Pressurised Heavy Water Reactor (PHWR or CANDU)	2
1.2	Water Chemistry	4
1.2.1	BWR primary water chemistry	4
1.2.2	PWR primary water chemistry	5
1.2.3	PHWR primary water chemistry	6
1.3	Structural materials in water cooled nuclear reactors	6
1.4	Formation and Transport of Activity in PHWR	8
1.5	Oxide formed on Structural Materials	9
1.6	Chemical decontamination of Primary Heat Transport (PHT) system	10
1.7	Corrosion control and prevention	11
1.8	Nanocoatings	11
2	Literature Review	11
2.1	Literature on hydrothermal studies of CS in presence of Ni^{2+} , Zn^{2+} and Mg^{2+} ions	14
3	Aim and Scope of the study	15

3.1	Aim	15
3.2	Scope of work	16

CHAPTER 2

EXPERIMENTAL METHODS

2	Purpose of the research program	17
2.1	Synthesis of Ferrite powder	20
2.1.1	Chemicals used in the synthesis process	20
2.1.1 (a)	Preparation of Zinc Ferrite powder	20
2.1.1 (b)	Preparation of Nickel Ferrite powder	20
2.1.1 (c)	Preparation of Magnesium Ferrite powder	20
2.2	Preparation of pellet	21
2.3	Preparation of lithium hydroxide	22
2.4	Hydrothermal method	23
2.4.1	Formation of magnetite (Fe_3O_4) on CS	23
2.4.2	Formation of oxides (Fe_3O_4 , NiFe_2O_4 , ZnFe_2O_4 and MgFe_2O_4) on CS	25
2.4.2.1	Pre-conditioning of autoclave	25
2.4.2.2	Ferrite formation	26
2.4.3	Thickness measurement	28
2.5	Pulsed Laser Deposition (PLD)	29
2.5.1	The mechanism of PLD	29
2.5.2	The main advantages of PLD process	31
2.6	Characterization of deposited oxide coating/film	33
2.6.1	X-Ray Diffraction (XRD)	33
2.6.1.1	Grazing Incidence-XRD (GI-XRD)	34
2.6.2	Scanning Electron Microscopy (SEM)	36
2.6.3	X-Ray Photoelectron Spectroscopy (XPS)	38
2.6.3.1	Principle of XPS	38
2.6.3.2	Instrumentation	39
2.6.4	Laser Raman Spectroscopy (Raman)	40

2.6.4.1	Raman Effect	41
2.6.4.2	Components of a Raman Spectrometer	41
2.6.5	Transmission Electron Microscopy (TEM)	43
2.6.6	Rutherford Backscattering Spectrometry (RBS)	47
2.6.6.1	Experimental set-up	48
2.6.6.2	Depth profile analysis	49
2.6.6.3	Applications of RBS	49
2.6.7	Inductively Coupled Plasma–Atomic Emission Spectroscopy (ICP-AES)	50
2.6.8	Scratch Test	51
2.6.9	Surface Profilometry	52
2.7	Electrochemical Techniques	53
2.7.1	Tafel Plot	54
2.7.2	Potentiodynamic Anodic Polarization (PDAP)	55
2.7.3	Electrochemical Impedance Spectroscopy (EIS)	57
2.7.3.1	Electrical equivalent circuit	58
2.7.3.2	Nyquist Plot	60
2.7.3.3	Bode Plot	61
2.7.4	Test Cell and Instrument	62
2.7.5	Mott-Schottky (MS) method	63

CHAPTER 3

FORMATION OF MAGNETITE COATING ON CARBON STEEL BY HYDROTHERMAL METHOD

3.1	Introduction	67
3.2	Mechanism of magnetite formation	69
3.3	Passivation studies	72
3.4	Corrosion rate evaluation of Fe ₃ O ₄ formation with different exposure time	74
3.4.1	Characterization of Fe ₃ O ₄ formed on CS	74

3.4.1.1	Thickness measurement	74
3.4.1.2	X-Ray Diffraction	75
3.4.1.3	Scanning Electron Microscopy	77
3.4.1.4	X-Ray Photoelectron Spectroscopy	78
3.4.1.5	Laser Raman Spectroscopy	80
3.4.2	Electrochemical Characterization	82
3.4.2.1	Potentiodynamic Anodic Polarization	82
3.4.2.2	Electrochemical Impedance Spectroscopy	83
3.4.2.3	Mott-Schottky method	86
3.5	Conclusion	88

CHAPTER 4

COMPARISON OF THE NICKEL FERRITE COATINGS DEVELOPED BY PULSED LASER DEPOSITION AND HYDROTHERMAL METHOD

Part I: NiFe₂O₄ deposition by PLD method

4.1	Introduction	89
4.2	Results and Discussion	89
4.2.1	X-Ray Diffraction Analysis	90
4.2.2	Laser Raman Spectroscopic Analysis	91
4.2.3	Scanning Electron Microscopic Analysis	93
4.2.4	X-Ray Photoelectron Spectroscopic Analysis	94
4.2.5	Electrochemical Characterization	97
4.2.5.1	Electrochemical Impedance Spectroscopy	97
4.2.5.2	Potentiodynamic Anodic Polarization	100
4.2.5.3	Semiconducting properties of the oxide film	102
4.2.6	Focused Ion Beam-SEM Analysis	104
4.2.7	Transmission Electron Microscopic Analysis	106
4.2.8	Scratch test	109
4.3	Conclusion	110

Part II: NiFe₂O₄ film formation by hydrothermal method

4.4	Introduction	111
4.5	Results and Discussion	111
4.5.1	Cation concentration and thickness measurement	112
4.5.2	Surface characterization of oxides	113
4.5.2.1	X-Ray Diffraction Analysis	113
4.5.2.2	Scanning Electron Microscopic Analysis	115
4.5.2.3	X-Ray Photoelectron Spectroscopic Analysis	117
4.5.2.4	Laser Raman Spectroscopic Analysis	119
4.5.3	Electrochemical Characterization	121
4.5.3.1	Potentiodynamic Anodic Polarization	121
4.5.3.2	Electrochemical Impedance Spectroscopy	123
4.5.3.3	Semiconducting properties of the oxide film	126
4.6.	Conclusion	128

CHAPTER 5

CORROSION RESISTANCE PROPERTY OF THE ZINC FERRITE COATINGS ON CARBON STEEL

Part I: ZnFe₂O₄ deposition by PLD method

5.1	Introduction	129
5.2	Results and Discussion	130
5.2.1	Laser Raman Spectroscopic Analysis	130
5.2.2	X-Ray Diffraction Analysis	132
5.2.3	Scanning Electron Microscopic Analysis	134
5.2.4	X-Ray Photoelectron Spectroscopic Analysis	136
5.2.5	Electrochemical Characterization	139
5.2.5.1	Potentiodynamic Anodic Polarization	139
5.2.5.2	Electrochemical Impedance Spectroscopy	141
5.2.5.3	Semiconducting properties of the oxide film	143
5.2.6	Scratch Test	145

5.3	Conclusion	146
Part II: ZnFe₂O₄ film formation by hydrothermal method		
5.4	Introduction	147
5.5	Results and Discussion	147
5.5.1	Cation concentration and thickness measurement	147
5.5.2	Surface characterization of oxides	149
5.5.2.1	X-Ray Diffraction Analysis	149
5.5.2.2	Scanning Electron Microscopic Analysis	151
5.5.2.3	X-Ray Photoelectron Spectroscopic Analysis	152
5.5.2.4	Laser Raman Spectroscopic Analysis	155
5.5.3	Electrochemical Characterization	157
5.5.3.1	Potentiodynamic Anodic Polarization	157
5.5.3.2	Electrochemical Impedance Spectroscopy	158
5.5.3.3	Semiconducting properties of the oxide film	162
5.6	Conclusion	165

CHAPTER 6

EFFECT OF MAGNESIUM FERRITE COATING ON THE CORROSION RESISTANCE OF THE CARBON STEEL

Part I: MgFe₂O₄ deposition by PLD method

6.1	Introduction	167
6.2	Results and Discussion	167
6.2.1	Laser Raman Spectroscopic Analysis	168
6.2.2	X-Ray Diffraction Analysis	169
6.2.3	Scanning Electron Microscopic Analysis	172
6.2.4	X-Ray Photoelectron Spectroscopic Analysis	174
6.2.5	Scratch Test	177
6.2.6	Rutherford Backscattering Spectrometry	178
6.2.7	Electrochemical Characterization	180
6.2.7.1	Electrochemical Impedance Spectroscopy	180

6.2.7.2	Potentiodynamic Anodic Polarization	183
6.2.7.3	Semiconducting properties of the oxide film	184
6.3	Conclusion	186
Part II: MgFe₂O₄ film formation by hydrothermal method		
6.4	Introduction	187
6.5	Results and Discussion	187
6.5.1	Cation concentration and thickness measurement	187
6.5.2	Surface characterization of oxides	189
6.5.2.1	X-Ray Diffraction Analysis	189
6.5.2.2	Scanning Electron Microscopic Analysis	190
6.5.2.3	X-Ray Photoelectron Spectroscopic Analysis	192
6.5.2.4	Laser Raman Spectroscopic Analysis	195
6.5.3	Electrochemical Characterization	197
6.5.3.1	Potentiodynamic Anodic Polarization	197
6.5.3.2	Electrochemical Impedance Spectroscopy	199
6.5.3.3	Semiconducting properties of the oxide film	202
6.6	Conclusion	205

CHAPTER 7

CONCLUSIONS AND SCOPE FOR FUTURE WORK

7.1	Conclusions	206
7.1.1	Pulsed laser deposition	206
7.1.2	Hydrothermal	207
7.2	Future Scope/Directions	208

	References	209
--	------------	-----

SYNOPSIS

The structural materials in water cooled nuclear power reactors are mainly iron and nickel based alloys. Carbon Steel is one of the alloys used as the out of core structural material in the primary heat transport system (PHT) of Indian Pressurized Heavy Water Reactors. Corrosion products are generated by the interaction of high temperature coolant with the structural materials of the primary heat transport system. Some of these corrosion products get neutron activated in the core and become activated corrosion products. Then they get re-dispersed to out of core locations where the oxide present over the surfaces acts as the host lattice for the incorporation of activated corrosion products. Some of these nuclides are long lived and results in the radiation field build-up in the reactor coolant circuit (1-2). Currently, these radioactive deposits are removed by decontamination process (3-4) which reduce the radiation fields and minimises the radiation hazards to the operating and maintenance personnel (5). The nickel ions released from nickel based steam generator tubes partially converts the magnetite layer to nickel ferrite. To further minimize the corrosion rates of these structural materials, apart from going for better corrosion resistant materials, efforts are being made worldwide to apply an adherent coating on the existing alloy surfaces, to modify the size of the oxide particles to nano-size and/or change the composition of the oxides by the addition of an external metal ion which could improve the adherence and protectiveness of the interfacial oxide film. It was found that the addition of nickel or zinc was found to suppress the

deposition of cobalt-60 in boiling water reactors [6] and the positive effects of zinc addition on corrosion film was reported [7-8] and applied to boiling water reactors and pressurized water reactors [9-10]. The protective nature of the oxide was enhanced by addition of magnesium ions as a passivating ion. Similar studies have been reported in literature for Boiling Water Reactor and Pressurised Water Reactor structural materials [11–12]. Abundance of zinc, magnesium or nickel in the coolant system is bound to develop corresponding ferrite coatings on carbon steel surface of the PHT system. In this work, attempts were made to deposit nickel ferrite, zinc ferrite and magnesium ferrite on carbon steel to obtain the coatings in nano size by pulsed laser deposition. Hydrothermal method which is closer to the real system of the power plant was carried out to incorporate the cations (Ni^{2+} , Zn^{2+} and Mg^{2+}) into the oxide lattice during its formation on carbon steel. Adhesion and the stability of the interface between the coatings and carbon steel play a crucial role in deciding the corrosion resistance property of carbon steel. The coatings were thoroughly characterized by different techniques to monitor its size, crystallinity, chemical composition, adhesion, surface morphology etc. The corrosion resistance and the electronic properties of these oxides were studied by electrochemical methods and were compared for the coatings obtained by the above two methods.

Chapter 1: Introduction

A general introduction on the types of reactors, their water chemistry, sources and formation of activated corrosion products, radiation field build

up and decontamination process are detailed. Brief literature review on synthesis by coprecipitation and deposition by PLD and hydrothermal method has been given. The aim and scope for carrying out this work are also described in this chapter.

Chapter 2: Experimental methods

The procedures followed to carry out the synthesis by coprecipitation method and depositions of the ferrites under study by pulsed laser deposition technique are given in this chapter. The thickness measurement of the coatings was carried out by stylus profilometer. To confirm the thickness of the coating over the carbon steel specimen, Rutherford Backscattering experiment was carried out. The oxide formations by incorporation of the cations (Ni^{2+} , Zn^{2+} and Mg^{2+}) by hydrothermal method are described. The measurement of oxide film thickness was carried out by Clarke's method. A brief description of the working principles of the various instruments used for the characterizations of the oxides has been discussed in this chapter. It includes X-ray diffraction, X-ray photoelectron spectroscopy, scanning electron microscopy, laser Raman spectroscopy, Rutherford Backscattering and Transmission electron microscopy. Analytical tools like inductively coupled plasma atomic emission spectroscopy for the analysis of the cations present in the formulation are discussed. Electrochemical techniques like electrochemical impedance spectroscopy, potentiodynamic anodic polarization and Mott-Schottky are briefed here.

Chapter 3: Formation of magnetite coating on carbon steel by Hydrothermal method

This chapter discusses the results of the corrosion parameters evaluated for the magnetite film obtained by hydrothermal method by the exposure of carbon steel in lithium hydroxide at 250 °C for 96, 240, 360 and 480 hours. The formation of the magnetite was confirmed by XRD. An increase in polarization resistance was observed for magnetite formed on carbon steel for 96 and 240 hours exposure when compared to the uncoated carbon steel whereas the polarization resistance decreased for 360 and 480 hours. However, the corrosion rate values obtained for the 96, 240 and 360 hours were almost similar with a slight increase in corrosion rate in case of magnetite formed in 480 hours duration. The thickness calculated by Clarke's method increased slightly for 240, 360 and 480 hours compared to the 96 hours. The defect density values calculated from the slopes of the Mott Schottky plot were found to be of similar order in all the cases. Hence, the exposure time was limited to 96 and 240 hours for further hydrothermal studies.

Chapter 4: Comparison of the nickel ferrite coatings developed by pulsed laser deposition and hydrothermal method

The synthesis of nickel ferrite and deposition on carbon steel by pulsed laser deposition is explained in the first part of this chapter. Then the characterization of the coatings by XRD, Raman, SEM and XPS are discussed and the corrosion resistance properties of these coatings by

electrochemical methods are discussed in detail. The nickel ferrite coating was found to be corrosion resistant with optimized thickness and defect density. The potentiodynamic anodic polarization tests showed that the nickel ferrite film was not stable at higher anodic potential. The incorporation of Ni^{2+} ions into the magnetite lattice by hydrothermal method and its characterization are discussed. Presence of nickel ions in the oxide lattice gradually increases the polarization resistance obtained from impedance spectroscopy which was found to be higher than that for the magnetite formed for the respective hour's exposure. However, the corrosion rate obtained from potentiodynamic anodic polarization studies were in the same order of magnitude in presence and absence of nickel ions. The corrosion rate was found to be less for 240 hours exposure with the open circuit potential shifting to the noble side and a broader passive region indicating that the oxide formed in presence of Ni^{2+} ions in the case of 240 hours exposure protects the carbon steel when compared to the uncoated carbon steel. The thickness of the oxide formed was in the range 0.24 to 0.64 μm for 24 to 240 hours exposed specimens.

Chapter 5: Corrosion Resistance Property of the Zinc Ferrite coatings on Carbon Steel

This chapter consists of two parts. The synthesis of zinc ferrite and its characterization by XRD are discussed in this chapter. The deposition of zinc ferrite on carbon steel by pulsed laser deposition and then the

characterization of these coatings by XRD, SEM and XPS are explained in detail. The corrosion resistance properties of these coatings evaluated by impedance and potentiodynamic anodic polarization methods are discussed. From the potentiodynamic anodic polarization studies it was observed that the passivation currents were in decreasing order: carbon steel > magnetite coated carbon steel > zinc ferrite coated carbon steel. Based on the values of corrosion current, the corrosion resistance was found to be in the following order: zinc ferrite coated carbon steel > magnetite coated carbon steel > carbon steel. The defect density lowered by one order magnitude and the corrosion resistance increased with the adherent additional ZnFe_2O_4 coating. The adhesive and stability of the coating was studied by scratch test. The second part of this chapter discusses the incorporation of Zn^{2+} ions into the magnetite lattice by hydrothermal method and the characterization of the film formed on carbon steel by XRD, SEM, Raman and XPS are given in detail and the corrosion resistance property evaluated by electrochemical techniques have been discussed in this chapter. The thickness of the oxide formed in presence of Zn^{2+} ions was lesser when compared to the oxide formed in presence of nickel or magnesium ions. In the presence of zinc ions, though the thickness of the ferrites reduced when compared to the magnetite formed, the polarization resistance increased and the corrosion rate decreased appreciably.

Chapter 6: Effect of magnesium ferrite coating on the corrosion resistance of the Carbon Steel

In this chapter, the first part discusses the synthesis of magnesium ferrite and its characterization by XRD, deposition of synthesized magnesium ferrite on magnetite coated carbon steel by pulsed laser deposition, characterization and the corrosion resistance properties of these coatings by electrochemical methods. It was observed that the polarization resistance obtained from impedance spectroscopy increased by the additional magnesium ferrite coating. Like in the case of nickel ferrite, the potentiodynamic anodic polarization studies showed that the coated magnesium ferrite coating was not stable at higher anodic potentials. The incorporation of Mg^{2+} ions into the magnetite lattice by hydrothermal method and its characterization by XRD, SEM, XPS and Raman are discussed in the second part of this chapter. Magnesium ion incorporation into the magnetite lattice showed similar values of polarization resistance from impedance studies for oxides formed in 96 and 240 hours of exposure at 250 °C and the corrosion rate values from potentiodynamic anodic polarization studies were similar to that obtained in presence of nickel ions. From the impedance studies it was observed that the corrosion resistance values increased and remained similar for the films formed in 96 and 240 hours when compared to uncoated carbon steel. Similar trend was observed by potentiodynamic anodic polarization method.

Chapter 7: Conclusions and Scope for Future Work

A brief summary of the conclusions drawn based on the results derived from the studies carried out on deposition of ferrites (NiFe_2O_4 , ZnFe_2O_4 and MgFe_2O_4) on the CS/ Fe_3O_4 substrate by pulsed laser deposition method and the corrosion behaviour of these coatings evaluated by electrochemical methods are detailed in this chapter. Important conclusions derived from the electrochemical studies of the oxide films formed in presence of metal ions (Ni^{2+} , Zn^{2+} and Mg^{2+}) by hydrothermal method are given in this chapter. Scopes for future work in this research area to investigate the growth and the nucleation mechanism in the formation of oxide film on the carbon steel substrate by hydrothermal method are given.

3. Salient Findings and Conclusions

a. Pulsed laser deposition

- The thickness of the coating optimized with lesser defects gave better protection on carbon steel.
- The corrosion rate obtained was less with a broader passive region for zinc ferrite coating by pulsed laser deposition compared to nickel ferrite and magnesium ferrite coating.
- The corrosion resistance followed the order: $\text{ZnFe}_2\text{O}_4 > \text{NiFe}_2\text{O}_4 \cong \text{MgFe}_2\text{O}_4 \cong \text{Fe}_3\text{O}_4$

b. Hydrothermal

- The thickness of the oxide formed by hydrothermal method in presence of zinc ions was less in comparison to the oxide formed in its absence.
- The oxide formed on carbon steel by hydrothermal method in presence of nickel ions was uniform and smooth whereas it was not uniform in case of zinc and magnesium ions.
- The difference in the corrosion rate of carbon steel exposed at 250 °C in the presence of cations (nickel, zinc and magnesium) for 240 hours, was marginal and the protection offered by the film over the metal followed the order: $\text{ZnFe}_2\text{O}_4 \cong \text{MgFe}_2\text{O}_4 \geq \text{NiFe}_2\text{O}_4 \cong \text{Fe}_3\text{O}_4$.

Future Scope/Studies

1. Studies on the nucleation and initial stages of growth of ferrites on carbon steel surface by hydrothermal method will further lead to find the role of particle size of the ferrite coatings on corrosion resistance properties.
2. Studies related to the mixed ferrite (Ni^{2+} , Zn^{2+} and Mg^{2+}) formation by the hydrothermal method in the presence of mixture of cations.
3. Effect of anions on the oxide formation.

References

- [1] K.A.Burrill, *Can. J. Chem. Eng.* 55 (1977) 54–61.
- [2] D.H.Lister, *Nucl. Sci. Eng.* 59 (1976) 406–426.
- [3] P.N.Moorthy, *Proc. on Experience with dilute chemical decontamination in Indian Nuclear Reactors*, IGCAR, Kalpakkam, India 12-13 Dec. 1995.
- [4] S.Velmurugan, S.V.Narasimhan, P.K.Mathur and K.S.Venkateswarulu, *J. Nucl. Technol.* 96 (1991) 248-258.
- [5] G.R.Dey et.al, *A new dilute chemical formulation for decontamination of PHT system surfaces of PHWRs*, *Curtwac.* (95) 183.
- [6] C.C.Lin, *Prog. Nucl. Energy*, 51(2) (2009) 207–224.
- [7] L.W.Niedrach and W.H.Stoddard, *Corros.* 42 (1986) 546–549.
- [8] H.Inagaki, A.Nishikawa, Y.Sugita and T.Tsuji, *J. Nucl. Sci. Technol.* 40 (2003) 143–152.
- [9] P.L.Andresen, G.S.Was, in: *Corrosion in the Nuclear Power Industry*, *ASM Handbook*, vol. 13C, ASM International, (2006) 404–406.
- [10] C.C.Lin, F.R.Smith, Y.Uruma, T.Taneichi and N.Ichikawa in:, *Operational Experience and New Technology for Management Proceedings*, *JAIF International Conference on Water Chemistry in Nuclear Power Plants*, Tokyo, Japan, 2 (1988) 386.
- [11] S.Velmurugan, S.Padma, S.V.Narasimhan, P.K.Mathur and P.N.Moorthy, *J. Nucl. Sci. Technol.* 33 (1996) 641–649.
- [12] D.H.Lister and G.Venkateswaran, *Nucl. Technol.* 125 (1999) 316–331.

LIST OF FIGURES

Figure No.	Figure Caption	Page No.
1.1	Schematic of PHT system of PHWR	3
2.1	Flowchart of the work	19
2.2	Photograph of the synthesized ferrite powders	21
2.3	Photograph of the pellets	22
2.4	Photograph of the target holders	22
2.5	Photograph of the experimental setup used for LiOH preparation	23
2.6	Schematic of Autoclave	25
2.7	Photograph of the Autoclave	27
2.8	Photograph of the Stainless Steel stand with CS specimens	27
2.9	Schematic of PLD system	29
2.10	Photograph of the Pulsed Laser Deposition system	32
2.11	Photograph of the substrate stand with CS specimen	32
2.12	Principle of Braggs law	34
2.13	Principle of SEM	37
2.14	Principle of XPS instrument	39
2.15	Excitation of vibrational energy level	41
2.16	Instrumentation of Laser Raman Spectroscopy	42
2.17	The ray diagrams of imaging mode and diffraction mode in Transmission Electron Microscope	46
2.18	The bright field and dark field modes for imaging	46
2.19	Schematic representation of a RBS set up	48
2.20	Schematic for scratch test	52
2.21	A typical Tafel plot	55
2.22	A typical potentiodynamic anodic polarization plot	56
2.23	Schematic representation of electrode/solution interface	58
2.24	Typical Nyquist Plot	60
2.25	Typical Bode Plot	62
2.26	Photograph of a) Electrochemical system and b) Electrochemical cell	63

2.27	Typical Mott Schottky plot	65
3.1	Typical magnetite structure	68
3.2	Double oxide layer formed by Fe ₃ O ₄ on CS	71
3.3	(a) EIS Nyquist and (b) PDAP plot of CS and CS/Fe ₃ O ₄	73
3.4	(a) GI-XRD pattern of uncoated CS and (b) XRD pattern of CS/Fe ₃ O ₄	75
3.5	SEM image of CS/Fe ₃ O ₄	77
3.6	EDAX of CS/Fe ₃ O ₄	78
3.7	XPS of (a) Fe 2p and (b) O 1s obtained from CS/Fe ₃ O ₄	79-80
3.8	Raman spectra of (a) CS/Fe ₃ O ₄ and (b) standard Fe ₃ O ₄	81
3.9	PDAP plot of CS/Fe ₃ O ₄ at different exposure time	83
3.10	(a) Nyquist, (b) Bode and (c) Phase angle plot of CS/Fe ₃ O ₄ at different exposure time	85-86
3.11	Mott Schottky plot of CS/Fe ₃ O ₄ at different exposure time	87
4.1	(a) XRD pattern of synthesized NiFe ₂ O ₄ powder and (b) GI-XRD pattern of CS/Fe ₃ O ₄ /NiFe ₂ O ₄	90
4.2	Raman spectrum of CS/Fe ₃ O ₄ /NiFe ₂ O ₄	92
4.3	(a) SEM image and (b) Cross section of CS/Fe ₃ O ₄ /NiFe ₂ O ₄	93
4.4	XPS spectra of (a) Ni 2p, (b) Fe 2p and (c) O 1s peaks obtained for CS/Fe ₃ O ₄ /NiFe ₂ O ₄	94-95
4.5	XPS spectra of Ni 2p _{3/2} from (a) NiFe ₂ O ₄ powder and (b) CS/Fe ₃ O ₄ /NiFe ₂ O ₄	96
4.6	EIS (a) Nyquist, (b) Bode and (c) Phase Angle plot of uncoated CS, CS/Fe ₃ O ₄ and CS/Fe ₃ O ₄ /NiFe ₂ O ₄ (thickness 200, 325 and 500 nm)	99-100
4.7	PDAP plot of uncoated CS, CS/Fe ₃ O ₄ and CS/Fe ₃ O ₄ /NiFe ₂ O ₄ (thickness 200, 325 and 500 nm)	102
4.8	Mott Schottky plot of CS/Fe ₃ O ₄ and CS/Fe ₃ O ₄ /NiFe ₂ O ₄	103
4.9	FIB-SEM of cross section of CS/Fe ₃ O ₄ /NiFe ₂ O ₄	105
4.10	EDAX of (a) 2-NiFe ₂ O ₄ coating, (b) 3-NiFe ₂ O ₄ coating, (c) 4-CS and (d) Elemental composition in atomic % of the marked area 2, 3 and 4	105
4.11	(a) HRTEM image, (b) Electron Diffraction, (c) HRTEM image of the interface and (d) Electron Energy Loss spectrum of O, Fe and Ni present on CS/Fe ₃ O ₄ / NiFe ₂ O ₄	107-108

4.12	Scratch Test for CS/Fe ₃ O ₄ /NiFe ₂ O ₄	109
4.13	(a) Nickel and Iron concentration and (b) oxide film thickness at the end of different exposure time	112
4.14	GI-XRD pattern of the oxides formed on CS exposed to 250 °C in presence of Ni ²⁺ ions for 24, 96 and 240 hours	113
4.15	FE-SEM images of CS exposed to 24, 96 and 240 hours in presence of Ni ²⁺ ions	115-116
4.16	XPS spectra of (a) Fe 2p, (b) Ni 2p and (c) O 1s peaks for CS/NiFe ₂ O ₄	118
4.17	Raman spectrum of the oxide films formed on CS exposed at 250 °C in LiOH in presence of Ni ²⁺ ions at (a) 24 hours, (b) 96 hours and (c) 240 hours	120
4.18	PDAP plot of CS exposed to 24, 96 and 240 hours in LiOH and Ni ²⁺ ions	122
4.19	(a) Nyquist, (b) Bode and (c) Phase angle plot of CS in LiOH and Ni ²⁺ ions	124
4.20	Corrosion rate and Polarization resistance comparison	126
4.21	Mott Schottky plot of CS exposed in LiOH and Ni ²⁺ ions	127
5.1	Raman spectra of (a) CS/Fe ₃ O ₄ /ZnFe ₂ O ₄ and (b) Standard ZnFe ₂ O ₄	131
5.2	(a) XRD pattern of synthesized ZnFe ₂ O ₄ powder and (b) GI-XRD pattern of CS/Fe ₃ O ₄ /ZnFe ₂ O ₄	132
5.3	(a) SEM image and (b) Cross section of CS/Fe ₃ O ₄ /ZnFe ₂ O ₄	134
5.4	EDAX spectrum of CS/Fe ₃ O ₄ /ZnFe ₂ O ₄	135
5.5	XPS spectra of (a) Fe 2p, (b) O 1s and (c) Zn 2p peaks obtained from CS/Fe ₃ O ₄ /ZnFe ₂ O ₄	136-137
5.6	XPS spectra of Zn 2p peaks obtained from CS/Fe ₃ O ₄ /ZnFe ₂ O ₄	138
5.7	PDAP plot of uncoated CS, CS/Fe ₃ O ₄ and CS/Fe ₃ O ₄ /ZnFe ₂ O ₄	139
5.8	(a) Nyquist, (b) Bode and (c) Phase angle plot of uncoated CS, CS/Fe ₃ O ₄ and CS/Fe ₃ O ₄ /ZnFe ₂ O ₄	141-142
5.9	Mott-Schottky plot of uncoated CS, CS/Fe ₃ O ₄ and CS/Fe ₃ O ₄ /ZnFe ₂ O ₄	144
5.10	Defect Density graph of CS, CS/Fe ₃ O ₄ and CS/Fe ₃ O ₄ /ZnFe ₂ O ₄	145
5.11	Scratch Test for CS/Fe ₃ O ₄ /ZnFe ₂ O ₄	146
5.12	(a) Zinc and Iron concentration and (b) Oxide film thickness at the end of different exposure time	148
5.13	GI-XRD patterns of the oxide formed on CS exposed to 250 °C	

	in presence of Zn^{2+} ions for 24, 96 and 240 hours	149
5.14	FE-SEM images of CS exposed to 24, 96 and 240 hours in presence of Zn^{2+} ions	151-152
5.15	XPS spectra of (a) Fe 2p, (b) Zn 2p and (c) O 1s peaks obtained for CS in presence of Zn^{2+} ions	152-153
5.16	Raman spectrum of the oxide films formed on CS exposed for (a) 24, (b) 96 and (c) 240 hours at 250 °C in LiOH in presence of Zn^{2+} ions	155
5.17	PDAP plot of CS exposed to 24, 96 and 240 hours in LiOH and Zn^{2+} ions	158
5.18	(a) Nyquist, (b) Bode and (c) Phase angle plot of CS exposed in LiOH and Zn^{2+} ions	160-161
5.19	Corrosion rate and Polarization resistance comparison	162
5.20	Mott Schottky plot of CS exposed to 24, 96 and 240 hours in LiOH and Zn^{2+} ions at (a) 100 Hz and (b) 10 Hz	164
6.1	Raman spectra of (a) CS/ Fe_3O_4 / $MgFe_2O_4$ and (b) Standard $MgFe_2O_4$	168-169
6.2	(a) XRD pattern of synthesized $MgFe_2O_4$ powder and (b) GI-XRD pattern of CS/ Fe_3O_4 / $MgFe_2O_4$	170
6.3	(a) SEM image, (b) Cross section FE-SEM image and (c) EDAX spectrum of CS/ Fe_3O_4 / $MgFe_2O_4$	172-173
6.4	XPS spectra of (a) Mg 1s, (b) Fe 2p, (c) Mg 2p with Fe 3p and (d) O 1s peaks obtained from (1) CS/ Fe_3O_4 / $MgFe_2O_4$ and (2) $MgFe_2O_4$ pellet used for deposition	175-177
6.5	Scratch Test for CS/ Fe_3O_4 / $MgFe_2O_4$	178
6.6	RBS spectrum for CS/ Fe_3O_4 / $MgFe_2O_4$	179
6.7	(a) Nyquist, (b) Bode and (c) Phase angle plot of uncoated CS, CS/ Fe_3O_4 and CS/ Fe_3O_4 / $MgFe_2O_4$	181-182
6.8	PDAP plots for uncoated CS, CS/ Fe_3O_4 and CS/ Fe_3O_4 / $MgFe_2O_4$	184
6.9	Mott-Schottky plots for CS, CS/ Fe_3O_4 and CS/ Fe_3O_4 / $MgFe_2O_4$	185
6.10	Defect Density graph for uncoated CS, CS/ Fe_3O_4 and CS/ Fe_3O_4 / $MgFe_2O_4$	185
6.11	(a) Magnesium and Iron concentration and (b) oxide film thickness at the end of different exposure time	188
6.12	GI-XRD patterns of the oxide formed on CS exposed to 250 °C in presence of Mg^{2+} ions for 24, 96 and 240 hours	189
6.13	FE-SEM images of CS exposed in LiOH and Mg^{2+} ions	191

6.14	XPS spectra of (a) Fe 2p, (b) Mg 2p, (c) Mg 1s, (d) Mg KLL Auger and C and (e) O 1s peaks obtained for CS in presence of Mg^{2+} ions	192- 194
6.15	Raman spectrum of the oxide films formed on CS at 250 °C in LiOH in presence of Mg^{2+} ions exposed for (a) 24, (b) 96 and (c) 240 hours	196
6.16	PDAP plot of CS exposed to 24, 96 and 240 hours in LiOH and Mg^{2+} ions	197
6.17	(a) Nyquist, (b) Bode and (c) Phase angle plot of CS exposed to 24, 96 and 240 hours in LiOH and Mg^{2+} ions	200- 201
6.18	Corrosion rate and Polarization resistance comparison	202
6.19	Mott Schottky plot of CS exposed in LiOH and Mg^{2+} ions	203- 204

LIST OF TABLES

Table No.	Table Caption	Page No.
1.1	Chemistry parameters in primary circuit of water cooled reactors	6
1.2	Composition of Materials (% w/w) used in a Nuclear Power Plant	7
1.3	Common radioactive isotopes and their source in the PHTS	9
1.4	Nature of the oxide layers formed on primary circuits of BWR, PHWR and PWR	10
1.5	Various deposition techniques	13
1.6	Literature survey on synthesis and deposition	13
2.1	Experimental solution for high temperature studies	25
2.2	Chemical composition of CS (weight %)	27
3.1	Impedance parameters obtained from EIS measurements	72
3.2	Corrosion parameters obtained from PDAP measurements	73
3.3	Calculated thickness of CS/Fe ₃ O ₄ for different exposure time	74
3.4	Crystallite size obtained for CS/Fe ₃ O ₄ for different exposure time	76
3.5	Quantitative analysis by EDAX of CS/Fe ₃ O ₄	78
3.6	Corrosion parameters obtained for CS/Fe ₃ O ₄ at different exposure time	83
3.7	Impedance parameters for CS/Fe ₃ O ₄ at different exposure time	84
3.8	Defect Density for CS/Fe ₃ O ₄ for different exposure time	88
4.1	Impedance parameters obtained from EIS measurements	100
4.2	Corrosion parameters obtained from PDAP measurements	102
4.3	Defect Density for CS/Fe ₃ O ₄ and CS/Fe ₃ O ₄ /NiFe ₂ O ₄	104
4.4	Crystallite size and Lattice parameter obtained from GI-XRD	114
4.5	Binding Energy and Quantification of the elements by XPS	119
4.6	Vibrational modes obtained for the oxides from Raman analysis	120
4.7	Corrosion parameters obtained from PDAP measurements	123
4.8	Impedance parameters obtained from EIS measurements	125
4.9	Log Z _{0.01 Hz} for nickel ferrite vs. exposure time in LiOH solution	125
4.10	Defect density values obtained from Mott Schottky analysis	128
5.1	Elemental composition from EDAX analysis	135

5.2	Corrosion parameters obtained from PDAP measurements	140
5.3	Impedance parameters obtained from EIS measurements	143
5.4	Crystallite size and Lattice parameter obtained from GI-XRD	150
5.5	Binding Energy and Quantification of the elements by XPS	155
5.6	Vibrational modes obtained for the oxides from Raman analysis	156
5.7	Corrosion parameters for different exposure time in LiOH and Zn ²⁺	158
5.8	Impedance parameters for different exposure time in LiOH and Zn ²⁺ ions	161
5.9	Log Z _{0.01 Hz} for Zinc Ferrite vs. exposure time in LiOH solution	161
5.10	Defect density values obtained from Mott Schottky analysis	163
6.1	FWHM values from XRD pattern of synthesized and deposited MgFe ₂ O ₄	171
6.2	Elemental composition from EDAX analysis	173
6.3	Impedance parameters obtained from EIS analysis	181
6.4	Corrosion parameters obtained from PDAP analysis	183
6.5	Crystallite size and Lattice parameter obtained from GI-XRD	190
6.6	Binding Energy and Quantification of the elements by XPS	195
6.7	Vibrational modes obtained for the oxides from Raman analysis	197
6.8	Corrosion parameters for different exposure time in LiOH and Mg ²⁺ ions	198
6.9	Impedance parameters for different exposure time in LiOH and Mg ²⁺ ions	201
6.10	Log Z _{0.01 Hz} for magnesium ferrite vs. exposure time in LiOH solution	201
6.11	Defect density values obtained from Mott Schottky analysis	204

List of Abbreviations

atm	atmosphere
BSE	Backscattered Electrons
BWR	Boiling Water Reactor
β_a	anodic Tafel slope
β_c	cathodic Tafel slope
BF	Bright Field
C_{dl}	Double Layer Capacitance
CPE	Constance Phase Element
CCD	Charged Coupled Device
CS	Carbon Steel
CANDU	CANDU (CANada Deuterium Uranium)
CS/Fe ₃ O ₄	Magnetite coating on carbon steel
CS/Fe ₃ O ₄ /MgFe ₂ O ₄	MgFe ₂ O ₄ coating on CS/Fe ₃ O ₄
CS/Fe ₃ O ₄ /ZnFe ₂ O ₄	ZnFe ₂ O ₄ coating on CS/Fe ₃ O ₄
CS/Fe ₃ O ₄ /NiFe ₂ O ₄	NiFe ₂ O ₄ coating on CS/Fe ₃ O ₄
DZO	Depleted Zinc Oxide
DCD	Dilute Chemical Decontamination
DF	Dark Field
DM	De-Mineralised
eV	electron Volts
E_{corr}	Corrosion potential
E_{pp}	Primary passivation potential
EDAX	Energy Dispersive X-ray
EELS	Electron Energy Loss Spectroscopy
EIS	Electrochemical Impedance Spectroscopy
FWHM	Full Width at Half Maximum
FESEM	Field Emission Scanning Electron Microscopy
FIB-SEM	Focused Ion Beam - Scanning Electron Microscopy
FEG	Field Emission Gun

GI-XRD	Grazing Incidence-X-Ray Diffraction
HWC	Hydrogen Water Chemistry
HRSEM	High Resolution Scanning Electron Microscopy
HRTEM	High Resolution Transmission Electron Microscopy
I_{ox}	oxidation current
I_{red}	reduction current
I_{corr}	corrosion current
ICDD	International Centre for Diffraction Data
ICP-AES	Inductively Coupled Plasma – Atomic Emission Spectroscopy
LRS	Laser Raman Spectroscopy
MHz	Mega Hertz
mpy	milli inches per year
μm	micro meter
mJ	milli Joule
MPa	Mega Pascal
nm	nano meter
NWC	Normal Water Chemistry
NMCA	Noble Metal Chemical addition
ppm	parts per million
ppb	parts per billion
PHT	Primary Heat Transport
PHWR	Pressurized Heavy Water Reactor
PWR	Pressurized Water Reactor
PDAP	Potentiodynamic Anodic Polarization
PLD	Pulsed Laser Deposition
R_p	Polarization resistance
R_{ct}	Charge transfer resistance
R_s	Solution resistance
R_{po}	Pore resistance
RBS	Rutherford Backscattering Spectrometry
RF	Radio Frequency

SCC	Stress Corrosion Cracking
SS	Stainless Steel
SE	Secondary Electrons
SAED	Selected Area Electron Diffraction
SEM	Scanning Electron Microscopy
SRIM	Stopping and Range of Ions in Matter
$T_{1/2}$	Half life
TEM	Transmission Electron Microscopy
U-235	Uranium 235
UHV	Ultra High Vacuum
XRD	X-Ray Diffraction

Chapter 1

Introduction

1. Introduction

Corrosion products are generated at high temperature and high pressure by the interaction of the structural materials with the coolant in the primary heat transport (PHT) system of pressurized heavy water reactor (PHWR). Some of these corrosion products get neutron activated in the core and are relocated over the out of core surfaces where the oxide present acts as the host for the incorporation of activated corrosion products. Decontamination processes are applied to remove these activated corrosion products which reduces the radiation fields and minimizes its effect to the operating and maintenance personnel. To further minimize the corrosion rates of these structural materials, efforts are being made worldwide by modifying the size of the oxide particles to nano size and/or by changing the composition of the oxides by the addition of an external metal ion viz. Ni^{2+} , Zn^{2+} and Mg^{2+} ions which could improve the adherence and protectiveness of the interfacial oxide film. This thesis is all about the development of nano-ferrite coatings of Ni, Zn and Mg on the structural materials of nuclear power plants like PHWR.

This chapter discusses the types of reactors, their water chemistry and formation of activated corrosion products, radiation field build up and decontamination of these surfaces using chemical formulations. The aim and scope of this work are presented along with a brief literature review.

1.1. Types of Reactors

1.1.1. Pressurised Water Reactor (PWR)

In the most common PWR, ordinary water is used as both coolant and moderator. The design is distinguished by having a primary cooling circuit which flows through the core of the reactor under very high pressure and a secondary circuit in which steam is generated to drive the turbine. Water, whose temperature in the reactor core reaches ~ 325 °C, is kept under a pressure of 150 atm to prevent its boiling. In the primary cooling circuit, the moderator is also water. The secondary circuit steam generators are under less pressure and the water is allowed to boil in the heat exchangers. The generated steam drives the turbine and produces electricity. The condensed steam is then returned to the heat exchangers in contact with the primary circuit.

1.1.2. Boiling Water Reactor (BWR)

It is similar to PWR, except that there is only a single circuit where the water is at a lower pressure ~ 75 atm and boils in the core at ~ 285 °C. This generated steam passes through the steam separators above the core and directed to the turbines of the reactor circuit. Most of the radioactivity in the water is very short-lived (mostly N-16 with $T_{1/2}$ of 7s).

1.1.3. Pressurised Heavy Water Reactor (PHWR or CANDU)

The PHWRs are CANDU (CANada Deuterium Uranium) reactors. These reactors use natural uranium (0.7% U-235) oxide as fuel and hence need a more efficient moderator compared to light water which is heavy water (D_2O). The primary side

heavy water is under high pressure so that the temperature of water reaches 300 °C without getting boiled. The primary coolant passes through the steam generator and generates steam in the secondary circuit (light water) which is then allowed to drive the turbines. Figure 1.1 shows the schematic of the PHT system of typical PHWR circuit [1].

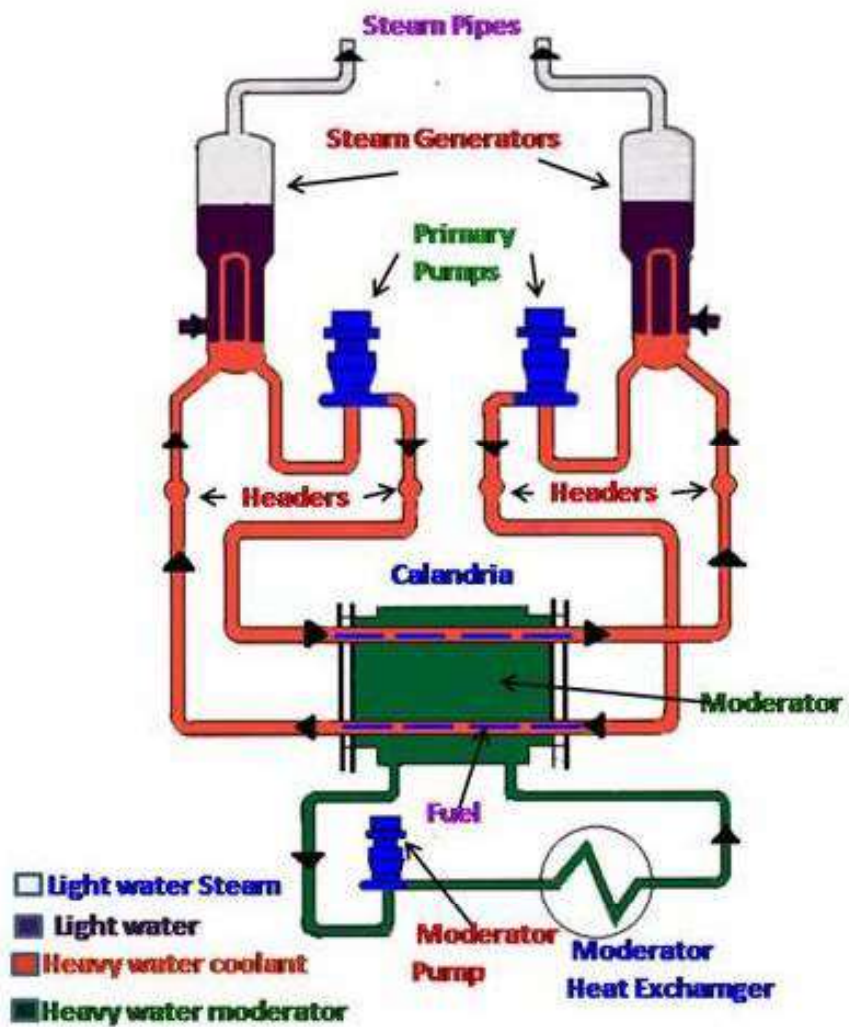


Figure 1.1: Schematic of PHT system of PHWR [1]

1.2. Water Chemistry

The operational safety of a nuclear power plant depends on the design, materials and the environment which is nothing but, water, in case of water cooled nuclear power plants. However, for an already operating plant, the design and materials are fixed and only the water chemistry can be tuned with. In this context, the water chemistry becomes very important. The major goals of water chemistry are i) to minimize corrosion release and to prevent corrosion degradation of systems and components, ii) to minimize radiation field build up and iii) to ensure compatibility with the fuel. By suitable water chemistry specifications tailor-made for each type of reactors, the above goals can be achieved.

1.2.1. BWR primary water chemistry

In earlier years, Boiling water reactors (BWRs) have been using ‘classic’ water chemistry also known as ‘normal water chemistry’ (NWC), with pure water of low conductivity and low impurity content. With this chemistry, an oxidizing environment prevailed in the circuit due to the presence of dissolved oxygen and hydrogen peroxide derived from radiolysis in the core, caused stress corrosion cracking (SCC) in components and piping’s made of stainless steel. To mitigate this, NWC was replaced with ‘hydrogen water chemistry’ (HWC) wherein hydrogen was injected into the feed water thereby reducing the oxidizing conditions necessary for SCC. However, HWC led to two main negative effects viz., i) a significant increase of the main steam line radiation levels due to more volatile ^{16}N species formed in the reactor water and ii) an increase in shutdown radiation fields due to structural changes of the oxide layers on inner system surfaces under reducing conditions. To

mitigate these problems, methods like ‘noble metal chemical addition’ (NMCA) wherein the oxide layers are modified by doping a catalyst in conjunction with the reduction of the feed water hydrogen concentration and zinc (depleted zinc oxide (DZO), to avoid Zn⁶⁵) addition were introduced respectively [2–6].

1.2.2. PWR primary water chemistry

The factors contributing to the PWR primary water coolant chemistry are pH, zinc injection and dissolved hydrogen [7]. The major corrosion product was considered to be magnetite (outer layer) and hence a pH_{300°C} of 6.9 was maintained to keep the solubility of magnetite close to the minimum and also to give a slightly positive temperature coefficient of solubility at this point. But, the major corrosion product turned out to be nickel ferrite (outer layer) and hence based on solubility and corrosion product transport, the pH_{300°C} of 7.4 was maintained to minimize dose rates and operational radiation exposure [8].

The beneficial effect of zinc (Zn) on shutdown dose rates in BWR units with Cu/Zn alloy condensers was observed [9]. Zn is also being added in the PWR units to reduce the dose rates explained by zinc's affinity for the tetrahedral sites of spinel oxide. Zn is also added to mitigate the initiation of primary water stress corrosion cracking on Alloy 600. The hydrogen concentration was applied to mitigate water radiolysis and to minimise crack growth rates.

1.2.3. PHWR primary water chemistry

The primary objectives of chemistry control in the PHT system of PHWR are to minimize the corrosion of CS and zirconium alloy surfaces operating under alkaline conditions and to reduce the radiolytic production of oxidizing species. Other objectives are to minimize deposition of corrosion products on the fuel and controlling the concentration of activated corrosion products and fission products in the system. These objectives are accomplished by dosing and control of primary coolant pH and deuterium concentration through regular additions of lithium hydroxide and hydrogen gas.

Table 1.1 gives chemistry parameters maintained in the primary circuit of the water cooled reactors namely BWR, PWR and PHWR.

Table 1.1: Chemistry parameters in primary circuit of water cooled reactors

Parameters	Primary Circuit		
	BWR	PWR	PHWR
Temperature	270-280 °C	325-340 °C	250-300 °C
Dissolved oxygen	~ 200 ppb (NWC)	< 10 ppb	< 10 ppb
	~ 20 ppb (HWC)		
Cl ⁻	< 0.2 ppm	< 0.15 ppm	< 0.2 ppm
pH _{RT}	7.0	10.5 using LiOH	10.5 using LiOH

1.3. Structural materials in water cooled nuclear reactors

A variety of alloys i.e. carbon steel, stainless steel, high nickel alloys, zirconium alloys and hard facing alloys have been used in reactors, depending upon the zone

where they are employed, based on the neutron economy, material strength, heat transfer efficiency and corrosion resistance. The elemental compositions of the metal alloys used in water cooled nuclear reactors are shown in Table 1.2. Apart from the elements shown in Table 1.2, ‘Si’ is also present as trace elements in carbon steel, stainless steel and Zr-1% Nb and ‘Mn’ is present in the range 0.4 - 0.9 % in carbon steel and 0 - 15 % in stainless steel. Depending on the reactor type, the surface areas of different materials exposed to the primary coolant differ considerably [10].

Table 1.2: Composition of Materials (% w/w) used in a Nuclear Power Plant

	Fe	Cr	Ni	Mo	Co	Zr	Sn	Cu	C	W
Carbon Steel	Bal	-	-	-	0.015	-	-	0-0.5	0.1-0.3	-
Stainless Steel	Bal	5-20	0-10	2-3	-	-	-	-	0-0.3	-
Zircaloy-2	0.1	0.1	0.05	-	-	Bal	1.5	-	-	-
Zircaloy-4	0.21	0.09	-	-	-	Bal	1.6	-	-	-
Zr-1% Nb	0.01	-	0.005	-	-	Bal	-	0.001	-	-
Zr-2.5% Nb	0.04	0.06	-	-	-	Bal	-	-	0.0185	-
Monel-400	2.5	-	63-70	-	0.1	-	-	Bal	-	-
Inconel-690	6-10	14-17	72	-	0.03	-	-	-	-	-
Incoloy-800	Bal	19-23	30-35	-	0.03	-	-	-	-	-
Stellite	-	20-33	0-13	0-6	50-60	-	-	-	0-2.5	5-20

A nuclear reactor is a complex system of different connected materials that behave optimally to ensure safe and efficient operation of the plant. Even under the stringent water chemistry control, the properties of the structural materials in nuclear reactors degrade under radiation and corrosive environments. The understanding of

degradation or failure mechanisms provides useful inputs in developing and implementing corrective measures. Hence, basic knowledge of different forms of corrosion is a prerequisite in understanding the materials selection and chemistry requirements of nuclear power plants.

1.4. Formation and Transport of Activity in PHWR

In CANDU reactors, heavy water is used as the coolant and moderator and the neutron absorption by deuterium atoms in heavy water will convert to radioactive tritium having a half-life of 12.3 years. The coolant also contains trace amount of dissolved ions and particulates due to the corrosion of the PHT system materials which get activated by the absorption of neutrons as it passes through the reactor core by different mechanisms. Zirconium alloy wear products released by the movement of fuel inside the fuel channel during refueling and fission products released by the failure of the fuel cladding are transported to out of the core locations along with the activated corrosion products and get incorporated into the oxide layers increasing the radioactivity levels. Co-60 is the major contributor of radiation fields with a long half life. Typical activation and fission products observed in the PHT and their half-lives are shown in Table 1.3.

Table 1.3: Common radioactive isotopes and their source in the PHT system

Activation product	Source	Half Life
Cr-51	Chromium alloys	27.7 days
Fe-59	Steels and iron alloys	44.6 days
Sb-124	Impurity in steels and iron alloys (bearings and wear surfaces)	60.2 days
Co-58	Nickel alloys	70.8 days
Mn-54	Steels and iron alloys	312.5 days
Co-60	Impurity in steels and iron alloys (hard-facing materials for wear resistance (e.g. Stellites))	5.27 years
I-131	Fission product	8.04 days
Xe-133	Fission product	5.24 days
Xe-135	Fission product	9.1 hours
Kr-85	Fission product	10.73 years
Kr-88	Fission product	2.84 hours

1.5. Oxide formed on Structural Materials

Depending on the composition of the structural material and coolant condition, the corroded metal ions deposit as different oxides on the structural material. The oxides formed on the structural material have duplex layers [11-12]. The inner layer formed in situ from the metal is thin and protective in nature. The outer layer formed due to the precipitation of corrosion product from the coolant is porous in nature. These oxide films acts as a host for the incorporation of active species into the primary circuit materials in nuclear power plants. In PHWR, carbon steel (CS) is exposed to reducing and an alkaline condition of the coolant and magnetite (Fe_3O_4) is formed

on the surface [13-14]. A nuclear reactor uses many alloys and the actual corrosion products consists of several transition metals other than iron, leading to the formation of substituted ferrites or chromites [15-16]. Table 1.4 gives the nature of the oxide layers formed on primary circuits of BWR, PHWR and PWR [17].

Table 1.4: Nature of the oxide layers formed on primary circuits of BWR, PHWR and PWR

Oxide Layers	BWR	PHWR	PWR
1 - Base Metal	SS	CS	SS
2 - Inner layer	FeCr ₂ O ₄ , Cr ₂ O ₃	Fe ₃ O ₄	FeCr ₂ O ₄ , Cr ₂ O ₃
3 - Outer layer	NiFe ₂ O ₄ , Fe ₃ O ₄ , Fe _{2-x} Cr _x O ₃ (2<x<0), Ni _x Fe _{3-x-y} Cr _y O ₄ (x≤1, y ≤1)	Fe ₃ O ₄ /NiFe ₂ O ₄	Fe ₃ O ₄ , NiFe ₂ O ₄ , Fe _{2-x} Cr _x O ₃ (2<x<0), Ni _x Fe _{3-x-y} Cr _y O ₄ (x≤1, y ≤1)
4 - Outermost layer	α-Fe ₂ O ₃	-	-

1.6. Chemical decontamination of Primary Heat Transport (PHT) system

Chemical decontamination processes are used for the removal of the deposited radionuclides to minimize the radiation dose to occupational workers. Dilute Chemical Decontamination (DCD) removes the radioactive deposits by dissolving the deposited oxide in a controlled manner. The DCD technology has been standardized for Indian PHWRs.

1.7. Corrosion control and prevention

Corrosion control and prevention would bring significant benefits to the industry, if the corrosion management strategies starting from design, manufacturing, operation, maintenance, in-service inspection and online monitoring are followed in a systematic way. The deposition of a protective film is an effective solution to protect the metal from a corrosive attack. Coatings can protect a substrate providing a barrier between the metal and its environment and/or through the presence of corrosion inhibiting chemicals in them. In order to provide adequate corrosion protection, the coating must be uniform, well adherent and pore free.

1.8. Nanocoatings

Nanocoatings on surfaces are the most important nanoscale engineering technology through which a vast range of functionalities and new physical effects can be achieved. In general, the corrosion resistance of nanocrystalline materials in aqueous solutions is of great importance in assessing a wide range of applications. To date, research in this area is still scarce and relatively few studies have addressed this issue. On the other hand, for nanostructured materials produced by electrodeposition, considerable advances in the understanding of microstructure on the corrosion properties have been made in recent years [18].

2. Literature Review

The literature survey on various synthesis methods of oxide powders was carried out. Many synthesis techniques have been developed such as solid state reaction [19], spray pyrolysis [20], sol-gel [21-22], hydrothermal [23-26], microemulsion

[27] and co-precipitation [28-29]. The morphology and chemical composition of the synthesized powder can be controlled efficiently by co-precipitation and sol-gel methods but sol-gel and hydrothermal methods are time consuming and difficult to maintain the reaction conditions. Co-precipitation is one of the successful techniques for synthesizing ultrafine powders with narrow particle size distribution [30-32]. The special attention was given on the literature published on the synthesis of ferrites namely nickel ferrite, zinc ferrite and magnesium ferrites. The properties of these ferrites are greatly affected by the characteristics of the powder such as particle size, morphology, purity and chemical composition by different synthesis methods. Hence, for the synthesis of the three ferrites, co-precipitation method was chosen in this work to achieve uniform particle size and purity.

The different deposition techniques are listed in Table 1.5. Pulsed Laser Deposition (PLD) method was chosen for the ex-situ deposition of the ferrites on CS due to its advantages of maintaining the stoichiometry of the ferrites to be coated and the thickness of the coating can be varied in faster time duration. Hydrothermal method which is closer to the real systems was chosen for the in-situ deposition of the ferrites on CS. Table 1.6 gives a brief literature survey on co-precipitation and deposition techniques.

Table 1.5: Various deposition techniques

Physical deposition	Chemical deposition
1. Evaporation techniques	1. Sol-gel technique
a. Vacuum thermal evaporation	2. Chemical bath deposition
b. Electron beam evaporation	3. Spray pyrolysis technique
c. Pulsed laser deposition	4. Plating
d. Arc evaporation	a. Electroplating technique
e. Molecular beam epitaxy	b. Electroless deposition
f. Ion plating evaporation	5. Chemical vapor deposition (CVD)
2. Sputtering techniques	a. Low pressure (LPCVD)
a. Direct Current (DC) sputtering	b. Plasma enhanced (PECVD)
b. Radio Frequency (RF) sputtering	c. Atomic layer deposition (ALD)
	6. Hydrothermal

Table 1.6: Literature survey on synthesis and deposition

Co-precipitation	Deposition
ZnFe ₂ O ₄ (33-36)*	PLD (45-52)*
NiFe ₂ O ₄ (37-40)*	Hydrothermal (53-59)*
MgFe ₂ O ₄ (41-44)*	

(* Numbers denote the references)

2.1. Literature on hydrothermal studies of CS in presence of Ni²⁺, Zn²⁺ and Mg²⁺ ions

As accumulation of radioactive cobalt (Co*) on oxides is the main reason for the radioactivity build up around the PHT system, major research has been carried out to reduce cobalt uptake. Jerzy A. Sawicki and Heather A. Allsop [55] used conversion electron and X-ray backscattering Mossbauer spectroscopy to identify iron compounds formed on carbon steel in simulated CANDU reactor coolant containing 15 to 60 ppb soluble zinc. Analysis of these specimens exposed to coolant in the absence of zinc indicated the formation of magnetite, whereas a layer of zinc ferrite ($Zn_xFe_{3-x}O_4$) was evidenced in the presence of zinc. T. Osato et.al [56] studied the effect of zinc and nickel addition on cobalt uptake using 316 L SS and CS in 285 °C water under HWC condition. The addition of zinc and nickel resulted in reduced cobalt uptake rates for all materials and reduction was highest at both chemical additions. Haginuma et. al [57] investigated the cobalt accumulation behaviour in 304 SS exposed to high temperature water containing 200 ppb dissolved oxygen. The effect of zinc addition on the cobalt accumulation in the outer layer is not apparent at the initial stage; however the cobalt accumulation is reduced after 500 hours exposure. The zinc addition suppresses the cobalt accumulation in the inner layer. It was also inferred that the cobalt suppression by zinc addition occurs by different mechanisms in oxygenated and deoxygenated conditions. In order to better understand the mechanism of zinc effect, electrochemical and electrical properties of oxide films were studied by J. Piippo et.al [58] on AISI 347, Incoloy 800 and Celsit V in a simulated PWR environment containing zinc. From this study it was observed that zinc is incorporated into the oxide film only after an initial period, during which

the electric field within the film diminishes because of increasing thickness of the film. Zinc had no effect on the properties of the oxides, indicating that the initial period needed for incorporation of zinc into the oxides is longer than the maximum exposure time of 200 hours. Vinit et. al [59] have studied the corrosion resistance of an additional magnesium ferrite coating over magnetite layer formed on CS in neutral medium and found an increase in the corrosion resistance property.

3. Aim and Scope of the study

3.1. Aim

Among all the structural materials listed in Table 1.2, CS, the alloy used in feeder pipes with a total surface area of 1500 m² in the primary circuit, is the least corrosion resistant material. Hence, CS was chosen for this work to study the effect of nano ferrites coating in enhancing the corrosion resistance.

The corrosion products formed over CS surfaces are mainly magnetite (Fe₃O₄) in the inner layer and Fe₃O₄/nickel ferrite (NiFe₂O₄) in the outer layer. The nickel released from nickel based steam generator tubes partially converts the Fe₃O₄ in the outer layer into NiFe₂O₄. Hence, NiFe₂O₄ was chosen as one of the ferrites for this study. Similarly, the beneficial effect of zinc injection known in BWR and PWRs is being tested for PHWR and its effect on CS. Zinc injection in PHWR may convert the Fe₃O₄ to ZnFe₂O₄. Hence, ZnFe₂O₄ was chosen as another ferrite for this work. Though zinc ion was successful in reducing the radiation field build-up in BWRs, the formation of active isotope ⁶⁵Zn by neutron activation leads to radioactive waste

management problems. In this context, the Mg^{2+} ion which has similar electronic configuration and size with respect to Zn^{2+} ion can be used to form $MgFe_2O_4$ [60]. Hence, $MgFe_2O_4$ was also taken up as the third ferrite for this study.

Thus, the aim of this work is to develop a nano ferrite of type MFe_2O_4 [$M= Ni, Zn$ and Mg] as a coating / film on CS or magnetite coated carbon steel (CS/Fe_3O_4) which would give a better corrosion resistance property compared to Fe_3O_4 .

3.2. Scope of work

- Synthesis of $NiFe_2O_4$, $ZnFe_2O_4$ and $MgFe_2O_4$ and its characterization by X-Ray diffraction and Laser Raman Spectroscopy. Deposition of as synthesized $NiFe_2O_4$, $ZnFe_2O_4$ and $MgFe_2O_4$ on CS/Fe_3O_4 by pulsed laser deposition technique in nano size.
- To incorporate nickel, zinc and magnesium ions in magnetite lattice during the formation of oxide film on CS by hydrothermal method in a static autoclave.
- To characterize the $NiFe_2O_4$, $ZnFe_2O_4$ and $MgFe_2O_4$ coatings/films on CS/Fe_3O_4 by PLD and on CS by hydrothermal technique respectively to monitor its size, crystallinity, chemical composition, adhesion and surface morphology.
- To study the corrosion resistance properties of $NiFe_2O_4$, $ZnFe_2O_4$ and $MgFe_2O_4$ coatings/films on CS specimens by electrochemical methods and based on this study the corrosion protection offered on CS by the ferrite coatings developed by two different techniques will be compared.

Chapter 2

Experimental methods

2. Purpose of the research program

The main objective of this research program was to develop a better corrosion resistance oxide film/coating than the naturally formed oxides on the carbon steel (CS) surfaces, one of the structural materials, in the primary heat transport (PHT) system of PHWRs and to understand their corrosion behaviour.

In this work, attempts were made to deposit nickel ferrite, zinc ferrite and magnesium ferrite on CS to obtain the coatings in nano size by pulsed laser deposition (PLD) method. Hydrothermal method, one closer to the real system of the power plant, was used for carrying out experiments to incorporate the cations (Ni^{2+} , Zn^{2+} and Mg^{2+}) into the oxide lattice during its formation on CS.

i). For the PLD method, three ferrites namely NiFe_2O_4 , ZnFe_2O_4 and MgFe_2O_4 were synthesized by co-precipitation method. The powders were then formed into pellets which were used as a target for the PLD process. Synthesis of the respective ferrites, pellet formation and the PLD procedures are explained in detail in this chapter.

ii). For the hydrothermal method, CS specimens were exposed for different time duration in presence of Ni^{2+} , Zn^{2+} and Mg^{2+} ions to form the corresponding oxides/ferrites by the autoclave method which is also discussed in detail.

iii). Surface characterization techniques: Grazing incidence X-ray diffraction (GI-XRD) and Laser Raman Spectroscopy (Raman) were used to identify and confirm the phases formed after synthesis and after the deposition on CS. X-ray Photoelectron Spectroscopy (XPS) was used for the quantification of the elements present in the oxides and ferrites formed on the CS specimen.

iv). Surface morphology techniques: Scanning Electron Microscopy (SEM) and Energy Dispersive X-ray microanalysis (EDAX) were used to investigate the morphology and composition of the deposited oxides and ferrites. Focused Ion Beam (FIB) - SEM and Transmission Electron Microscopy (TEM) were used for the analysis of the interface between the substrate and the ferrite coating.

v). Electrochemical techniques: To know the corrosion resistance of the coated specimens, potentiodynamic anodic polarization (PDAP) and electrochemical impedance spectroscopy (EIS) were used. Mott Schottky method was used to understand the semiconducting properties of the ferrite coated CS.

Flow chart of the work carried out by (a) PLD and (b) hydrothermal method are as given in Figure 2.1.

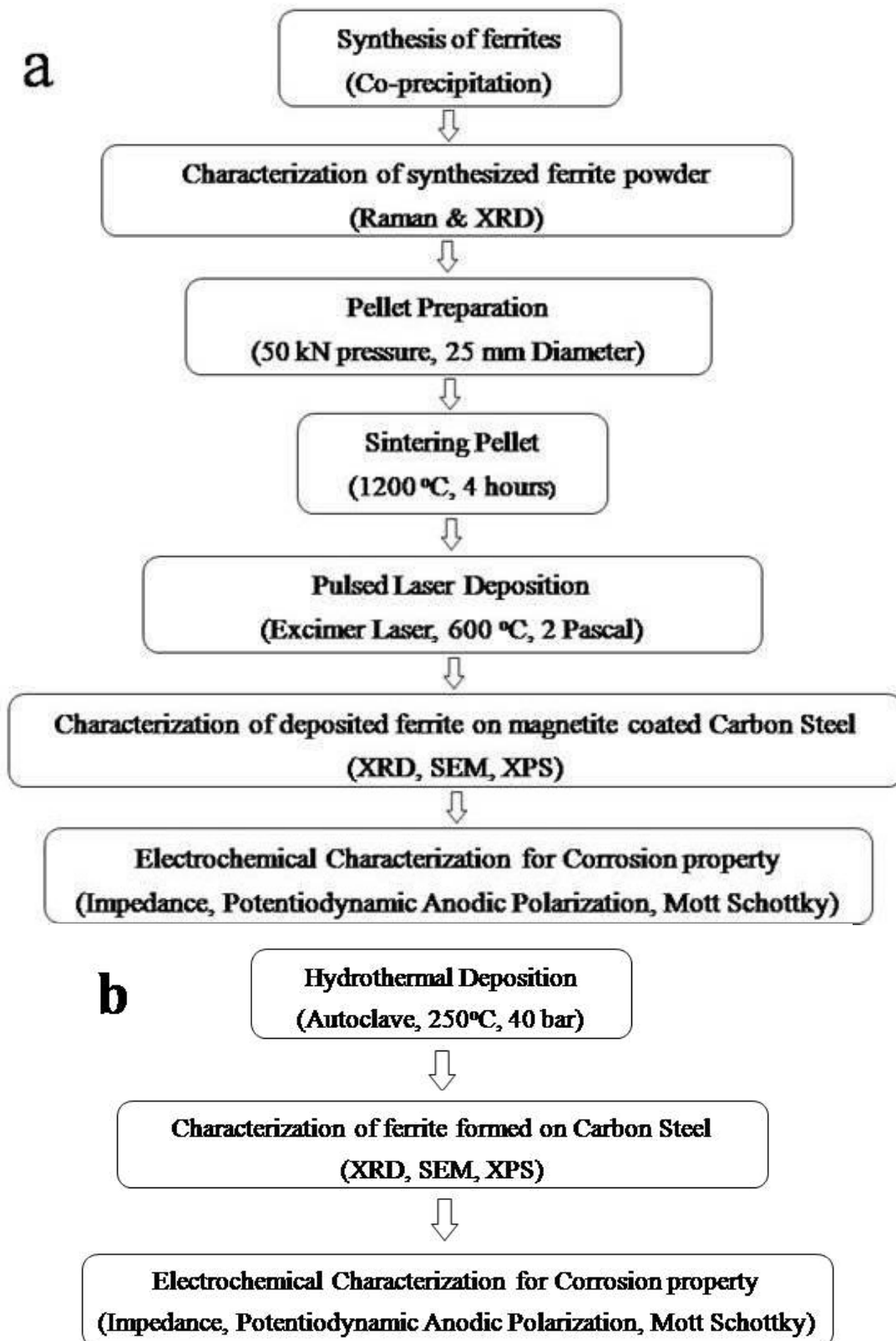


Figure 2.1: Flowchart of the work

2.1. Synthesis of Ferrite powder

2.1.1. Chemicals used in the synthesis process

2.1.1 (a) Preparation of Zinc Ferrite powder: Zinc (II) Sulphate ($\text{ZnSO}_4 \cdot 7\text{H}_2\text{O}$) and Ammonium Iron (II) Sulphate ($\text{NH}_4\text{Fe}(\text{SO}_4)_2$)

2.1.1 (b) Preparation of Nickel Ferrite powder: Nickel (II) Sulphate (NiSO_4) and Ammonium Iron (II) Sulphate ($\text{NH}_4\text{Fe}(\text{SO}_4)_2$)

2.1.1 (c) Preparation of Magnesium Ferrite powder: Magnesium (II) Sulphate (MgSO_4) and Ammonium Iron (II) Sulphate ($\text{NH}_4\text{Fe}(\text{SO}_4)_2$)

The stoichiometric amounts of the above mentioned salts were dissolved in 500 ml of double distilled water. Sodium hydroxide (NaOH) was added to the above solution by continuously stirring and the precipitate started forming till the pH reached 10.5. The precipitate was then allowed to settle and washed with distilled water so that the pH of solution reached ~ 8.0 . The precipitate was kept in an oven at 110°C till all the water evaporated to form a hard solid mass. This hard solid mass was crushed to powder using mortar and pestle and transferred to a crucible. This powder was then calcined in a muffle furnace at 650°C for 6 hours to form the respective ferrites in single phase. The weight of the calcined powder was taken. The formations of stoichiometric synthesized ferrites (NiFe_2O_4 , ZnFe_2O_4 and MgFe_2O_4) in the powder were confirmed by Raman spectroscopy and powder XRD. The photograph of the synthesized powders is shown in Figure 2.2. All the three ferrites obtained were brown in color.

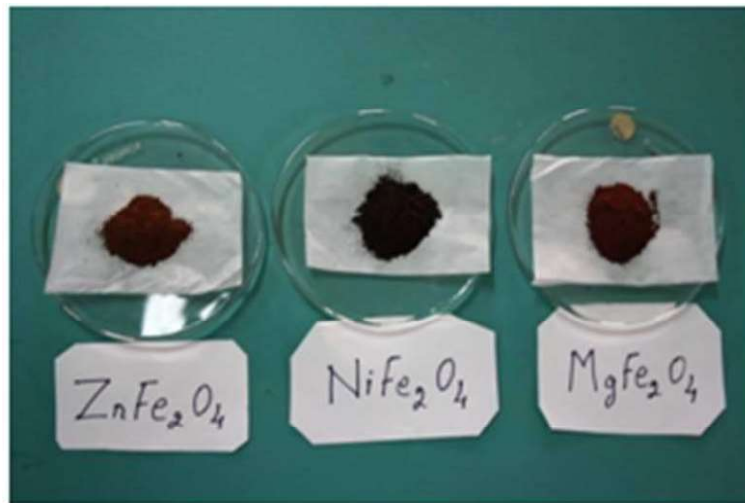
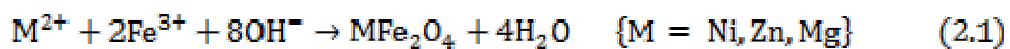


Figure 2.2: Photograph of the synthesized ferrite powders

The overall chemical reaction for the formation of MFe_2O_4 may be written by the following equation (2.1) [61-62].



2.2. Preparation of pellet

The synthesized powder was compacted into a 25 mm diameter circular pellet of 3 mm thickness by applying a pressure of 26 MPa using hydraulic press and sintered at 1200 °C for 4 hours, then cooled to room temperature to obtain the target required for deposition. The experimental density of sintered target was calculated to be 4.14 g/cm³ against the theoretical density of 5.1 g/cm³. The achieved density was ~ 80 % of theoretical value required for the PLD target preparation. The photograph of the pellets is shown in Figure 2.3.

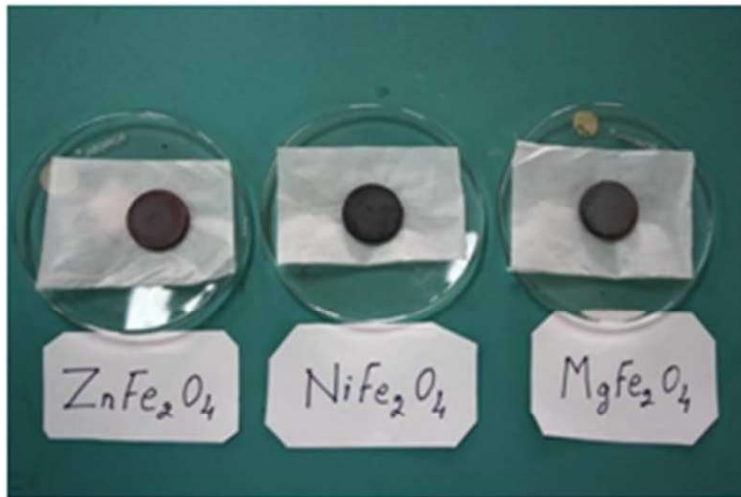


Figure 2.3: Photograph of the pellets

The prepared pellets were stuck to the holders used as targets in the PLD process.

The photograph given in Figure 2.4 shows the target holder.



Figure 2.4: Photograph of the target holders

2.3. Preparation of lithium hydroxide

The lithium hydroxide (LiOH) solutions were prepared by passing suitable amounts of lithium carbonate ($LiCO_3$) solution through regenerated anion (OH^-) resin column

with an optimized flow rate of 15 mL / min to achieve complete conversion of LiCO_3 to LiOH . Fresh LiOH containing 1.5 ppm of Li^+ ion was prepared for each electrochemical experiment and the pH was in the range 10.2 - 10.4 and conductivity was in the range 40 - 47 $\mu\text{S}/\text{cm}$. The experimental set up for LiOH preparation is as shown in Figure 2.5.



Figure 2.5: Photograph of the experimental setup used for LiOH preparation

2.4. Hydrothermal method

2.4.1. Formation of magnetite (Fe_3O_4) on CS

Direct deposition of the ferrites on CS by PLD was not feasible as the coatings were peeling off and not adherent. Hence, Fe_3O_4 formed on CS specimens ($\text{CS}/\text{Fe}_3\text{O}_4$) were used as a substrate for the PLD process. Fe_3O_4 was formed on CS in a stainless steel (SS-304) lined autoclave, the schematic is shown in Figure 2.6 (used for passivation only) using alkaline LiOH solution which was collected as explained in

section 2.3 in a round bottom flask by deaerating with argon gas. This flask was connected to the autoclave and deaerated for two hours along with the experimental LiOH solution and 0.3 ml of Hydrazine was added in 500 ml LiOH solution to scavenge the remaining oxygen. After two hours, the experimental solution was transferred to the autoclave in which the CS specimens (approximately 30 Nos.) were arranged as shown in Figure 2.8. The temperature of the autoclave vessel was raised to 130 °C and the autoclave was vented out and then the temperature was raised to 250 °C and maintained at $250\text{ °C} \pm 0.2\text{ °C}$ for 96 hours duration. After the 96 hours exposure, the autoclave temperature was reduced to 25 °C and once the temperature of the solution cooled to 25 °C, the specimens were removed and rinsed with de-mineralised (DM) water, dried and preserved in a desiccator for the deposition process. Oxide film thickness was calculated by weighing the CS specimens before and after the exposure to the autoclave solution as explained in section 2.4.3. A magnetite film developed by exposing the CS for 96 hours was found to be sufficient / optimum for the PLD of various ferrite coatings.

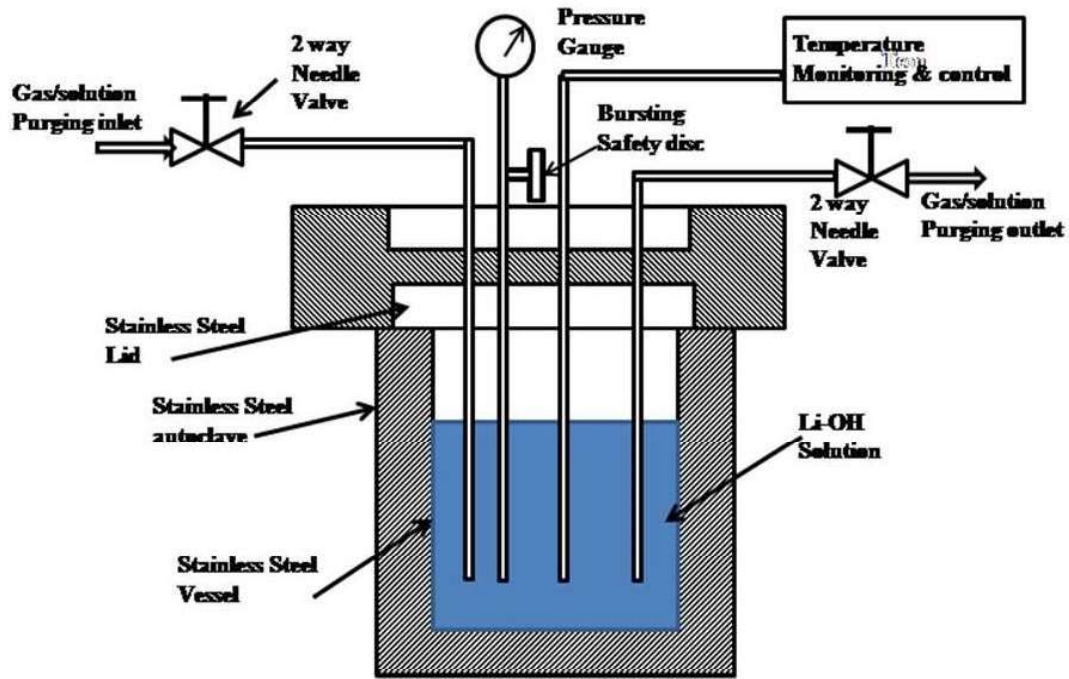


Figure 2.6: Schematic of Autoclave

2.4.2. Formation of oxides (Fe_3O_4 , $NiFe_2O_4$, $ZnFe_2O_4$ and $MgFe_2O_4$) on CS

2.4.2.1. Pre-conditioning of autoclave

The autoclave was pre-conditioned with the experimental solution as given in Table 2.1 for 96 hours duration at 250 °C for three consecutive times in absence of the specimen under study.

Table 2.1: Experimental solution for high temperature studies

Ferrite formation	Experimental solution
Fe_3O_4	LiOH
$NiFe_2O_4$	LiOH + Ni^{2+} (1000 ppb)
$ZnFe_2O_4$	LiOH + Zn^{2+} (1000 ppb)
$MgFe_2O_4$	LiOH + Mg^{2+} (1000 ppb)

2.4.2.2. Ferrite formation

The CS specimens, of size (1 cm × 1 cm) and composition in weight % as given in Table 2.2, were polished with different grades of silicon carbide (SiC) papers starting from 80 and final finish with 800 grit. Then, they were washed with distilled water, degreased with acetone, dried in air and preserved in a desiccator for further experimental use. The experimental apparatus used for the formation of the coating at high temperature was an autoclave made up of Hastelloy B of 1 litre capacity as shown in Figure 2.7. This autoclave consisted of temperature and pressure control facilities along with gas purging. The CS specimens (12 Nos.) were arranged in a stainless steel (SS) stand as shown in Figure 2.8 and placed inside the autoclave. The experimental LiOH solution with pH and conductivity of 10.3 and 43 $\mu\text{S}/\text{cm}$ respectively at 25 °C were deaerated by continuous purging with argon gas. The dissolved oxygen was maintained < 10 ppb by initial argon gas purging and venting at 130 °C. After each exposure duration (24, 96 and 240 hours) the autoclave temperature was reduced to 25 °C and the specimens were removed once the autoclave temperature reached 25 °C and then rinsed with demineralised (DM) water, dried and used for characterization and corrosion studies. Oxide film thicknesses were calculated by weighing the CS specimens before and after the exposure to the autoclave solution as mentioned in section 2.4.3. As there was no significant change in the corrosion resistance values for magnetite above 240 hours, a maximum exposure time of 240 hours was fixed for the formation of the various ferrites.

Table 2.2: Chemical composition of CS (weight %)

Elements	C	Si	Mn	Cr	Ni	Fe
Weight %	0.16	0.35	0.85	< 0.3	< 0.14	Balance



Figure 2.7: Photograph of the Autoclave

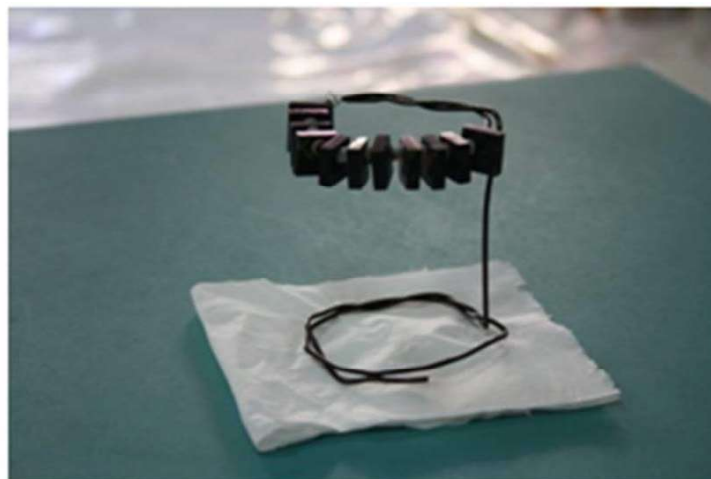


Figure 2.8: Photograph of the Stainless Steel stand with CS specimens

For NiFe₂O₄, ZnFe₂O₄ and MgFe₂O₄ formation, 1000 ppb of Ni²⁺, Zn²⁺ and Mg²⁺ was added in the form of salts of nickel sulphate, zinc sulphate and magnesium sulphate respectively to the experimental solution. The autoclave was heated to 250 °C in three hours and the temperature was maintained at 250 ± 0.2 °C for the entire duration of the experiment. All the oxide film formation studies were carried out in a Hastelloy B autoclave where nickel is the main constituent of the inner surface. Analysis of the experimental solution, after the respective hours exposure was carried out by ICP-AES to quantify the ions present in the solution.

2.4.3. Thickness measurement

The standard ASTM G1-90 procedure [63] was used to measure the thickness of the oxide layer formed on the CS surface after the exposure in the autoclave. The oxide formed specimen and a blank specimen of identical surface area were immersed in a Clarke's solution (mixture of SnCl₂ (5 g) and Sb₂O₃ (2 g) in 100 mL of 11.6 M HCl solution) for 30s [64]. From the weight loss, the thickness of the oxide layer was calculated as given in equation (2.2).

Thickness of oxide layer in μm

$$\frac{(W_1 - W_2) - (W_3 - W_4) \times 10^4}{A \times \rho} \quad (2.2)$$

where 'W₁' is the weight of oxide formed specimen before descaling in g, 'W₂' is weight of oxide formed specimen after descaling in g, 'W₃' is weight of blank specimen before descaling in g, 'W₄' is weight of blank specimen after descaling in g, 'A' is surface area of the oxide formed specimen in cm², and 'ρ' is density of the

oxide formed and 10^4 is the factor to convert cm to μm . The thickness of the Fe_3O_4 formed on CS was calculated and found to be $\sim 0.45 \mu\text{m}$.

2.5. Pulsed Laser Deposition (PLD)

Pulsed Laser Deposition process uses high power laser to ablate the material from the target and deposits onto a substrate in a vacuum atmosphere. The impact of the laser energy creates an expanding coating plume and subsequently condenses as a solid material on a substrate. Figure 2.9 shows the basic schematic of PLD system.

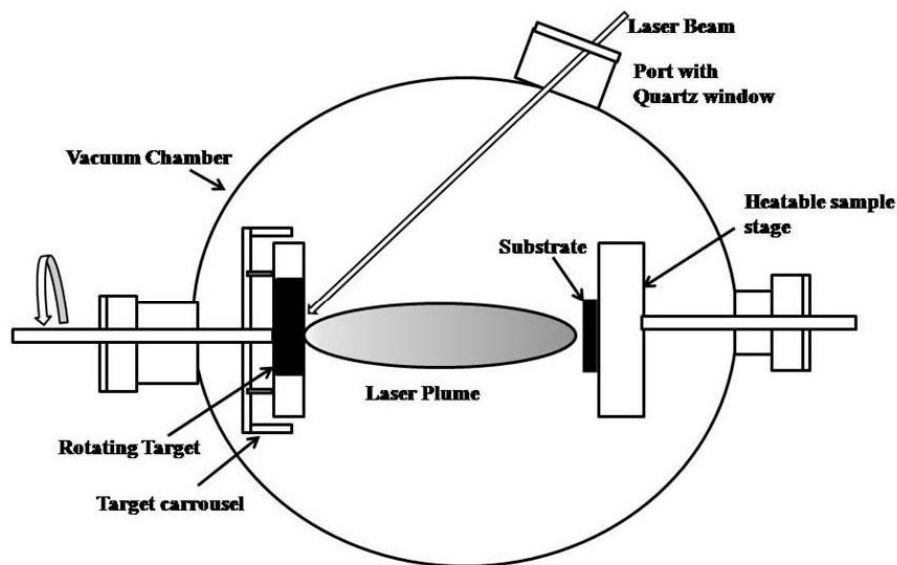


Figure 2.9: Schematic of PLD system

2.5.1. The mechanism of PLD

The principle of PLD is a complex phenomenon involving the following four stages. Each stage in PLD is critical to the formation of crystalline, stoichiometric and uniform thin film. The properties of the thin films can be controlled by laser

intensity, substrate temperature, and gas pressure and incident angle of the coating plume.

First stage: The laser beam is focused onto the surface of the target. At sufficiently high flux densities and short pulse duration, all elements in the target are rapidly heated up to their evaporation temperature. Materials are dissociated from the target surface and ablated out with stoichiometry as in the target.

Second stage: The emitted materials move towards the substrate. The spot size and the temperature of the laser have significant effects on the uniformity of deposited film. The target-to-substrate distance governs the angular spread of the ablated materials.

Third stage: This stage determines the quality of thin film. The ejected high energy species impinge onto the substrate surface and may induce various type of damage to the substrate. These energetic species sputter some of the surface atoms and a collision region is formed between the incident flow and sputtered atoms. Film grows after a thermalized region is formed which acts as a source for condensation of particles. When the condensation rate is higher than the rate of particles supplied by the sputtering, thermal equilibrium condition can be reached quickly and film grows on the substrate surface.

Fourth stage: Nucleation and growth of crystalline film depends on density, energy, degree of ionization, type of the condensing material, temperature and physical-chemical properties of the substrate. The nucleation depends on the interfacial energies between the three phases i.e. substrate, the condensing material and the vapor. The critical size of the nucleus depends on the deposition rate and the

substrate temperature. High temperature favors rapid and defect free crystal growth whereas low temperature results in disordered and amorphous structures.

2.5.2. The main advantages of PLD process

1. Conceptually simple: A laser beam vaporizes a target producing a film with the same composition as the target
2. Versatile: A large variety of materials and mixtures can be deposited in a wide variety of gases over a broad range of gas pressures
3. Ability: To preserve the stoichiometric ratio of the target material
4. Good adhesion between coating and substrate
5. Coating at room temperature
6. Cost-effective: One laser can serve many vacuum systems
7. Fast: High quality samples can be grown reliably in 10 or 15 minutes
8. Scalable: As complex oxides move toward volume production
9. Optimized thickness is obtained faster

In this study, PLD technique was used to deposit NiFe_2O_4 , ZnFe_2O_4 and MgFe_2O_4 on $\text{CS/Fe}_3\text{O}_4$. KrF excimer laser ($\lambda = 248$ nm, 5 ns pulse duration, 10 Hz repetition rate) model Lambda Physik, COMPex 102 (Figure 2.10) was used for deposition of NiFe_2O_4 , ZnFe_2O_4 and MgFe_2O_4 thin film on $\text{CS/Fe}_3\text{O}_4$ substrate. The beam was focused to 2 mm on a rotating target. The deposition of the above ferrites was carried out in a high-vacuum chamber, evacuated to a base pressure lower than 8×10^{-6} Torr by means of a turbo-molecular pump. To maintain the stoichiometry of the deposited film, O_2 gas pressure of 3×10^{-2} Torr was used inside the chamber. The

substrate (Figure 2.11) temperature and the energy of the laser beam during deposition were maintained at 600 °C and 500 mJ respectively. The target-to-substrate distance was maintained at 5 cm. The optimization of the thickness was carried out with NiFe₂O₄ coating. The deposition time was varied to obtain NiFe₂O₄ film thickness of approximately 200, 325 and 500 nm as measured by Stylus Profilometer. Based on the studies on NiFe₂O₄ film, a maximum thickness of 500 nm (corresponding to maximum corrosion resistance) was fixed for the deposition of ZnFe₂O₄ and MgFe₂O₄ films.

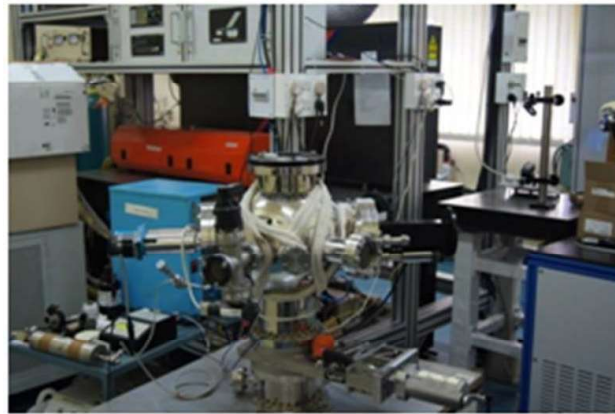


Figure 2.10: Photograph of the Pulsed Laser Deposition system

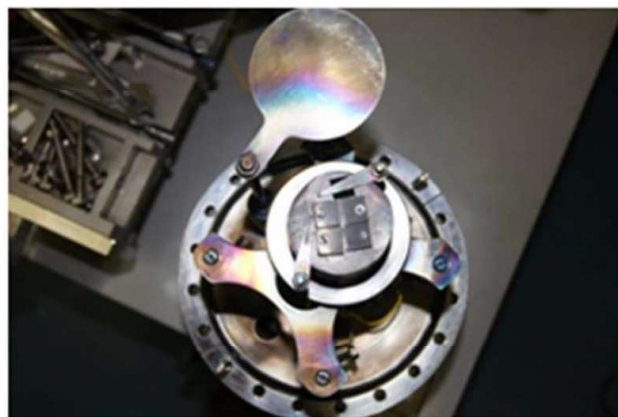


Figure 2.11: Photograph of the substrate stand with CS specimen

2.6. Characterization of deposited oxide coating/film

2.6.1. X-Ray Diffraction (XRD)

X-rays are mainly used in crystallography studies, because X-ray wavelength (0.1 nm) is similar to the 'd' spacing of planes in a crystal lattice. X-ray diffraction (XRD) is a technique which follows the principle of Bragg's law as shown in Figure 2.12. It is a method for determining the arrangement of atoms within a crystal, in which a beam of X-rays strikes a crystal and causes the beam of light to spread into many specific directions. It is based on constructive (presence of peak) and destructive (absence of peak) interference of monochromatic X-rays with a crystalline sample. X-rays consist of three basic units: an X-ray tube, a sample holder and an X-ray detector. X-rays are generated in a cathode ray tube by heating a tungsten filament to produce electrons, accelerating the electrons toward a suitable target (Cu, Fe, Mo, Cr, Co) by applying a voltage, and bombarding the target material with electrons. When electrons have sufficient energy ($>10^4$ eV) to dislodge inner shell electrons of the target material, characteristic X-ray spectra are produced. Copper is the most common target material for single crystal diffraction, with Cu radiation = 1.541 Å. These X-rays are collimated and directed onto the sample. As the sample and detector are rotated, the intensity of the reflected X-rays is recorded. When the geometry of the incident X-rays strike the sample and satisfies the Bragg Equation as given in equation (2.3), constructive interference occurs. A detector records and processes this X-ray signal and converts the signal to a count rate which is manipulated to a device such as a printer or computer monitor [65-66].

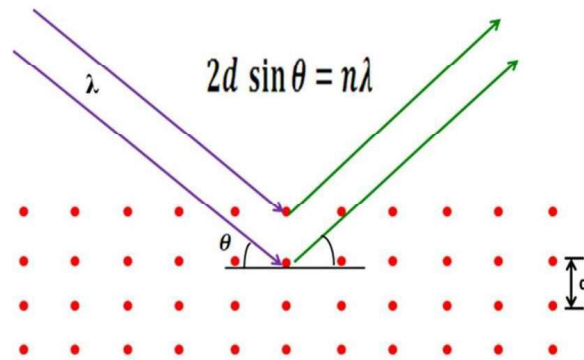


Figure 2.12: Principle of Bragg's law

$$n\lambda = 2d \sin \theta \quad (2.3)$$

where, λ = wavelength of X-ray, θ = Incident angle and d = Inter planar spacing.

The geometry of an X-ray diffractometer is such that the sample rotates in the path of the collimated X-ray beam at an angle θ while the X-ray detector is mounted on an arm to collect the diffracted X-rays and rotates at an angle of 2θ .

2.6.1.1. Grazing Incidence-XRD (GI-XRD)

It is used to study thin film surfaces because wave penetration is limited. In this, source of X-ray (incident angle) is fixed at low angle (0.5°). Sample holder and detector are variable. In GI-XRD, information from the substrate is not detected and it is more about surface of thin film. In the case of a stress-free material, the interplanar spacing ' d ' for a particular reflection ($h k l$) is constant from one crystallite to another. When it is deformed elastically, the lattice spacing of the crystallites change from their stress free values and a shift in the Bragg angle is observed. The strain calculated from this shift is termed as lattice strain. The lattice strain depends upon the orientation of the reflecting group of crystallites with respect to the direction of

stress [67]. In thin film, the peak position and the Full Width at Half Maximum (FWHM) of the diffraction peak contains information about the sample [68]. The average crystallite size of oxides was determined from the Scherrer formula given by equation (2.4),

$$L = \frac{K\lambda}{\beta \cos\theta} \quad (2.4)$$

where L is the average particle size, K is the Scherrer constant related to the shape and index (hkl) of crystals [69], λ is the wavelength of incident radiation and β is obtained from the Warren and Biscoe equation given by equation (2.5) [70],

$$\beta^2 = B^2 - b^2 \quad (2.5)$$

where 'B' and 'b' are the full width at half maxima for the sample under investigation and a standard sample respectively.

In this study, the synthesized powders were characterized by XRD using STOE diffractometer in the Bragg-Brentano geometry on these films with Cu k_{α} as the incident radiation ($\lambda = 1.541 \text{ \AA}$) in the range of $2\theta = 10^{\circ}$ – 90° with a step size of 0.05° .

High Resolution X-ray Diffraction instrument (Bruker D8 Discover) was used for the analysis of NiFe_2O_4 , ZnFe_2O_4 and MgFe_2O_4 coated on $\text{CS/Fe}_3\text{O}_4$ samples using GI-XRD in parallel beam geometry. Gobel mirror, a graded multilayer parabolic X-ray beam conditioner was used to convert the divergent X-ray beam from a line focus tube to an intense monochromatic parallel beam of $\text{CuK}_{\alpha 1}$ ($\lambda=1.541 \text{ \AA}$) operated at 6

kW. GI-XRD patterns were obtained for these samples by fixing the incident angle θ at 0.5° and 2θ at 15° to 85° with a step size and scan speed of 0.05° and 4 sec/step respectively.

2.6.2. Scanning Electron Microscopy (SEM)

Figure 2.13 shows the principle of SEM used for acquiring information about the surface morphology. In this method, the sample is probed by an electron beam scanned across the surface. Different types of radiations from the specimen are displayed. Secondary electron (SE) imaging uses electrons emitted by the specimen with energies between 0 and 50 eV and is the most common mode of operation of SEM since these electrons are easy to collect and carry information about the surface topography of the specimen. Another mode of SEM is backscattered electrons (BSE) which are electrons emitted from the specimen with energies between 50 eV and the incident beam energy E_0 . Back scattered electrons carry information about substrate atoms and atomic mass. For this microscopy, the specimens were coated with gold and an electron gun produces a finely focused beam of electrons called the primary electron beam. This beam of electrons passes through electromagnetic lenses and directed over the samples surface, knocking out the electrons out of the coating, producing secondary electrons, which are transmitted to an electron collector, amplified and used to produce an image on a viewing screen. The resolution is 20 nm and it can magnify the objects up to 10,000 times. It can be used in elemental analysis based on distribution of elements of different atomic numbers on the surface.

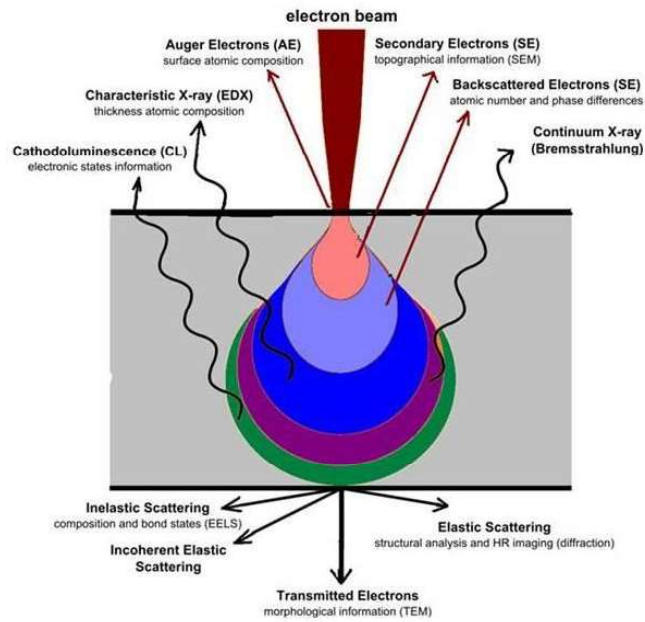


Figure 2.13: Principle of SEM

In this study, the surface morphology and the elemental composition of the PLD coated oxide samples were characterized by HR-SEM (Helios Nanolab 600i) operating at 20 keV electron beam energy. Energy Dispersive X-ray Spectroscopy (EDAX) analysis of the samples was carried out using 20 keV beam energy and the microscope was fitted with an X-max 80 mm² EDAX detector from Oxford Instruments. The oxide films formed on CS in presence of Ni²⁺, Zn²⁺ and Mg²⁺ ions were characterized by FE-SEM (Supra 55, Carl Zeiss) operating at an acceleration voltage between 100 V to 30 KV with a resolution of 0.8 nm at 15 KV and 1.6 nm at 1 KV. Thicknesses and uniformity of PLD coatings were studied by cross sectional FE-SEM. The samples were placed vertically and molded using araldite and hardener. The molded sample was then polished up to 1200 grade by SiC paper followed by diamond polishing of 0.5 μm size. The samples were cleaned with soap solution, water and acetone. The polished side of the coated samples was used for cross section images by FE-SEM (Carl Zeiss).

2.6.3. X-Ray Photoelectron Spectroscopy (XPS)

XPS is a spectroscopy of photoelectrons generated from atom due to X-ray hitting the materials and these photoelectrons provide both elemental and chemical information from all kinds of solid material. XPS is a surface sensitive technique due to inelastic scattering losses of photoelectrons; as a result only photoelectrons from top few atomic layers are detected.

2.6.3.1. Principle of XPS

Bombarding a sample in ultra high vacuum with soft X-ray (~1.5 KeV) gives rise to the emission of photoelectrons from core shells. If the energy of monochromatic X-rays is known ($h\nu$) and the kinetic energy of the emitted photoelectrons (K_e) is measured with an electron spectrometer then the binding energy (B_e) of the atomic orbital from which the electron originates can be calculated by the equation (2.6).

$$B_e = h\nu - K_e - \phi \quad (2.6)$$

The work function (ϕ) is the minimum amount of energy an individual electron needs to escape from the surface and get detected by the spectrometer. The typical value of the spectrometer work function is around 4.5 eV. Each element produces a unique set of electrons with specific energies. An XPS spectrum is obtained by measuring the number of these electrons as a function of binding (or kinetic) energy. With the exception of H and He, all elements can be detected. Figure 2.14 shows a typical schematic of XPS principle.

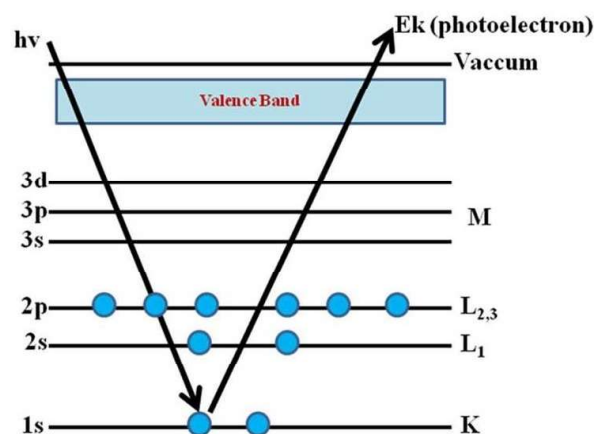


Figure 2.14: Principle of XPS instrument

2.6.3.2. Instrumentation

Electron spectrometers are made up of components such as source, sample holder, analyzer, detector, signal processor and readout. It works under the ultra high vacuum of 10^{-10} Torr. In XPS equipment, vacuum is required to avoid energy loss of photoelectrons due to scattering by gas molecules and to avoid surface contamination due to adsorption of gas molecules from the measurement chamber. Ultra high vacuum (UHV) less than 10^{-9} Torr were achieved by rotary and turbomolecular pumps in the preliminary stage and ion pumps for UHV level with auxiliary titanium sublimation pumps. The energy of soft X-ray and FWHM must be optimized to cover the whole range of elements and their chemical information. Al and Mg K_{α} are mostly being used as a source. Al k_{α} X-ray energy is 1486.6 eV and FWHM is 0.85 eV while for Mg k_{α} , X-ray energy is 1253.6 eV and FWHM is 0.75 eV. Most photoelectron spectrometers use hemispherical type electron analyzer where electron beam is deflected by an electrostatic magnetic field generated between the two hemispherical plates. The deflection of electron beam follows the

curved path and the radius of curvature depends on the kinetic energy of electron and the magnitude of an electrostatic field. Scanning of various kinetic energy electrons is carried out by focusing them at the detector by varying the field strength. The analyzer is maintained at or below 10^{-5} Torr pressure [71]. Electron spectroscopy for chemical analysis provides qualitative and quantitative information about the elemental composition and oxidation states of elements of solid surfaces. It also provides useful structural information [72]. A low resolution, wide scan of XPS spectra gives the elemental composition of samples.

In this study, XPS (Model VG ESCALAB MK200X, UK) was used with Al k_{α} as an X-ray source and 150 mm hemispherical analyzer at 20 eV pass energy, for collecting the photoelectrons. The instrument was calibrated with Au $4f_{7/2}$ line at 84.0 eV with 1.6 FWHM [73]. Carbon 1s peak at 285.1 eV was used as an internal standard for charge correction in the case of insulating samples. The data acquisition and deconvolution of the spectra were carried out using dedicated software 'Eclipse V2.1' supplied along with the instrument. The component spectra were fitted with a Gaussian-Lorentzian peak functions on a Shirley background.

2.6.4. Laser Raman Spectroscopy (Raman)

Spectroscopic techniques are powerful for characterization as they provide fundamental information about the structure and surface reaction intermediates under controlled environments.

2.6.4.1. Raman Effect

Raman Effect results from the inelastic scattering of electromagnetic radiation by matter. It gives information about the properties of molecules and structure from their vibrational transitions. Figure 2.15 shows the excitation of vibrational energy level.

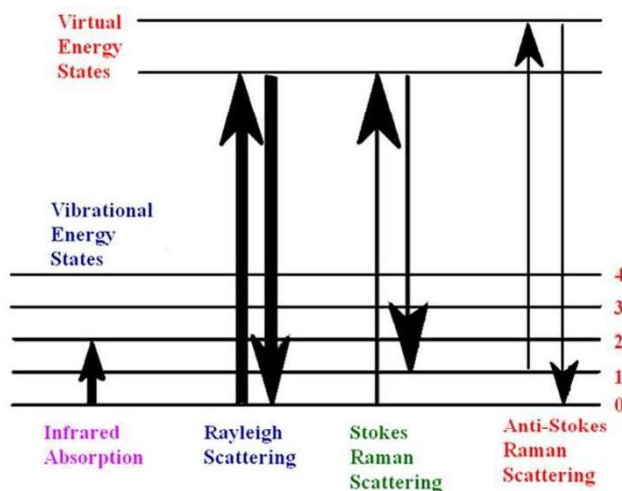


Figure 2.15: Excitation of vibrational energy level

2.6.4.2. Components of a Raman Spectrometer

Figure 2.16 shows the schematic of the Raman spectrometer with three components viz., an excitation source, a sampling apparatus and a detector. Modern Raman instrumentation has been developed with laser as an excitation source, a spectrometer for the detector and either a microscope or a fiber optic probe for the sampling apparatus.

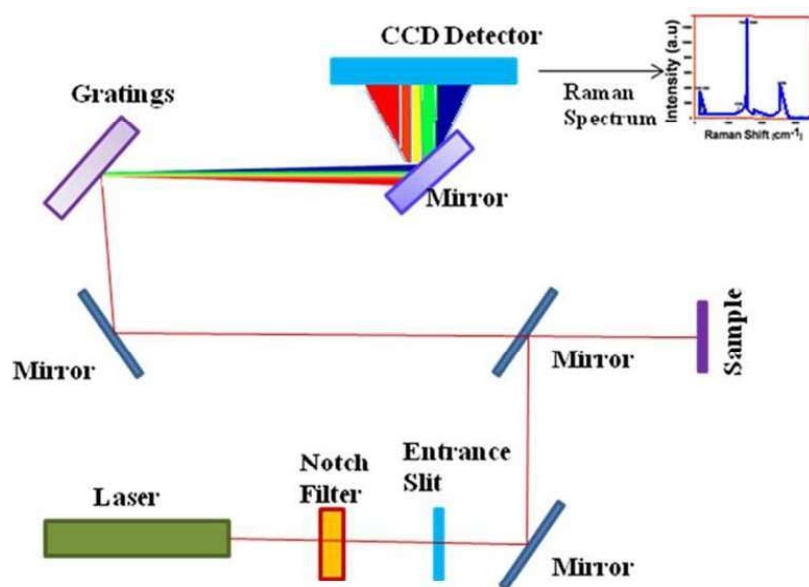


Figure 2.16: Instrumentation of Raman spectroscopy

Raman spectroscopy has the ability to measure a shift in wavelength /or frequency, hence, a monochromatic excitation source, a laser with narrow bandwidth and extremely stable frequency is used because the qualities of the Raman peaks are directly affected by the sharpness and stability of the excitation light source. Raman scattering is very weak and requires long integration times to collect enough photons for a measurable signal and hence, a Charged Coupled Device (CCD) is used to increase the sensitivity of the spectrometer. To resolve the closely spaced peaks, a high resolution spectrometer with 532 and 785 nm laser excitation wavelengths are used. Typical spectral ranges of as low as 65 cm⁻¹ to as high as 4000 cm⁻¹ with a spectral resolution of 3 cm⁻¹ are used. A Raman probe capable of directing and focusing the monochromatic excitation source to the sample, collecting the scattered light and directing it to the spectrometer are used. Since a pure signal is extremely important, a narrow band pass filter is placed in the optical path of the excitation

source before it reaches the sample. Since the Raman Effect is extremely weak, the signal must be collected at a 0° angle normal to the sample. This causes interference from Rayleigh scattering and therefore it is essential to filter the collected signal through the use of a long pass filter before it is directed to the spectrometer.

In this study, Raman spectra were recorded on the sample using HORIBA Jobin Yvon HR 800 spectrometer with 514.5 nm Ar^+ ion laser. Laser power was optimized considering the (S/N) ratio to 0.5 mW. Spectrometer is equipped with CCD detector which is air cooled to -70°C and edge filter which can cut off the Rayleigh line close to 100 cm^{-1} . Raman spectra acquisition was carried out for 30 sec using a 50X long working distance objective lens and 1800 grooves/mm grating.

2.6.5. Transmission Electron Microscopy (TEM)

TEM uses electron beam capable of displaying magnified images of a thin specimen ($< 100\text{ nm}$), typically with a magnification in the range 10^3 to 10^6 to create an image. In addition, TEM is also used to produce an electron diffraction pattern which is very useful for analyzing crystallographic nature of specimens. The electron beam is focused on to sample surface by using electromagnetic lenses. Electron beam is transmitted through the specimen, which is transparent to electron. Electron beam after interaction with the specimen carries information about the structure of the specimen that is magnified by the objective lens system of the microscope. The spatial variation in this information is viewed by projecting the magnified electron image onto a fluorescent viewing screen coated with a phosphor or a scintillator material such as zinc sulphide. The image can be photographically recorded by

exposing a photographic film or plate directly to the electron beam, or a high resolution phosphor may be coupled by means of a lens optical system or a fiber optic light guide to the sensor of a CCD (Charged Coupled Device) camera. The image detected by the CCD may be displayed on a monitor or computer. The high energy electrons (typically 200 keV) used in a transmission electron microscope penetrates easily through many planes of thin specimen. The wavelength of high energy electrons is in picometer range and the spacing between atoms in a solid is about a hundred times larger, the array of atoms in crystal act as a diffraction grating to the electrons which are diffracted. That is, some fraction of them will be scattered to particular angles, determined by the crystal structure of the sample. This results in a series of bright spots for single crystal and bright ring for polycrystalline materials (since grain size \ll beam diameter at the specimen). Since the beam is focused on the particular particle, crystal or area it is called as selected area electron diffraction. This diffraction information can be correlated to the crystal structure or space group.

The ray diagrams of imaging mode and diffraction mode of operation in an electron microscope are shown in Figure 2.17. A transmission electron microscope is constituted of: (1) two or three condenser lenses to focus the electron beam on the sample, (2) an objective lens to form the diffraction in the back focal plane and the image of the sample in the image plane and (3) some intermediate lenses to magnify the image or the diffraction pattern on the screen. If the sample is thin (< 200 nm) and constituted of light chemical elements, the image presents a very low contrast when it is focused. To obtain amplitude contrasted image, an objective diaphragm is inserted in the back focal plane to select the transmitted beam (and possibly few

diffracted beam): the crystalline parts in Bragg orientation appear dark and the amorphous or the non-Bragg oriented parts appear bright. This imaging mode is called the bright field mode (BF) (Figure 2.18). If the diffraction is constituted by many diffracting phases, each of them can be differentiated by selecting one of its diffracted beams with the objective diaphragm. To do that, the incident beam must be tilted so that the diffracted beam is put on the objective lens axis to avoid the off-axis aberrations (Figure 2.18). This mode is called the dark field mode (DF). The BF and DF modes are used for imaging materials to nanometer scale. The selected area diaphragm is used to select only one part of the imaged sample for example a particle or a precipitate. This mode is called selected area electron diffraction (SAED). The spherical aberrations of the objective lens limit the area of the selected object to a few hundred nanometers. Nevertheless, it is possible to obtain diffraction patterns of a smaller object by focusing the electron beam with the projector lenses to obtain a small spot size on the object surface (2-10 nm).

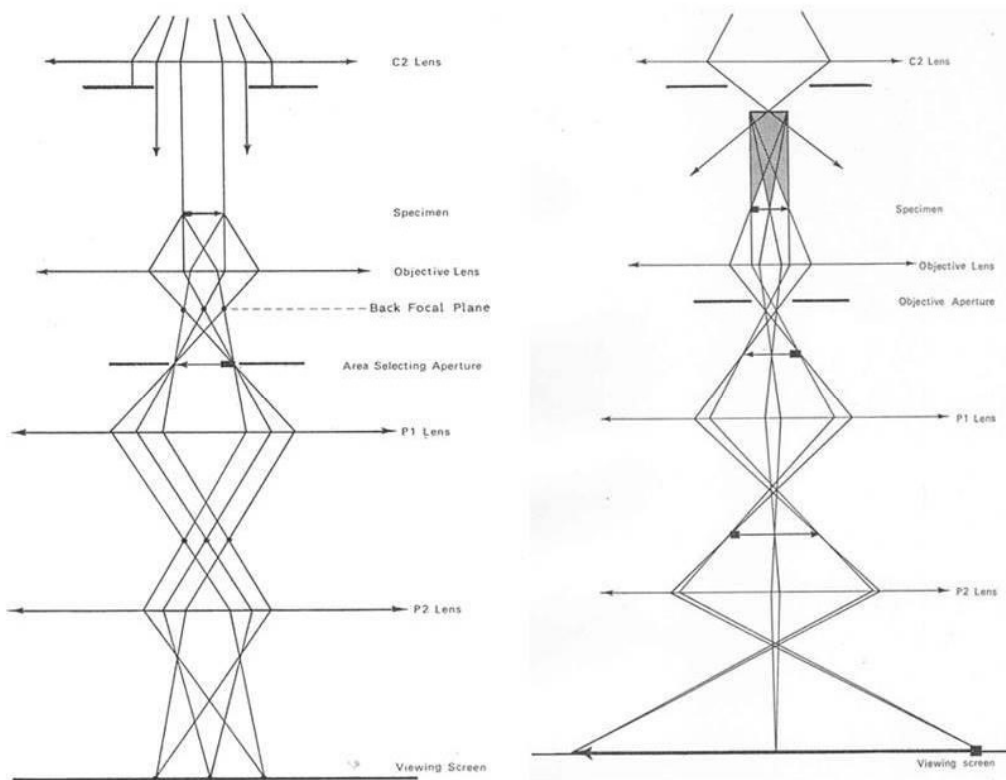


Figure 2.17: The ray diagrams of imaging mode and diffraction mode in Transmission Electron Microscope.

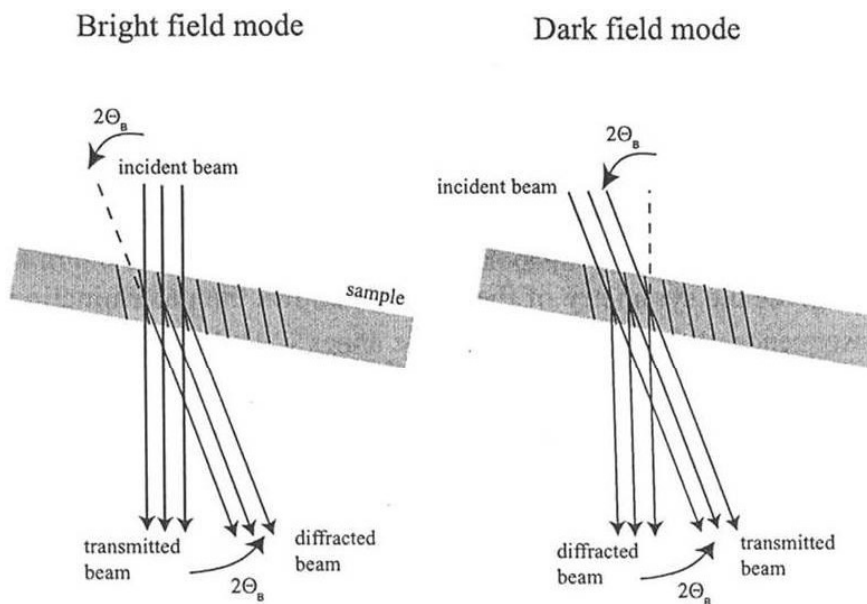


Figure 2.18: The bright field and dark field modes for imaging

In this study, the cross sectional specimen of the PLD deposited NiFe₂O₄ coating prepared by FIB-SEM were characterized by LIBRA 200 FE (Carl Zeiss Germany), a High Resolution Transmission Electron Microscope (HRTEM) operated at 200 keV, equipped with Schottky field emission gun (FEG) source and an in-column omega energy filter. The information limit of the microscope is 0.13 nm. Elemental analysis was performed by electron energy loss spectroscopy (EELS) conducted in the TEM.

2.6.6. Rutherford Backscattering Spectrometry (RBS)

RBS is a well established technique for thin film characterization in which a beam of high energy (2 MeV) helium ions is directed at a sample. The helium ions elastically scattered by nuclei in the sample are detected. The higher the mass of an atom that is hit by a helium ion, the higher the energy of the ion will be after backscattering. This results in mass discrimination. By counting the helium ions as a function of energy, the number of atoms of each element present can be determined. An advantage of RBS is that it yields the amount of atoms present quantitatively without the need for any calibration standard. Furthermore, the crystallinity of samples can be investigated using channeling RBS. Using RBS, information can be obtained from the surface down to a depth of approximately 2 μm without the need for sputtering. This makes the technique fast and eminently suitable for applications in thin film research. As backscattering can only occur from atoms that are heavier than the projectile ion, hydrogen cannot be detected by RBS. Properties such as thickness, composition at the surface and contamination are critical parameters of thin films. The thickness of the ferrite coatings developed by PLD on carbon steel surface was

analyzed by Rutherford backscattering spectroscopy which can measure accurately through the depth of the thin film surface without destruction of the material. It provides information regarding in-depth profiling in a non-destructive manner.

2.6.6.1. Experimental set-up

The apparatus for Rutherford backscattering analysis of thin solid surface typically consist of three components:

1. A source of helium ions.
2. An accelerator to energize the helium ions.
3. A detector to measure the energy of scattered ions.

Figure 2.19 shows the experimental setup for the RBS measurement.

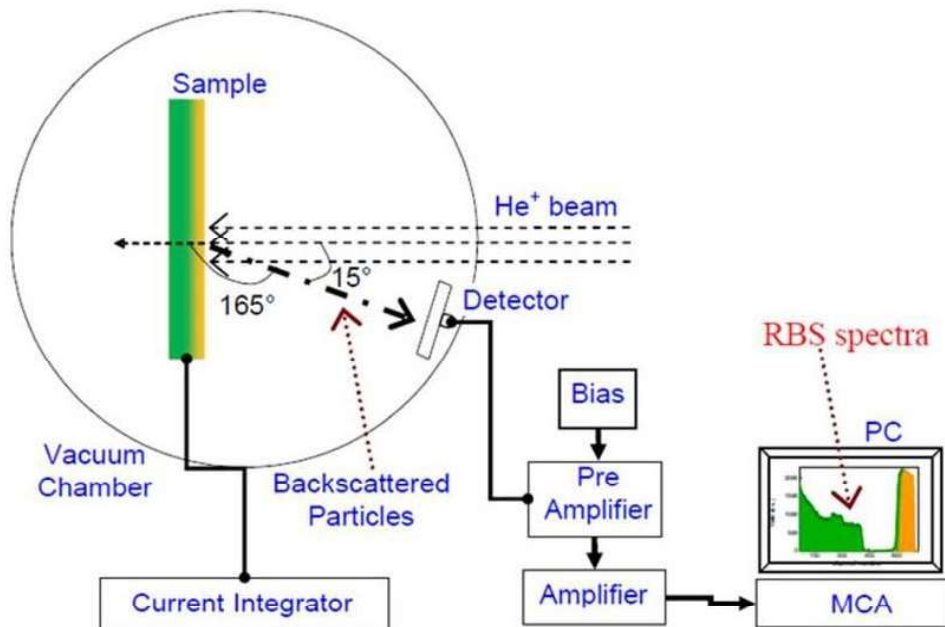


Figure 2.19: Schematic representation of a RBS set up

2.6.6.2. Depth profile analysis

It is a good approximation in thin film analysis that the total energy loss ΔE is proportional to depth, 't'. With this approximation, one can derive the relation between energy width ΔE of the signal from a film of thickness ' Δt ' as given in equation (2.7),

$$\Delta E = \Delta t \left(k \frac{dE}{dx_{in}} + \frac{1}{\cos \theta} \frac{dE}{dx_{out}} \right) \quad (2.7)$$

Where, θ = lab scattering angle, k is the kinematic factor and the subscripts "in" and "out" indicate the energies at which the rate of loss of energy or dE/dx is evaluated.

2.6.6.3. Applications of RBS

Various application of RBS include (1) Determination of composition of films, multilayers and bulk material, (2) Implantation profiles including dose calibration, (3) Surface and bulk contamination, (4) Interface mixing and reaction and (5) Diffusion profiles.

In the present work, Resonant Rutherford Backscattering Spectrometry (RRBS) has been widely used for analysis of light elements (low Z) like C, O and N in high Z matrix. The RRBS measurements were performed using 1.7 MV Tandem accelerators (HVEE, The Netherlands). The backscattered alpha particles were detected by a surface barrier silicon detector with scattering angle of 165° from the incident beam direction. The $^{16}\text{O}(\alpha,\alpha)^{16}\text{O}$ reaction with the resonant energy 3.04 MeV was chosen to measure the oxygen concentration in the samples and alpha

particles of energy varying from 3.04 to 3.19 MeV were used for profiling of oxygen in the sample.

2.6.7. Inductively Coupled Plasma – Atomic Emission Spectroscopy (ICP-AES)

An inductively coupled plasma spectrometer is a tool for detection of metals in solution in the concentration range of percentage to ultra-trace level. In plasma torch, liquid sample is injected into argon gas plasma contained by a strong magnetic field generated by RF generator. The plasma generates a temperature of approximately 8000 °C. At this temperature all elements become thermally excited and the electrons emit light at their characteristic wavelengths as they return to ground state. This light is collected by the spectrometer and passes through a diffraction grating that serves to resolve the light into a spectrum of its constituent wavelengths. Within the spectrometer, this diffracted light is then collected by photomultiplier tubes as detector and amplified to yield an intensity measurement that can be converted to an elemental concentration by comparison with calibration standards. This technique, also known as inductively coupled plasma - optical emission spectrometer (ICP-OES), is a very sensitive technique for identification and quantification of elements in a sample [74]. Most of the ICP-AES instruments are designed to detect a single wavelength at a time (monochromator) and this can be done in sequential scanning. Since an element can emit at multiple wavelengths and this wavelength can be captured simultaneously with polychromator, detection limits typically range from parts per million (ppm) to sub parts per billion (ppb), depending on the element and instrument.

In this research work, the ICP-AES from HORIBA JOBIN YVON model ULTIMA 2 was used for elemental analysis. The instrument has sequential scanning based on Czerny Turner monochromator with 1 meter focal length and a high frequency 40.68 MHz RF generator. The instrument gives resolution < 10 pm up to 430 nm and < 18 pm up to 430-800 nm. The relative standard deviation was less than 1.5% for elements analyzed by the technique.

2.6.8. Scratch Test

Scratch test is a method of mechanically testing the coating on the specimen surface. In this method, an indenter is used to generate a groove on the specimen surface by applying a progressively increasing normal force with the scan length of 3 mm, according to the ASTM standard C1624–05 [75]. Figure 2.20 shows the schematic of the scratch test. The general objective of performing scratch test in materials is to investigate the mechanisms of deformation or the removal of the material. It is also used to measure the hardness and evaluate the adhesion of the coating with the substrate. Adhesion property measurements are based on progressive loading to sense the failure of coating and to determine whether the failure is adhesive or cohesive. The results of a scratch test can vary widely depending on the specimen analyzed. Scratch test effects range from plastic grooving in a ductile material, to chipping in a brittle material, to interfacial de-adhesion of a coated specimen [76].

In this work, scratch test was carried out on CS/Fe₃O₄/NiFe₂O₄, CS/Fe₃O₄/ZnFe₂O₄ and CS/Fe₃O₄/MgFe₂O₄ using linear scratch test equipment (Revtect, M/s. CSM, Switzerland) and the scratch was made by 200 μ m radius hemispherical, Rockwell

type diamond indenter. During the scratch test, the load was increased gradually from 1 to 3 N at the rate of 3 N/min for a distance of 3 mm and parameters like applied normal load, tangential force, frictional force, penetration depth and acoustic emission were recorded automatically during the test.

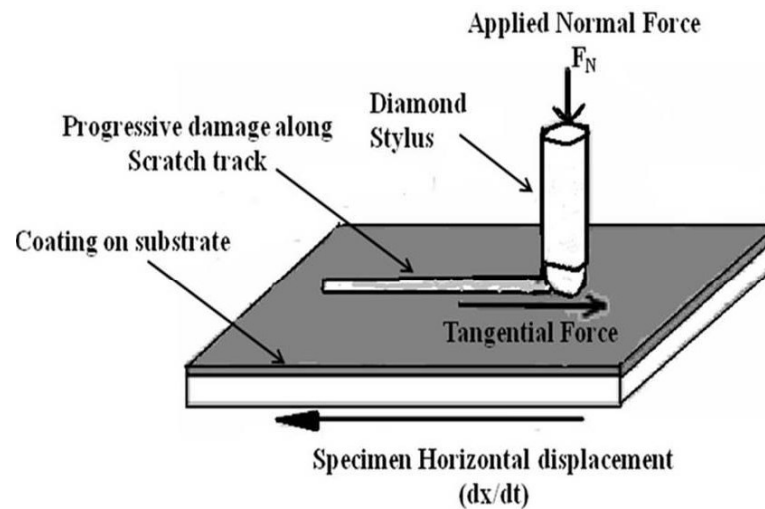


Figure 2.20: Schematic for scratch test

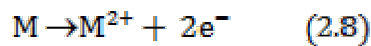
2.6.9. Surface Profilometry

Thickness of films developed by PLD process was measured by profilometer (DEKTAK XT). This method is used to measure the thicknesses in the range of 20 nm - 1 mm with 1 nm accuracy. NiFe_2O_4 , ZnFe_2O_4 and MgFe_2O_4 deposited on Si substrate along with the $\text{CS/Fe}_3\text{O}_4$ substrate and a step was created by putting a mask on the Si substrate. The diamond profiler of diameter 12.5 microns with vertical resolution of 1.5 nm was made to travel on the film across the mask on the substrate. The step size was measured by taking the difference between the height of

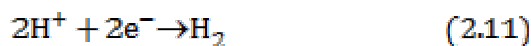
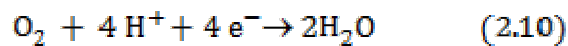
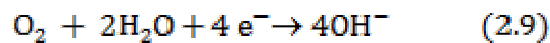
coated and uncoated regions of the sample. Three values of the steps were measured for each coating and the average value was taken as the thickness.

2.7. Electrochemical Techniques

Corrosion of metals proceeds by either chemical or electrochemical route or both simultaneously. In wet corrosion process, occurring in electrically conducting media (electrolytes), the electrochemical process consists of oxidation (electrons release or anodic chemical reaction) and reduction (electrons consume or cathodic chemical reaction) reactions. When the metal is immersed in acid solution the anodic electrochemical reaction follows equation (2.8).



Several reducing electrochemical reactions are possible depending on the reducible species present in the solution. Reduction of dissolved oxygen and reduction of water are the possible cathodic reactions given by the equations (2.9-2.11) [77].



At equilibrium, both oxidation and reduction rate are equal and corresponding potential represents the 'corrosion potential (E_{corr}) or open circuit potential (OCP)' of the system. As in the process of oxidation and reduction, there is a flow of electrons which

generates current. The currents correspond to reduction process is I_{red} and to oxidation process is I_{ox} . At equilibrium, $I_{\text{red}} = I_{\text{ox}}$ are equal and opposite in direction as given in equation (2.12).

$$I_{\text{total}} = I_{\text{red}} - I_{\text{ox}} = 0 \quad (2.12)$$

As net current is zero, any direct current measurement gives zero value. If I_{ox} or I_{red} could be directly measured at E_{corr} , calculating the naturally occurring corrosion rate would be a simple operation. The current (I_{ox} or I_{red}) at E_{corr} is called corrosion current or I_{corr} . The corrosion rate (milli inches per year) can be calculated using the equation (2.13) if I_{corr} is known:

$$\text{Corrosion Rate (mpy)} = \frac{0.13 \times I_{\text{corr}} \times E.W}{A \times D} \quad (2.13)$$

where, 'E.W' is the equivalent weight (in g/eg.) of the material under study, 'A' is the area of the specimen, 'D' is the density in g/cm^3 and 0.13 is the metric and time conversion factor. Calculation of I_{corr} is possible by the polarization of the specimen. In polarization, a corroding system is taken away from its equilibrium by imposing a potential other than its OCP. The degree of polarization is a measure of how the rates of the anodic and the cathodic reactions are retarded by various environmental and/or surface processes. The value of I_{red} or I_{ox} at E_{corr} can be determined by polarizing in a systematic manner and measuring the resulting current.

2.7.1. Tafel Plot

A Tafel plot is generated by an increase in potential stepwise (0.1 mV/sec) about 250 mV anodically and cathodically from the open circuit potential (OCP) and measuring

the corrosion current as shown in Figure 2.21 [77]. The corrosion current (I_{corr}) measured is used to calculate the corrosion rate by using equation (2.13). I_{corr} can be obtained by the intersection of the tangents at the linear Tafel region on either side of OCP. Tafel constants are calculated by measuring the slope of these extrapolated lines. Anodic linear region gives anodic Tafel constant (β_a) and cathodic linear region gives the cathodic Tafel constant (β_c).

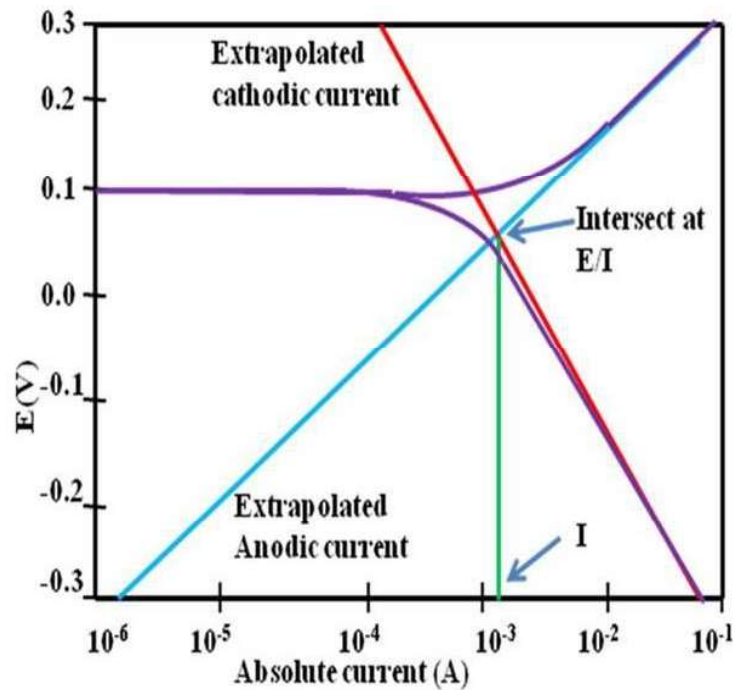


Figure 2.21: A typical Tafel plot

$$I_{\text{corr}} = \frac{(\beta_a \times \beta_c)}{(2.3 \times R_p \times (\beta_a + \beta_c))} \quad (2.14)$$

where, β_a , β_c = Tafel constants and 2.3 = the natural log of ten.

2.7.2. Potentiodynamic Anodic Polarization (PDAP)

This technique is used to find out the active/passive characteristics of a given metal solution system [78-79]. In PDAP, the specimen potential is scanned at slow rate in a positive direction from E_{corr} and measured current. The graph is plotted between the applied potential vs. the logarithm of the measured current as shown in Figure 2.22.

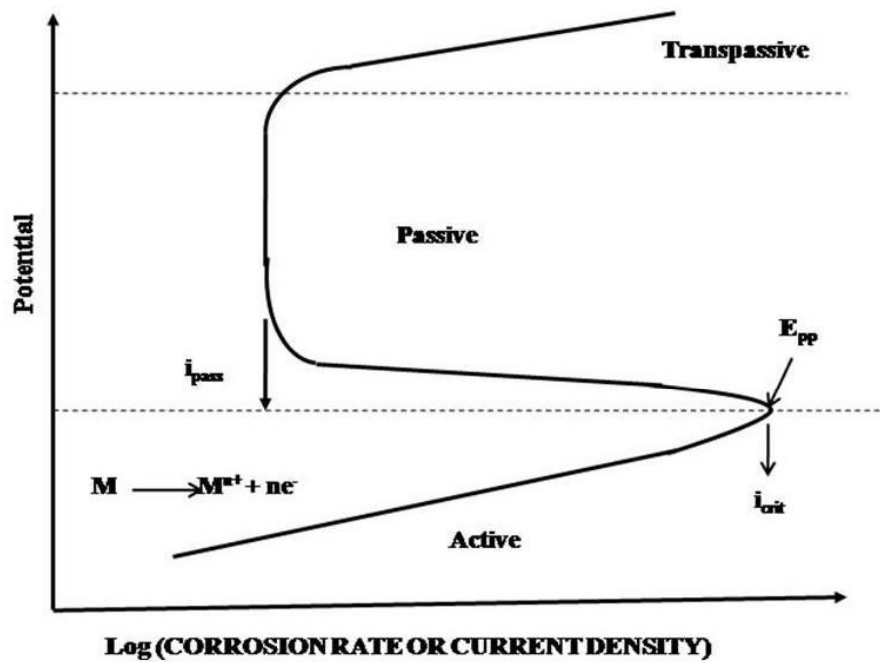


Figure 2.22: A typical potentiodynamic anodic polarization plot

The graph shows different regions, in active dissolution region metal loss increases rapidly with increase in potential, in passive region corrosion rate is negligible and in transpassive region the corrosion again increases due to the oxidative dissolution of passive films. Passive region current density and transpassive region's potential gives information about the degree of passivation and the stability of passive films. Lower current density in the passive region indicates a higher degree of passivation and higher transpassive potential means greater stability of the passive film. The anodic current

where the transformation of the active to passive behavior takes place is known as critical current density (i_{crit}) and corresponding potential is called primary passivation potential (E_{pp}).

2.7.3. Electrochemical Impedance Spectroscopy (EIS)

EIS is a powerful tool for explaining the behaviour of electrochemical processes such as corrosion and adsorption occurring at electrode/electrolyte interfaces. In general, thick high quality coatings have infinite resistance and very low capacitance. Their high resistance results in very small currents especially at low frequencies where resistive elements in the models dominate. Their low capacitances results in small AC currents. With coating degradation and corrosion progress capacitance of the coating increases with the resistance of the coating decreasing and the charge transfer resistance of the metal substrate decreases with the double layer capacitance of the metal interface increasing. The value of the double layer capacitance depends on many variables including electrode potential, temperature, ionic concentrations, types of ions, oxide layers, electrode roughness, impurity adsorption, etc. EIS is used to calculate R_p which can be subsequently used to calculate corrosion rate and I_{corr} with the equations 2.13 and 2.14 respectively. During EIS experiments, a small amplitude ac signal (1 to 10 mV) is applied to the system being studied. The small amplitude chosen is to maintain a linearity in the current and potential curve of the electrochemical system. Therefore, it is a non-destructive method compared to dc electrochemical technique [80]. EIS can also provide information of the system under examination such as electrochemical mechanisms, reaction kinetics and detection of localized corrosion. Impedance

implies obstruction to current or electron flow. In the case of direct current (DC), only resistance obstructs the electron flow. However, with alternating current (AC), other circuit elements such as capacitors and inductors also influence the electron flow. These elements can affect not only the magnitude of an alternating current waveform, but also its time dependent characteristics or phase. AC impedance (Z) is usually defined as a vector form because the vector expression permits its amplitude and its phase characteristics as given by equation (2.15).

$$Z_{\text{total}} = Z' + Z''j, \quad j = \sqrt{-1} \quad (2.15)$$

where, Z' = real impedance and Z'' = imaginary impedance

The amplitude of impedance is $|Z| = \text{Sqrt} ((Z')^2 + (Z'')^2)$ and phase is $\tan \theta = (Z''/Z')$

The real and imaginary components of impedance at a number of frequencies are required to describe the full electrochemical system.

2.7.3.1. Electrical equivalent circuit

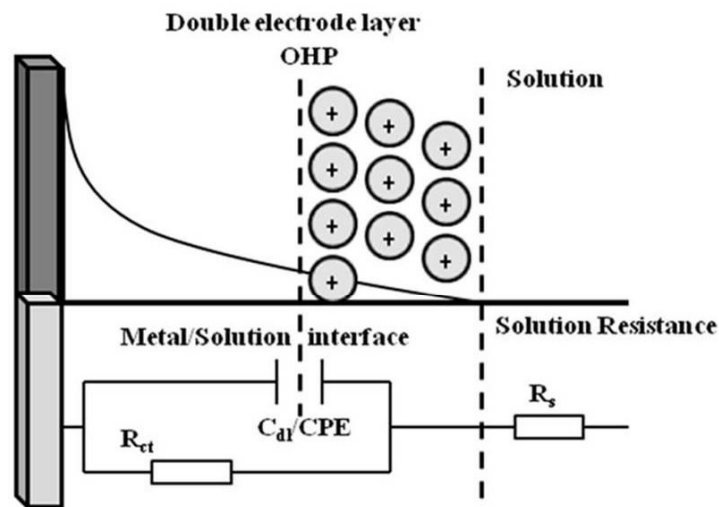


Figure 2.23: Schematic representation of electrode/solution interface

A metal/solution interface is represented as given in Figure 2.23.

C_{dl} : represents the double layer capacitance which arises due to charge separation between the charges on the electrode and the ions in the solution.

R_p : represents polarization resistance at the electrode/solution interface. R_p values permit the calculation of electrochemical reaction rates.

R_s : is the uncompensated or solution resistance between the working and reference electrodes. This resistance depends on the ionic concentration, types of ions, temperature and geometry of the area in which current is carried.

When AC potential is applied to this type of system, the total impedance is as given in equation (2.16).

$$Z = \frac{R}{1 + \omega^2 C^2 R^2} - \frac{j\omega CR^2}{1 + \omega^2 C^2 R^2} \quad (2.16)$$

where, ω = Frequency of AC potential, C = Capacitance and R = Resistance

An intact coating behaves as a dielectric and can be represented by a capacitor. When in contact with an electrolyte, the coating starts to absorb water and the electrolyte enters the pores of the coating. While entering the pores, the electrolyte causes a decrease in the pore resistance R_{p0} which can be considered as initially infinite. Misinterpretation of coating evolution may arise from an erroneous impedance data fitting. Consequently, it is sometimes better to restrict the data interpretation to simple parameters as the global resistance of the system represented by the low frequency impedance modulus ($|Z|_{0.01\text{Hz}} \sim R_s + R_p + R_{ct}$) and the coating capacitance values obtained from high frequency impedance modulus.

2.7.3.2. Nyquist Plot

It is plotted between real Z (in phase component, Z') and imaginary Z (out of phase component, Z'') as shown in Figure 2.24.

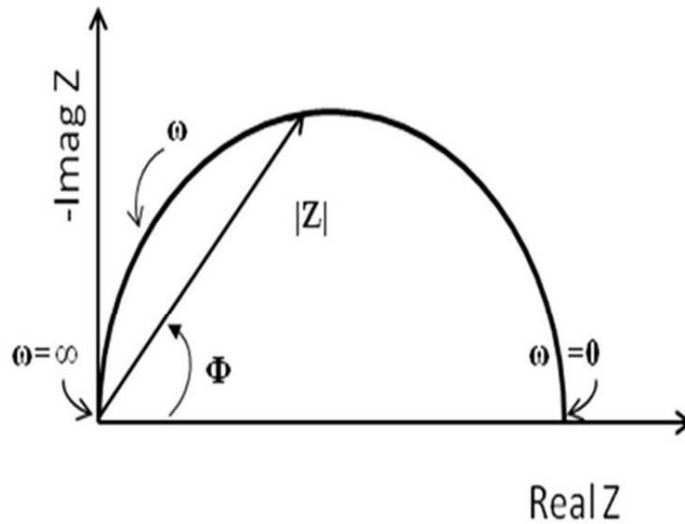


Figure 2.24: Typical Nyquist Plot

In practice, the measured impedance spectra may differ from ideal or theoretical behaviour. The loops (or time constants) do not show a perfect semi circle shape in Nyquist representation. This non-ideal behaviour may arise from coating heterogeneities such as roughness and inhomogeneous composition. In such a case, the coating cannot be described by a simple capacitor. This one is generally replaced by a constant phase element (CPE) whose impedance is given by equation (2.17).

$$Z_{\text{CPE}} = \frac{1}{Y_0 (i\omega)^{-n}} \quad (2.17)$$

'n' accounts for non-ideal behaviours: when it equals to 1, the CPE is a pure capacitance and when it equals zero, the CPE is a pure resistance.

2.7.3.3. Bode Plot

The Bode plot provides a clear description of the behavior of the electrochemical system under study in which frequency values are implicit. Some electrochemical processes have more than one rate determining step and each step represents a system impedance component and contributes to the overall reaction rate constant. The Bode plot can distinguish among these steps and provide information on their rates or relaxation times. Figure 2.25 shows a typical Bode plot which gives the absolute impedance '|Z|' and the phase shift 'θ' of the impedance as a function of frequency. Since frequency appears on the X-axis, the dependency of the impedance on the frequency is observed from the plot. The log |Z| vs. log f plot gives the values of R_p and R_s. At the highest frequency region on the right of the X-axis, the ohmic resistance log (R_s) dominates and can be obtained from the high frequency horizontal plateau. At the lowest frequency region on the left of the X-axis, polarization resistance log (R_s+R_p) contributes and can be obtained from the horizontal plateau. At intermediate frequencies, the plot is a straight line with a slope of -1. Extrapolating this line to the log |Z| axis at log f = 0 yields the value of C_{dl} as given in equation (2.18).

$$|Z| = \frac{1}{C_{dl}} \quad (2.18)$$

The Bode plot format also shows the phase angle (θ). At the high and low frequency limits, where the behavior of the Randles cell is resistor-like, the phase angle is nearly zero. At intermediate frequencies, θ increases as the imaginary component of the impedance increases.

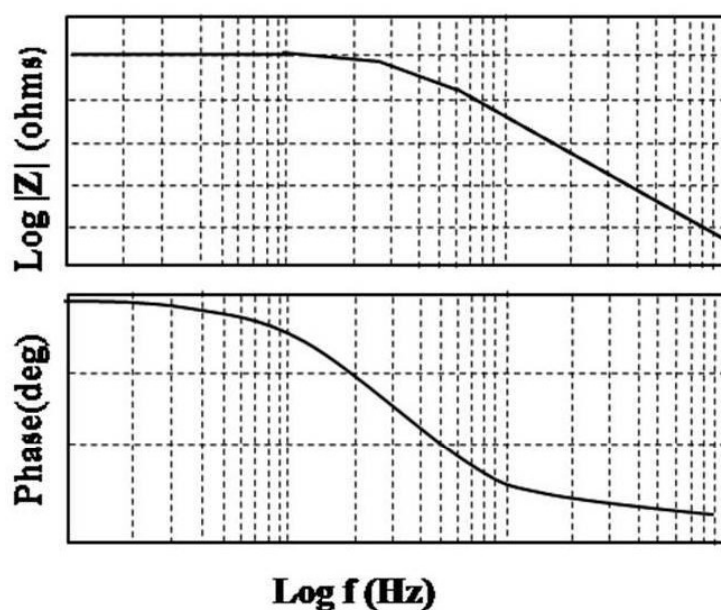


Figure 2.25: Typical Bode Plot

2.7.4. Test Cell and Instrument

The test cell and the electrochemical instrument used in this study are shown in Figure 2.26. The cell was a conventional three electrode with a platinum foil as counter electrode, saturated calomel through a luggin capillary as reference electrode and the metal specimen (CS, CS/Fe₃O₄, CS/Fe₃O₄/Ferrites) as a working electrode. The experiments were performed with LiOH solutions at 25°C in deaerated environment using an Eco Chemie Autolab PG STAT 30 system. The samples were allowed to attain stable open-circuit potential (OCP) before starting the electrochemical measurements. In this study, all the potentiodynamic anodic polarization scans were obtained by polarizing the working electrode from -0.4 V to +1.2 V with respect to OCP at a scan rate of 0.5 mV per second. The cathodic and anodic Tafel slopes were obtained individually from the plot within the Tafel region \pm 50-250 mV with respect to OCP. The corrosion current (i_{corr}) and corrosion potential (E_{corr}) were determined from the

intersection of anodic and cathodic Tafel lines and the corrosion rate (mpy) was calculated from i_{corr} [80]. Impedance spectra from different samples were recorded at OCP by applying a sinusoidal voltage of ± 10 mV in the frequency range of $10^4 - 0.005$ Hz.

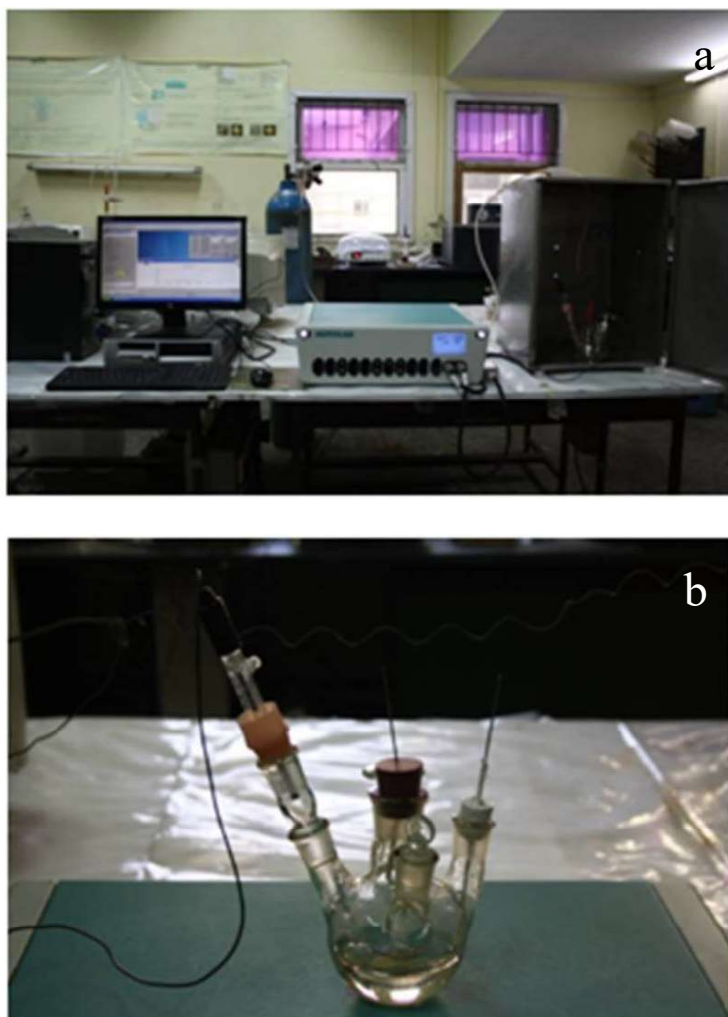


Figure 2.26: Photograph of a) Electrochemical system and b) Electrochemical cell

2.7.5. Mott-Schottky (MS) method

Generally, the substrate (nature and content of alloying elements), the environment (temperature, aerated, deaerated, neutral, acidic or alkaline) and also specific

experimental conditions (anodic polarization) affect both the chemical composition and the structure of the passive layer [81-82]. Passive films are mainly made up of metallic oxides or hydroxides which are envisaged as semiconductors. Consequently, semiconducting properties are often observed on the surfaces of the passivating metals [83-85]. In alkaline solutions, the main effect of increasing pH on film formation is thickening of the passive film because iron oxides are more stable in alkaline solutions [86]. Mott–Schottky measurements were carried out to understand the semiconducting properties of oxide films formed in-situ in an autoclave and deposited ex-situ by PLD. This method involves the capacitance measurement as a function of potential under depleted condition where the relation given by equations (2.19) and (2.20) is obeyed and these measurements were performed for a set of six frequencies namely 10^4 , 10^3 , 10^2 , 10, 5 and 1 Hz. The working electrodes were polarized in the cathodic direction in successive steps of 50 mV Vs. SCE from + 0.1 V to -1.2 V Vs. SCE.

$$\frac{1}{C^2} = \frac{2}{\epsilon_0 \epsilon e N_D \left(E - E_{FB} - \frac{kT}{e} \right)} \quad (2.19) \text{ for n-type semiconductor}$$

$$\frac{1}{C^2} = \frac{2}{\epsilon_0 \epsilon e N_D \left(-E + E_{FB} + \frac{kT}{e} \right)} \quad (2.20) \text{ for p-type semiconductor}$$

where 'e' is the electron charge (-1.602×10^{-19} C), ' N_D ' is the donor density for n-type semiconductor (cm^{-3}), ' N_A ' is the acceptor density for p-type semiconductor (cm^{-3}), ' ϵ ' is the dielectric constant of the oxide film, ' ϵ_0 ' is the vacuum permittivity (8.854×10^{-12} Fm⁻¹), ' k ' is the Boltzmann constant (1.38×10^{-23} J K⁻¹), ' T ' is the absolute temperature and ' E_{FB} ' is the flat band potential [87]. Flat band potential can

be determined from the extrapolation of the linear portion to $C^{-2} = 0$. The slope of this plot is associated with the semiconducting behavior of the oxide film. Positive slope is typical of n-type semiconductors while negative slope is typical of p-type semiconductors. Typical Mott Schottky plot is as shown in Figure 2.27. Doping densities of these oxide films were calculated from the slope of Mott–Schottky plots, if its dielectric constant ϵ is known. The values of 'C' obtained from equation (2.18) or (2.19) can be correlated with the thickness 'd' of the passive oxide film by using the formula given in equation (2.21).

$$C = \frac{\epsilon \epsilon_0 d}{d} \quad (2.21)$$

where, ' ϵ ' is the dielectric constant of the medium under study, ' ϵ_0 ' is the dielectric constant of the air.

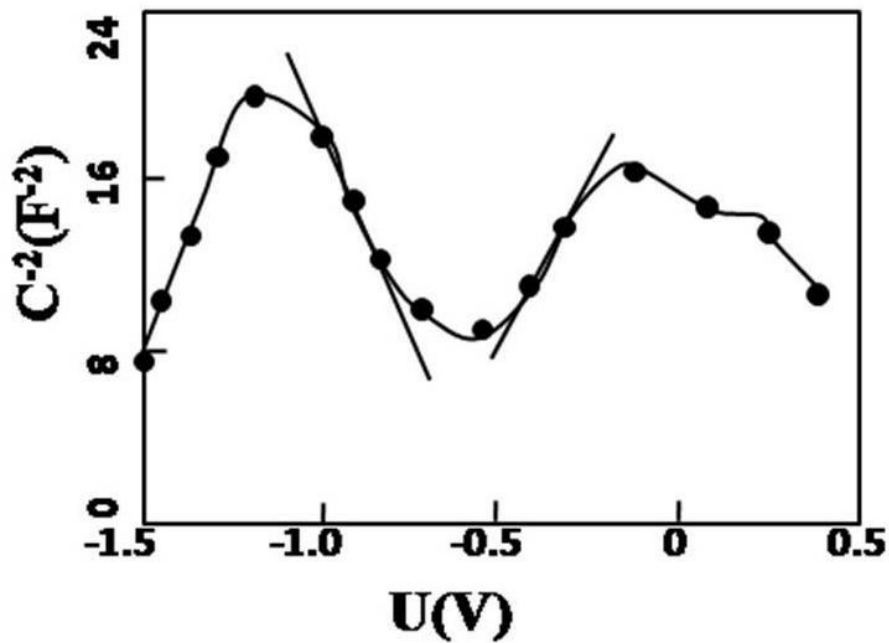


Figure 2.27: Typical Mott Schottky plot

In this study, Mott–Schottky plots of the coated specimens acquired at 100 Hz in LiOH solution (pH 10.2) at room temperature was taken for analysis. The reason to take this frequency data for analysis is that in this frequency the imaginary impedance of the system was found to respond to change in applied potential. In the case of anodic oxide film growth, the Point Defect Model [88-89] suggests that the cation vacancies are injected into the oxide film from the film/solution interface and are annihilated at the metal/film interface, while oxygen vacancies are produced at the metal/film interface and are annihilated at the film/solution interface. A high doping density is typical of a defective oxide layer which, in turn, is associated with a lower corrosion resistance [90]. Changes in donor density correspond to non-stoichiometry defects in the passive film which is a clear indication of the formation of a highly disordered oxide [91].

Chapter 3

Formation of magnetite coating on carbon steel by hydrothermal method

3.1. Introduction

Magnetite (Fe_3O_4) is generally prepared by wet methods or solid phase reactions. The hydrothermal method involves low temperature, improved control of powder homogeneity and uniform particles. The polycrystalline substituted magnetite is prepared by hydrothermal method [92]. The formation of thin passive films on the mild steel surface in alkaline media, by the application of different anodic potentials, was characterized for the morphology, composition and electrochemical behavior. The results indicated that the surface films composed of oxides containing Fe^{2+} and Fe^{3+} . The Fe^{2+} contributions disappear when the potential of the film formation is increased in passive domain [93]. Corrosion protection of steel by deposition of Fe_3O_4 coating containing aluminum and chromium cations was studied by Nasrazadani by analyzing the chemical composition of top few mono layers using X-Ray photoelectron spectroscopy and polarization resistance measurement techniques in caustic solution [94]. Zhu et.al prepared a dense black coating composed of Fe_3O_4 ultrafine particles by hydrothermal treatment of the carbon steel substrate in the $\text{N}_2\text{H}_4\cdot\text{H}_2\text{O}-\text{FeSO}_4-\text{NaOH}$ solution at $150\text{ }^\circ\text{C}$. It was inferred that the corrosion resistance increased by Fe_3O_4 coating from the electrochemical experiments [95]. Typically the surfaces of the CS pipelines are covered with a Fe_3O_4 film which is formed in a pre-commissioning operation (called as hot conditioning). This film continues to grow during the reactor operation period under alkaline water chemistry (pH 10-10.5) and dissolved oxygen levels of less than 10 ppb. The solubility of Fe_3O_4 in water at $\text{pH} > 9.8$ increases with the increase in temperature from $150\text{ }^\circ\text{C}$ to $300\text{ }^\circ\text{C}$. The behavior of CS in hydroxide solutions at elevated temperatures ($> 100\text{ }^\circ\text{C}$) is of practical interest to the power industries since

many nuclear power plants employ dilute hydroxide solutions as heat transport media. In nuclear stations, lithium hydroxide is often chosen as the alkalizing agent since lithium gives rise to fewer radiation problems than other alkali ions [96]. Fe_3O_4 forms a protective oxide film on the internal surfaces of the PHT system of PHWRs. The surface is passivated with Fe_3O_4 film formed at high temperature water (250 °C) under alkaline condition with low dissolved oxygen. Protection of internal surfaces against corrosion can be further improved by having a passive film containing nano crystallites. Fe_3O_4 is a member of spinel group having the standard formula $\text{A}(\text{B})_2\text{O}_4$. It is an inverse spinel structure with tetrahedral A-sites occupied by Fe^{3+} ions and octahedral B-sites occupied by both Fe^{2+} and Fe^{3+} ions, two different metal ions in two different sites. It can be represented as $[\text{Fe}^{3+}]_{\text{Td}}[\text{Fe}^{2+}, \text{Fe}^{3+}]_{\text{Oh}}\text{O}_4$. The color of Fe_3O_4 is black and the well formed crystals are octahedral in shape. Figure 3.1 represents the typical Fe_3O_4 inverse spinel structure [97].

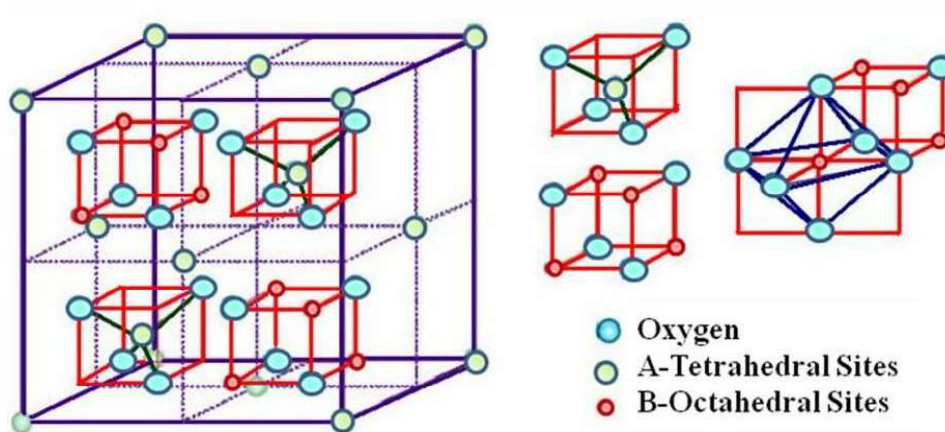
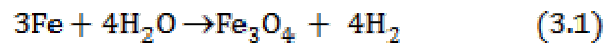


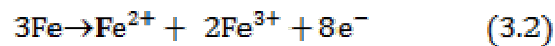
Figure 3.1: Typical magnetite structure [97]

3.2. Mechanism of magnetite formation

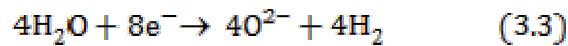
Electrochemical reactions are provided by the general corrosion of metals in water. CS in contact with high temperature water develops protective Fe_3O_4 films according to the overall reaction as given in equation (3.1) [98].



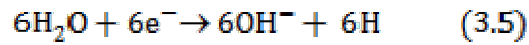
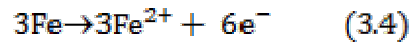
Mechanistically, equation (3.1) is a combination of two half-reactions, the anodic or oxidation process by equation (3.2).



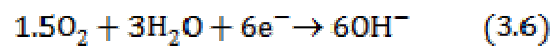
and the cathodic or reduction process by equation (3.3).



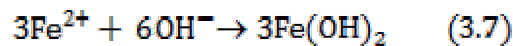
The half-reactions occur at the same rate simultaneously. According to the classic Wagner and Traud theory [99], the anodic sites on the metal, where metal ions dissolve, are separate from the cathodic sites, where electrons are discharged, oxide ions form and hydrogen is released. The electrons are transported between the anodic and cathodic sites and the metal ions and oxide ions interact and precipitate as Fe_3O_4 . For the oxidation to be uniform, the sites must be mobile across the surface. In high-temperature water the oxidation at the metal-oxide interface produces ferrous ions according to equation (3.4) and the hydrogen produced in the accompanying reduction is given by equation (3.5).



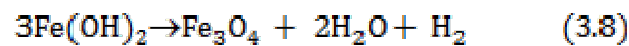
where H is in the form of hydrogen atoms that migrate through the metal. If dissolved oxygen is present in neutral or alkaline water, equation (3.5) is replaced by the more favorable equation (3.6)



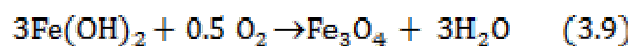
and hydrogen production ceases. The ferrous ions and hydroxide ions from (3.4) and (3.5 or 3.6) interact to form soluble ferrous hydroxide given by equation (3.7)



but ferrous hydroxide oxidizes and precipitates as Fe_3O_4 according to the Schikorr reaction [100] as shown in equation (3.8).



If oxygen is present the oxidation of ferrous hydroxide proceeds via the more favorable reaction given by equation (3.9).



At the metal-oxide interface, about half of the ferrous hydroxide precipitates as inner layer Fe_3O_4 and the other half, along with hydrogen molecules generated at the metal-oxide by (3.8), diffuse through the developing Fe_3O_4 film to the oxide coolant interface. If the coolant is reducing and saturated in dissolved iron as in the CS of PHWRs, it precipitates as outer layer Fe_3O_4 according to (3.8); the molecular hydrogen is then dispersed in the bulk of the flowing coolant. In the presence of dissolved oxygen, the outer layer precipitates according to (3.9) and the Fe_3O_4 film develops completely without the evolution of hydrogen. The duplex films of Fe_3O_4 consist of fine grained inner layer particles of about ten nanometres in size, overlaid with octahedra crystallites of sizes up to ten micrometers grown from solution. Figure 3.2 shows the duplex structure of the oxides formed on CS surface.

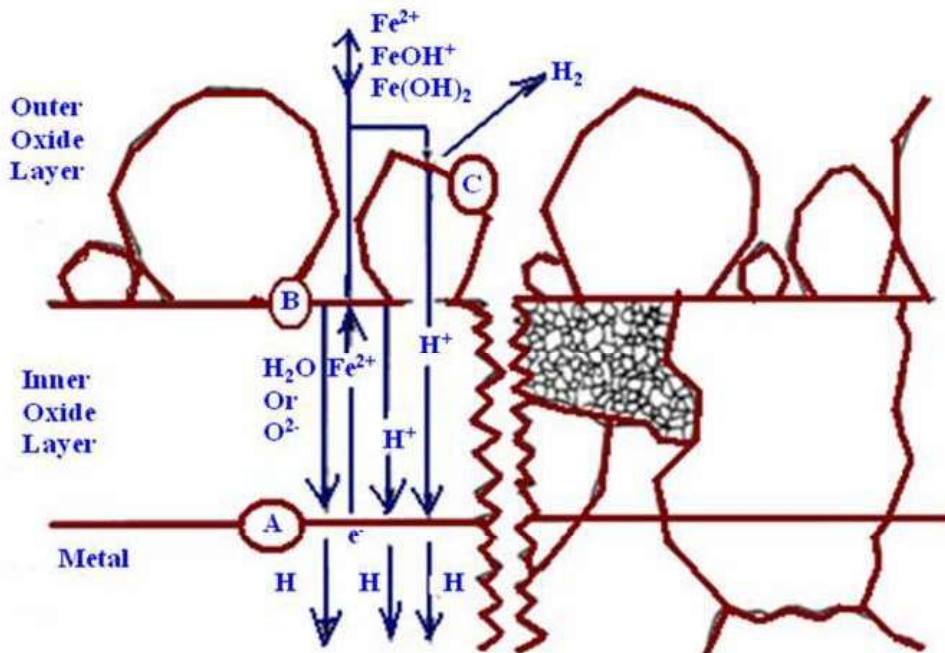


Figure 3.2: Double oxide layer formed by Fe_3O_4 on CS

In this chapter, the studies were carried out (1) to find the corrosion parameters for uncoated CS and Fe₃O₄ formed on CS (CS/Fe₃O₄) used as a substrate in PLD and (2) to optimize the number of hours to be exposed in an autoclave for the hydrothermal experiments to be carried out with incorporation of cations (Ni²⁺, Zn²⁺ and Mg²⁺) by analyzing the trend in the corrosion rate.

3.3. Passivation studies

As described in chapter 2, passivation studies were carried out for the formation of Fe₃O₄ film over CS a surface which was used as a substrate for the PLD process. In all specimens a uniform, black coating of inverse spinel Fe₃O₄ structure was obtained. The coated CS surfaces were confirmed by GI-XRD and Raman Spectroscopy. The polarization resistance and the corrosion rate of the coatings were evaluated by electrochemical experiments. Table 3.1 and Table 3.2 gives the impedance and corrosion parameters respectively for CS/Fe₃O₄ and compared with the data obtained for uncoated CS. Figure 3.3 (a) and (b) shows the EIS Nyquist and PDAP plot respectively for CS and CS/Fe₃O₄. The results from the table and figure clearly shows that the polarization resistance of CS/Fe₃O₄ increased when compared to the polarization resistance of the uncoated CS and a reduction in the corrosion rate was observed.

Table 3.1: Impedance parameters obtained from EIS measurements

Specimen	R _s (KΩ)	R ₁ (KΩ)	Q ₁ (μF)	n	R ₂ (KΩ)	Q ₂ (mF)	n
Uncoated CS	0.487	0.607	0.44	0.85	9.5	0.49	0.63
CS/Fe ₃ O ₄	0.543	0.801	0.97	0.79	191.2	0.19	0.85

Table 3.2: Corrosion parameters obtained from PDAP measurements

Specimen	PDAP				
	b_c (V/dec)	b_a (V/dec)	OCP (V)	i_{corr} ($\mu\text{A}/\text{cm}^2$)	Corrosion Rate (mpy)
Uncoated CS	-0.236	0.283	-0.497	1.194	0.552
CS/ Fe_3O_4	-0.148	0.414	-0.424	0.219	0.101

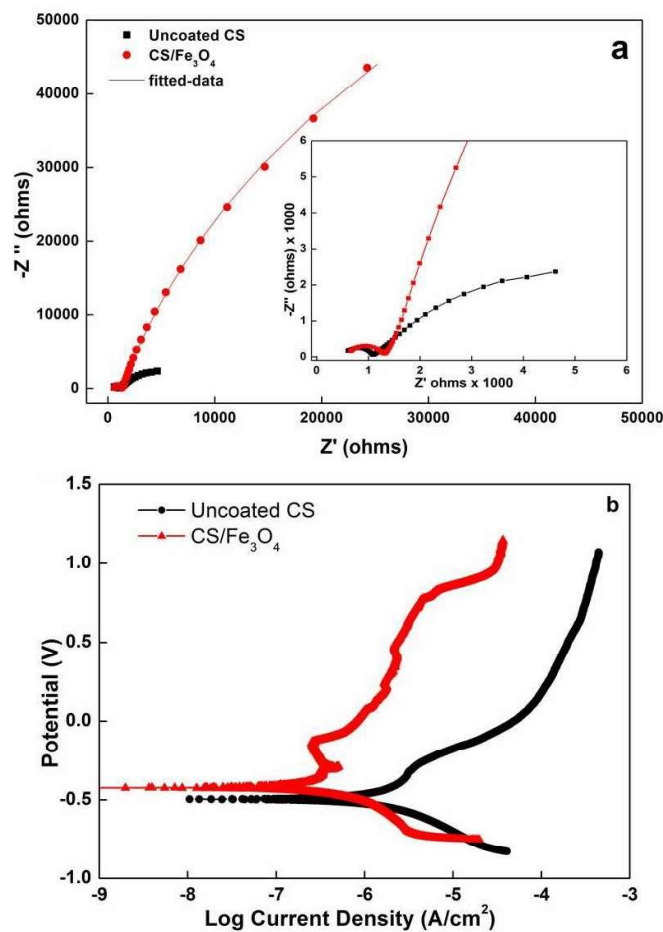


Figure 3.3: (a) EIS Nyquist and (b) PDAP plot of CS and CS/ Fe_3O_4

The PLD coating was carried out over CS/ Fe_3O_4 specimen (Fe_3O_4 formed in 96 hours) and the above experimental data were used for the comparison with the

nickel ferrite, zinc ferrite and magnesium ferrite coatings data obtained from the PLD process which will be covered in chapters 4, 5 and 6 respectively.

3.4. Corrosion rate evaluation of Fe₃O₄ formation with different exposure time

The corrosion rate was evaluated using the electrochemical techniques. Electrochemical experiments were carried out to know the trend in the corrosion rate with different exposure time (96, 240, 360 and 480 hours). Polarization resistances (R_p) of CS/Fe₃O₄ from EIS measurements were compared with that of uncoated CS. Results indicate that CS/Fe₃O₄ showed higher R_p values compared to the value obtained for uncoated CS.

3.4.1. Characterization of Fe₃O₄ formed on CS

3.4.1.1. Thickness measurement

The thicknesses of the specimens after the formation of the Fe₃O₄ in 96, 240, 360 and 480 hours were evaluated by Clarke's method. Table 3.3 gives the thickness values calculated for the specimens exposed for different time duration. It was observed that the thicknesses of the coatings slightly increased with increase in exposure time.

Table 3.3: Calculated thickness of CS/Fe₃O₄ formed at different exposure time

Exposure Time	Thickness (μm)
96 hours	0.48
240 hours	0.55
360 hours	0.57
480 hours	0.67

3.4.1.2. X-Ray Diffraction

The GI-XRD pattern of the uncoated CS and the XRD pattern of CS/Fe₃O₄ are shown in Figures 3.4 (a) and (b) respectively.

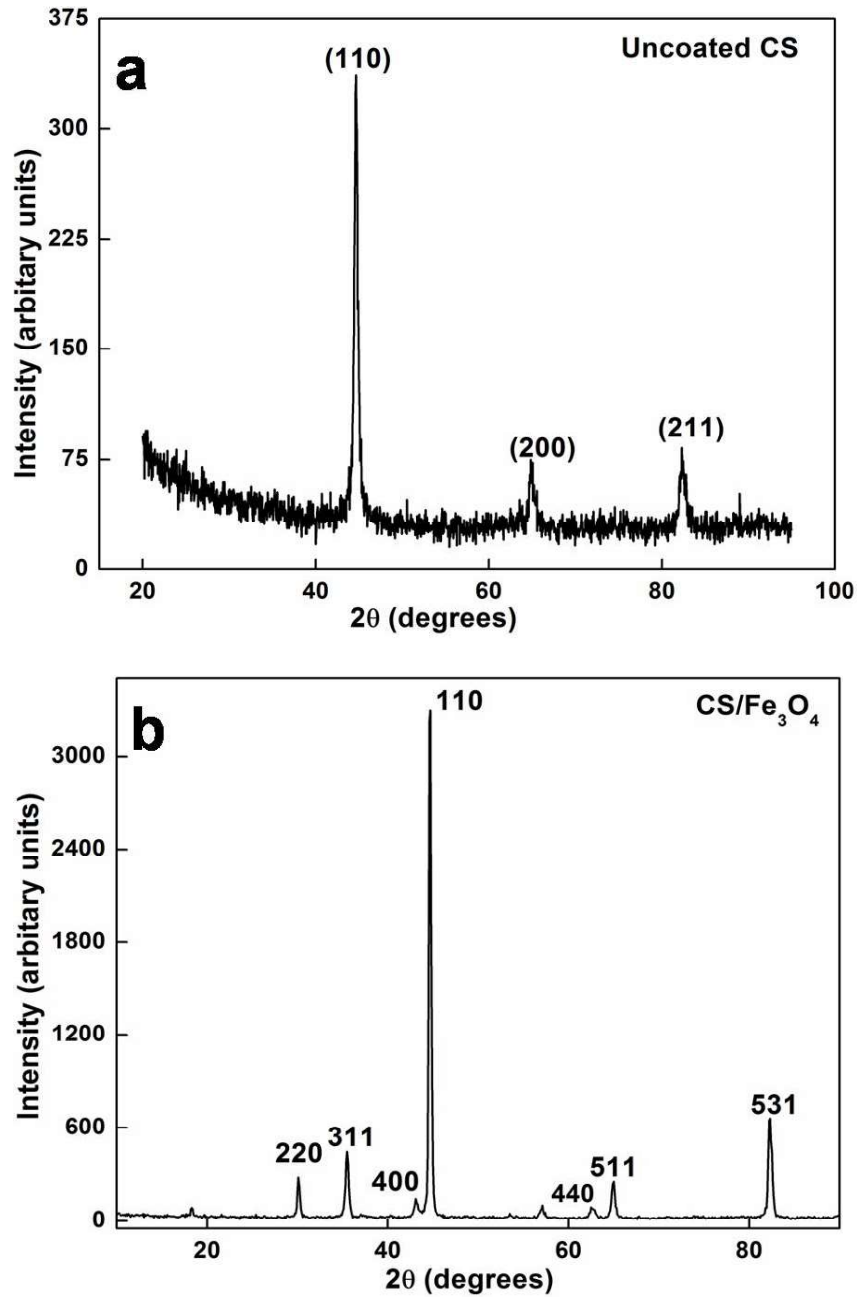


Figure 3.4: (a) GI-XRD pattern of uncoated CS and (b) XRD pattern of CS/Fe₃O₄

All the peaks of Figure 3.4 (a) could be indexed to metal iron consistent with the values from the standard database card (ICDD.No.00-044-1290). All the peaks of Figure 3.4 (b), except for those of the iron (peak (110) in Figure 3.4 (a)), could be indexed as cubic Fe₃O₄ with cell parameter a=8.408 Å, which was in good agreement with the values obtained (8.40) from the standard card (ICDD.No.01-080-6403) and was nearly equal to that for bulk Fe₃O₄ (8.397 Å) implying less oxygen deficiency [101]. It had a face-centered cubic crystal structure of space group Fd-3m. The strong and sharp peaks indicated that the Fe₃O₄ film formed was well-crystallized. No impurity peaks of Fe₂O₃ or FeO were detected. The average crystallite size calculated using the Debye Scherrer's formula is given in Table 3.4 for the CS/Fe₃O₄ obtained by exposure to different duration. It could be seen from the table that the values of the crystallite size obtained were almost similar for the CS/Fe₃O₄ obtained in case of 240, 360 and 480 hours exposure.

Table 3.4: Crystallite size obtained for CS/Fe₃O₄ for different exposure time

Exposure Time	Crystallite size (nm)
96 hours	15.90
240 hours	19.24
360 hours	20.92
480 hours	21.72

3.4.1.3. Scanning Electron Microscopy

The oxide films formed on CS exhibit two layers as explained in section 3.2. In LiOH solutions, the outer layer crystals are poorly defined octahedra whereas in NaOH these crystals have well-defined hexagonal prismatic morphology [96]. The surface morphology of CS/Fe₃O₄ by hydrothermal method was studied by SEM. Figure 3.5 shows the top view SEM image of the film formed in 96 hours exposure which clearly revealed the regular morphology of the Fe₃O₄ particles on the exterior surface. CS/Fe₃O₄ specimen showed the presence of uniformly covered regular octahedron shaped particulates. The outer layer (~500 – 1000 nm size) particles precipitated from the solution were larger in size than the inner layer (~50 - 200 nm size) particles formed due to the oxidation of the base metal.

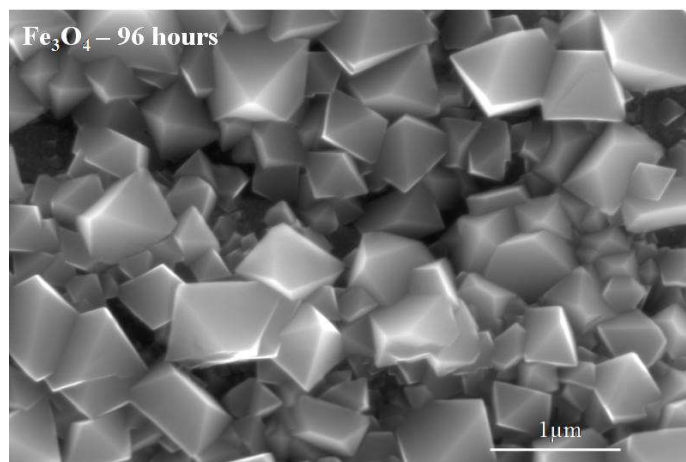


Figure 3.5: SEM image of CS/Fe₃O₄

The chemical composition of the Fe₃O₄ coating was analyzed by EDAX and the EDAX spectrum is shown in Figure 3.6. The strong peaks for Fe and O were found in the spectrum. There were no other peaks in the spectrum, implying the absence of impurity under the hydrothermal condition. Quantitative analysis by EDAX revealed

that the atomic percentage composition of Fe and O were 36% and 64%, respectively. The atomic and weight percentages of CS/Fe₃O₄ are presented in the Table 3.5. The XRD pattern (Figure 3.4 b) and the EDAX spectrum (Figure 3.6) revealed that the film was composed of only pure Fe₃O₄.

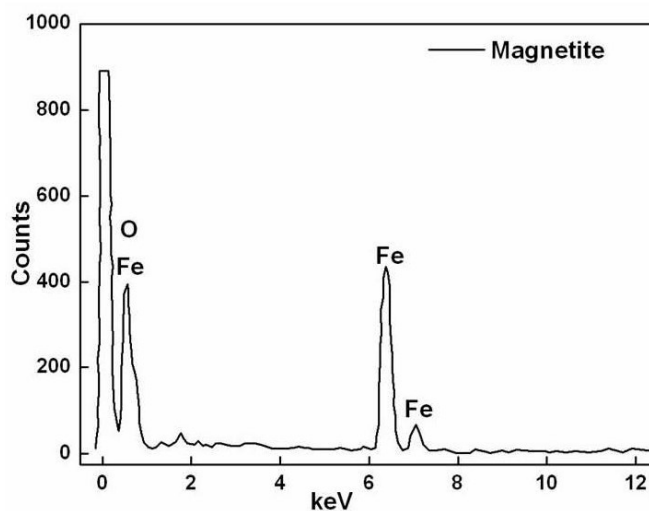


Figure 3.6: EDAX of CS/Fe₃O₄

Table 3.5: Quantitative analysis by EDAX of CS/Fe₃O₄

	Weight (%)	Atomic (%)
O K	33.95	64.21
Fe K	66.05	35.79

3.4.1.4. X-Ray Photoelectron Spectroscopy

XPS is a powerful characterization technique used to determine the purity of Fe₃O₄ films. The broadening of the Fe 2p_{1/2} and Fe 2p_{3/2} peaks and the absence of a satellite peak at ~718 eV is characteristic of magnetite [102]. Generally, the Fe 2p spectra of the surface correspond to iron oxohydroxides or hydroxides and also a

contribution of Fe_3O_4 can be inferred. $\text{Fe } 2p_{3/2}$ photoelectron peaks obtained from $\text{CS}/\text{Fe}_3\text{O}_4$ is shown in Figure 3.7. The binding energy value of $\text{Fe } 2p_{3/2}$ was observed at around 711.2 eV and matched well with the literature value [103]. In Fe_3O_4 , 2 Fe^{3+} and 1 Fe^{2+} ions contribute for the $\text{Fe } 2p_{3/2}$ peak. Since Fe^{3+} was the dominant species in Fe_3O_4 , the peak was observed at 711.2 eV with peak width of 4 eV. Higher peak width of $\text{Fe } 2p_{3/2}$ in Fe_3O_4 was due to the presence of Fe^{2+} and Fe^{3+} . The O 1s spectra showed two components. The component with the minor binding energy of O 1s ($\sim 530 - 530.1$ eV) corresponded to O^{2-} from the oxide (metal-O-metal bond, oxygen-M-oxygen) and the other component ~ 532.5 eV was attributed to physically adsorbed water. In Fe_3O_4 coated CS only one peak was observed for O 1s at 530.1 eV indicating that the oxygen atoms were in the O^{2-} form in the lattice. From the above XRD and XPS analyses it was concluded that the coating on CS composed of Fe_3O_4 only.

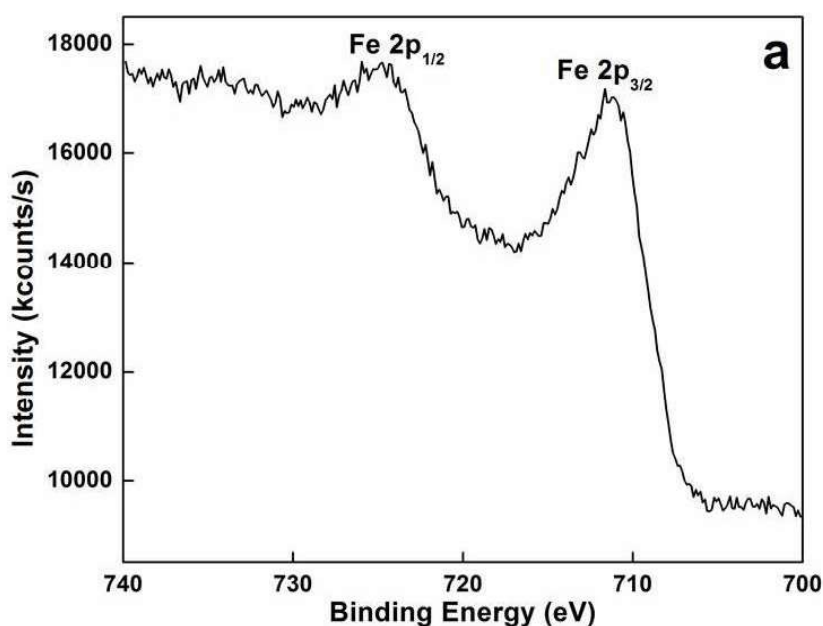


Figure 3.7 (a): XPS of Fe 2p obtained on $\text{CS}/\text{Fe}_3\text{O}_4$

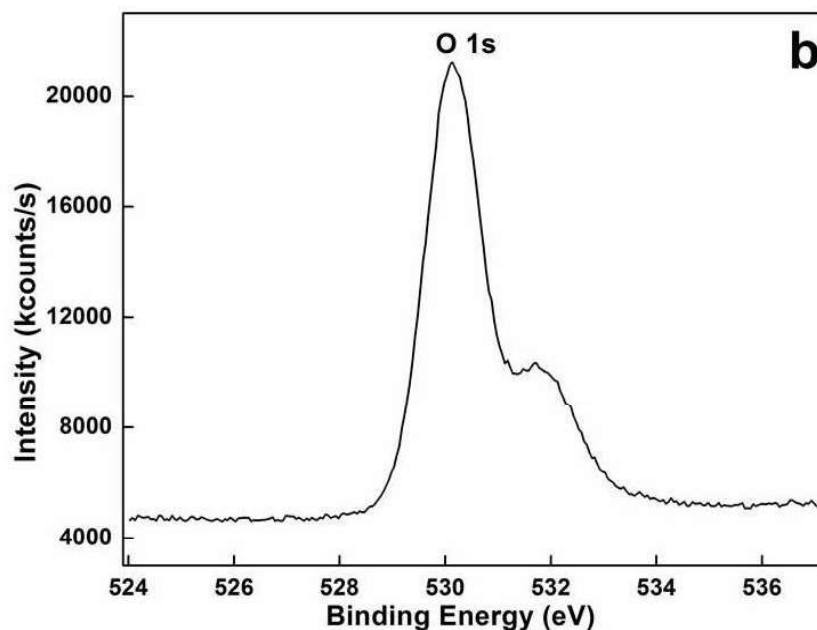


Figure 3.7 (b): XPS of O 1s obtained on CS/Fe₃O₄

3.4.1.5. Laser Raman Spectroscopy

Figure 3.8 shows the Raman spectra recorded on the CS/Fe₃O₄ surface formed during the hydrothermal treatment. The observed Raman shift value in the spectra indicates the formation of the Fe₃O₄ phase over the CS surface. Fe₃O₄ is an inverse spinel structured iron oxide, which shows five Raman active modes namely A_{1g}, E_g and 3T_g. For the Fe₃O₄ phase, A_{1g} is the high intensity peak at 672.6 cm⁻¹ due to the Fe³⁺-O bond in the tetrahedral void. Raman shift values observed in the Fe₃O₄ film (Figure 3.8 a) were compared with standard Fe₃O₄ (Figure 3.8 b).

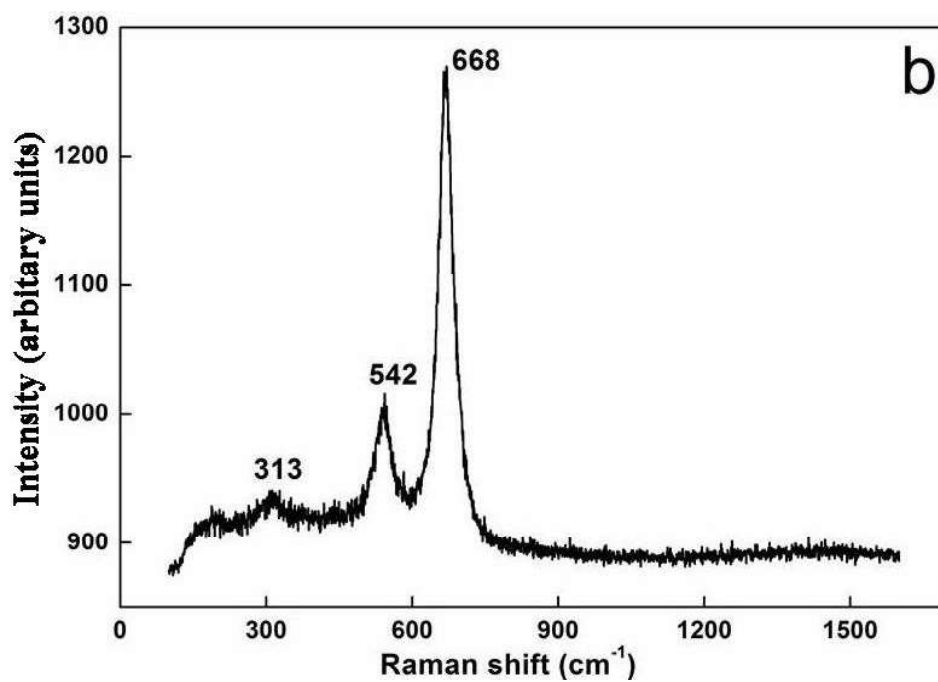
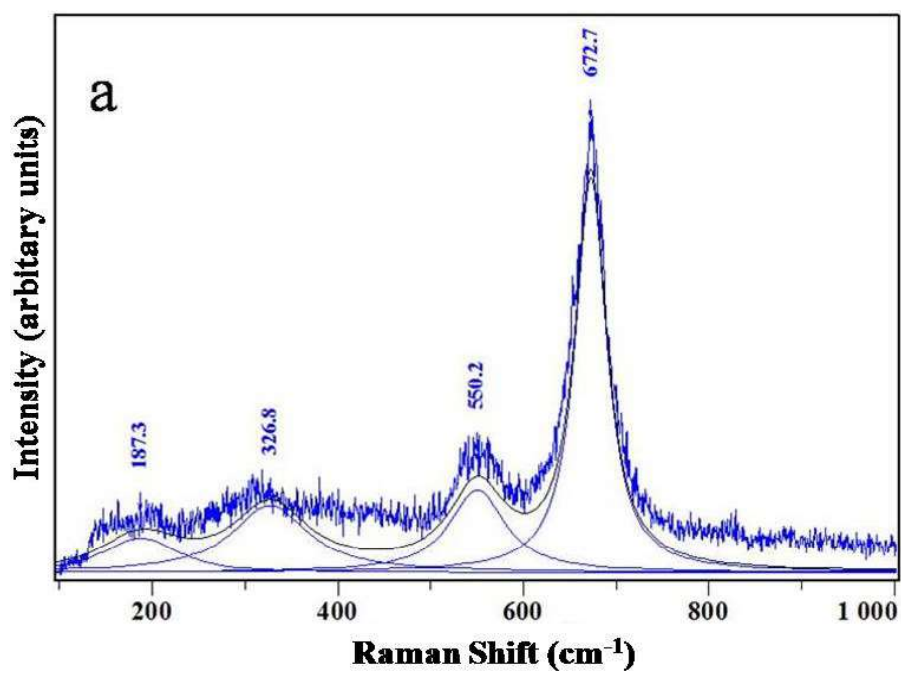


Figure 3.8: Raman spectra of (a) CS/Fe₃O₄ and (b) standard Fe₃O₄

3.4.2. Electrochemical Characterization

3.4.2.1. Potentiodynamic Anodic Polarization

Figure 3.9 shows the PDAP curve for CS and CS/Fe₃O₄ in deaerated LiOH aqueous medium at room temperature. The corrosion parameters obtained from these measurements are given in Table 3.6. The OCP for Fe₃O₄ coating obtained in 96 hours shifted to active side (-0.662 V vs. SCE) and further exposure to 240, 360 and 480 hours shifted the OCP towards the noble side (-0.277, -0.428 and -0.209 V vs. SCE) compared to uncoated CS (-0.495 V vs. SCE). In all the cases, an active to passive transition was observed due to the formation of ferric hydroxide film at the anodic potentials. It was observed that before the coated specimen was transferred to a passive state, an active current peak occurred which could be attributed to the oxidation of Fe²⁺ to Fe³⁺ ions in the passive film [104]. Based on the corrosion current values, the corrosion resistance was found to be in the following order: CS/Fe₃O₄ (96 ≅ 240 ≅ 360 ≅ 480 hours) > CS. Hence, the corrosion resistance increased with the adherent Fe₃O₄ coating. Since the pH of the electrolyte was alkaline and the solution was deaerated, the main cathodic reaction could be the reduction of H₂O and the anodic reaction, the metal ion release from base metal.

Table 3.6: Corrosion parameters for CS/Fe₃O₄ at different exposure time

CS/Fe ₃ O ₄	PDAP				
	b _c (V/dec)	b _a (V/dec)	OCP (V)	i _{corr} (μA/cm ²)	Corrosion Rate (mpy)
Uncoated CS	-0.236	0.283	-0.497	1.194	0.552
96 hours	-0.112	0.326	-0.662	0.138	0.064
240 hours	-0.202	0.365	-0.277	0.097	0.045
360 hours	-0.145	0.294	-0.428	0.103	0.048
480 hours	-0.123	0.188	-0.209	0.220	0.101

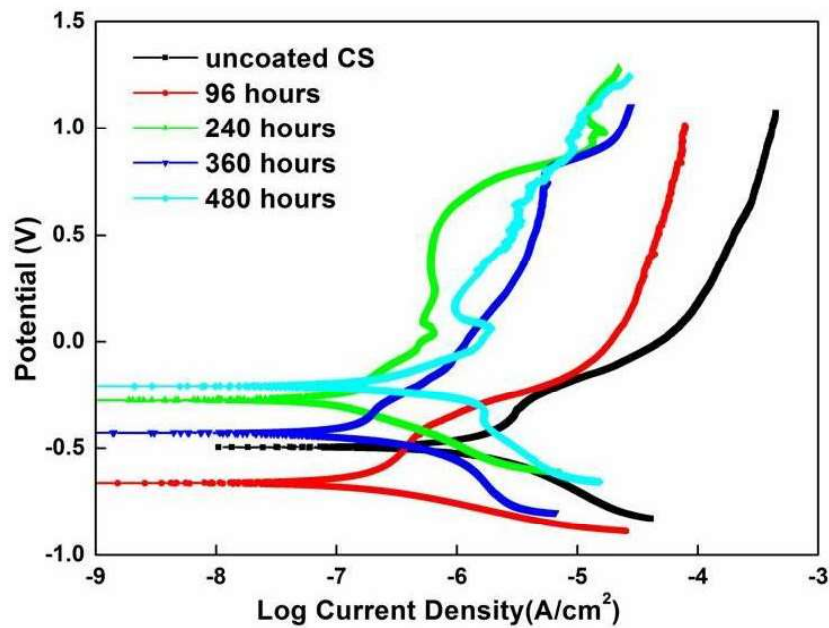


Figure 3.9: PDAP plot of CS/Fe₃O₄ at different exposure time

3.4.2.2. Electrochemical Impedance Spectroscopy

The Nyquist (Figure 3.10 (a)) and Bode (Figures 3.10 (b) and (c)) diagrams for the coated samples obtained at E_{corr} using EIS in deaerated LiOH solution at room

temperature are shown in Figure 3.10. Existence of two semicircles in the Nyquist diagram (Inset Figure 3.10 (a)) indicated the formation of two time constants attributed to processes occurring near metal/film and film/solution interface for the uncoated CS and metal/oxide and oxide/solution interface for CS/Fe₃O₄. The thin film formed over uncoated CS could be iron hydroxide/oxy hydroxide. R₂ is the charge transfer resistance which is a measure of electron transfer across the metal/film interface and it is inversely proportional to the rate of corrosion. The impedance parameters fitted from the curve are presented in Table 3.7. An increasing trend in the charge transfer resistance (R₂) was observed in Fe₃O₄ coated CS formed in 96 and 240 hours indicating a better corrosion resistance whereas it decreased for Fe₃O₄ coating formed by exposure to 360 and 480 hours. The 'n' value away from 1 indicated the presence of a non-homogeneous surface. The Bode spectra presented in Figure 3.10 (b) showed a significant increase in the low frequency impedance modulus in all the cases compared to uncoated CS.

Table 3.7: Impedance parameters for CS/Fe₃O₄ at different exposure time

CS/Fe ₃ O ₄	R ₁ (KΩ)	Q ₁ (μF)	n	Q ₂ (mF)	n	R ₂ (KΩ)	R ₃ (KΩ)
Uncoated CS	0.487	0.44	0.85	0.49	0.63	9.5	0.607
96 hours	0.446	0.09	0.93	0.56	0.80	32.1	0.597
240 hours	0.546	2.22	0.66	0.32	0.90	121.7	0.554
360 hours	0.490	0.31	0.87	0.27	0.89	82.8	0.772
480 hours	0.899	0.10	0.91	0.24	0.86	39.7	1.137

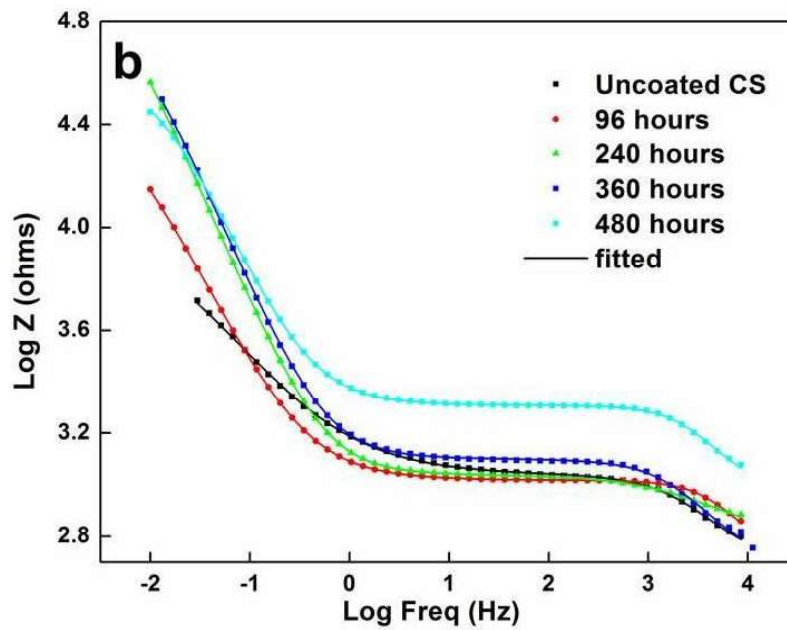
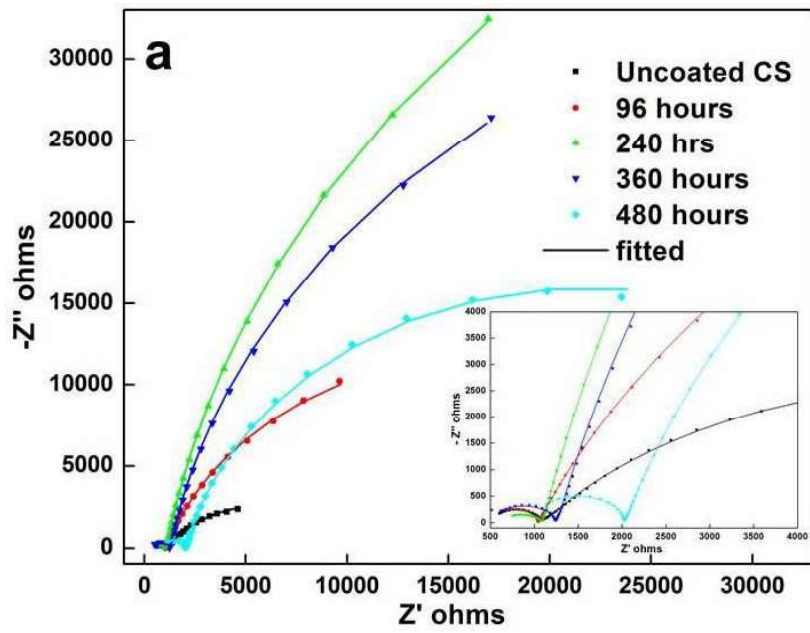


Figure 3.10: (a) Nyquist and (b) Bode plot of CS/Fe₃O₄ at different exposure time

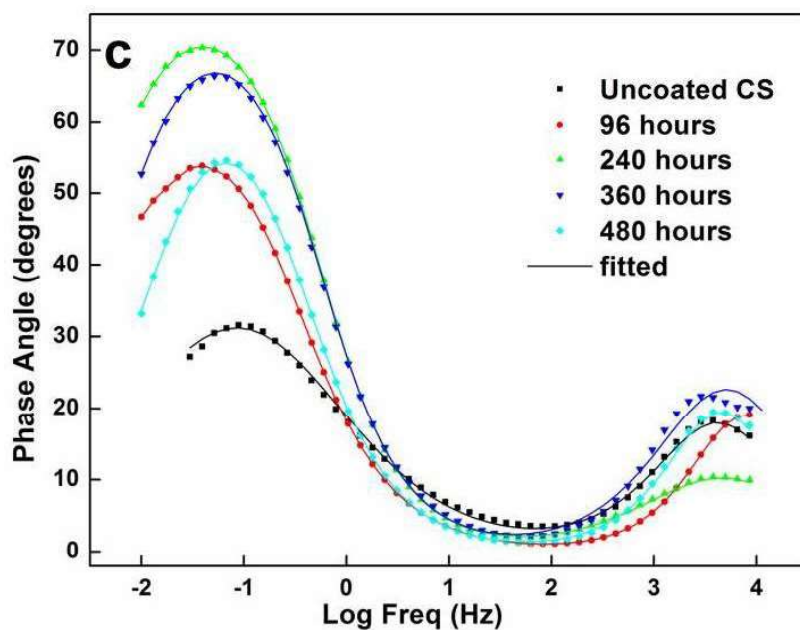


Figure 3.10 (c): Phase angle plot of CS/Fe₃O₄ at different exposure time

3.4.2.3. Mott-Schottky method

Mott-Schottky (MS) plots of the coated specimens acquired at 100 Hz in LiOH solution (pH 10.2) at room temperature are shown in Figure 3.11. MS plot of this frequency was chosen since the imaginary impedance of the system responded well for the variation in applied potential. The oxide coated specimens were found to follow Mott-Schottky relationship at a certain potential range. It was observed that the electronic properties of all the oxide films formed on CS were similar. The curves obtained for CS/Fe₃O₄ for all the exposure times present a positive slope from -0.8 V_{SCE} upward to more anodic potentials. The flat band potential was in the range -0.8 to -1.0 V for the coated specimens. This variation of the square root dependence of the capacitance with the applied potential is typical of an n-type semiconductor and the main defects in the oxide film are cation interstitials or anion vacancies (oxygen) acting as electron donors [105]. In this oxide coated CS the

donor type defects are O^{2-} ions and Fe^{2+} interstitials. The defect densities were calculated from the slope of the linear portion of the Mott–Schottky plots using $\epsilon = 12$ for CS/ Fe_3O_4 and 20 for CS [106]. A high doping density is typical of a defective oxide layer which, in turn, is associated with a lower corrosion resistance [90]. Defect densities calculated for CS/ Fe_3O_4 for different exposure time are given in Table 3.8. Though the orders of the defect density were similar there was a slight reduction in the defect density compared to the uncoated CS. The reduction in the number of defects in the oxide film indicated the formation of less conductive and more protective oxide layers. This result confirmed the increase in corrosion resistance for the oxide coated specimens compared to uncoated CS.

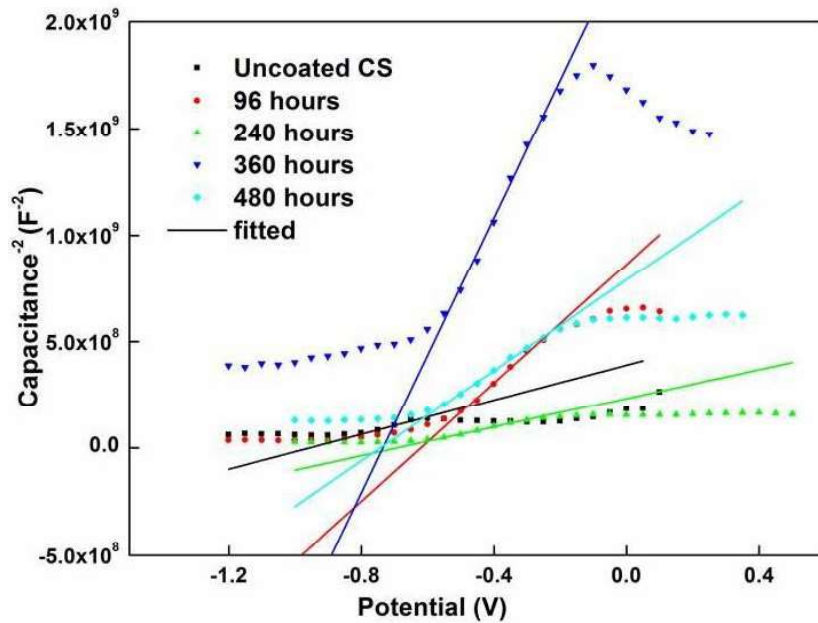


Figure 3.11: Mott Schottky plot of CS/ Fe_3O_4 at different exposure time

Table 3.8: Defect Density of CS/Fe₃O₄ at different exposure time

CS/Fe ₃ O ₄	Defect Density (cm ⁻³)
Uncoated CS	4.29 x 10 ¹⁹
96 hours	1.88 x 10 ¹⁹
240 hours	1.71 x 10 ¹⁹
360 hours	1.43 x 10 ¹⁹
480 hours	1.70 x 10 ¹⁹

3.5. Conclusion

Magnetite formed on CS in an autoclave with different exposure time increased in thickness and defect density reduced inferring better corrosion resistance / protection to the base metal. The exposure time were limited to 96 and 240 hours for further experiments, since above 240 hours the corrosion rates were almost similar.

Chapter 4

Comparison of the nickel ferrite coatings developed by pulsed laser deposition and hydrothermal method

Part I: NiFe₂O₄ deposition by PLD method

4.1. Introduction

As discussed earlier, the corrosion products formed over CS surfaces are mainly Fe₃O₄ in the inner layer and Fe₃O₄/nickel ferrite (NiFe₂O₄) in the outer layer. The nickel released from nickel based steam generator tubes partially converts the Fe₃O₄ present in the outer layer into NiFe₂O₄. NiFe₂O₄ is an inverse spinel in which Ni²⁺ ions occupy the octahedral sites and the deposited NiFe₂O₄ coating on CS/Fe₃O₄ by PLD method at high temperature could change the distribution of cations (Ni²⁺ and Fe³⁺) between tetrahedral and octahedral sites at the interface between Fe₃O₄ and NiFe₂O₄. Hence, the performance of these coatings in predicting the corrosion resistance property is important. In part I of this chapter, studies were carried out to evaluate the corrosion resistance property of the nano NiFe₂O₄ coating over CS/Fe₃O₄ by varying the thickness of the former.

4.2. Results and Discussion

The unit cell of NiFe₂O₄ is formed by 56 atoms, 32 oxygen anions dispersed in a cubic close packed structure and 24 cations occupying 8 of the 64 tetrahedral sites (A sites) and 16 of the 32 octahedral sites (B sites) [107]. In NiFe₂O₄, Ni²⁺ ions occupy the B sites surrounded by 6 oxygen atoms. The characterization of the deposited NiFe₂O₄ is explained in the following sections.

4.2.1. X-Ray Diffraction Analysis

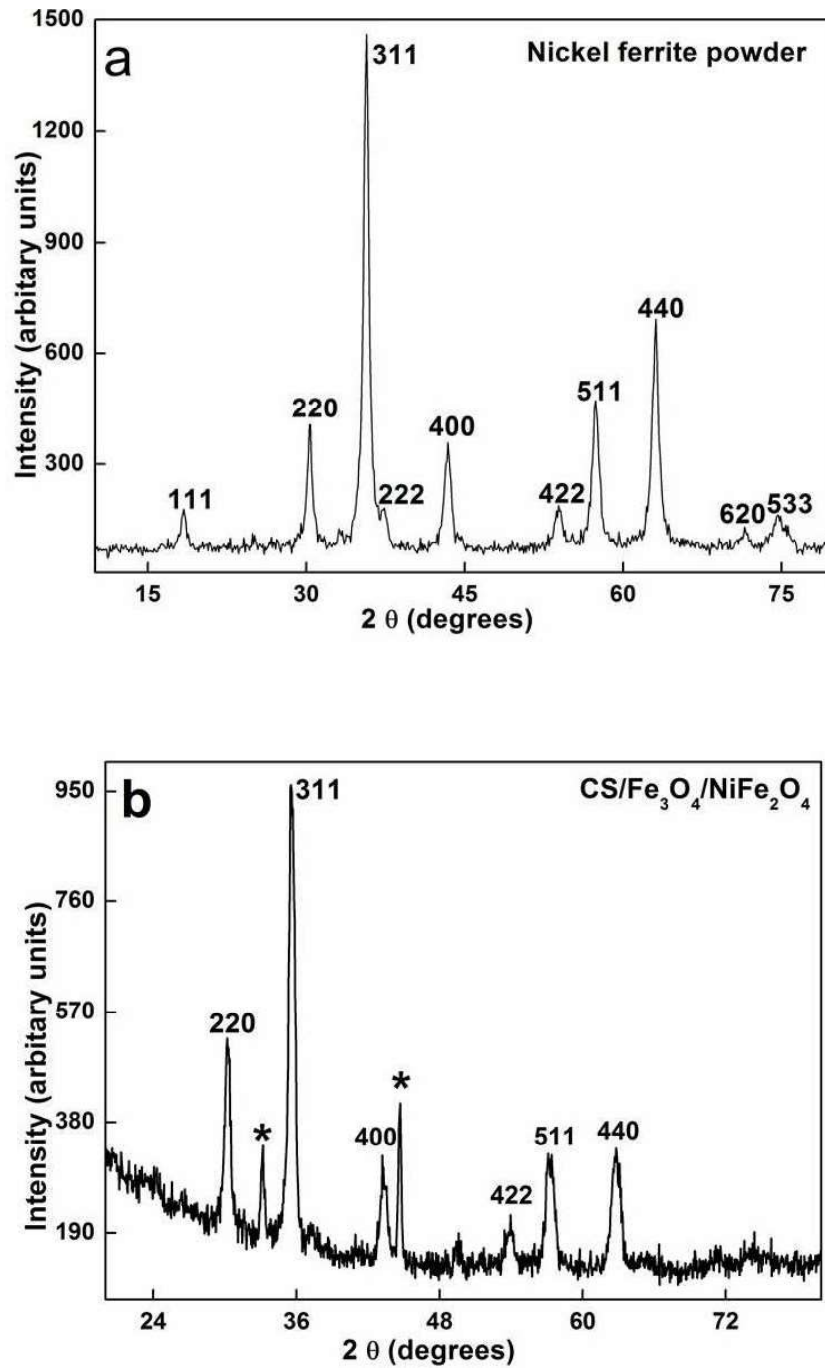


Figure 4.1: (a) XRD pattern of synthesized NiFe₂O₄ powder and (b) GI-XRD pattern of CS/Fe₃O₄/NiFe₂O₄

The XRD pattern of (a) synthesized NiFe₂O₄ powder and (b) GI-XRD pattern of CS/Fe₃O₄/NiFe₂O₄ coating are shown in Figure 4.1. The pattern of both synthesized and deposited NiFe₂O₄ displayed sharp and well resolved diffraction peaks with good crystallinity. All peaks detected at the $2\theta = 18.36^\circ, 30.34^\circ, 35.71^\circ, 37.39^\circ, 43.44^\circ, 53.84^\circ, 57.41^\circ, 63.01^\circ, 71.62^\circ$ and 74.66° clearly pointed to the formation of the NiFe₂O₄ phase (ICDD.No.04-014-8286). The peaks are well indexed to the crystal plane of spinel ferrite (h k l) (111), (220), (311), (222), (400), (422), (511), (440), (620) and (533) respectively. This confirms that the synthesis of NiFe₂O₄ by co-precipitation method and deposition by PLD method are feasible. The lattice parameter calculated for synthesized NiFe₂O₄ powder and coating were 8.33 Å and 8.38 Å respectively. The peaks marked as * in Figure 4.1 (b) at $2\theta = 33.17^\circ$ and 44.71° were the signals from the base metal (CS) and no diffraction peaks of other impurities were observed. The average crystallite size calculated by using Debye Scherrer's equation for synthesized NiFe₂O₄ powder and the deposited NiFe₂O₄ were 14 nm and 26 nm respectively [65].

4.2.2. Laser Raman Spectroscopic Analysis

Ferrites are spinel oxide with five Raman active modes namely A₁, E_g and 3T_g [108]. Figure 4.2 shows the Raman spectrum recorded for CS/Fe₃O₄/NiFe₂O₄. The structure of NiFe₂O₄ can be considered as a mixture of two sub lattices with Fe³⁺ and Ni²⁺ ordered over the A and B-sites. In nanocrystalline samples asymmetry is partly due to confinement and size-distribution of nanoparticles [109]. The Raman modes E_g, T_{2g} (3) and T_{2g} (2) are due to symmetric bending of oxygen with respect to metal ion, asymmetric bending of oxygen and asymmetric stretching of Fe (Ni) and O

respectively. T_{2g} (2) and T_{2g} (3) correspond to the vibrations of octahedral group. T_{2g} (1) is due to translational movement of the tetrahedron (metal ion at tetrahedral site together with four oxygen atoms) [110]. CS/ Fe_3O_4 / $NiFe_2O_4$ showed five peak maxima at 194.8, 336.3, 486.9, 577.1 and 699 cm^{-1} . Frequencies above 600 cm^{-1} , i.e., peak maxima at 699 cm^{-1} in CS/ Fe_3O_4 / $NiFe_2O_4$ are assigned to A_{1g} mode which is due to symmetric stretching of oxygen atoms along Fe-O (and Ni-O) bonds in the tetrahedral coordination [111]. Reduction in grain size or change in cation distribution between tetrahedral and octahedral sites results in the broadening of modes in the Raman spectra due to which FWHM changes [112]. The peak observed at 486.9 cm^{-1} involves Fe^{3+} vibration at octahedral site. There is a negligible displacement of metal atoms in modes A_{1g} , E_g and T_{2g} (3) [113].

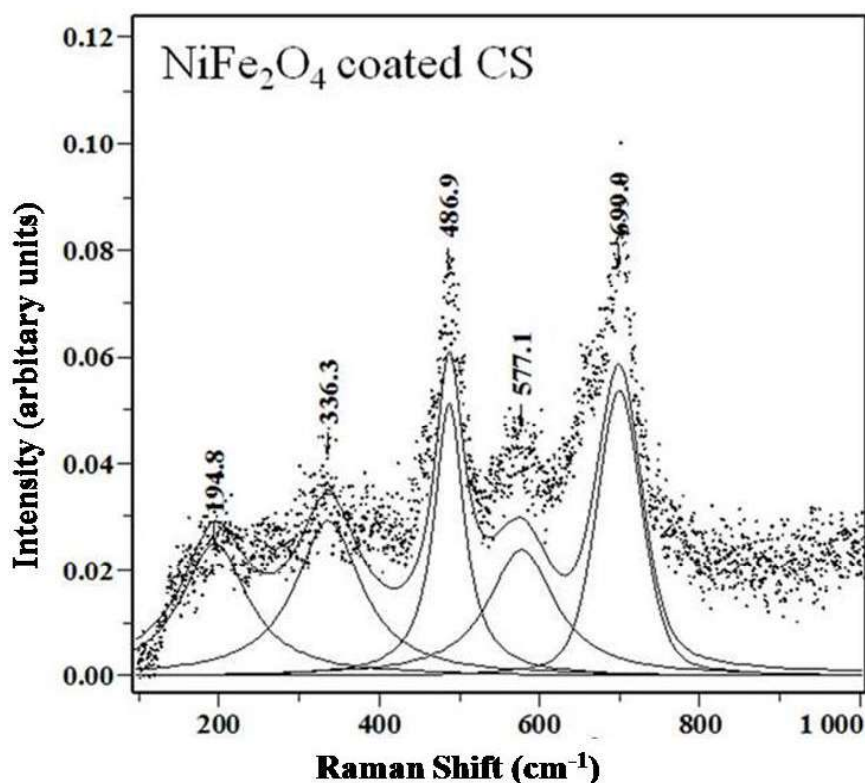


Figure 4.2: Raman spectrum of CS/ Fe_3O_4 / $NiFe_2O_4$

4.2.3. Scanning Electron Microscopic Analysis

The surface morphology from SEM and the cross section of the coating from FE-SEM of CS/Fe₃O₄/NiFe₂O₄ are as shown in Figure 4.3 (a) and (b) respectively. Figure 4.3 (a) showed that the substrate was uniformly covered by the NiFe₂O₄ film and nanocrystalline grains were formed by agglomeration of smaller particles having almost similar shapes. The porous Fe₃O₄ was not visible after the deposition of NiFe₂O₄. The thickness of the coating measured was 1.1 μm which included the magnetite coating.

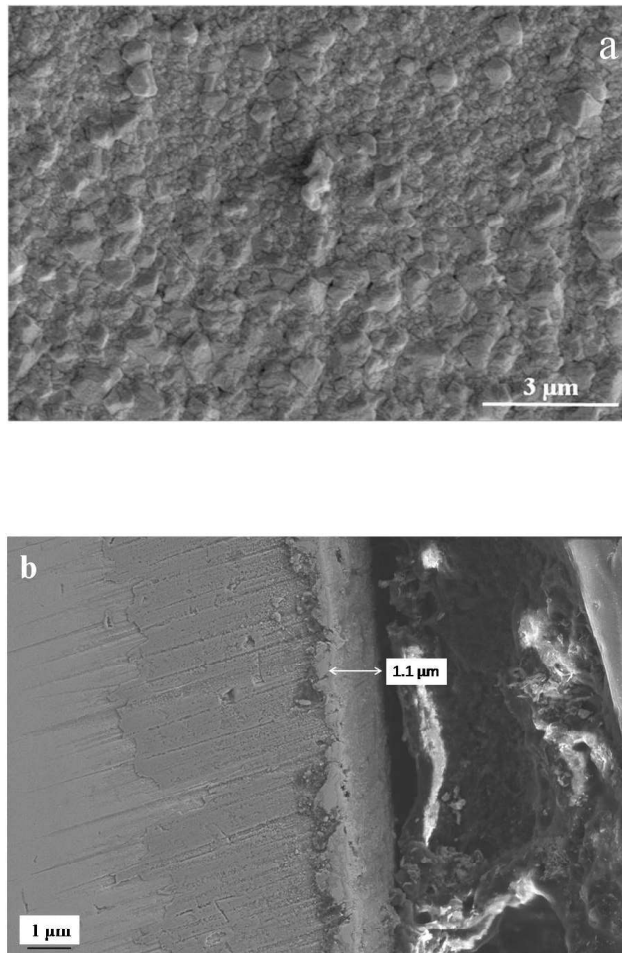


Figure 4.3: (a) SEM image and (b) Cross section of CS/Fe₃O₄/NiFe₂O₄

4.2.4. X-Ray Photoelectron Spectroscopic Analysis

XPS was used to characterize the chemical composition of the CS/Fe₃O₄/NiFe₂O₄. XPS spectra of (a) Ni 2p, (b) Fe 2p and (c) O 1s peaks obtained for CS/Fe₃O₄/NiFe₂O₄ are shown in Figure 4.4. Fe 2p_{3/2} photoelectron peaks obtained from CS/Fe₃O₄/NiFe₂O₄ are shown in Figure 4.4 (b). The binding energy value of Fe 2p_{3/2} was observed at around 711.1 eV that matched well with the literature value [103]. Fe 2p_{3/2} was associated with a small satellite peak around 719 eV. The narrower peak width of Fe 2p_{3/2} indicated the presence of single oxidation state of Fe (Fe³⁺). Ni 2p_{3/2} peak was observed at around 855 eV and Ni 2p_{1/2} was observed at 862 eV (Figure 4.4 a) which are the characteristic binding energies for Ni 2p revealing the oxidation state of Ni²⁺ as expected. As shown in Figure 4.4 (c), O 1s peak observed at 530.1 eV for the coated specimen indicated that the oxygen atoms were in the O²⁻ form in the lattice.

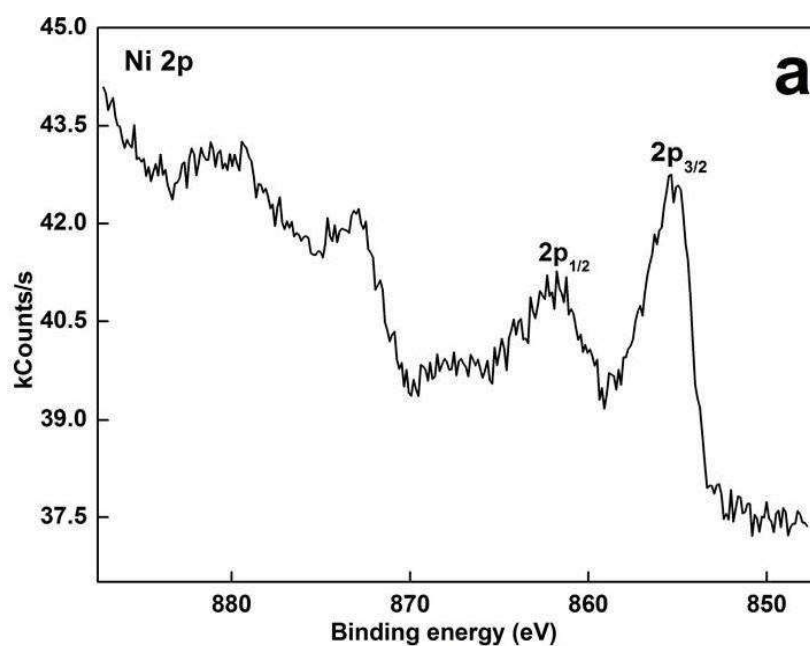


Figure 4.4: (a) XPS spectrum of Ni 2p obtained for CS/Fe₃O₄/NiFe₂O₄

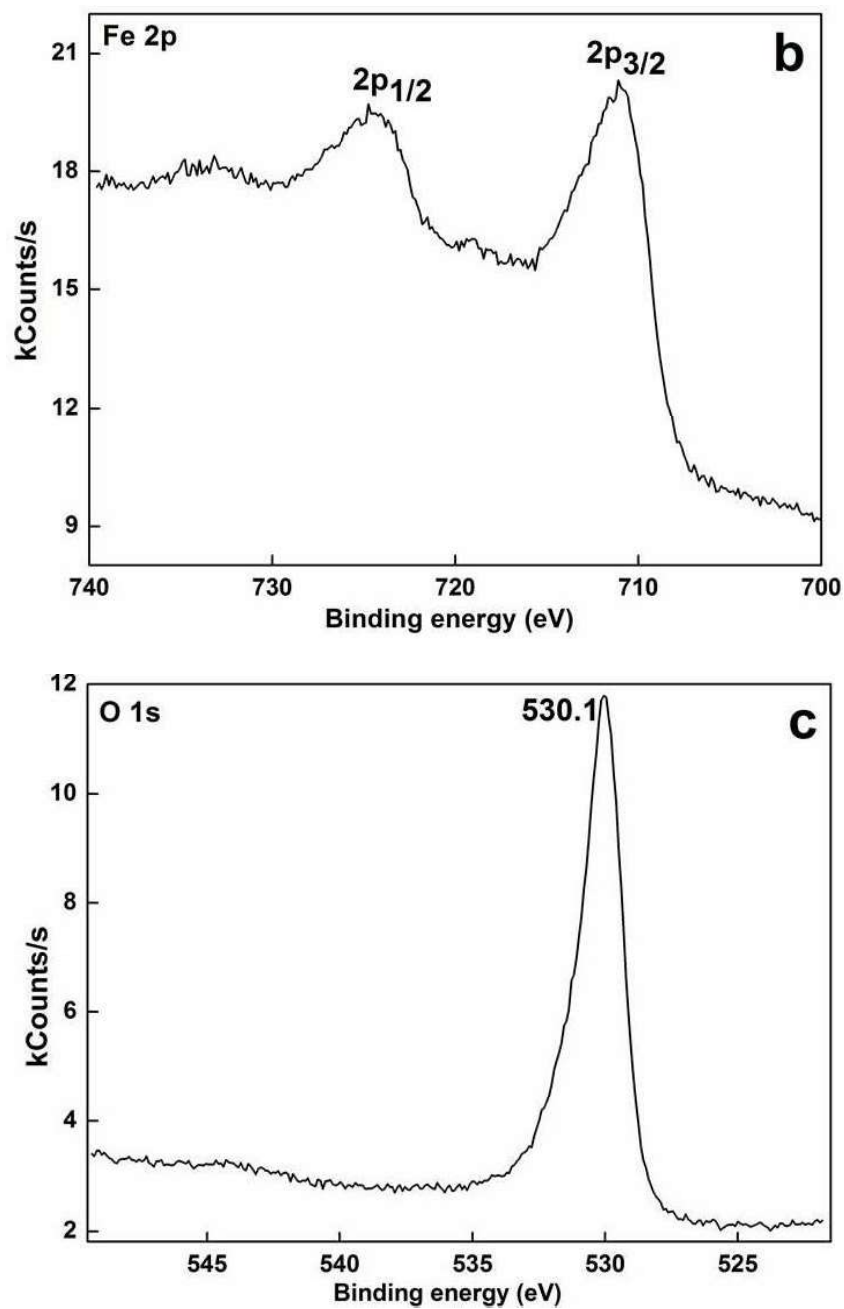


Figure 4.4: XPS spectra of (b) Fe 2p and (c) O 1s obtained for CS/Fe₃O₄/NiFe₂O₄

From the above GI-XRD and XPS analyses it appeared that the NiFe₂O₄ coating on CS/Fe₃O₄ was composed of NiFe₂O₄ only. Quantitative analyses showed that the % of the elements Fe, Ni and O present were 14%, 8% and 78% respectively.

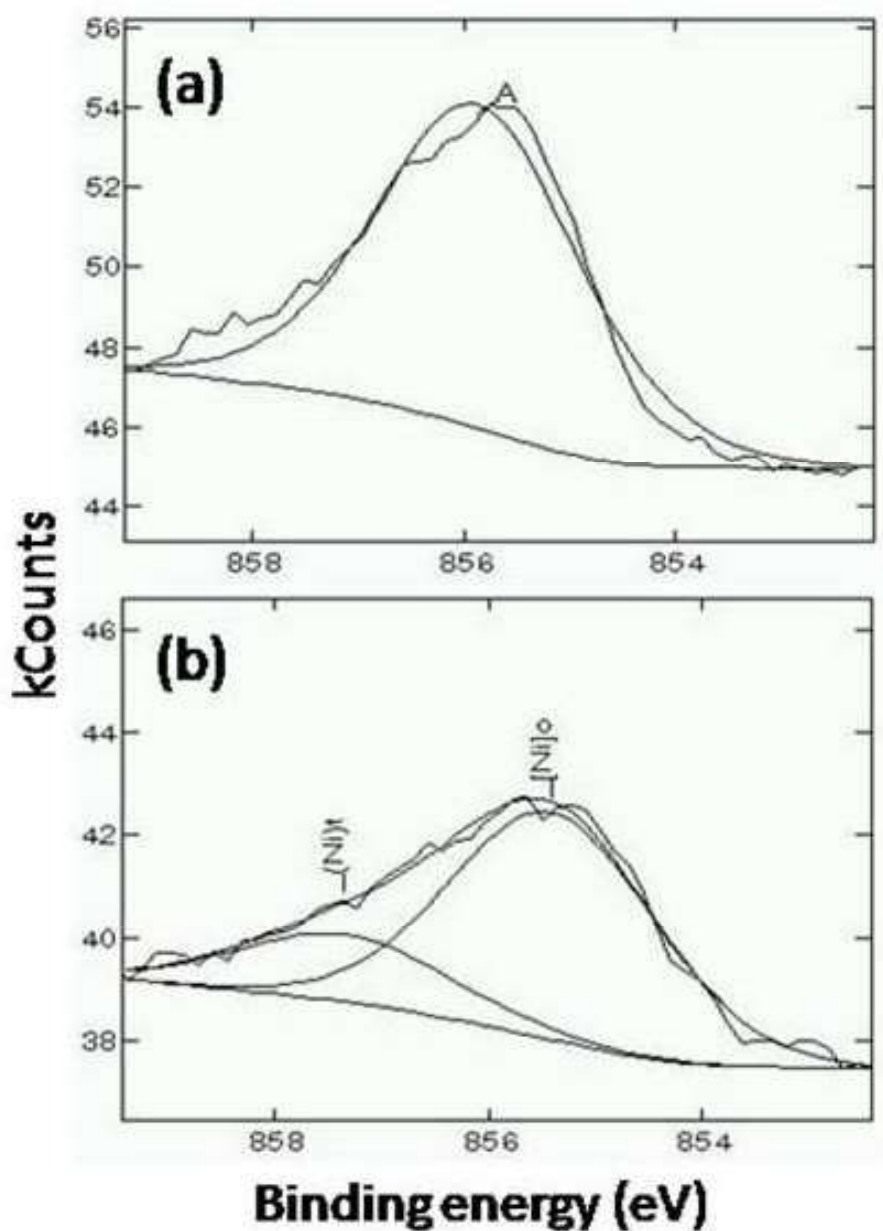


Figure 4.5: XPS spectra of Ni $2p_{3/2}$ from (a) NiFe_2O_4 powder and (b) $\text{CS}/\text{Fe}_3\text{O}_4/\text{NiFe}_2\text{O}_4$

Further analysis of the Ni $2p_{3/2}$ peak was carried out by deconvolution to determine the distribution of the Ni^{2+} ions between the tetrahedral and the octahedral sites at the $\text{Fe}_3\text{O}_4/\text{NiFe}_2\text{O}_4$ interface. In Figure 4.5, Ni $2p_{3/2}$ peak acquired from the

CS/Fe₃O₄/NiFe₂O₄ (Figure 4.5 (b)) was compared with the NiFe₂O₄ powder (Figure 4.5 (a)). The peak width of the Ni 2p_{3/2} peak from the powder was around 2.3 eV; but increased to 2.8 eV in the coatings. The wider peak was fitted with the regular peak width of Ni 2p_{3/2} in ferrite (2.3 eV) at 855.4 eV and another peak at 856.8 eV. The higher energy peak was assumed to be the peak from Ni²⁺ in tetrahedral sites [114]. It appears from this analysis that though Ni²⁺ is preferred in octahedral site, it can occupy the tetrahedral sites also due to nanocrystalline nature of the coating.

4.2.5. Electrochemical Characterization

In this study, Fe₃O₄ coating and NiFe₂O₄ coating of thicknesses 200, 325 and 500 nm are labelled as CS/Fe₃O₄, CS/Fe₃O₄/NiFe₂O₄-1, CS/Fe₃O₄/NiFe₂O₄-2 and CS/Fe₃O₄/NiFe₂O₄-3 respectively. The CS data is given for comparison.

4.2.5.1. Electrochemical Impedance Spectroscopy

The Nyquist, Bode and Phase angle plots for the uncoated and coated samples obtained at OCP using EIS in deaerated LiOH solution at 28 °C is shown in Figure 4.6 (a-c) respectively. Nyquist plot showed two semicircles due to the presence of two time constants attributed to processes occurring near metal/film and film/solution interface for the uncoated CS and metal/oxide and oxide/solution interface for CS/Fe₃O₄ and NiFe₂O₄ coated on CS/Fe₃O₄ with three different thicknesses. The impedance parameters fitted from the curve are presented in Table 4.1 where R_s represents the solution resistance, R₁ and Q₁ are the resistance and constant phase element with respect to the oxide/solution interface and R₂ and Q₂

are the resistance and constant phase element corresponding to metal/oxide interface. A high resistance value (R_1+R_2) obtained for CS/Fe₃O₄/NiFe₂O₄-3 compared to uncoated CS and CS/Fe₃O₄ indicated that nano NiFe₂O₄ coating of 500 nm thick offered better corrosion resistance. At low frequencies, the phase angle for the CS/Fe₃O₄/NiFe₂O₄-3 increased implying increased capacitance as observed from Figure 4.6 (c). From the Bode plot (Figure 4.6 b) it was observed that the impedance was higher for CS/Fe₃O₄/NiFe₂O₄-1 in the higher frequency region indicating the nature of the coating was good but due to the presence of defect density of same order as present in case of CS/Fe₃O₄ (given in section 4.2.5.3), the impedance reduced in the lower frequency region. The values of the exponent 'n' obtained by fitting the EIS data were between 0.63 and 0.89 for all the samples. The $0.5 < 'n' < 1$ values are associated to the heterogeneity and complexity of the electrode surface [115]. The value of 'n' (0.78) associated with Q₂ in case of CS/Fe₃O₄/NiFe₂O₄-1 was less compared to the other coatings indicating that the surface heterogeneity increased and the 200 nm thick coating was not sufficient to provide resistance better than the CS/Fe₃O₄. The Bode spectra also showed a significant increase in the low frequency impedance modulus, indicating an increase in corrosion resistance in case of CS/Fe₃O₄/NiFe₂O₄-3 coating. The impedance behavior of CS/Fe₃O₄ and CS/Fe₃O₄/NiFe₂O₄-2 were similar and the magnitude of their impedance values suggested that they offered a better corrosion resistance compared to the CS/Fe₃O₄/NiFe₂O₄-1 specimen.

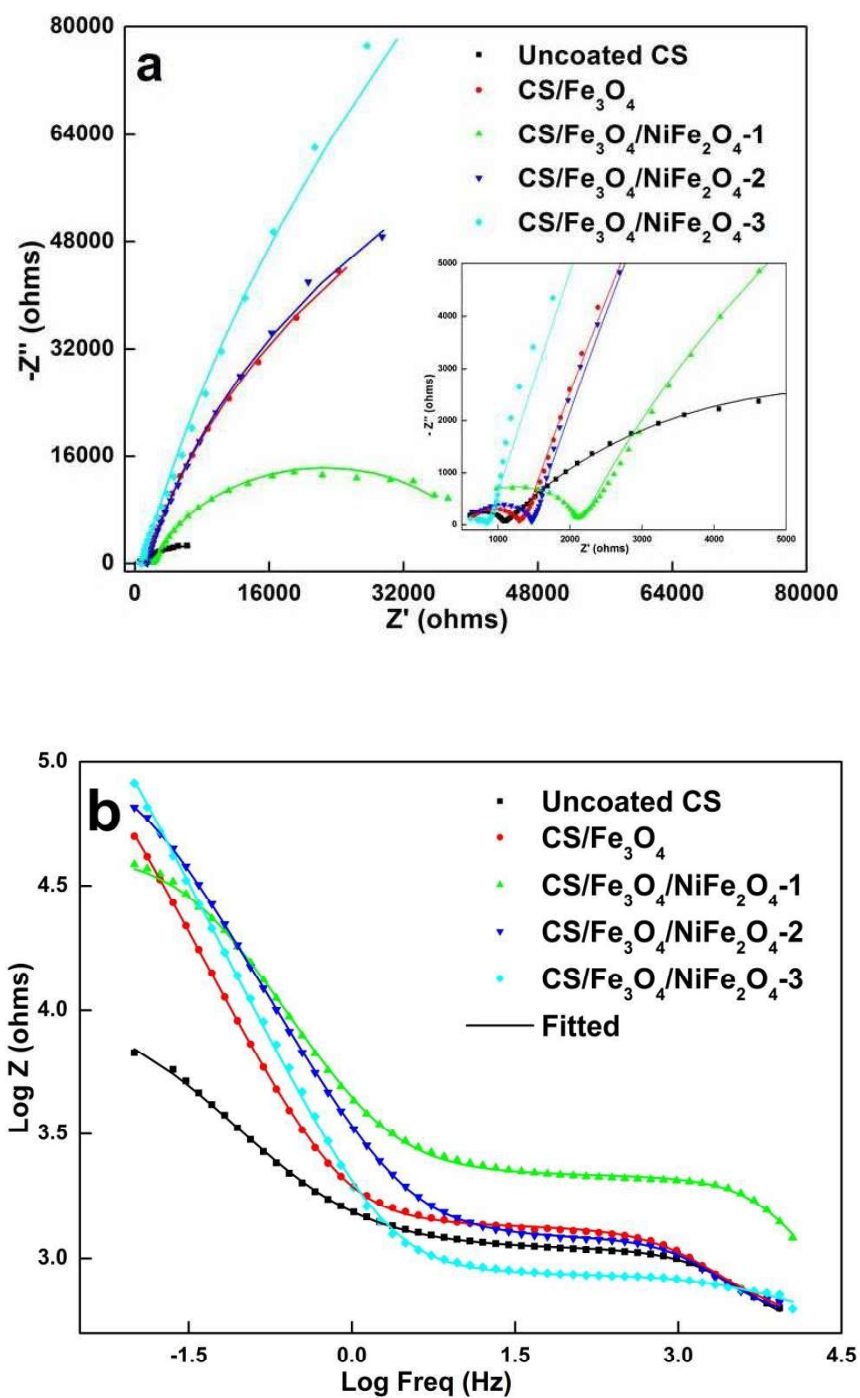


Figure 4.6: EIS (a) Nyquist and (b) Bode plot of uncoated CS, CS/Fe₃O₄ and CS/Fe₃O₄/NiFe₂O₄ (thickness 200, 325 and 500 nm)

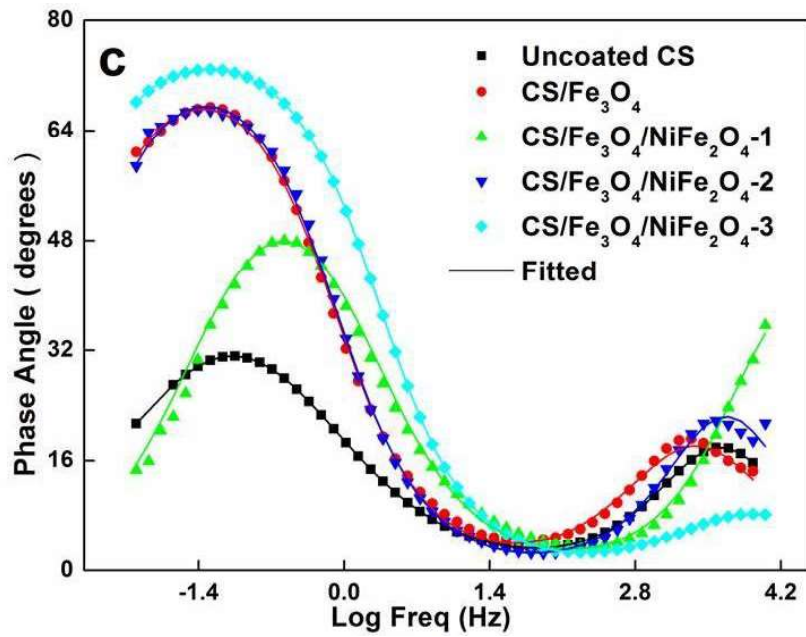


Figure 4.6: (c) EIS Phase Angle plot of uncoated CS, CS/Fe₃O₄ and CS/Fe₃O₄/NiFe₂O₄ (thickness 200, 325 and 500 nm)

Table 4.1: Impedance parameters obtained from EIS measurements

Specimen	R _s (KΩ)	R ₁ (KΩ)	Q ₁ (μF)	n	R ₂ (KΩ)	Q ₂ (mF)	n
Uncoated CS	0.487	0.607	0.44	0.85	9.5	0.49	0.63
CS/Fe ₃ O ₄	0.543	0.801	0.97	0.79	191.2	0.19	0.85
CS/Fe ₃ O ₄ /NiFe ₂ O ₄ -1	0.372	1.775	0.04	0.88	40.8	0.07	0.78
CS/Fe ₃ O ₄ /NiFe ₂ O ₄ -2	0.566	0.910	0.19	0.89	195.4	0.17	0.86
CS/Fe ₃ O ₄ /NiFe ₂ O ₄ -3	0.548	0.314	1.49	0.72	552.0	0.12	0.86

4.2.5.2. Potentiodynamic Anodic Polarization

Figure 4.7 shows the PDAP curve for CS, CS/Fe₃O₄, CS/Fe₃O₄/NiFe₂O₄-1, CS/Fe₃O₄/NiFe₂O₄-2 and CS/Fe₃O₄/NiFe₂O₄-3 in deaerated LiOH medium at 28 °C. The corrosion parameters obtained from the PDAP analysis are given in Table 4.2. The OCP for CS/Fe₃O₄/NiFe₂O₄ (all the three thickness) had shifted towards the

noble side (-0.230 V, -0.374 V and -0.259 V respectively vs. SCE) compared to the uncoated CS and CS/Fe₃O₄ (-0.497 V and -0.424 V respectively vs. SCE). A small shoulder is observed on the anodic portion in the case of the uncoated CS which could be due to the formation of the iron hydroxide film. The passivation region for CS/Fe₃O₄ was broad and observed in the range -0.125 to +0.799 V whereas for all the three CS/Fe₃O₄/NiFe₂O₄ specimens the passivation region was very small and an increase in the current was observed which could be due to the instability of the film at higher anodic potentials. Based on the values of corrosion current, the corrosion resistance was found to be in the following order: CS/Fe₃O₄/NiFe₂O₄-3 ≥ CS/Fe₃O₄/NiFe₂O₄-2 > CS/Fe₃O₄ > CS/Fe₃O₄/NiFe₂O₄-1 > CS. Though the total resistance (R₁+R₂) value was higher in case of CS/Fe₃O₄/NiFe₂O₄-3 compared to the CS/Fe₃O₄/NiFe₂O₄-2, the corrosion rate values were similar for both the coatings. Though the PDAP curve for CS/Fe₃O₄/NiFe₂O₄-1 and CS/Fe₃O₄/NiFe₂O₄-2 shifted to lower current region compared to uncoated CS but compared to CS/Fe₃O₄ both the curves were in the higher current region and hence these two coatings were not protective. It was reported in the literature that the strain/defects imparted into thin films due to differences in lattice constant between the film and the substrate [116], may influence the properties and quality of thin films. Table 4.3 gives the defect density values for the CS/Fe₃O₄ and CS/Fe₃O₄/NiFe₂O₄-1, which are almost similar and this may be the reason for the higher corrosion rate value for CS/Fe₃O₄/NiFe₂O₄-1 compared to the CS/Fe₃O₄. Hence, the NiFe₂O₄ coating improves the corrosion resistance compared to CS and CS/Fe₃O₄, having an optimum thickness with lesser defects for providing better protection.

Table 4.2: Corrosion parameters obtained from PDAP measurements

Specimen	PDAP				
	b_c (V/dec)	b_a (V/dec)	OCP (V)	i_{corr} ($\mu\text{A}/\text{cm}^2$)	Corrosion Rate (mpy)
Uncoated CS	-0.236	0.283	-0.497	1.194	0.552
CS/ Fe_3O_4	-0.148	0.414	-0.424	0.219	0.101
CS/ $\text{Fe}_3\text{O}_4/\text{NiFe}_2\text{O}_4$ -1	-0.316	0.334	-0.230	0.670	0.310
CS/ $\text{Fe}_3\text{O}_4/\text{NiFe}_2\text{O}_4$ -2	-0.269	0.133	-0.374	0.090	0.041
CS/ $\text{Fe}_3\text{O}_4/\text{NiFe}_2\text{O}_4$ -3	-0.213	0.236	-0.259	0.124	0.057

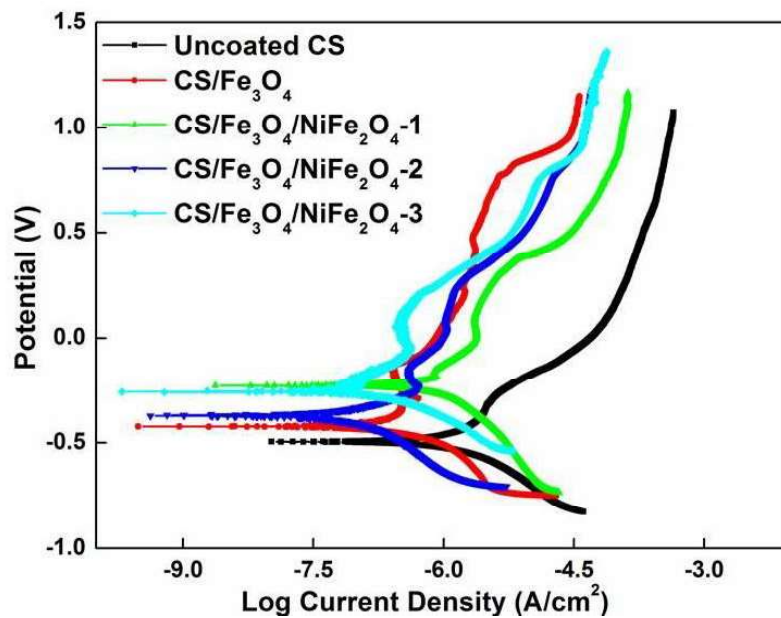


Figure 4.7: PDAP plot of uncoated CS, CS/ Fe_3O_4 and CS/ $\text{Fe}_3\text{O}_4/\text{NiFe}_2\text{O}_4$ (thickness 200, 325 and 500 nm)

4.2.5.3. Semiconducting properties of the oxide film

The anodic passive film as suggested by Chao et al. [117] contains a high concentration of point defect such as metal vacancies, electrons and holes. Mott Schottky plots of the coated specimens acquired at 100 Hz in LiOH solution (pH

10.2) at 28 °C are shown in Figure 4.8. It was observed that the electronic properties of all the coated specimens were similar. The curves obtained for CS/Fe₃O₄ and all the three NiFe₂O₄ coating presented a positive slope from -0.8 V_{SCE} upward to more anodic potentials. This inverse dependency of square of capacitance with the applied potential is typical of an n-type semiconductor and the main donor type defects in the oxide film are cation interstitials or anion vacancies (oxygen) acting as electron donors [105]. The defect density concentrations corresponding to coated specimens are given in Table 4.3. The 200 nm NiFe₂O₄ coating on CS/Fe₃O₄ was not sufficient to minimize the defects which may be the cause for increased corrosion as charge transfer is easily possible through these defects. The electronic conductivity of the oxide film is proportional to the density of point defects in the oxide coating which acts as the tunnel for the migration of electron or ion, and the decrease of ‘N’ for CS/Fe₃O₄/NiFe₂O₄-3 makes the charge transport process difficult through the oxide film [118]. This result confirmed the increase of corrosion resistance of NiFe₂O₄ coating in comparison to uncoated CS and CS/Fe₃O₄.

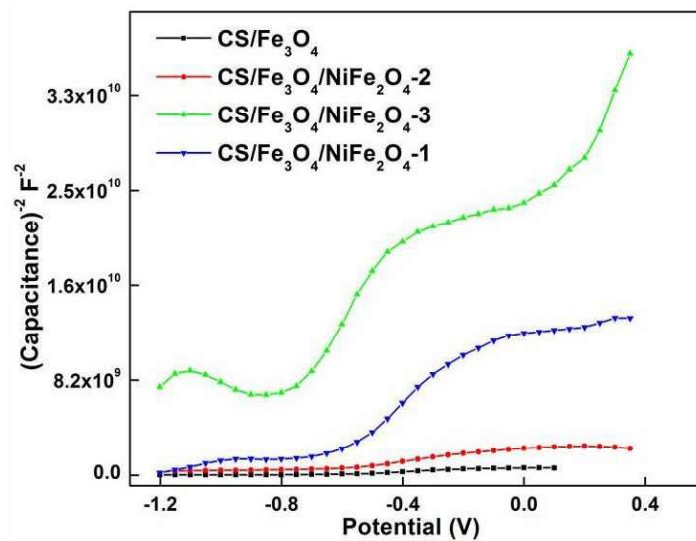


Figure 4.8: Mott Schottky plot of CS/Fe₃O₄ and CS/Fe₃O₄/NiFe₂O₄

Table 4.3: Defect Density for CS/Fe₃O₄ and CS/Fe₃O₄/NiFe₂O₄

Specimen	Defect Density (cm ⁻³)
CS/Fe ₃ O ₄	2.72 x 10 ¹⁹
CS/Fe ₃ O ₄ /NiFe ₂ O ₄ -1	1.11 x 10 ¹⁹
CS/Fe ₃ O ₄ /NiFe ₂ O ₄ -2	9.65 x 10 ¹⁸
CS/Fe ₃ O ₄ /NiFe ₂ O ₄ -3	7.92 x 10 ¹⁷

4.2.6. Focused Ion Beam-SEM Analysis

From the electrochemical studies, it was observed that the 200 nm thick NiFe₂O₄ coating showed a higher corrosion rate value than the CS/Fe₃O₄. FIB-SEM analysis was carried out to understand the bonding of the NiFe₂O₄ coating over CS/Fe₃O₄. Figure 4.9 shows the cross section of the NiFe₂O₄ coating on CS/Fe₃O₄ prepared by FIB in-situ-lift out technique. This technique suits cross sectional preparation of thin film samples for TEM because it involves sequential removal of material from each layer of site specific region of interest and with uniform thickness. Lamellae were thinned down to less than 100 nm to make it electron transparent. The elemental compositions of the NiFe₂O₄ coating was investigated by using EDAX spot analysis on the lamellae as given in Figure 4.10. The EDAX spectrum confirmed the presence of Ni, Fe and O in the inner layer marked as 2 and 4 as shown in Figure 4.10 (a) and (b). The top layer marked as 1 is the Pt layer deposited at the sample surface to protect the region of interest from curtaining effect of ion beam. The layer marked as 4 is the bulk CS substrate with Fe as the major element which is shown in Figure 4.10 (c). NiFe₂O₄ coating of ~ 200 nm thicknesses is observed between the bulk Fe below and top Pt coating. The elemental composition of the marked area 2,

3 and 4 is given in Figure 4.10 (d) and it was observed that the Ni content was slightly lower than the actual stoichiometric composition.

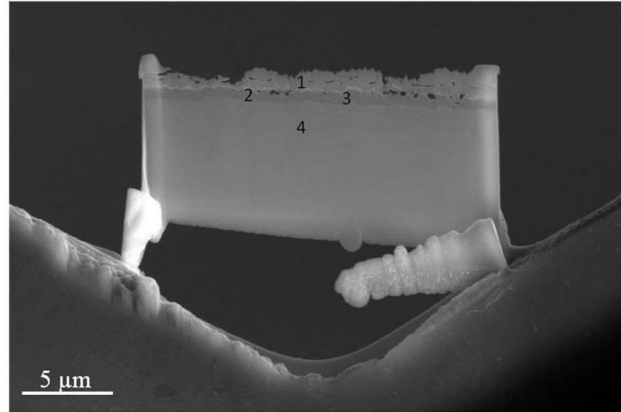


Figure 4.9: FIB-SEM of cross section of CS/Fe₃O₄/NiFe₂O₄

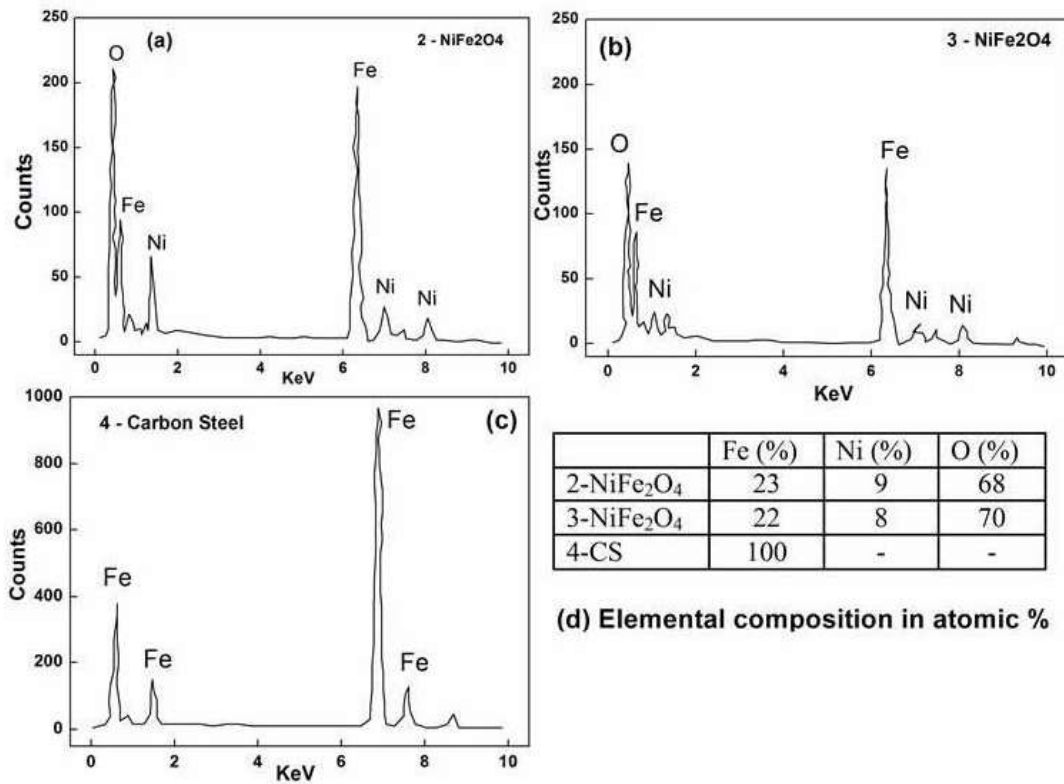


Figure 4.10: EDAX of (a) 2-NiFe₂O₄ coating, (b) 3-NiFe₂O₄ coating, (c) 4-CS and (d) Elemental composition in atomic % of the marked area 2, 3 and 4

4.2.7. Transmission Electron Microscopic Analysis

TEM analysis performed on lamellas fabricated by focused ion beam (FIB) technique as shown in Figure 4.11 (a). The figure indicates the growth direction, exhibits the high-resolution transmission electron microscopic lattice fringes of (311) planes with the lattice spacing of 0.249 nm between the adjacent planes. These structural studies clearly illustrate the formation of large amount of distinct uniform nanoparticles of NiFe₂O₄. The corresponding selected area electron diffraction (SAED) pattern is shown in Figure 4.11 (b) and the 'd' values calculated from the diffraction rings were compared with the 'd' values from ICDD and was found to be comparable. The bright electron diffraction rings for NiFe₂O₄ film showed that the NiFe₂O₄ film was nano crystalline. This fact is also supported by the XRD results, in which peak intensities of NiFe₂O₄ film were small compared to the synthesized powder. All of these rings can be indexed to spinel structures, which is also consistent with the GI-XRD data. It was observed from Figure 4.11 (c) that the interface between the NiFe₂O₄ coating and the CS/Fe₃O₄ to be smooth and uniform. However, the defect density value obtained in case of NiFe₂O₄ coating was found to be higher when compared to the defect density value obtained for CS/Fe₃O₄ as shown by Mott-Schottky analysis. In addition, the spinel type structure of nickel ferrite has also been confirmed by the relevant diffractogram. The chemical composition and the electronic structure of deposited NiFe₂O₄ over CS/Fe₃O₄ were investigated using EELS as shown in Figure 4.11 (d). The positions of the peaks were comparable with that observed in the XPS spectrum. The presence of O K edge, Fe L edge, and Ni L edge indicates the sample composition of O, Fe, and Ni. The Fe L edge showed two main peaks (L₃ and L₂), which correspond to the electron

excitations from the spin orbit splitting levels $2p_{3/2}$ and $2p_{1/2}$ to the empty density of states in the material conduction band.

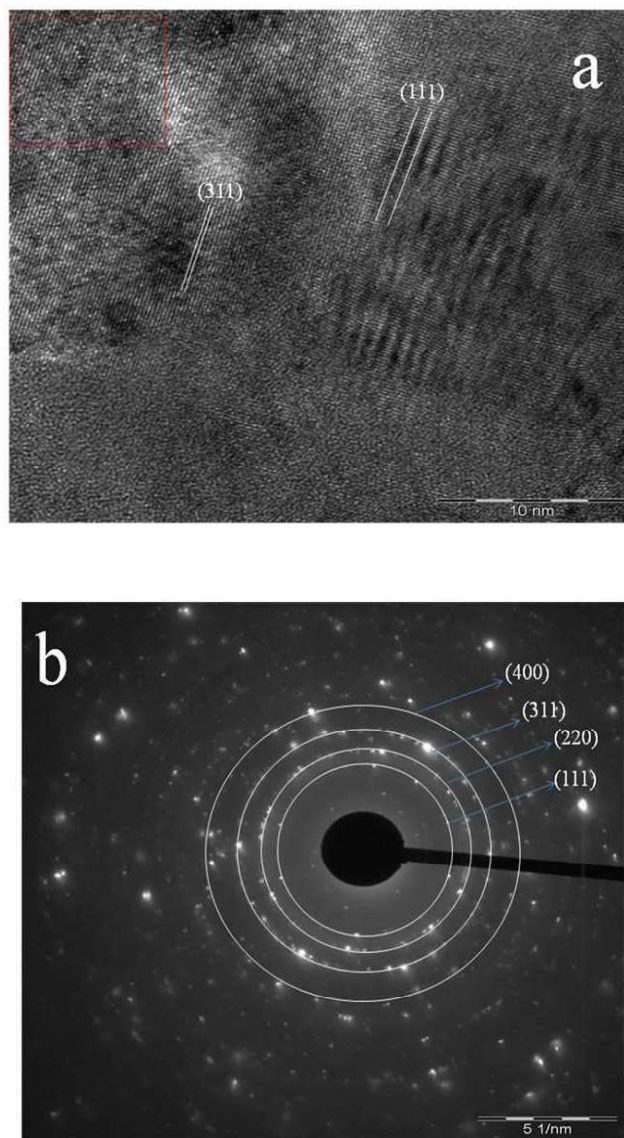


Figure 4.11: (a) HRTEM image and (b) Electron Diffraction on CS/Fe₃O₄/NiFe₂O₄

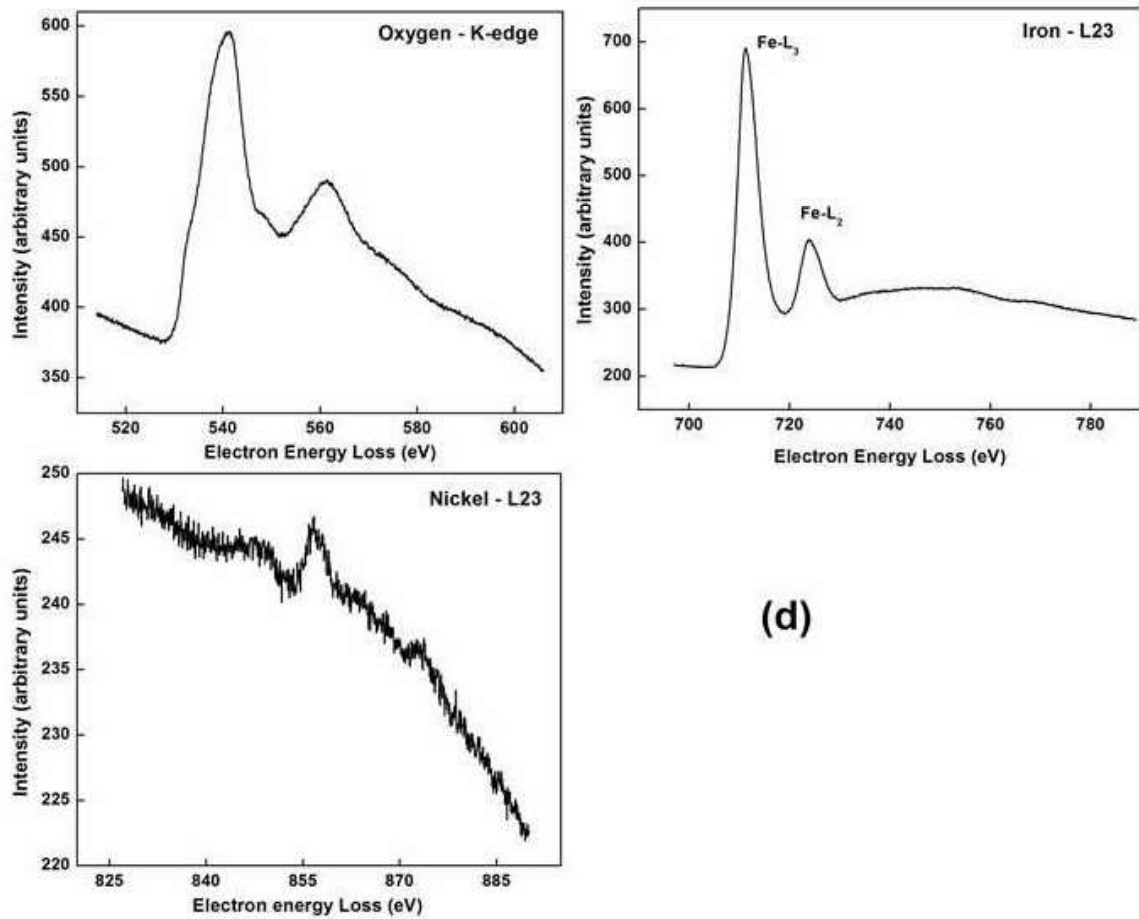
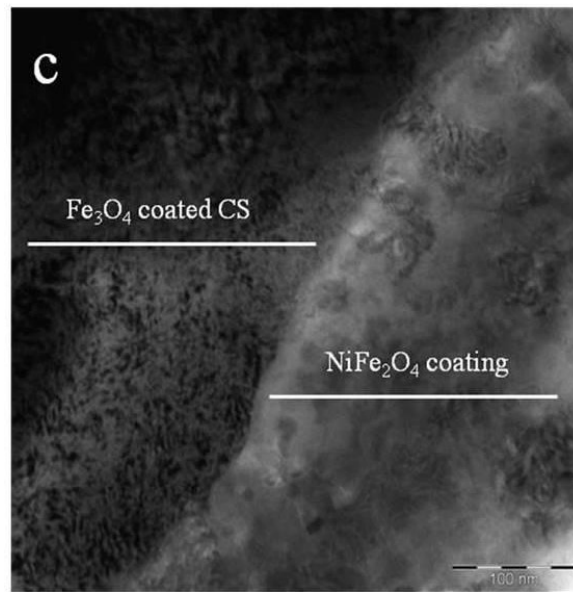


Figure 4.11: (c) HRTEM image of the interface (d) Electron Energy Loss spectrum of O, Fe and Ni on CS/Fe₃O₄/NiFe₂O₄

4.2.8. Scratch test

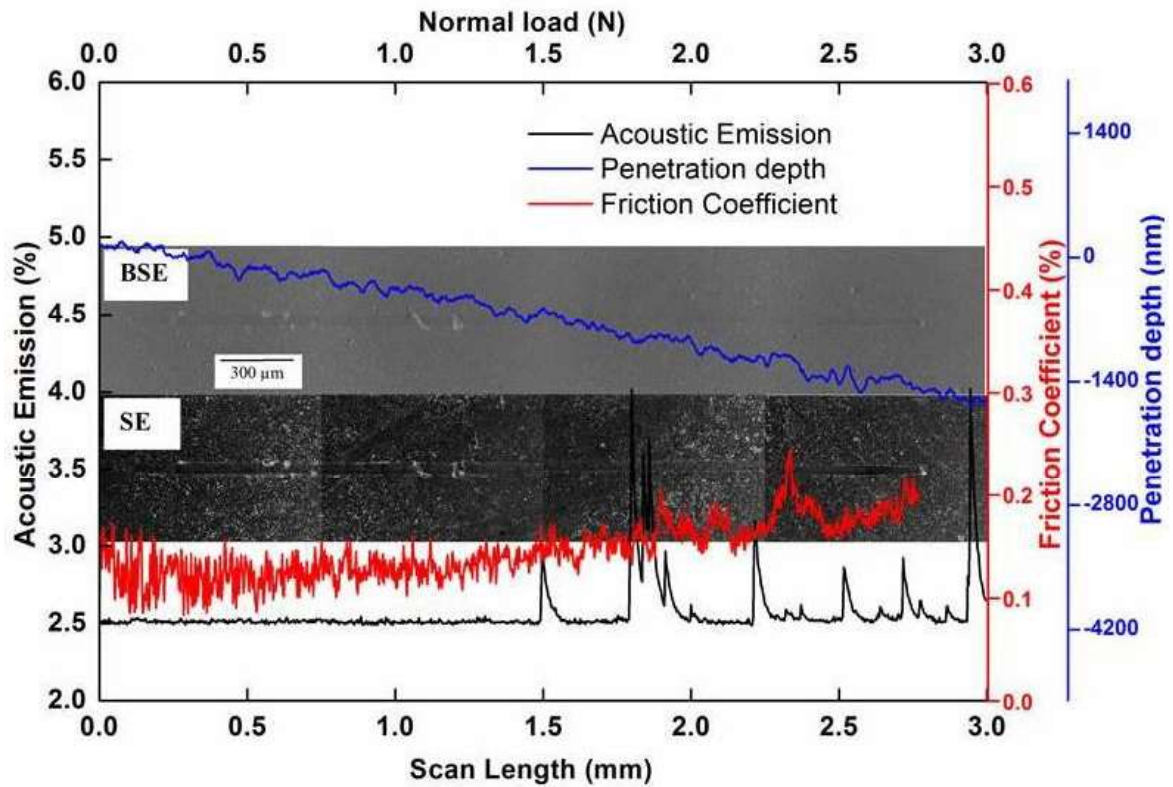


Figure 4.12: Scratch Test for CS/Fe₃O₄/NiFe₂O₄

The friction coefficient, acoustic signal, penetration depth, normal load applied against scratch length is plotted along with SEM image of scratch performed on CS/Fe₃O₄/NiFe₂O₄ are as shown in the Figure 4.12. As the applied normal load increases during a scratch test, the coating undergoes failure resulting in the generation of elastic waves with increasing frequency and the severity of failure are detected and recorded by acoustic emission. Acoustic emission signal along with detailed SEM microscopic analysis of the coating gives information about the damage occurred on the coating. The fluctuations in the friction coefficient observed till 1.8 N load can be correlated with different mechanisms of energy dissipation

with the change in contact conditions leading to deformation. In this case, the film detached at around 1.2 N load as observed from SEM which seems to be the first critical load of failure.

4.3. Conclusion

Thin film of nano size NiFe_2O_4 coating on $\text{CS/Fe}_3\text{O}_4$ by PLD improves the protectiveness of the CS substrate. The powder XRD analysis revealed the high purity and single phase of the synthesized NiFe_2O_4 and GI-XRD analysis of the film confirmed the single phase spinel structure formation on $\text{CS/Fe}_3\text{O}_4$. The chemical composition of NiFe_2O_4 was quantified by XPS. HR-SEM and TEM images confirm that the coating was uniformly distributed with similar shape and narrow sized distribution. Mott-Schottky analysis showed that the coating with less defect density showed improvement in the corrosion resistance. AC impedance and DC polarization measurements showed increase in corrosion resistance property of NiFe_2O_4 coating on $\text{CS/Fe}_3\text{O}_4$ with thickness above 325 nm when compared to $\text{CS/Fe}_3\text{O}_4$ and uncoated CS. Scratch test showed that the coating failed at 1.2 N load.

Part II: NiFe₂O₄ film formation by hydrothermal method

4.4. Introduction

In hydrothermal process, the properties of the oxides formed on CS depend on the water chemistry, temperature and the alloy composition [119]. Ferrites like Fe₃O₄ and NiFe₂O₄ having spinel structure dominate the corrosion product oxide inventory and play a major role in the activity transport process. Addition of nickel or zinc was found to suppress the cobalt-60 deposition [120] and the positive effects of zinc addition on corrosion film was reported [121-122] and applied to boiling water reactors and pressurized water reactors [123].

In the present work, attempts were made to incorporate nickel ions into the Fe₃O₄ lattice during its formation by hydrothermal method for 24, 96 and 240 hours and the oxide formed was characterized by LRS, XRD, XPS and SEM measurements. The corrosion resistances of these oxides were studied by EIS and PDAP in LiOH medium and the electronic properties were studied by Mott-Schottky (MS) measurements.

4.5. Results and Discussion

Magnetite is a mixed valence iron oxide containing Fe²⁺ and Fe³⁺ ions in an inverse spinel structure. From the past studies, it has been found that nickel often combines with iron oxides to form spinels [124]. NiFe₂O₄ also has an inverse spinel structure with tetrahedral A-sites occupied by Fe³⁺ ions and octahedral B-sites occupied by Ni²⁺ and Fe³⁺ ions. It can be represented as [Fe³⁺]_{Td}[Ni²⁺Fe³⁺]_{Oh}O₄.

4.5.1. Cation concentration and thickness measurement

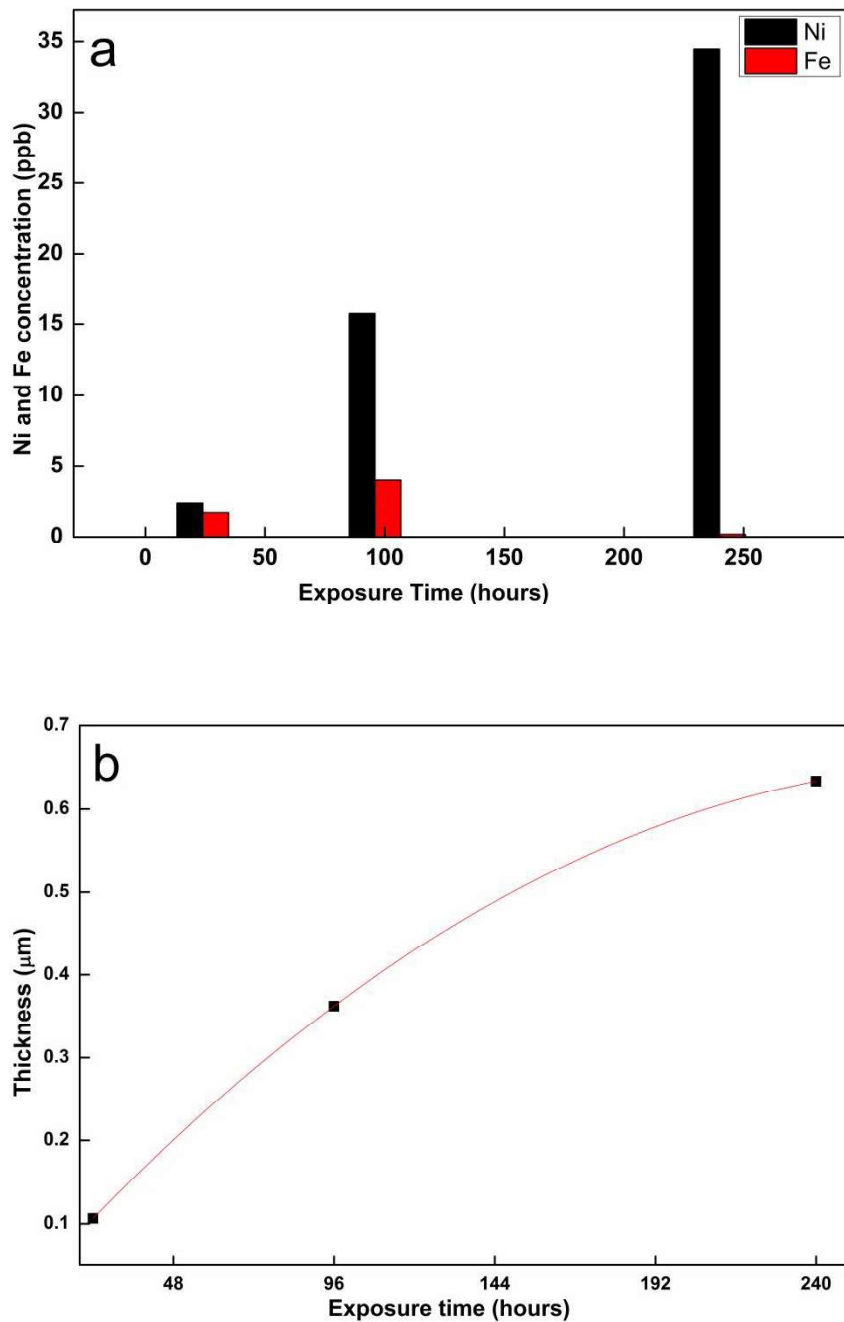


Figure 4.13: (a) Nickel and Iron concentration and (b) oxide film thickness at the end of different exposure time

The nickel and iron ion concentrations in the autoclave solution measured after the exposure experiments are as given in Figure 4.13 (a). Nickel concentration of 1000

ppb was taken at the start of the experiment. The decrease in the concentration of nickel in the autoclave solution indicates the transport of the nickel from solution to the CS specimen. As described in chapter 2 section 2.4.3, the thickness of the oxides was measured by Clarke's method and Figure 4.13 (b) shows the oxide film growth on CS. The thickness of the oxide film formed on the CS as a function of exposure time followed a parabolic nature.

4.5.2. Surface characterization of oxides

4.5.2.1. X-Ray Diffraction Analysis

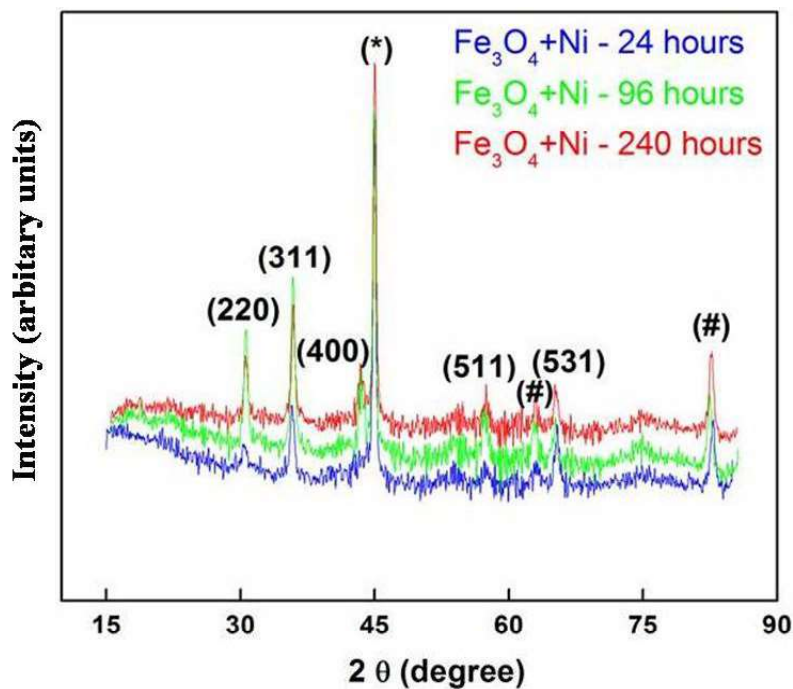


Figure 4.14: GI-XRD pattern of the oxides formed on CS exposed to 250 °C in presence of Ni²⁺ for 24, 96 and 240 hours

Table 4.4: Crystallite size and Lattice parameter obtained from GI-XRD

	Exposure Time	Crystallite size (nm)	Lattice Parameter (Å)
Fe ₃ O ₄	24 hours	14.71	8.31
+	96 hours	16.98	8.44
Ni ²⁺	240 hours	19.83	8.40

Figure 4.14 shows the GI-XRD patterns of the oxide films formed on CS exposed to 250 °C in LiOH and Ni²⁺ for different time duration. Characteristic peaks for the oxides formed in 24, 96 and 240 hours suggest a spinel structure oxide film. The GI-XRD pattern showed that the formed spinel consisted entirely of crystalline NiFe₂O₄ having preferred orientation along (311) plane which increased with increased exposure time and was compared with the standard data of cubic spinel (NiFe₂O₄) from the database (ICDD.No.01-074-9276). Lattice parameter for the oxide film was 8.31, 8.44 and 8.40 for 24, 96 and 240 hours exposed specimens suggesting the incorporation of nickel into the magnetite lattice. The lattice parameter of NiFe₂O₄ in the literature is 8.34. The crystallite size and the lattice parameter of all the oxides formed were estimated from the FWHM using Scherrer's equation and are given in Table 4.4. When the particle size decreases, the fraction of atoms which lie near the surface increases [125] which may be the cause for the variation in the observed values of lattice parameter. Additional peak of base material marked as '*' was observed in the GI-XRD pattern at 45°. Small peaks marked as '#' were seen at 64.6° and 82° and was indexed to FeO(OH) which is the intermediate layer in the Fe₃O₄ formation. The intensity of the diffraction peaks were less for the 24 hours exposed CS specimen in comparison to the 96 and 240 hours exposed specimen.

4.5.2.2. Scanning Electron Microscopic Analysis

Figure 4.15 shows the FE-SEM morphologies of the oxide films formed on CS exposed to 250 °C in LiOH and Ni²⁺ for different time duration. The surface of the specimen was covered with porous and octahedron shaped oxide particles. The size of the outer particles precipitated from the solution was bigger than the inner particles which are grown from the base metal. For the 24 hours exposure itself, the CS specimen was fully covered with the ferrite crystals. The size of the inner layer crystals was smaller in case of 24 hours exposed specimen and the outer layer particles were bigger and few in numbers. In the case of 96 hours exposed specimen the particles were full of similar sizes and shapes with a few clusters of agglomerated particles. With increasing exposure to 240 hours the thickness of the outer layer increased with bigger size ferrite crystals occupying the major portion of the oxide formed on CS.

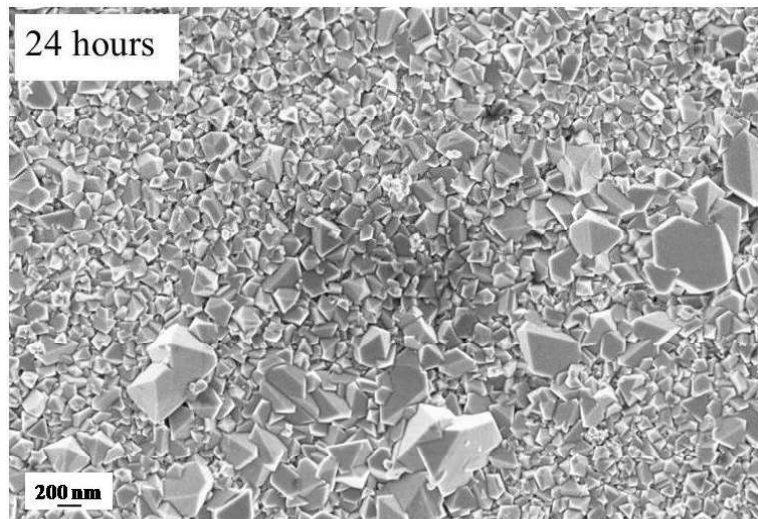


Figure 4.15: FE-SEM images of CS exposed to 24 hours in presence of Ni²⁺ ions

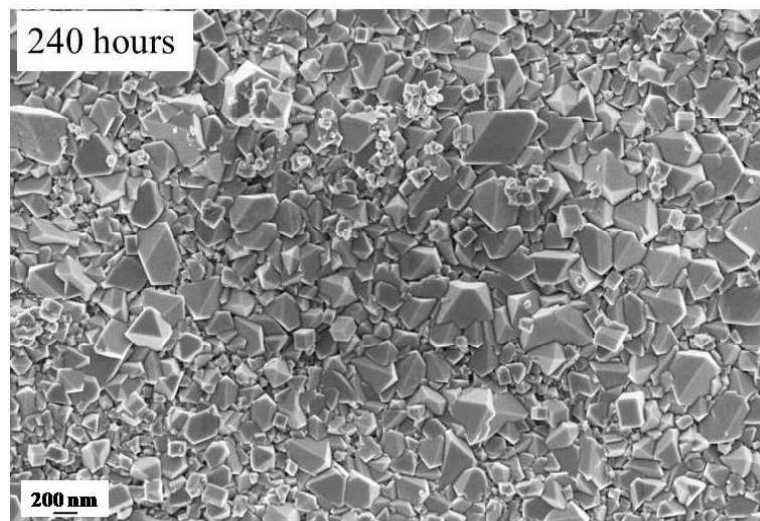
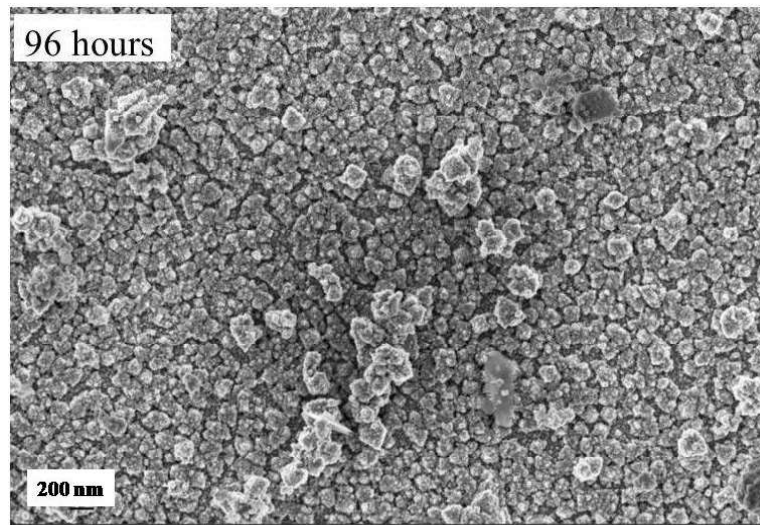


Figure 4.15: FE-SEM images of CS exposed to 96 and 240 hours in presence of Ni^{2+} ions

4.5.2.3. X-Ray Photoelectron Spectroscopic Analysis

XPS spectra of (a) Fe 2p, (b) Ni 2p and (c) O 1s peaks obtained for CS in presence of Ni²⁺ ions exposed for 24, 96 and 240 hours are as shown in Figure 4.16. Fe 2p_{3/2} photoelectron peaks obtained for all the three oxide formed samples are shown in Figure 4.16 (a). Ni 2p_{3/2} peak from the oxide formed on CS was observed at around 856 eV and Ni 2p_{1/2} was observed at 874 eV as indicated in Figure 4.16 (b). The binding energy values of Fe 2p_{3/2} observed at around 711 eV matched well with the literature value [103]. As NiFe₂O₄ contains Fe³⁺ type iron only, an increase in binding energy (711.4 eV) may be due to the change in oxygen environment of Fe in NiFe₂O₄. Only one peak was observed for O 1s at 530.6 eV for all the specimens indicating that the oxygen atoms are in the O²⁻ form in the lattice. From the above XRD and XPS analyses, it was clear that the oxide grown on the CS sample was composed of NiFe₂O₄ only. The binding energy values and the quantification of the oxides formed at different exposure hours are given in Table 4.5 which shows that the % of the elements remained same for 96 and 240 hours. The stoichiometric ratio of Ni:Fe was observed to be 1:2.

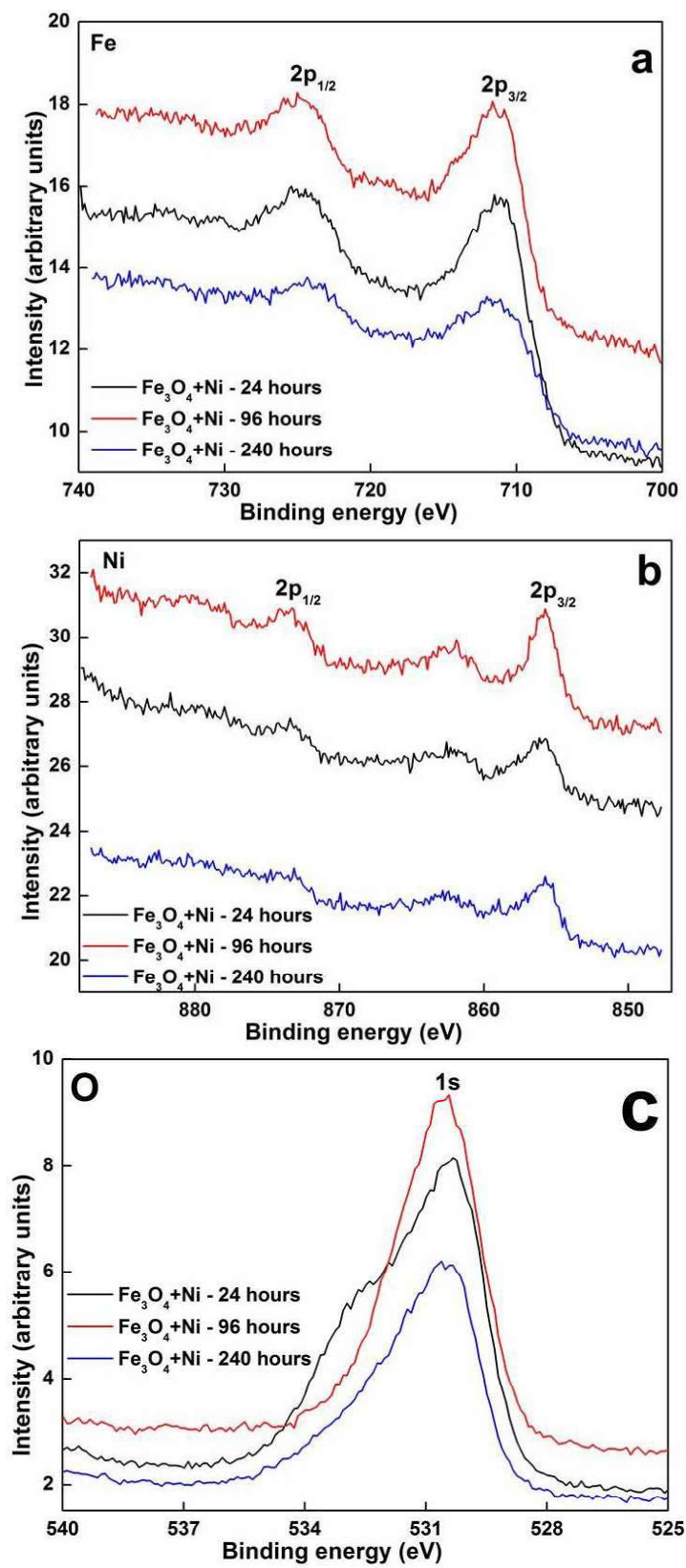


Figure 4.16: XPS spectra of (a) Fe 2p, (b) Ni 2p and (c) O 1s for CS/ NiFe_2O_4

Table 4.5: Binding Energy and Quantification of the elements by XPS

Exposure Time (hours)	Fe		Ni		O	
	Binding Energy (eV)	(%)	Binding Energy (eV)	(%)	Binding Energy (eV)	(%)
24	711.4	15	856.1	4.5	530.6	81
96	711.2	14	856.2	7	530.6	79
240	711.8	14	856.0	7	530.6	79

4.5.2.4. Laser Raman Spectroscopic Analysis

Figure 4.17 shows the Raman spectra recorded on the oxide films formed on carbon steel exposed to 250 °C LiOH with 1000 ppb of Ni²⁺ as a function of exposure time, namely, 24, 96 and 240 hours. The Raman shifts of vibrational modes are as tabulated in the Table 4.6. Five Raman active modes A₁, E_g and 3T_g were assigned [108]. The data fitting was carried out for Raman spectra obtained on CS surface when exposed to solution in absence and presence of nickel, which showed four peak maxima. Modes above 660-720 cm⁻¹ corresponds to the tetrahedral sub lattice (A_{1g} symmetry) which is due to the motion of the oxygen atoms in tetrahedral group and below 460-660 cm⁻¹ refers to the octahedral sub lattice (T_{2g} symmetry) [126, 111]. The oxide film formed on CS surface in the presence of soluble nickel shift in the A_{1g} peak to higher wave numbers compared to the oxide formed in absence. The mass difference between the two ions (Ni²⁺ and Fe³⁺) shifts the A_{1g} mode of the lightest ion Ni²⁺ to higher wave number (678 - 682 cm⁻¹) and the heaviest ion Fe³⁺ to lower wave number 672 cm⁻¹. The changes in relative peak intensity and peak position in the oxides formed may be due to the incorporation of Ni²⁺ ions into the magnetite lattice.

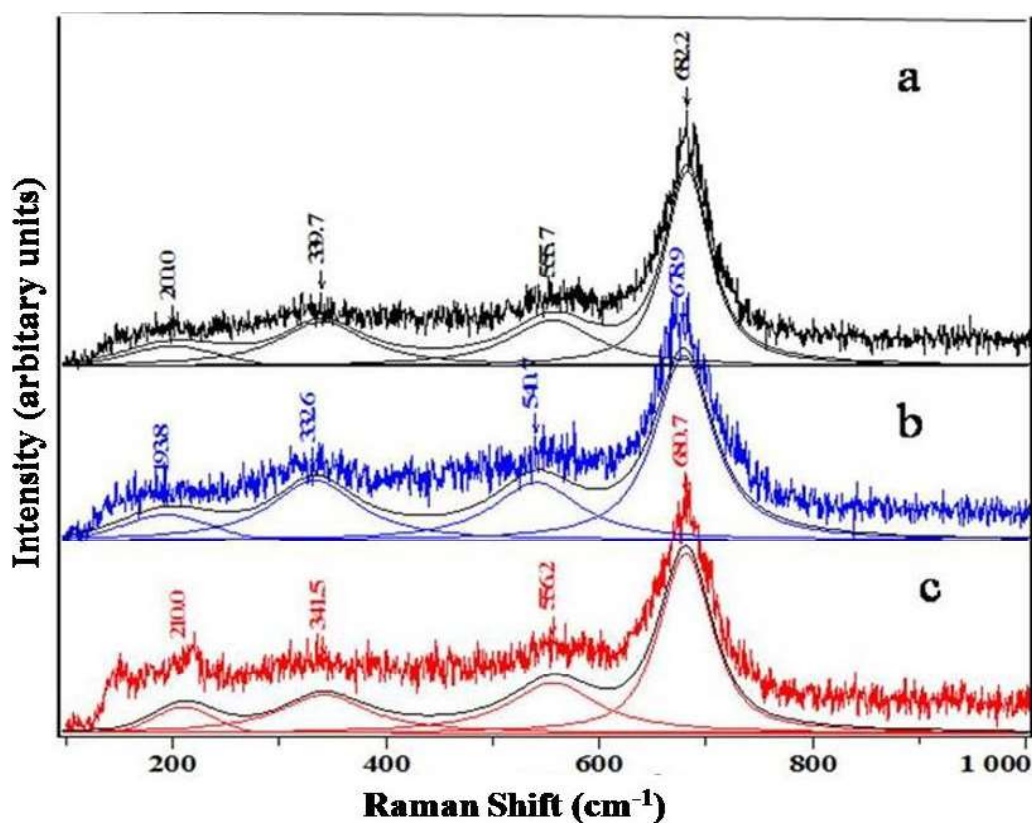


Figure 4.17: Raman spectrum of the oxide films formed on CS exposed at 250 °C in LiOH in presence of Ni²⁺ at (a) 24 hours, (b) 96 hours and (c) 240 hours

Table 4.6: Vibrational modes obtained for the oxides from Raman analysis

Raman mode	A _{1g}	T _{2g} (1)	T _{2g} (2)	E _g	T _{2g} (3)
Fe ₃ O ₄	672.6	551.2	-	323.9	187.0
NiFe ₂ O ₄ - 24 hours	682.2	555.7	-	339.7	200.0
NiFe ₂ O ₄ - 96 hours	678.9	540.7	-	332.6	193.8
NiFe ₂ O ₄ - 240 hours	680.7	556.2	-	341.5	210.0

Further, the Raman frequency depends on the Fe(Ni)-O and bond length. The shift toward lower wave number is attributed to the crystalline disorder and also to the presence of grain boundaries, which are large in small sized nanomaterials [109].

The wave number position of the bands does not change significantly with different exposure time in presence of nickel ions.

4.5.3. Electrochemical Characterization

4.5.3.1. Potentiodynamic Anodic Polarization

Figure 4.18 shows the PDAP curve for uncoated CS and the oxides formed in presence of Ni^{2+} ions for 24, 96 and 240 hours in deaerated LiOH aqueous medium at 28 °C. The corrosion parameters obtained from these measurements are tabulated in Table 4.7. The OCP for the oxide formed in 24 and 96 hours shifted towards the active side (-0.661 V and -0.590 V vs. SCE respectively) whereas the OCP in the case of oxide formed in 240 hours (-0.161V vs. SCE) showed a positive shift compared to the OCP of the uncoated CS (-0.497 V vs. SCE). A negative potential shift indicated that the cathodic reaction is inhibited [127]. The current densities for the oxides formed in presence of Ni^{2+} ions in 24, 96 and 240 hours exposure had magnitudes lower than that observed for uncoated CS. The transition region was observed in the range -0.4 to 0 V for 96 hours exposed CS and +0.1 V to +0.7 V for 240 hours exposed CS. The passivation currents were in decreasing order: CS > 24 hours > 96 hours > 240 hours showing increased corrosion resistance of the oxide film formed on CS in presence of Ni^{2+} ions with increased exposure time. The PDAP curve for oxide formed in 240 hours showed a positive shift in the potential and lowered current density when compared to the uncoated CS indicating that the oxide formed in this case offered better protection to the uncoated CS compared to the oxide formed in 24 and 96 hours. Based on the values of corrosion current, the

corrosion resistance was found to be in the following order: CS < 24 hours < 96 hours < 240 hours. The cathodic reaction in absence of oxygen and anodic reactions that take place in this system are as given below in equation (4.1) and (4.2).

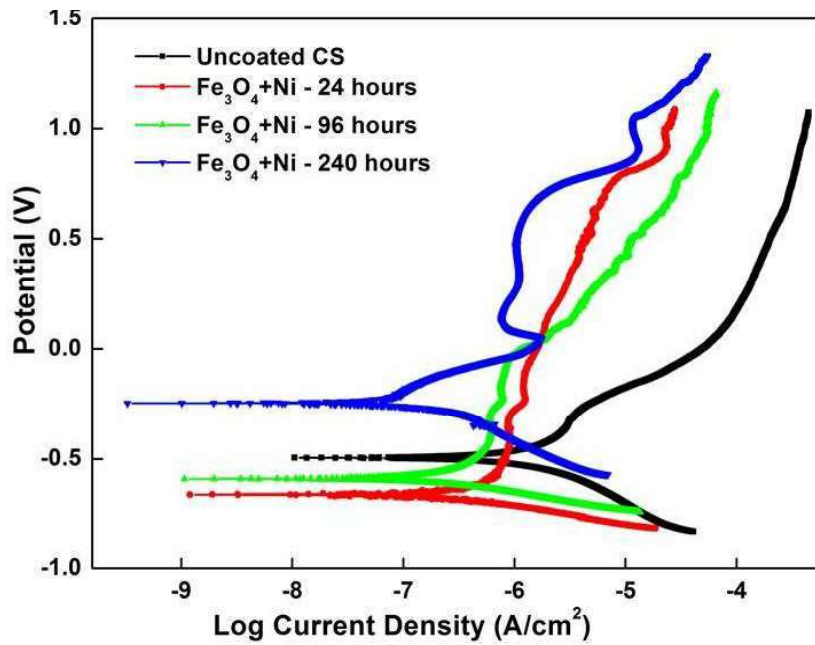
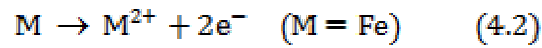
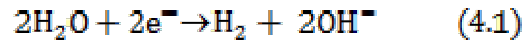


Figure 4.18: PDAP plot of CS exposed to 24, 96 and 240 hours in LiOH and Ni^{2+}

Table 4.7: Corrosion parameters obtained from PDAP measurements

Specimen	PDAP				
	b_c (V/dec)	b_a (V/dec)	OCP (V)	i_{corr} ($\mu\text{A}/\text{cm}^2$)	Corrosion Rate (mpy)
Uncoated CS	-0.236	0.283	-0.497	1.194	0.552
24 hours	-0.087	0.475	-0.661	0.394	0.182
96 hours	-0.081	0.375	-0.590	0.224	0.103
240 hours	-0.254	0.136	-0.161	0.102	0.047

4.5.3.2. Electrochemical Impedance Spectroscopy

Figure 4.19 shows the EIS spectra for uncoated CS and the oxides formed in presence of Ni^{2+} ions for 24, 96 and 240 hours in deaerated LiOH aqueous medium at 28 °C. Table 4.8 gives the impedance parameters. Oxides formed showed two time constants as observed from the Nyquist plots at different frequency ranges which could be due to the changes in surface morphology and thickness with increasing exposure time. Oxide formed in case of 24, 96 and 240 hours exposure showed increased capacitive loop which could be related to increase in protectiveness of the oxide. The EIS Bode spectra (Figure 4.19 (b)) demonstrate that systems with nickel ferrite formation for different exposed time behaved inhibitive. The impedance modulus at low-frequency part increased with exposure time. This behavior could be attributed to the formation of a layer at the bottom of the pores on the steel surface. In order to evaluate oxide coating performance, the low-frequency impedance modulus values obtained at 0.01 Hz ($|Z|_{0.01 \text{ Hz}}$) were used to estimate the resistance of the coating [127]. Table 4.9 shows the values of impedance modulus with exposure time. This provided better anticorrosive properties.

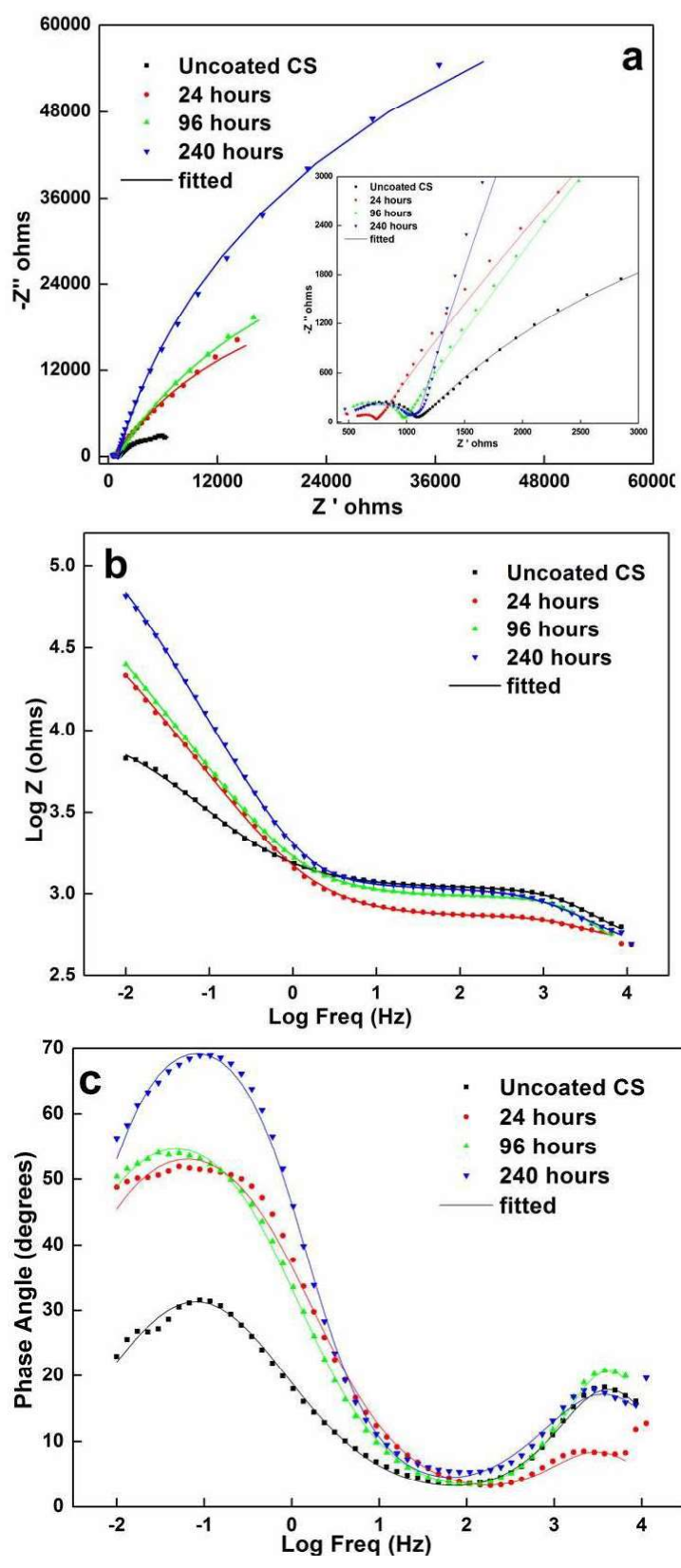


Figure 4.19: (a) Nyquist, (b) Bode and (c) Phase angle plot of CS in LiOH

The Bode impedance values observed at high frequency region followed the order: 24 hours < CS = 96 hours = 240 hours whereas at low frequency region the Bode impedance value follows the order CS < 24 hours = 96 hours < 240 hours. It was observed from Table 4.8 that the polarization resistance (R_2) increased from 66.7 k Ω to 162 k Ω and coating capacitance decreased from 0.270×10^{-3} F/cm 2 to 0.133×10^{-3} F/cm 2 with increase in the exposure time suggesting that the thickening of the oxide film improved the film passivity. Figure 4.20 gives the trend of the corrosion rate and polarization resistance in the absence and presence of nickel ions.

Table 4.8: Impedance parameters obtained from EIS measurements

Specimen	R_s (K Ω)	Q_1 (μ F)	n	Q_2 (mF)	n	R_2 (K Ω)	R_1 (K Ω)
Uncoated CS	0.487	0.44	0.85	0.49	0.63	9.5	0.607
24 hours	0.414	1.261	0.76	0.270	0.70	66.7	0.322
96 hours	0.422	0.213	0.93	0.255	0.72	90.1	0.546
240 hours	0.418	1.653	0.72	0.133	0.87	161.9	0.681

Table 4.9: Log $|Z|_{0.01 \text{ Hz}}$ for nickel ferrite vs exposure time in LiOH solution

	Log $ Z _{0.01 \text{ Hz}}$
Uncoated CS	3.872
24 hours	4.333
96 hours	4.399
240 hours	4.817

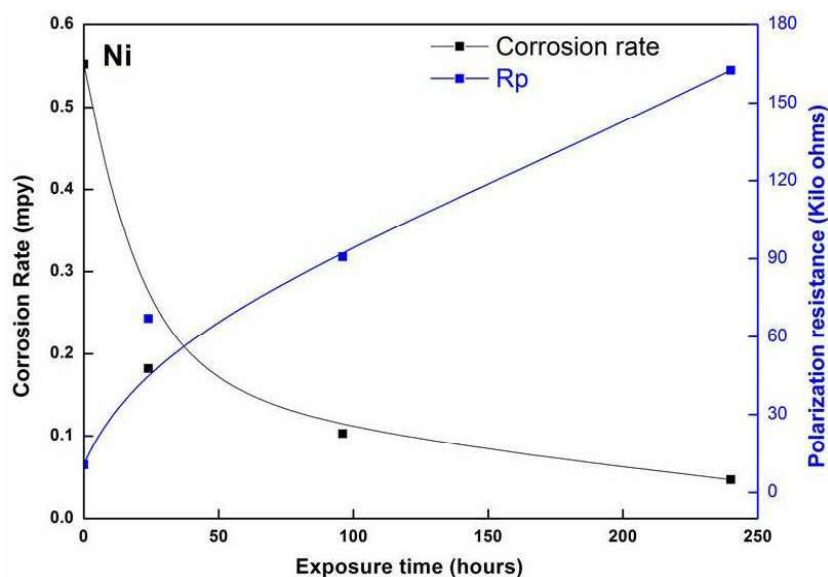


Figure 4.20: Corrosion rate and Polarization resistance comparison

4.5.3.3. Semiconducting properties of the oxide film

In the present work, the Mott–Schottky measurements for the oxides formed on CS in presence of nickel ions for different exposure times were carried out at 1000, 100, 10 and 5 Hz in the potential range -1.2 to 1.2 V. For the calculation of N_D /or N_A , the dielectric constant 'ε' was assumed as 12 for the passive films on CS. Figure 4.21 shows the inverse dependency of square of capacitance with the applied potential (Mott–Schottky representation) obtained at 100 Hz and 10 Hz frequencies for the passive film formed anodically on CS in LiOH solution. The curves obtained for uncoated and oxide formed on CS presents a positive slope from -0.8 V_{SCE} upward to more anodic potentials representing an n-type semiconductor and the main defects in the oxide film are cation interstitials or anion vacancies (oxygen) acting as electron donors [104]. The oxide formed on CS showed two positive slopes in the case of 100 Hz frequency indicating two donor levels and one positive and one negative slopes in case of 10 Hz indicating the conversion of n-type to the p-type at higher anodic potentials. As can be observed, the Mott–Schottky plots are frequency dependent. Such behaviour is an indication of the highly disordered nature of the oxide film, which is characteristic of amorphous semiconductors. C^{-2} increased with

increasing frequency. This frequency effect as suggested by Di-Paola et al. [128] is attributed to the ionic part of the space charge layer. Because of the low ionic mobility, these ionic charges give a contribution to the capacitance only at lower frequencies. Chastukhin et.al studied the dissolution kinetics of magnetite and hematite in HCl and H₂SO₄ solutions at different concentrations and temperatures and showed that the dissolution kinetics of iron oxides depended on the difference between the concentrations of the dislocations and other defects on the particle surface [129].

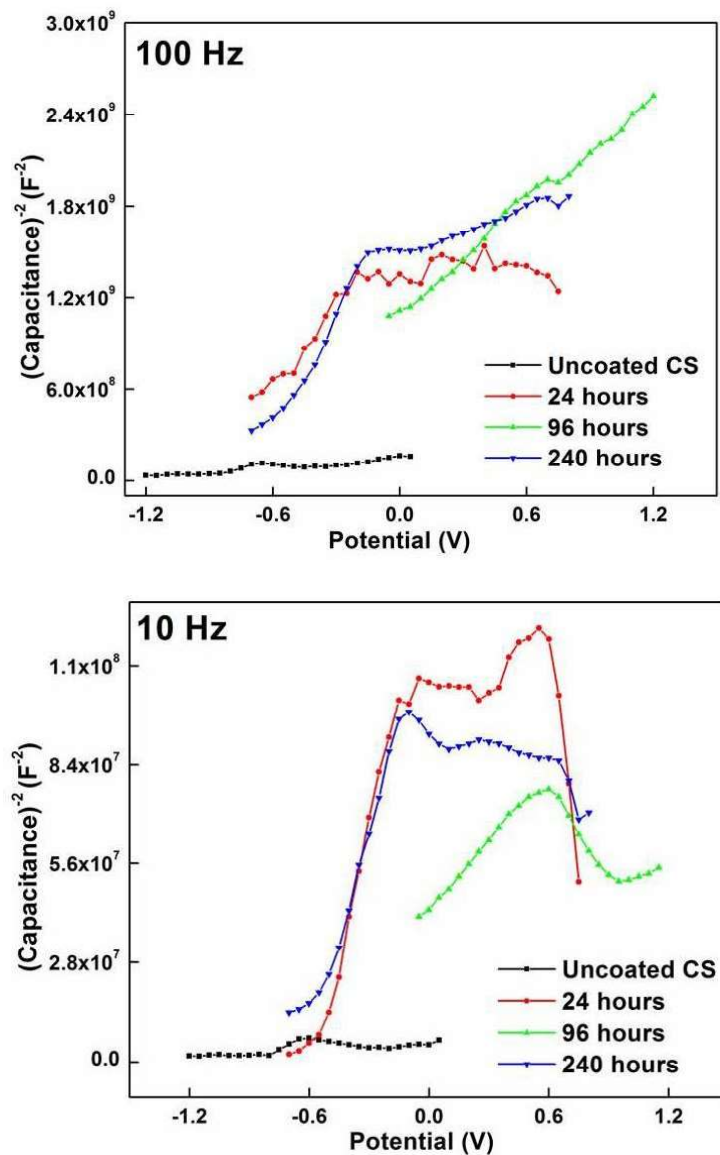


Figure 4.21: Mott Schottky plot of CS exposed in LiOH and Ni²⁺

Table 4.10 gives the defect density values calculated from MS plot obtained at 100 Hz frequency showed that the defect density reduced with increase in exposure time. Hence, nickel ions in the spinel structure reduced the defects which inhibit transportation of ions from the metal to solution and minimize the corrosion rate.

Table 4.10: Defect density values obtained from Mott Schottky analysis

	Defect Density (cm ⁻³)
Uncoated CS	4.29 x 10 ¹⁹
24 hours	2.08 x 10 ¹⁸
96 hours	2.15 x 10 ¹⁸
240 hours	9.81 x 10 ¹⁷

4.6. Conclusion

Nano size nickel ferrite film was formed on CS in presence of nickel ions by hydrothermal method. Nano size spinel was confirmed by GI-XRD. SEM analysis showed that the morphology was different for different exposure time and the grains grow in size for longer exposure time. Quantification of the elements present in the oxides formed on CS for different exposure time was done by XPS. The nickel incorporation into the magnetite lattice remained same for 96 and 240 hours indicating that the higher exposure time does not improve the nickel intake. Impedance and corrosion experiments showed the effectiveness of the nano sized oxides in improving the corrosion resistance of CS.

Chapter 5

Corrosion Resistance Property of the Zinc Ferrite coatings on Carbon Steel

PART I: ZnFe₂O₄ deposition by PLD method

5.1. Introduction

It is known that zinc ion can replace the cobalt ion from oxides on primary circuit surfaces in Boiling Water Reactors (BWRs) thereby reducing the man-rem problem [121-122]. The experience with Pressurized Water Reactors (PWRs) has shown that these reactors benefitted not only in terms of radiation field but also in mitigating the susceptibility to Primary Water Stress Corrosion Cracking (PWSCC). Presently, zinc injection has become one of the key parameters of primary coolant chemistry optimization. In PHWRs, though the corrosion rate of CS is reduced by forming a passive Fe₃O₄ layer, the radioactivity transport problems necessitate further reduction in the metal ion release. Though the role of MIP in reducing corrosion is not very clear, in boiling water reactors it was observed that the addition of zinc ion (Zn²⁺) at ppb level reduced the release of corrosion products into the coolant by modifying the oxide layer over the structural materials [130]. The use of nano particles for anticorrosion coatings has achieved significant attention and importance [131]. Several researchers have shown that nano particles are better alternatives for anticorrosion coatings in composites and polymers [132-133].

In part I of this chapter, attempts were made to form an additional nano zinc ferrite (ZnFe₂O₄) coating on CS/Fe₃O₄ by PLD technique. The oxides formed were characterized by Raman spectroscopy, XRD, XPS and SEM measurements. Mott-Schottky analysis [134] was carried out in aqueous LiOH at room temperature, to understand the electronic properties of these oxides. The corrosion resistance and the stability of these oxides in LiOH medium were studied by electrochemical methods such as EIS and PDAP.

5.2. Results and Discussion

ZnFe₂O₄ has a normal spinel structure with tetrahedral A-sites occupied by Zn²⁺ ions and octahedral B-sites occupied by Fe³⁺ ions. It can be represented as [Zn²⁺]_{Td}[Fe³⁺Fe³⁺]_{Oh}O₄.

5.2.1. Laser Raman Spectroscopic Analysis

Figure 5.1 shows the Raman spectra recorded on CS/Fe₃O₄/ZnFe₂O₄ developed by PLD. Raman shift values observed in the ZnFe₂O₄ film (Figure 5.1 (a)) were compared with standard ZnFe₂O₄ (Figure 5.1 (b)). The space group of the cubic spinel zinc ferrite is O_h⁷ (Fd3m) with eight formula units per unit cell. Five first-order Raman active modes of spinel structured ferrites were observed at ambient conditions. A visual inspection of the spectra showed that four Raman bands at 203, 322, 484 and 700 cm⁻¹ with a shoulder at 657 cm⁻¹ were present in the range 200-800 cm⁻¹, while there were two other bands at ~ 1140 and 1337 cm⁻¹. It is well known that in ferrites, the modes above 600 cm⁻¹ are attributed to the motion of the oxygen atoms in tetrahedral AO₄ group and the other low wave number modes represent the characteristics of the octahedral BO₆ site [135]. The mode corresponding to E_g was absent. The observed modes were assigned according to Wang et.al [136] in which the authors had studied the behavior of zinc ferrite at high pressure and observed that the inverted zinc ferrite system might lead to the masking of few Raman modes. Hence, the absence of these modes may be due to cation inversion and also to the effect of small crystallites, which leads to the broadening of

the modes. The Raman bands observed at ~ 1140 and 1337 cm^{-1} could not be assigned to any particular mode (may be overtones or combination peaks).

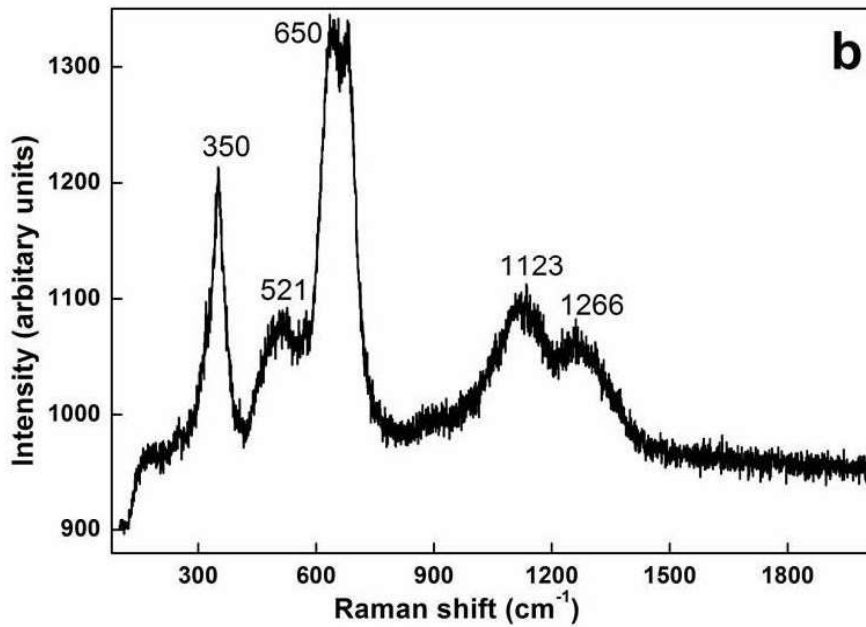
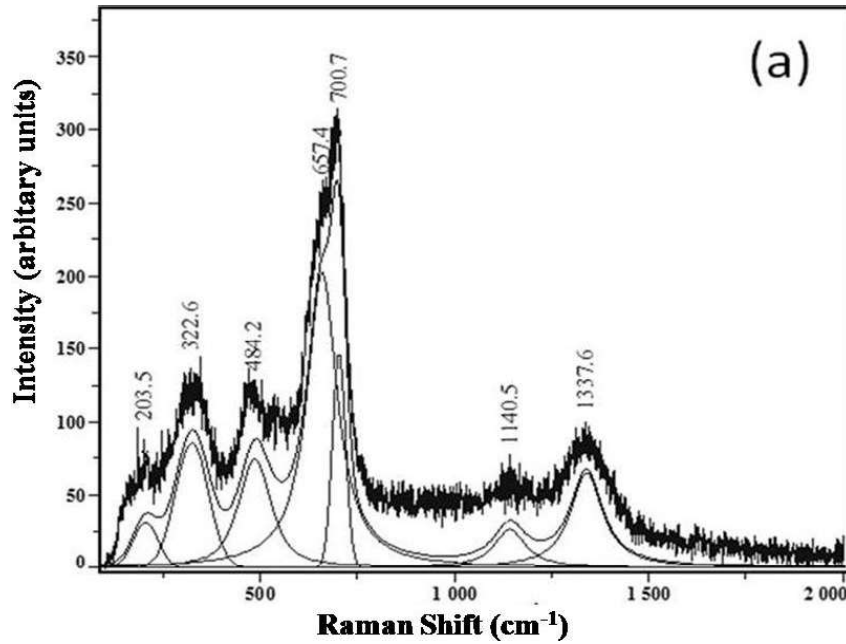


Figure 5.1: Raman spectra of (a) CS/ Fe_3O_4 / ZnFe_2O_4 and (b) Standard ZnFe_2O_4

5.2.2. X-Ray Diffraction Analysis

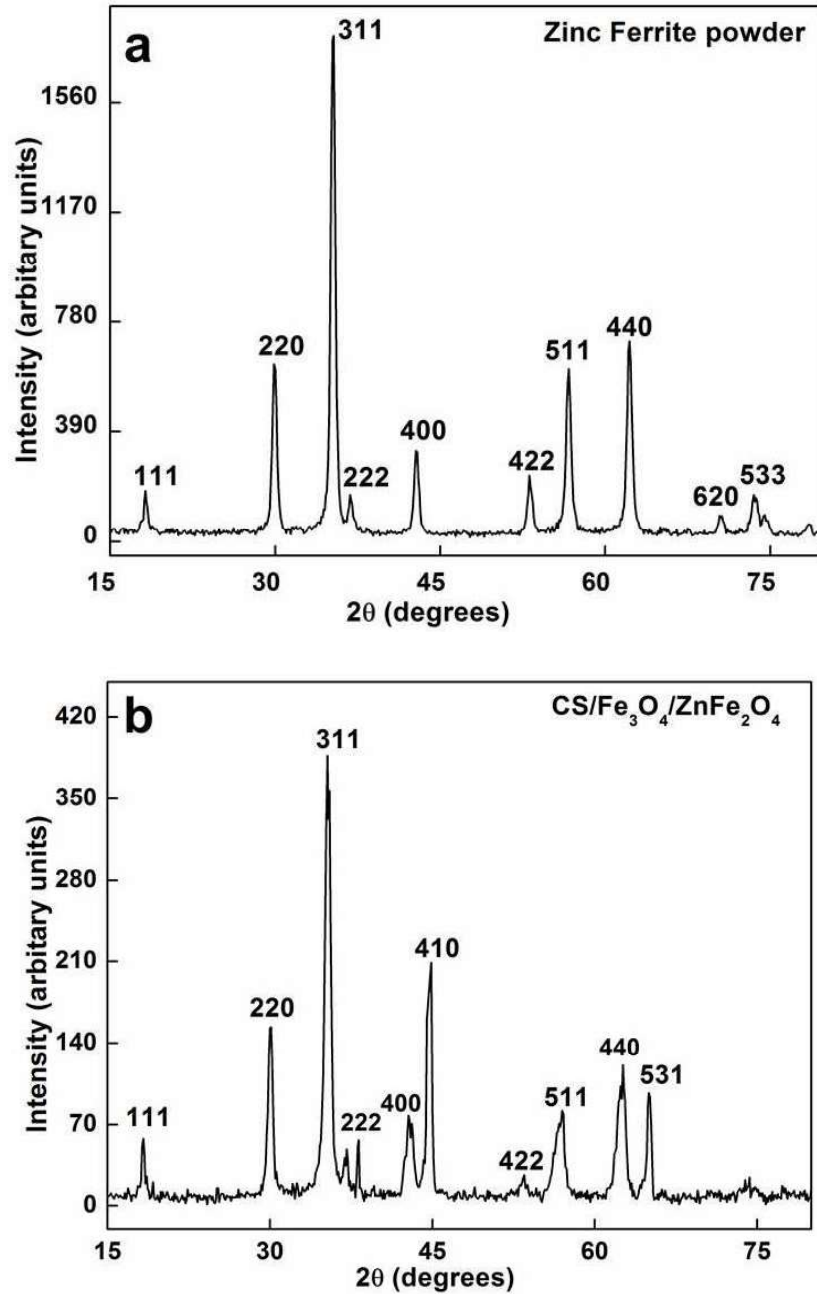


Figure 5.2: (a) XRD pattern of synthesized ZnFe₂O₄ powder and (b) GI-XRD pattern of CS/Fe₃O₄/ZnFe₂O₄

XRD pattern of (a) synthesized ZnFe₂O₄ powder and (b) GI-XRD pattern of CS/Fe₃O₄/ZnFe₂O₄ are shown in Figure 5.2. The lattice parameter 'a' was calculated

from diffraction planes by using the formula given in equation (5.1) useable only for cubic crystal structures as spinels [137].

$$d_{hkl} = \frac{a}{\sqrt{(h^2 + k^2 + l^2)}} \quad (5.1)$$

where 'd' is the interplanar spacing, and h, k and l are the Miller indices of the crystal planes with highest intensity. The ZnFe₂O₄ powder sample (Figure 5.2 (a)) showed the characteristic reflection of cubic spinel phase with planes (111), (220), (311), (222), (400), (511) and (440) (ICDD.No.01-074-8584). Lattice parameter was computed by using the plane with (hkl, 311) of highest intensity and was found to be 8.433 Å which is similar to the lattice parameter observed from the literature for ZnFe₂O₄ [138]. The GI-XRD pattern in Figure 5.2 (b) revealed well developed reflections of ZnFe₂O₄ coating. Strong Bragg reflections were seen in the GI-XRD pattern with the characteristic peak corresponding to the (111), (220), (311), (222), (400), (511) and (440) plane (ICDD.No.01-074-8584). It has face-centered cubic crystal structure (space group Fd-3m) with unit cell dimension a=8.433 Å. The average crystallite size calculated from the FWHM using Scherrer's formula was about 13 nm. The sharp peaks represented that all the ferrites were crystalline in nature of single phase. The peaks indexed as (410) and (531) were obtained from the base metal.

5.2.3. Scanning Electron Microscopic Analysis

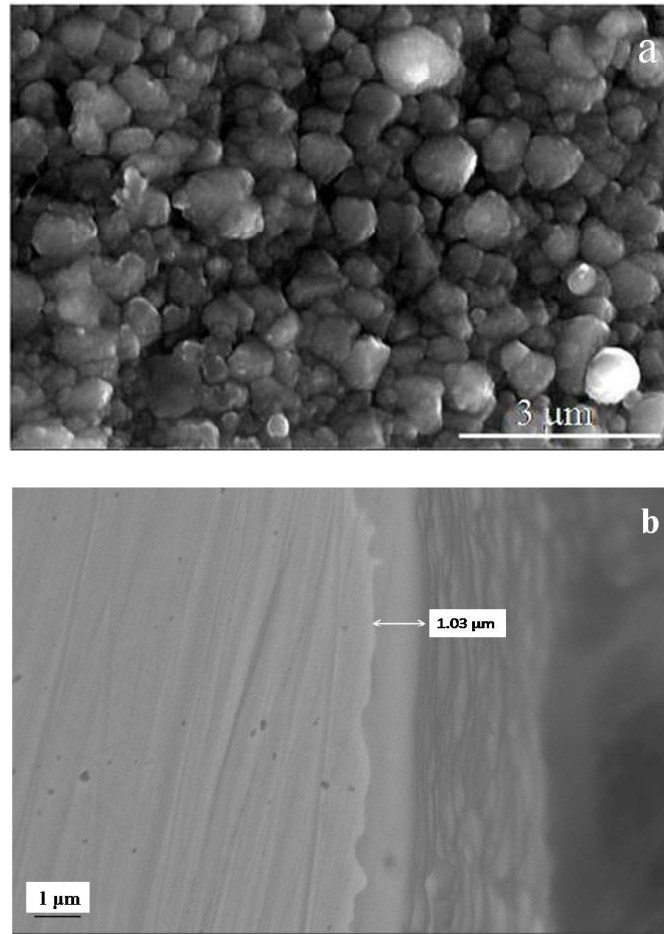


Figure 5.3: (a) SEM image and (b) Cross section of CS/Fe₃O₄/ZnFe₂O₄

The surface and crystallite morphology of ZnFe₂O₄ formed on CS/Fe₃O₄ by PLD was studied by SEM technique. Figure 5.3 (a) shows the micrograph and (b) cross section recorded in the secondary electron mode of PLD grown film. The ZnFe₂O₄ coated on CS/Fe₃O₄ was found to be smooth, non-porous and uniform shaped particles. ZnFe₂O₄ particles were smaller (~300 to 500 nm) than Fe₃O₄ particles (~ 1 micron) on which the ZnFe₂O₄ grew. Cross-sectional FE-SEM analysis (Figure 5.3 (b)) showed that the thickness of ZnFe₂O₄ coating was 1.03 μm which included the magnetite coating (0.45 μm).

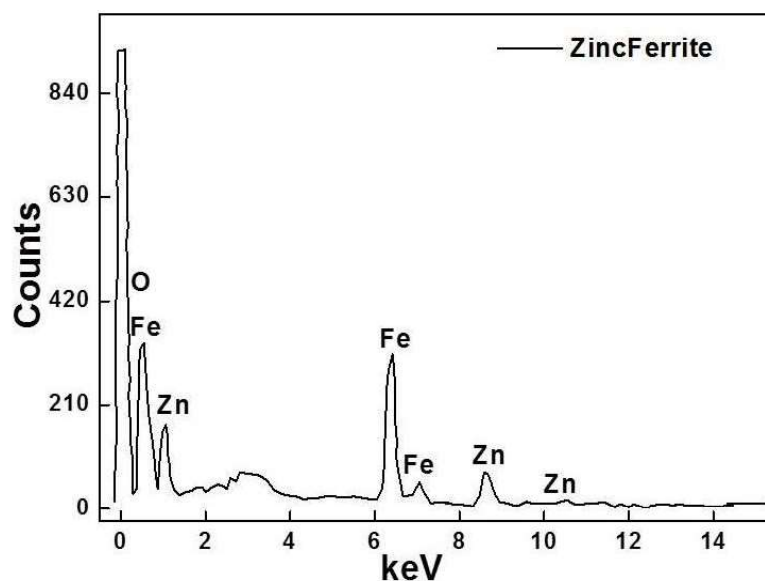


Figure 5.4: EDAX spectrum of CS/Fe₃O₄/ZnFe₂O₄

The elemental compositions were investigated by EDAX as shown in Figure 5.4 for CS/Fe₃O₄/ZnFe₂O₄ which confirms the presence of Zn, Fe and O. The atomic and weight percentages of ZnFe₂O₄ are presented in the Table 5.1 and the stoichiometry of the deposited ZnFe₂O₄ was close to 1:2.

Table 5.1: Elemental composition from EDAX analysis

Element	Series	Zinc Ferrite coated Carbon Steel	
		Weight %	Atomic %
Zn	K	21.84	10.24
Fe	K	43.93	24.12
O	K	34.24	65.63

5.2.4. X-Ray Photoelectron Spectroscopic Analysis

Fe $2p_{3/2}$ photoelectron peaks obtained from CS/Fe₃O₄/ZnFe₂O₄ are shown in Figure 5.5 (a). The binding energy value of Fe $2p_{3/2}$ was observed at around 711.2 eV that matched well with the literature value [103]. Zn $2p_{3/2}$ peak from CS/Fe₃O₄/ZnFe₂O₄ was observed at around 1022.8 eV and Zn $2p_{1/2}$ was observed at 1045.7 eV as indicated in Figure 5.5 (c). This revealed the oxidation state of Zn²⁺ as expected. The peak at 1022.8 eV indicated the formation of ZnFe₂O₄ with zinc atom occupying the tetrahedral site. Only one peak was observed for O 1s at 530.1 eV indicating that the oxygen atoms are in the O²⁻ form in the lattice as shown in Figure 5.5 (b). From the XRD and XPS analyses it was confirmed that the CS/Fe₃O₄/ZnFe₂O₄ was composed of ZnFe₂O₄ only.

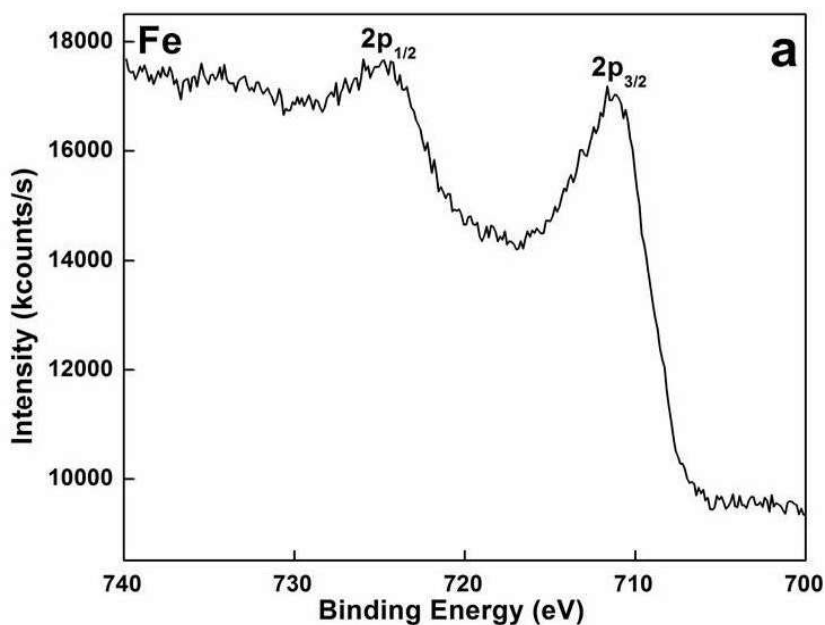


Figure 5.5 (a): XPS spectrum of Fe 2p obtained from CS/Fe₃O₄/ZnFe₂O₄

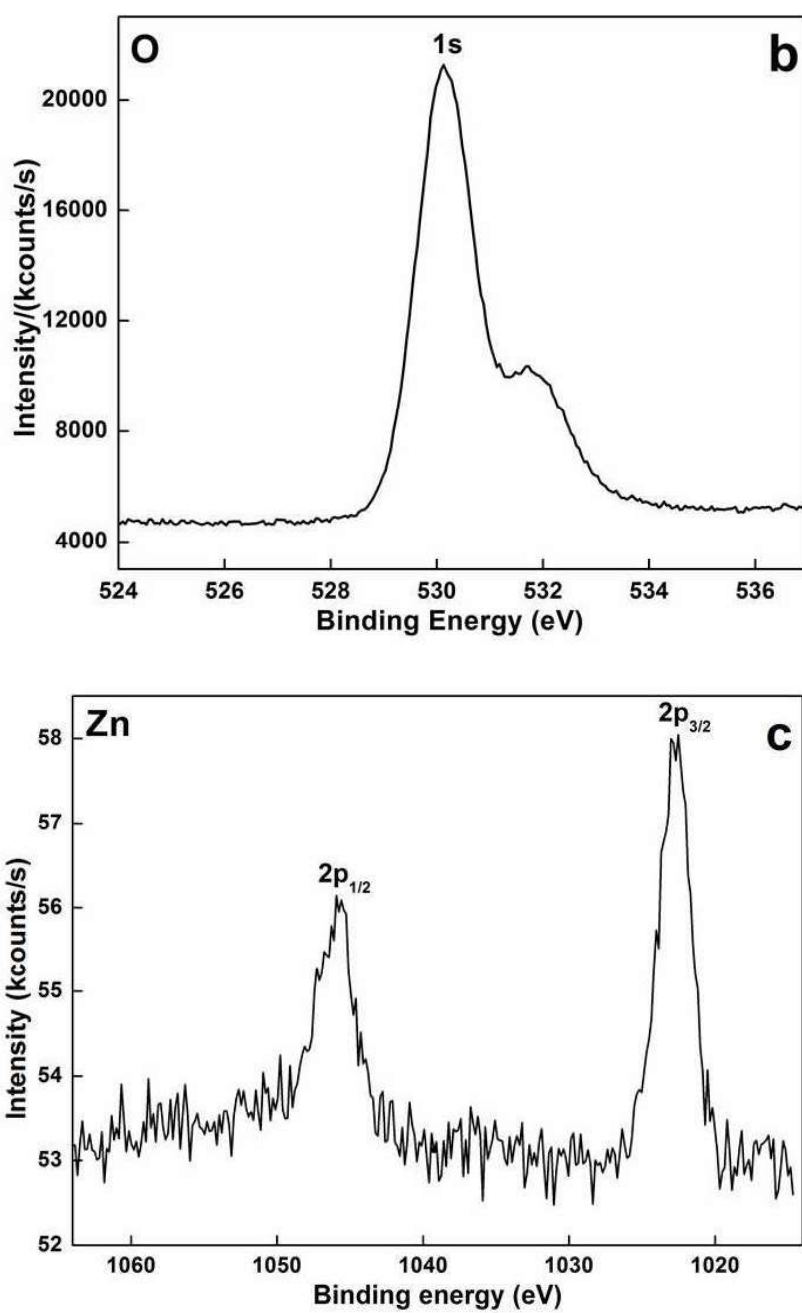


Figure 5.5: XPS spectra of (b) O 1s and (c) Zn 2p peaks obtained from CS/Fe₃O₄/ZnFe₂O₄

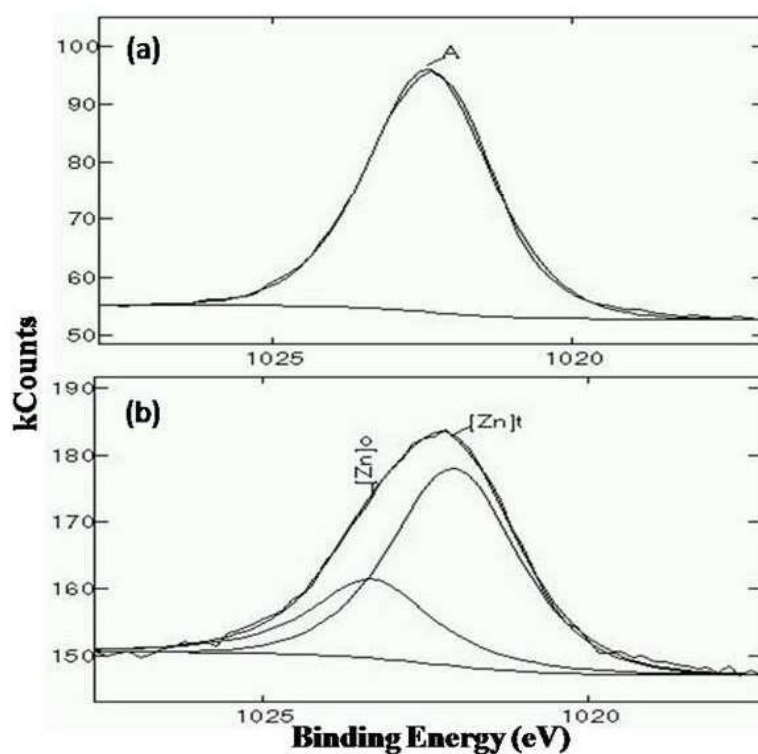


Figure 5.6: XPS spectra of Zn 2p peaks obtained from CS/Fe₃O₄/ZnFe₂O₄

Zn 2p_{3/2} peak obtained from the ZnFe₂O₄ powder (Figure 5.6 (a)) and that from the CS/Fe₃O₄/ZnFe₂O₄ (Figure 5.6 (b)) were compared after the deconvolution for more information. Zn 2p_{3/2} peak was seen at 1022.1 eV with FWHM 2.2 eV in normal ZnFe₂O₄ powder. Zn 2p_{3/2} peak obtained from the coating was wider (2.8 eV) and hence deconvoluted into two peaks. The peak at 1022.1 eV was due to Zn²⁺ at regular tetrahedral sites and the peak at around 1023.5 eV indicated Zn²⁺ in octahedral sites [103]. Hence, it appeared that in nano coatings of ZnFe₂O₄, Zn²⁺ ions were distributed in both A and B sites of the spinels.

5.2.5. Electrochemical Characterization

Generally, the corrosion resistance of coatings is attributed to the inertness of the coating to chemical attacks. But these coatings can exhibit corrosion between the coating and the metal substrate if defects are present. The electrolyte could penetrate inside through these defects and enhance the substrate corrosion. In the present context, the CS substrate acts as an anode and the coating material as the cathode. Thus, corrosion current develops which could be a good measure of the coating porosity [139-140]. The electrochemical corrosion results are explained below.

5.2.5.1. Potentiodynamic Anodic Polarization

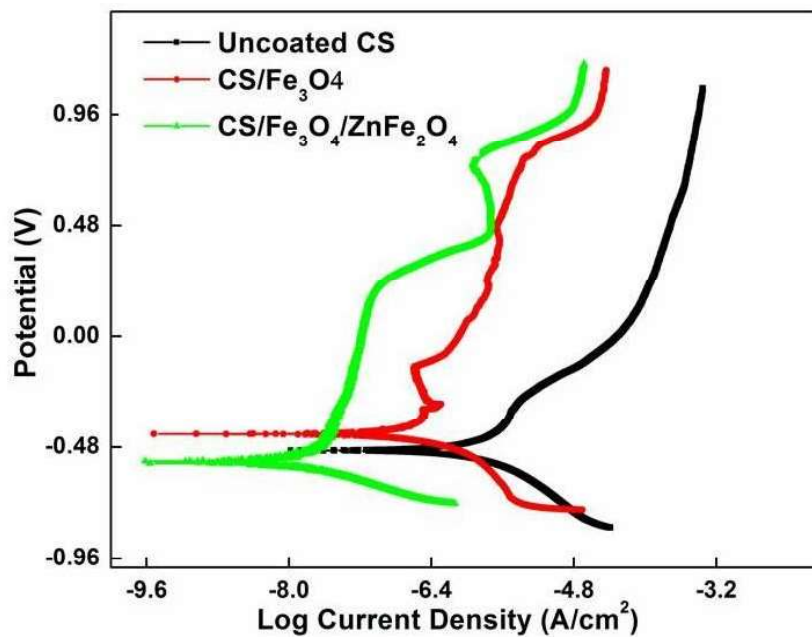


Figure 5.7: PDAP plot of uncoated CS, CS/Fe₃O₄ and CS/Fe₃O₄/ZnFe₂O₄

Figure 5.7 shows the PDAP curve for uncoated CS, CS/Fe₃O₄ and CS/Fe₃O₄/ZnFe₂O₄ in deaerated LiOH aqueous medium at room temperature. The corrosion parameters obtained from these measurements are given in Table 5.2. The

OCP in case of CS/Fe₃O₄ coating has shifted towards the noble side (-0.424 V vs. SCE) compared to uncoated CS (-0.497 V vs. SCE). The OCP obtained in the case of CS/Fe₃O₄/ZnFe₂O₄ (-0.541 V vs. SCE), showed a negative shift compared to OCP of uncoated CS (-0.497 V vs. SCE) confirming the cathodic protective nature of the coating [140]. The ZnFe₂O₄ coating has lower chemical activity than the uncoated CS and hence possesses better chemical stability in the external environment and hence a lower corrosion rate compared to uncoated CS. The CS/Fe₃O₄/ZnFe₂O₄ showed an active to passive transition due to the formation of ferric hydroxide film at more anodic potentials. The transition region was observed in the range -0.125 to +0.799 V for CS/Fe₃O₄ and -0.45 V to +0.19 V for CS/Fe₃O₄/ZnFe₂O₄. It was observed that before the coated specimen was transferred to a passive state, an active current peak occurred which could be attributed to the oxidation of Fe²⁺ to Fe³⁺ ions in the passive film [104, 141]. The passivation currents were in decreasing order showing increased protectiveness of ZnFe₂O₄ film (CS > CS/Fe₃O₄ > CS/Fe₃O₄/ZnFe₂O₄). Based on the values of corrosion current, the corrosion resistance was found to be in the following order: CS/Fe₃O₄/ZnFe₂O₄ > CS/Fe₃O₄ > CS. Hence, the corrosion resistance increased with the adherent additional ZnFe₂O₄ coating.

Table 5.2: Corrosion parameters obtained from PDAP measurements

Specimen	PDAP				
	b _c (V/dec)	b _a (V/dec)	OCP (V)	i _{corr} (μA/cm ²)	Corrosion Rate (mpy)
Uncoated CS	-0.236	0.283	-0.497	1.194	0.552
CS/Fe ₃ O ₄	-0.148	0.414	-0.424	0.219	0.101
CS/Fe ₃ O ₄ /ZnFe ₂ O ₄	-0.114	0.809	-0.541	0.018	0.010

5.2.5.2. Electrochemical Impedance Spectroscopy

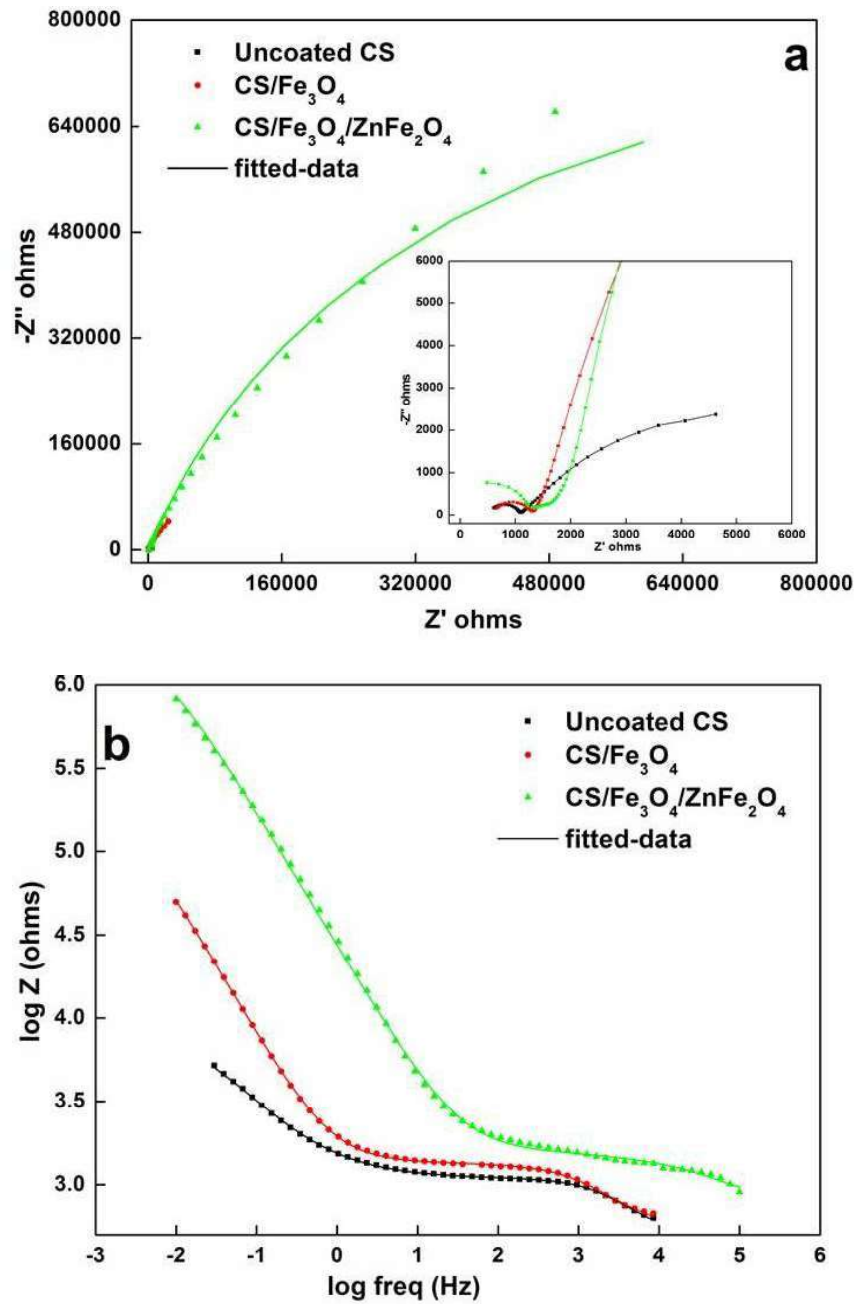


Figure 5.8: (a) Nyquist and (b) Bode plot of uncoated CS, CS/Fe₃O₄ and CS/Fe₃O₄/ZnFe₂O₄

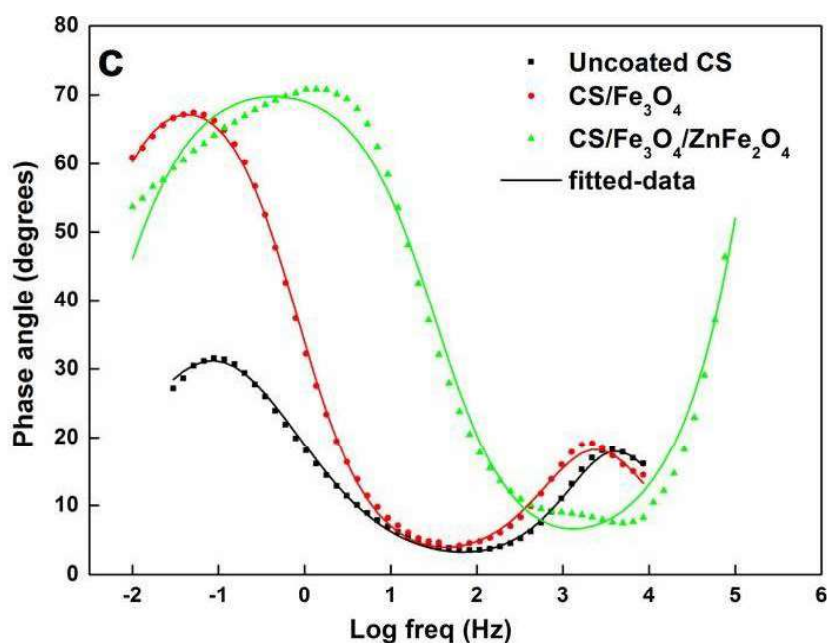


Figure 5.8 (c): Phase angle plot of uncoated CS, CS/Fe₃O₄ and CS/Fe₃O₄/ZnFe₂O₄

The Nyquist (Figure 5.8 (a)) and Bode (Figure 5.8 (b) and 5.8 (c)) diagrams for the coated samples obtained at OCP using EIS in deaerated LiOH solution at room temperature are shown in Figure 5.8. Existence of two semicircles in the Nyquist diagram (Inset Figure 5.8 (a)) indicated the formation of two time constants as explained in chapter 4 section 4.2.5.1. Thus, R_1 for the CS could represent the resistance of this film. R_2 is the charge transfer resistance which is a measure of electron transfer across the metal/film interface and it is inversely proportional to the rate of corrosion. The impedance parameters fitted from the curve are presented in Table 5.3. A high charge transfer resistance (R_2) was obtained in ZnFe₂O₄ coated specimen showing better corrosion resistance. This behavior was also confirmed in the PDAP measurements. Thick and high quality coatings characteristically have almost infinite resistance and very low capacitance. The resistance (R_1 and R_2)

values followed the order: $CS/Fe_3O_4/ZnFe_2O_4 > CS/Fe_3O_4 > CS$ and the constant phase element (Q_1 and Q_2) followed the order: $CS/Fe_3O_4/ZnFe_2O_4 < CS/Fe_3O_4 < CS$ indicating that the deposited coating is protective. $ZnFe_2O_4$ coating over CS/Fe_3O_4 was uniform and smooth which possibly reduced the number of pores at the $Fe_3O_4/ZnFe_2O_4$ interface. The reduction in the number of pores restricted the movement of the species from the bulk towards the oxide solution interface resulting in lower values of the constant phase element (Q_1). The 'n' value was away from 1 which indicated the presence of a non-homogeneous surface. The Bode spectra presented in Figure 5.8 (b) showed a significant increase in the impedance modulus in the full frequency range, indicating an increase in corrosion resistance in case of $ZnFe_2O_4$ coating.

Table 5.3: Impedance parameters obtained from EIS measurements

Specimen	R_s ($K\Omega$)	R_1 ($K\Omega$)	Q_1 (μF)	n	R_2 ($K\Omega$)	Q_2 (mF)	n
Uncoated CS	0.487	0.607	0.44	0.85	9.5	0.49	0.63
CS/Fe_3O_4	0.543	0.801	0.97	0.79	191.2	0.19	0.85
$CS/Fe_3O_4/ZnFe_2O_4$	0.100	4.190	0.04	0.57	1809.0	0.01	0.81

5.2.5.3. Semiconducting properties of the oxide film

Mott-Schottky plots of the coated specimens acquired at 100 Hz in 1.5 ppm LiOH solution (pH 10.2) at room temperature are shown in Figure 5.9. It was observed that the electronic properties of both the oxide films on CS were similar. The curves

obtained for CS/Fe₃O₄ and CS/Fe₃O₄/ZnFe₂O₄ presented a positive slope from -0.6 V_{SCE} upward to more anodic potentials.

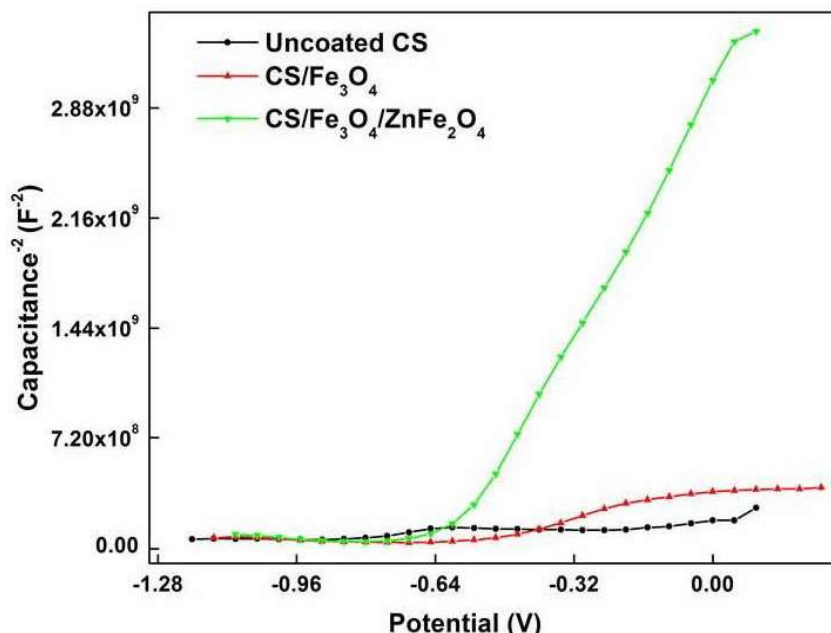


Figure 5.9: Mott-Schottky plot of uncoated CS, CS/Fe₃O₄ and CS/Fe₃O₄/ZnFe₂O₄

As observed from the polarization scan (Figure 5.7) above 0.3 V, the film was not stable and hence the region above that was not used for analysis. The flat band potential was ~ 0.6 V for all the coated specimen. This variation of the inverse dependency of square of capacitance with the applied potential is typical of an n-type semiconductor and the main defects in the oxide film were cation interstitials or anion vacancies (oxygen) acting as electron donors [104]. The defect densities were calculated from the slope of the linear portion of the Mott–Schottky plots using $\epsilon = 12$ for CS/Fe₃O₄, 20 for CS [106] and 100 for ZnFe₂O₄ [142]. This concentration corresponds to the number of defects in the film. A high doping density is typical of a defective oxide layer which, in turn, is associated with a lower corrosion resistance [90]. The defect density concentrations corresponding to uncoated and coated

specimens are shown in Figure 5.10. The lower charge carrier concentration was observed for ZnFe_2O_4 coated on $\text{CS}/\text{Fe}_3\text{O}_4$. Changes in donor density correspond to non-stoichiometry defects in the passive film which is a clear indication of the formation of a highly disordered oxide [91]. The reduction of the number of defects in the oxide film with different coatings revealed in Figure 5.10 also pointed to the formation of less conductive and more protective oxide layers. This result confirmed the increase of corrosion resistance as observed from the Nyquist and PDAP plots for both the oxide coated specimens compared to uncoated CS.

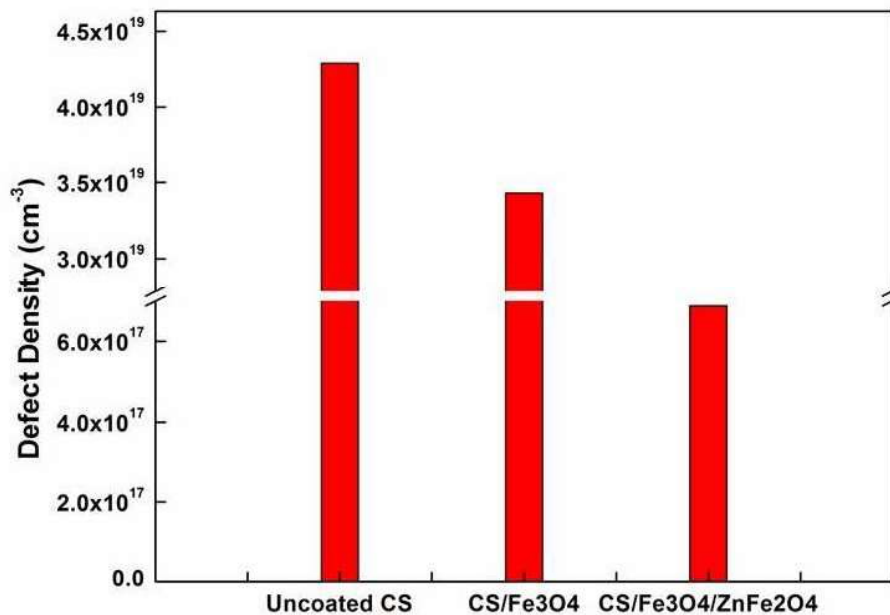


Figure 5.10: Defect Density graph of CS, $\text{CS}/\text{Fe}_3\text{O}_4$ and $\text{CS}/\text{Fe}_3\text{O}_4/\text{ZnFe}_2\text{O}_4$

5.2.6. Scratch Test

The friction coefficient, acoustic signal, penetration depth, normal load applied against scratch length is plotted along with SEM image of scratch performed on $\text{CS}/\text{Fe}_3\text{O}_4/\text{MgFe}_2\text{O}_4$ are as shown in the Figure 5.11.

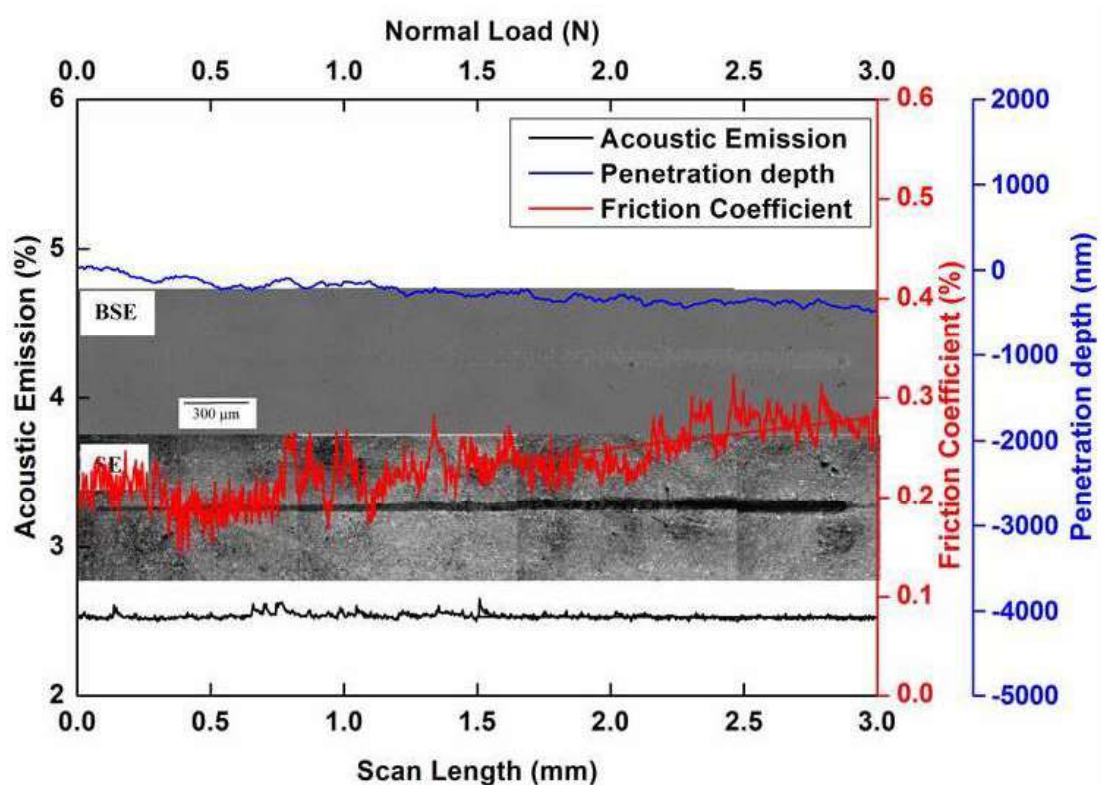


Figure 5.11: Scratch Test for CS/Fe₃O₄/ZnFe₂O₄

The fluctuations in the friction coefficient gradually increased throughout the scan length. The first critical failure was observed after 1.5 N load. According to the scratch profile and the respective information suggests that this film was adherent enough. Buckling cracks were formed after 1.5 N load and buckling spallation was observed.

5.3. Conclusion

XRD measurements confirmed the formation of nano size ZnFe₂O₄ coating deposited by PLD technique. ZnFe₂O₄ coating on CS required an intermediate layer of Fe₃O₄ for good adherence to the CS surface. Electrochemical DC and AC

measurements showed the effectiveness of the nano-sized ZnFe_2O_4 coating in improving the protectiveness of the oxides present on CS. Mott-Schottky analysis showed that the defect density was less for ZnFe_2O_4 coated CS indicating improvement in the corrosion resistance. Scratch test showed that the zinc ferrite coating was adherent with the substrate.

Part II: ZnFe_2O_4 film formation by hydrothermal method

5.4. Introduction

In the present work, attempts were made to incorporate Zn^{2+} ions into the Fe_3O_4 lattice during its formation by hydrothermal method for 24, 96 and 240 hours and the oxide formed was characterized by laser Raman spectroscopy, XRD, XPS and SEM measurements. The corrosion resistances of these oxides in LiOH medium were studied by EIS and PDAP and the electronic properties of these oxides were carried out by Mott-Schottky (MS) measurements in aqueous LiOH.

5.5. Results and Discussion

ZnFe_2O_4 is represented as $[\text{Zn}^{2+}]_{\text{Td}}[\text{Fe}^{3+}\text{Fe}^{3+}]_{\text{Oh}}\text{O}_4$.

5.5.1. Cation concentration and thickness measurement

The zinc and iron ion concentration in the autoclave solution measured after the exposure experiments are as given in Figure 5.12 (a). Zinc concentration of 1000 ppb was taken at the start of the experiment. The decrease in the concentration of zinc in the autoclave solution indicates the transport of zinc from solution to the

specimen surface. The increase in the concentration of the Fe ions in the autoclave solution for 24 hours exposed specimen indicated that corrosion was higher. Figure 5.12 (b) shows the oxide film growth on the CS surface. From the graph, it was evident that the oxide formation followed a parabolic law. The thickness of the oxide obtained in presence of zinc ions were less compared to that obtained in presence of nickel ions.

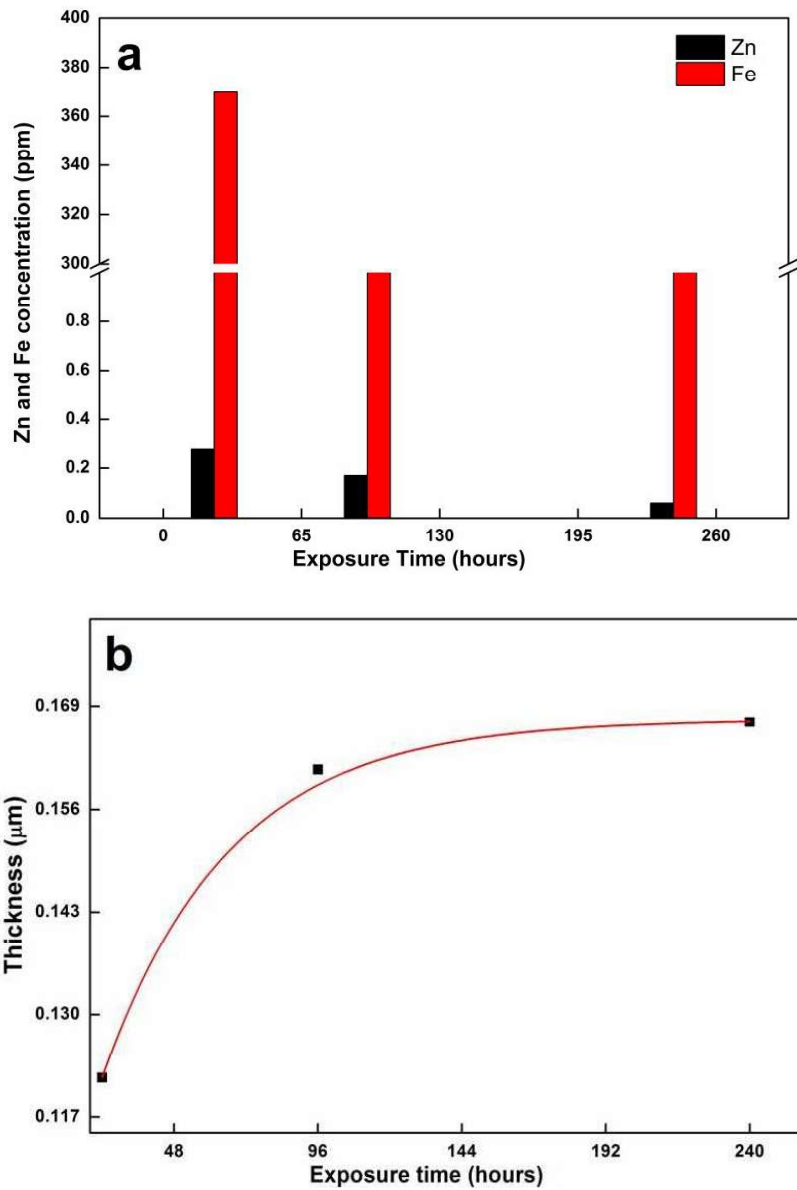


Figure 5.12: (a) Zinc and Iron concentration and (b) oxide film thickness at the end of different exposure time

To start with the incorporation of the Zn^{2+} ions into the magnetite lattice, the concentration of the Zn^{2+} ions was taken as 200 ppb. Since the autoclave used was Hastelloy, the Ni^{2+} ions from the nickel lined autoclave body also contributed in ferrite formation. The presence of Ni^{2+} along with Zn^{2+} ions was incorporated into the oxide lattice which was observed by XPS. Hence, the concentration of the metal ions under study was increased to 1000 ppb and the autoclave was pre-conditioned three times with each metal ion under study without the CS specimens to avoid the leaching of nickel ions in the experimental solution as explained in chapter 2 section 2.4.2.1.

5.5.2. Surface characterization of oxides

5.5.2.1. X-Ray Diffraction Analysis

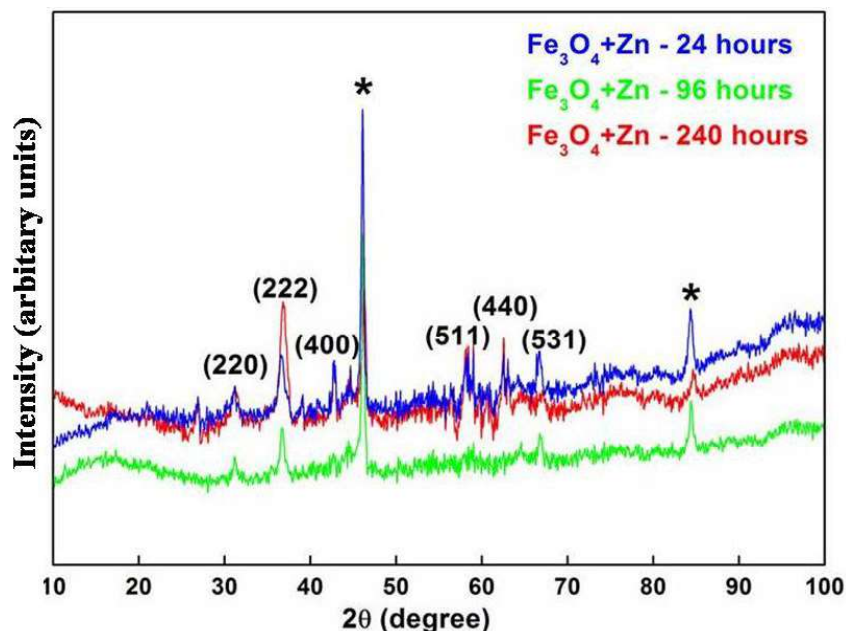


Figure 5.13: GI-XRD patterns of the oxide formed on CS exposed to 250 °C in presence of Zn^{2+} for 24, 96 and 240 hours

Table 5.4: Crystallite size and Lattice parameter obtained from GI-XRD

	Exposure Time	Crystallite size (nm)	Lattice Parameter (Å°)
Fe ₃ O ₄	24 hours	9.7	8.48
+	96 hours	11.7	8.47
Zn ²⁺	240 hours	10.4	8.44

Figure 5.13 shows the GI-XRD patterns of the oxide films formed on CS exposed to 250 °C in LiOH and Zn²⁺ for different time duration. Characteristic peaks for the oxides formed in 24, 96 and 240 hours suggested a spinel structure for oxide film. The GI-XRD pattern showed that the formed spinel consisted entirely of crystalline ZnFe₂O₄ having preferred orientation along (222) plane and its intensity increased with exposure time and was compared with the standard data of cubic spinel (ZnFe₂O₄) from the database (ICDD.No.01-074-8584). Lattice parameter values for the oxide films were 8.48, 8.47 and 8.44 for 24, 96 and 240 hours exposed specimens suggesting the incorporation of zinc ions into the magnetite lattice. The lattice parameter of ZnFe₂O₄ in the literature is 8.44 [138]. The crystallite size and the lattice parameter of all the oxides formed were estimated from the FWHM using Scherrer's equation and are given in the Table 5.4. When the particle size decreases, the fraction of atoms near the surface increases, which may be the cause for the variation in the lattice parameter [125]. Additional peak of base material marked as '*' was observed in the GI-XRD pattern at 45°. Small peaks marked as '#' were seen at 64.6° and 82° due to FeO(OH) which is the intermediate layer in the Fe₃O₄ formation. The intensity of the diffraction peaks were less for the 24 hours exposed CS specimen in comparison to the 96 and 240 hours exposed specimen.

5.5.2.2. Scanning Electron Microscopic Analysis

Figure 5.14 shows the SEM morphologies of the oxide films formed on CS exposed to 250 °C in LiOH and Zn^{2+} for 24, 96 and 240 hours exposed specimen. The surface of the specimen was fully covered with octahedron shaped oxide particles. The size of the outer particles precipitated from the solution was bigger than the inner particles which are grown from the base metal. The size of the particles increased with increase in exposure time.

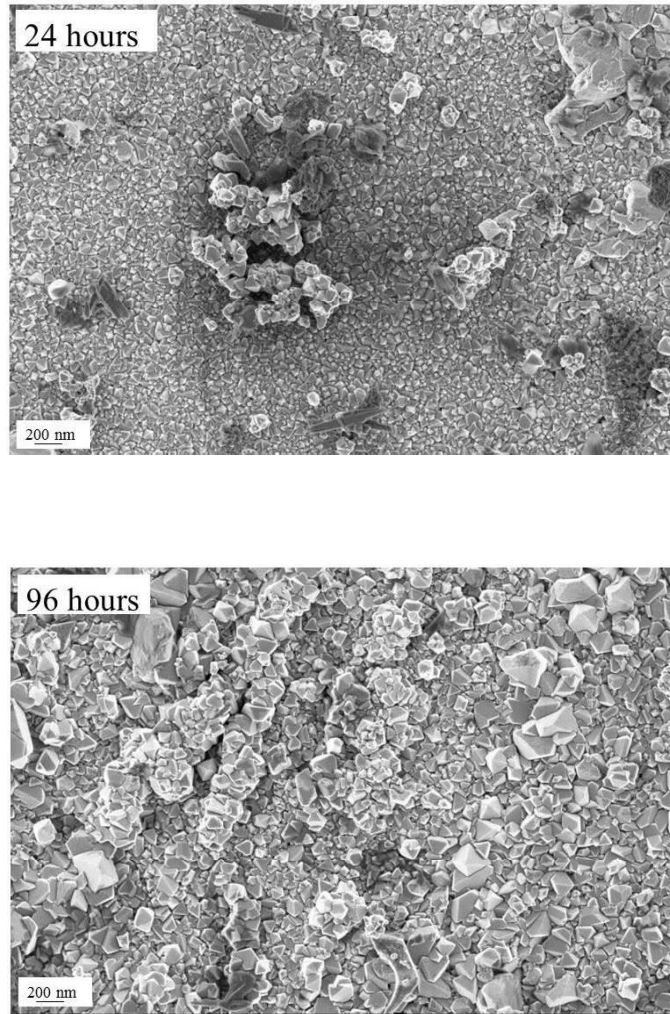


Figure 5.14: FE-SEM images of CS exposed to 24 and 96 hours in presence of Zn^{2+} ions

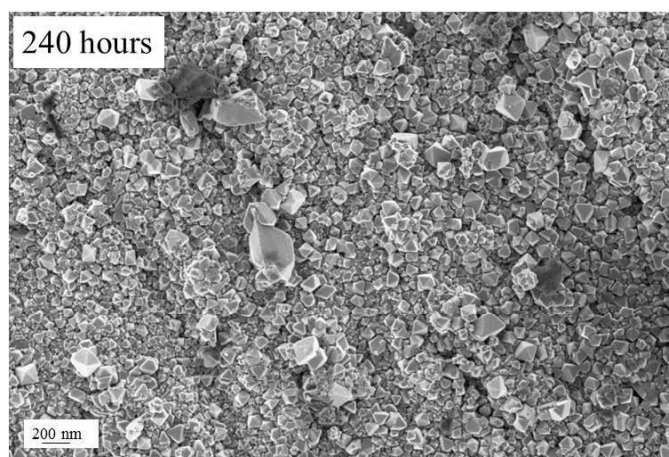


Figure 5.14: FE-SEM images of CS exposed to 240 hours in presence of Zn^{2+} ions

5.5.2.3. X-Ray Photoelectron Spectroscopic Analysis

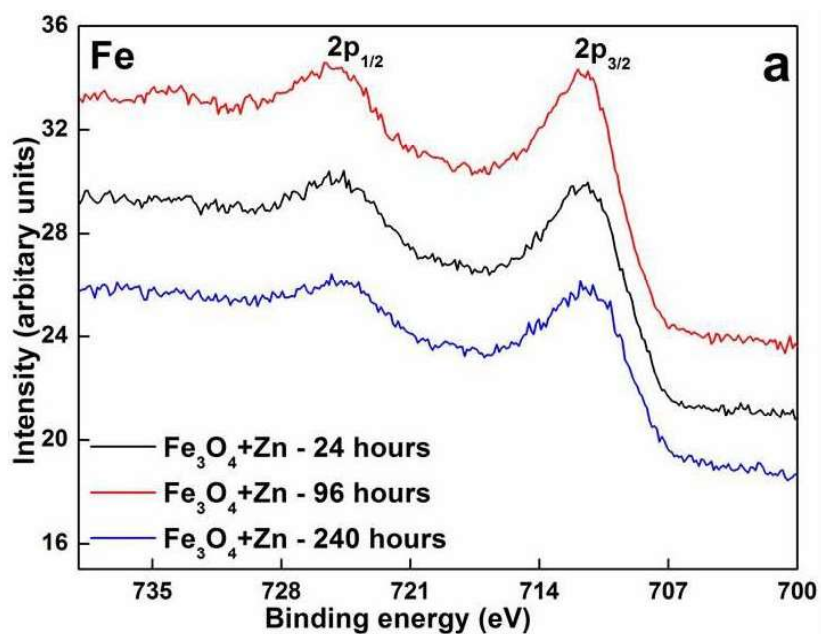


Figure 5.15: XPS spectra of (a) Fe 2p obtained for CS in presence of Zn^{2+} ions

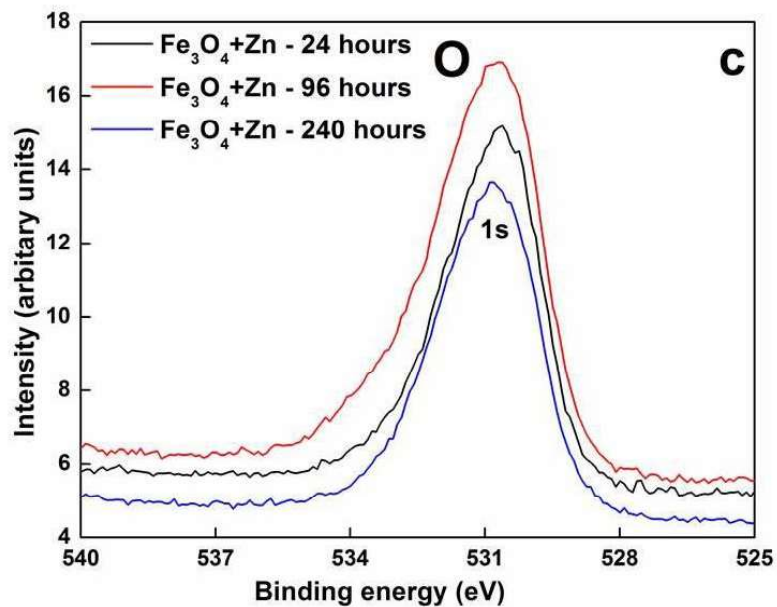
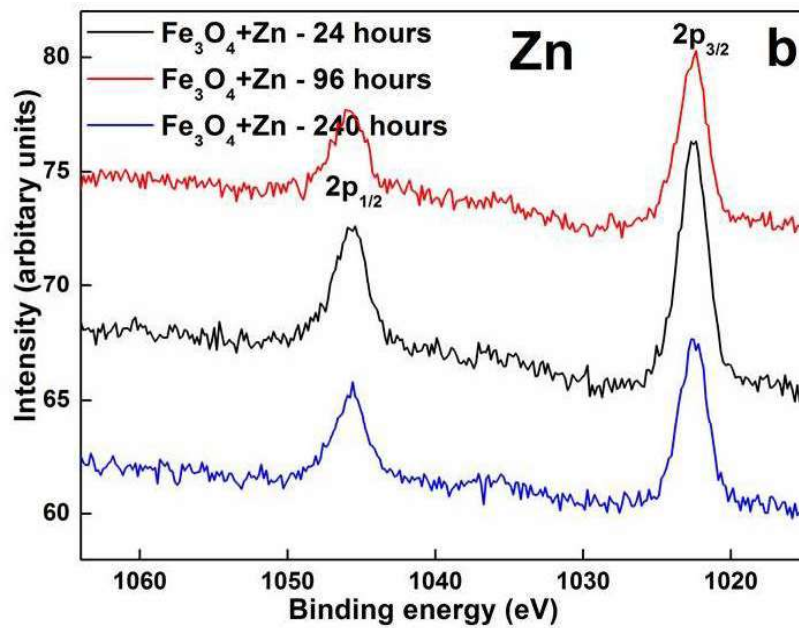


Figure 5.15: XPS spectra of (b) Zn 2p and (c) O 1s peaks obtained for CS in presence of Zn²⁺ ions

XPS spectra of (a) Fe 2p, (b) Zn 2p and (c) O 1s peaks obtained for CS in presence of Zn^{2+} ions exposed for 24, 96 and 240 hours are as shown in Figure 5.15. The spinel crystalline structure (AB_2O_4) with tetrahedral and octahedral sites for metal atoms is confirmed. Fe $2p_{3/2}$ photoelectron peaks obtained for all the three oxide formed samples are as shown in Figure 5.15 (a). The binding energy values of Fe $2p_{3/2}$ and Fe $2p_{1/2}$ were observed at around 710-711 eV and 724-725 eV respectively. Generally, Fe 2p states of the Fe atom could be used to distinguish the variation between Fe^{2+} and Fe^{3+} . The peak with the range of 710-711 eV was attributed to the Fe^{3+} cation located at the octahedral site in the spinel structure. The peak range of 724-725 was endorsed to the Fe^{2+} cation located at the tetrahedral site in the spinel structure. Zn exhibits binding energies at 1021 eV and 1044 eV, which corresponds to Zn $2p_{3/2}$ and Zn $2p_{1/2}$ electrons respectively in the Zn^{2+} oxidation state. Zn $2p_{3/2}$ and Zn $2p_{1/2}$ peaks from the oxide formed CS were observed at around 1022.4eV and 1045.6 eV respectively as indicated in Figure 5.15 (b). Since, zinc ferrite contains Fe^{3+} type iron only, an increase in binding energy in zinc ferrite oxides (711.5 eV) may be due to the change in oxygen environment of Fe in zinc ferrite. Only one peak was observed for O 1s at 530.6 eV for all the specimens indicating that the oxygen atoms are in the O^{2-} form in the lattice. The XPS measurement results were related to XRD observations conforming the single cubic phase of the ferrite. The binding energy values and the quantification of the oxides formed at different exposure time are given in Table 5.5 which showed that the % of the elements remained same for the 96 and 240 hours. In this zinc ferrite formation, the stoichiometric ratio was not observed to be 1:2.

Table 5.5: Binding Energy and Quantification of the elements by XPS

Exposure Time (hours)	Fe		Zn		O	
	Binding Energy (eV)	(%)	Binding Energy (eV)	(%)	Binding Energy (eV)	(%)
24	711.7	15	1022.8	6	530.8	79
96	711.7	14	1022.6	4	530.9	82
240	711.5	14	1022.8	4	530.9	82

5.5.2.4. Laser Raman Spectroscopic Analysis

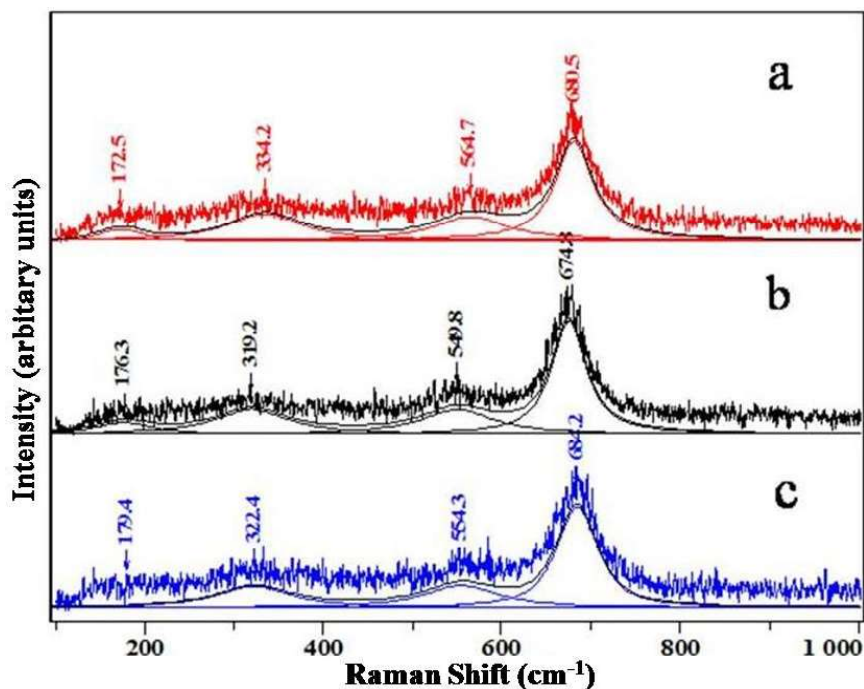


Figure 5.16 : Raman spectrum of the oxide films formed on CS exposed for (a) 24, (b) 96 and (c) 240 hours at 250 °C in LiOH in presence of Zn²⁺ ions

Figure 5.16 shows the Raman spectra of the oxide films formed on CS exposed to 250 °C in LiOH and Zn²⁺ ions (1000 ppb) as a function of exposure time i.e., (a) 24

hours, (b) 96 hours and (c) 240 hours and the vibrational modes are as given in Table 5.6. The curve fitting of the Raman data recorded on the oxide film formed on CS in presence of soluble zinc showed four peak maxima [108].

Table 5.6: Vibrational modes obtained for the oxides from Raman analysis

Raman mode	A _{1g}	T _{2g} (1)	T _{2g} (2)	E _g	T _{2g} (3)
CS/Fe ₃ O ₄	672.6	551.2	-	323.9	187.0
ZnFe ₂ O ₄ - 24 hours	680.5	564.7	-	334.2	172.5
ZnFe ₂ O ₄ - 96 hours	674.8	549.8	-	319.2	176.3
ZnFe ₂ O ₄ - 240 hours	684.2	554.3	-	322.4	179.4

The oxide film formed in presence of zinc ions exposed for 24 and 240 hours showed the peak maxima at higher wave numbers compared to the oxide formed in absence of zinc ions as observed in Table 5.6. T_{2g}(3) peak was not observed for 24 hours exposed specimen. The mass difference between the two ions (Zn²⁺ and Fe³⁺) shifted the A_{1g} mode of the lightest ion Zn²⁺ to higher wave number (674 - 684 cm⁻¹) and the heaviest ion Fe³⁺ to lower wave number 672 cm⁻¹. The changes in relative peak intensity and peak position in the oxides formed may be due to the incorporation of Zn²⁺ ions into the magnetite lattice. Further, the Raman frequency also depends on the Fe(Zn)-O and bond length. The shift in wave number was attributed to the crystalline disorder and also to the presence of grain boundaries, which were large in small-sized nanomaterials [109]. The wave number position of the bands did not change significantly with different exposure time in presence of zinc ions.

5.5.3. Electrochemical Characterization

5.5.3.1. Potentiodynamic Anodic Polarization

Figure 5.17 shows the PDAP curve for uncoated CS and the oxides formed in presence of Zn^{2+} ions for 24, 96 and 240 hours in deaerated LiOH aqueous medium at 28 °C. The corrosion parameters obtained from these measurements are given in Table 5.7. The OCP for the oxide formed in 24 hours shifted towards the active side (-0.616 V vs. SCE) and to the noble side in the case of oxide formed in 96 hours (-0.302 V vs. SCE) compared to the uncoated CS (-0.497 V vs. SCE). The magnitudes of current densities for the oxide formed in presence of zinc in 24, 96 and 240 hours exposure were lower than that observed for uncoated CS. The passivation region observed was broad in the range -0.2 to 0.76 V for 24 hours exposed CS and for 96 and 240 hours exposed CS the passivation region was not observed and the current increased slowly. Based on the values of corrosion current, the corrosion resistance was found to be in the following order: CS < 24 hours < 96 hours < 240 hours. The incorporation of the Zn^{2+} ions into the magnetite lattice reduced the corrosion rate by one order of magnitude compared to the corrosion rate of uncoated CS but no significant difference was observed among the corrosion rates for different exposure time. Though the oxide film formed at 96 hours showed a noble shift in potential, the film formed was inferior due to the increase in current at anodic potential. The cathodic and anodic reactions that could take place in this system are as explained in chapter 4 section 4.5.3.1. The solution was analyzed for the metal ions by ICP-AES after the electrochemical measurement was completed. The solution showed appreciable amount of iron (ppb range) in the solution.

Table 5.7: Corrosion parameters for different exposure time in LiOH and Zn²⁺

Specimen	PDAP				
	b _c (V/dec)	b _a (V/dec)	OCP (V)	i _{corr} (μA/cm ²)	Corrosion Rate (mpy)
Uncoated CS	-0.236	0.283	-0.497	1.194	0.552
24 hours	-0.108	0.375	-0.616	0.156	0.072
96 hours	-0.225	0.183	-0.302	0.067	0.031
240 hours	-0.135	0.360	-0.471	0.040	0.019

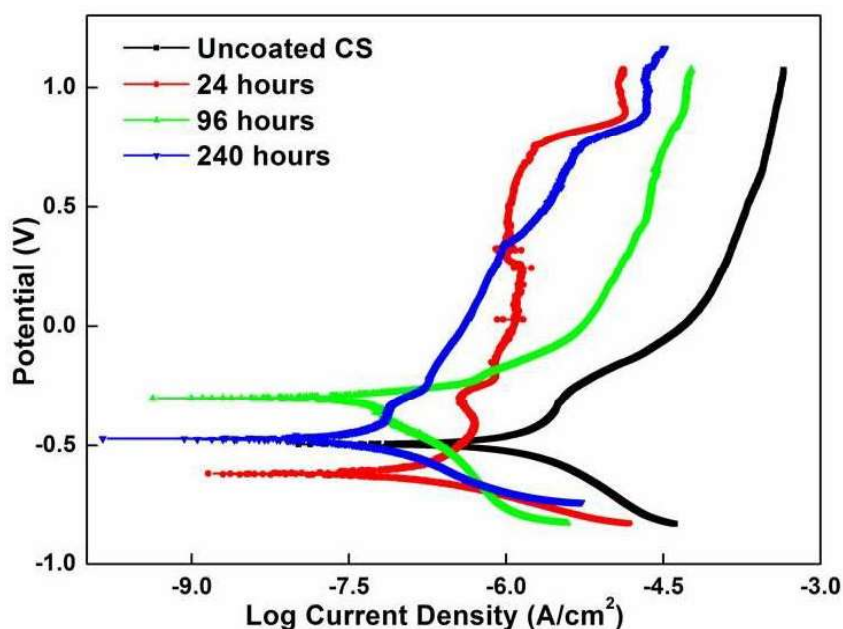


Figure 5.17: PDAP plot of CS exposed to 24, 96 and 240 hours in LiOH and Zn²⁺

5.5.3.2. Electrochemical Impedance Spectroscopy

Figure 5.18 shows the EIS spectra for uncoated CS and the oxides formed in presence of Zn²⁺ ions for 24, 96 and 240 hours in deaerated LiOH aqueous medium

at 28 °C. Oxides formed showed two time constants as observed from the Nyquist plots at different frequency ranges. Oxide formed in case of 24, 96 and 240 hours exposure showed increased capacitive loop which can be related to increase in protectiveness of the oxide. Table 5.8 gives the impedance values from EIS analysis. The EIS Bode spectra (Figure 5.18 (b)) demonstrate that the zinc ferrite formation for different exposure time showed less corrosion resistance at high frequency compared to the uncoated CS whereas at low frequency region the resistance for the 96 and 240 hours exposed specimen increased when compared with the uncoated and 24 hours exposed CS specimen. The impedance modulus at low-frequency region increased with exposure time. In order to evaluate oxide coating performance, the low-frequency impedance modulus values obtained at 0.01 Hz ($|Z|_{0.01 \text{ Hz}}$) were used to estimate the resistance of the coating [127]. Table 5.9 shows the values of this parameter versus exposure time. It was observed from Table 5.8 that the total polarization resistance (R_1+R_2) increased from 19.53 k Ω to 164.58 k Ω with increase in the exposure time suggesting that the thickening of the oxide film improved the film passivity. Figure 5.19 gives the trend of the corrosion rate and polarization resistance in absence and presence of zinc ions. The figure depicted that the corrosion rate reduced and the polarization resistance increased with the increase in the exposure time in presence of Zn^{2+} ions.

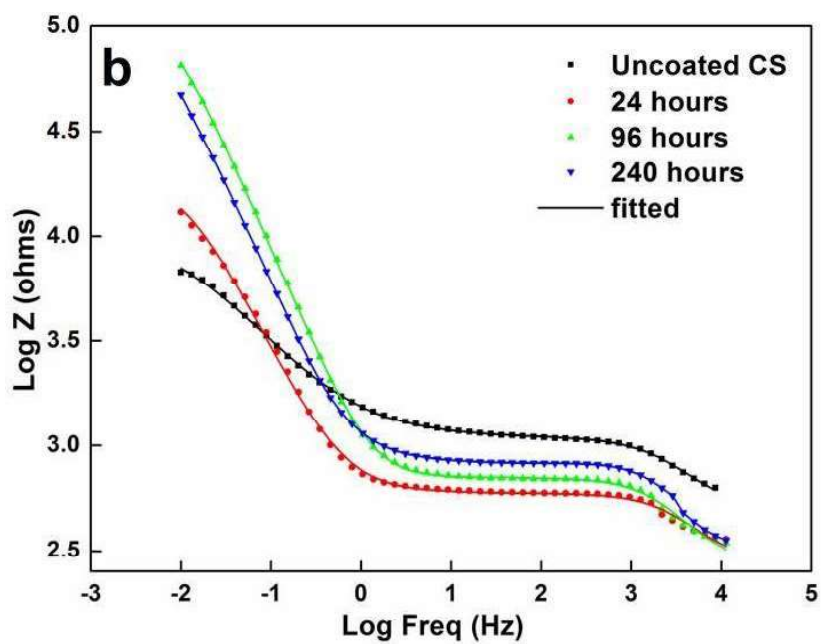
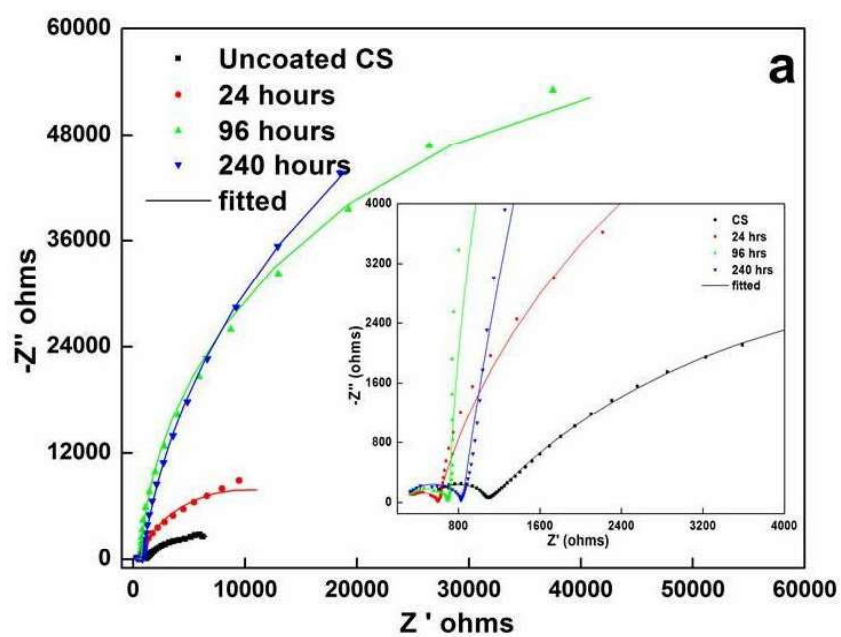


Figure 5.18: (a) Nyquist and (b) Bode plot of CS exposed to in LiOH and Zn^{2+}

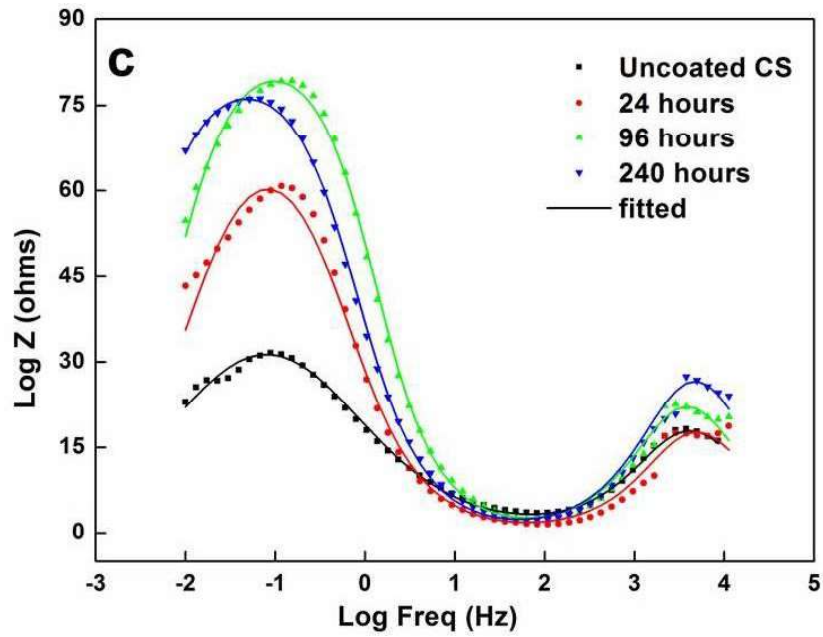


Figure 5.18 (c): Phase angle plot of CS exposed in LiOH and Zn^{2+}

Table 5.8: Impedance parameters for different exposure time in LiOH and Zn^{2+}

Specimen	R_s (K Ω)	Q_1 (μ F)	n	Q_2 (mF)	n	R_2 (K Ω)	R_1 (K Ω)
Uncoated CS	0.487	0.44	0.85	0.49	0.63	9.5	0.607
24 hours	0.280	0.485	0.89	0.534	0.88	19.21	0.316
96 hours	0.273	0.461	0.89	0.181	0.98	112.6	0.434
240 hours	0.263	0.329	0.89	0.261	0.94	164.0	0.577

Table 5.9: $\text{Log } |Z|_{0.01 \text{ Hz}}$ for Zinc Ferrite vs exposure time in LiOH solution

	$\text{Log } Z _{0.01 \text{ Hz}}$
Uncoated CS	3.872
24 hours	4.115
96 hours	4.639
240 hours	4.675

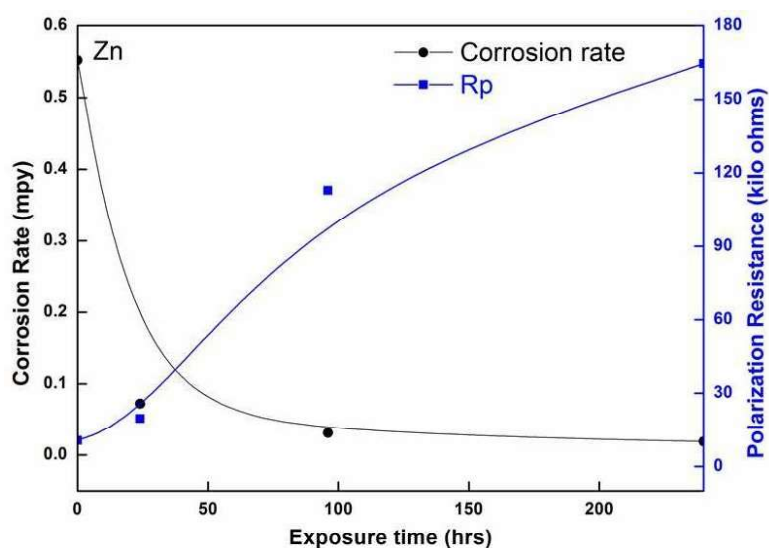


Figure 5.19: Corrosion rate and Polarization resistance comparison

5.5.3.3. Semiconducting properties of the oxide film

It is generally acknowledged that oxygen ions must be transported from the film/solution interface to the metal/film interface, resulting in the penetration of the barrier layer into the substrate metal phase. On the other hand, metal ions are transported in the reverse direction, with the relative fluxes of these species depending on the energies of formation of the respective vacancies. In the present work, the Mott–Schottky measurement for the oxide formed on CS in presence of zinc ions for different exposure times was carried out at 1000, 100, 10 and 5 Hz in the potential range -1.2 to 1.2 V. For the calculation of N_D /or N_A , the dielectric constant ' ϵ ' was assumed as 12 for the passive films on CS. Figure 5.20 showed the C^{-2} versus potential obtained at 100 and 10 Hz for the passive film formed anodically on CS in LiOH solution. The oxide coated specimens were found to follow Mott-Schottky relationship at a certain potential range. The curves obtained for uncoated and oxide formed on CS presented a positive slope from -0.8 V_{SCE}

upward to more anodic potentials. This variation of the capacitance⁻² with the applied potential is typical of an n-type semiconductor and the defects in the oxide film are cation interstitials or anion vacancies (oxygen) acting as electron donors [104]. The oxide formed CS showed two positive slopes in case of 100 Hz and 10 Hz indicating two donor levels at higher anodic potentials. Such behaviour is an indication of the highly disordered nature of the oxide film, which is characteristic of amorphous semiconductors. With increasing frequency, C⁻² increased which is attributed to the ionic part of the space charge layer [128]. Because of the low ionic mobility, these ionic charges give a contribution to the capacitance only at lower frequencies. Table 5.10 gives the defect density values calculated for MS plot obtained at 100 Hz frequency showed that the defect density values were almost similar with increase in exposure time for the potential region in the range -0.6 to -0.25 V. At higher potential region in the range -0.25 to +0.5 V, the defect density increased for 96 and 240 hours which is also reflected from the PDAP curve by the absence of the passivation and a slight increase in the current density with increase in potential in the anodic region. Hence zinc ions present in the spinel structure inhibit transportation of ions from the metal to solution and minimize the corrosion rate.

Table 5.10: Defect density values obtained from Mott Schottky analysis

100 Hz	Defect Density (cm ⁻³)	
	-0.6 to -0.25 V	-0.25 to +0.5 V
Uncoated CS	4.29 x 10 ¹⁹	-
24 hours	1.22 x 10 ¹⁹	5.88 x 10 ¹⁹
96 hours	5.41 x 10 ¹⁹	2.01 x 10 ²⁰
240 hours	9.66 x 10 ¹⁸	1.38 x 10 ²⁰

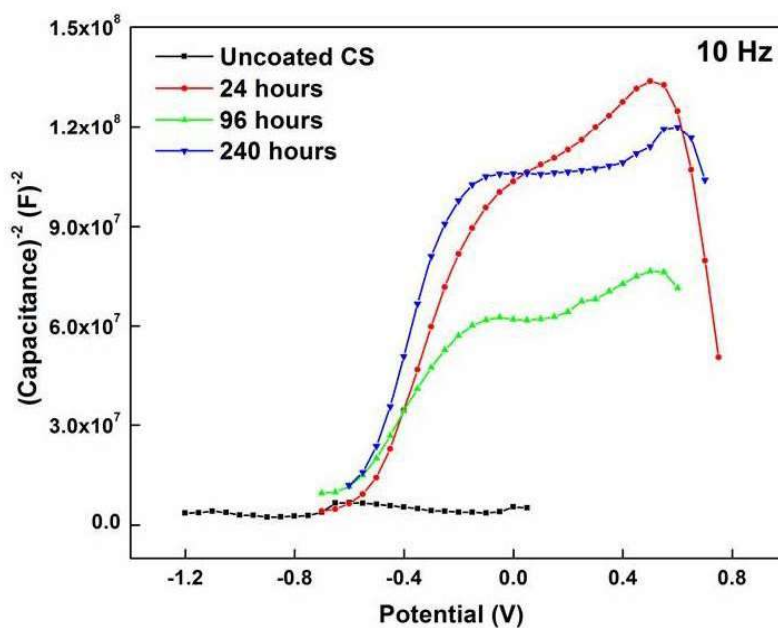
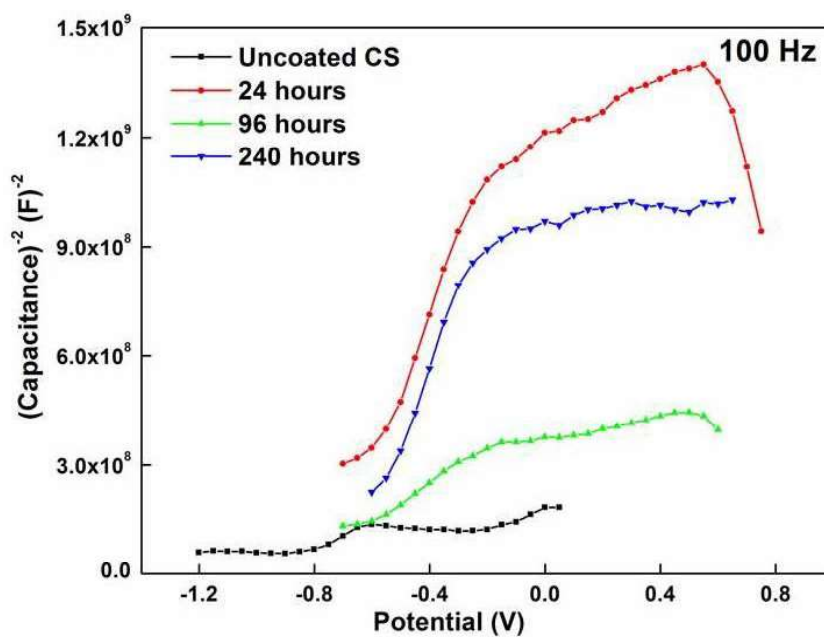


Figure 5.20: Mott Schottky plot of CS exposed to 24, 96 and 240 hours in LiOH and Zn^{2+} at (a) 100 Hz and (b) 10 Hz

5.6. Conclusion

Zinc ferrite film was formed on CS in presence of zinc ions by hydrothermal method and was confirmed by XRD. SEM analysis showed that the CS surface was uniformly covered. XPS analysis was used for the quantification of the elements present in the oxides formed on CS for different exposure time. The zinc incorporation into the magnetite lattice remained same for 96 and 240 hours indicating that the higher exposure time does not improve the zinc intake. Electrochemical corrosion experiments showed an increase in polarization resistance from impedance and reduction in corrosion rate by PDAP and hence the enhancement in corrosion resistance of CS.

Chapter 6

Effect of magnesium ferrite coating on the corrosion resistance of the Carbon Steel

Part I: MgFe₂O₄ deposition by PLD method

6.1. Introduction

In BWRs, it was observed that the addition of zinc ions at ppb level reduced not only the release of corrosion products into the coolant but also the pickup of ⁶⁰Co by modifying the oxide layer over the structural materials [130]. Studies with zinc ion injection gives rise to Zn⁶⁵ activity, hence an alternative to Zn²⁺ ion is being explored. In PHWR, under the primary coolant chemistry conditions, magnetite is the most commonly formed corrosion product on CS and reduction in corrosion product release was observed due to Mg²⁺ ion passivation in simulated PHWR - PHT coolant conditions [143]. Hence, apart from modifying the oxide films with the addition of external metal ions, it has to be seen whether modifying these oxides to nano size would improve the adherence and protectiveness of the interfacial film. In this chapter, attempts were made to form an additional nano magnesium ferrite (MgFe₂O₄) coating on CS/Fe₃O₄ by PLD technique. Characterization and electrochemical studies similar to NiFe₂O₄ and ZnFe₂O₄ as explained in Chapters 4 and 5 were also carried out for MgFe₂O₄ to see the effect of this coating on the corrosion behavior of CS.

6.2. Results and Discussion

MgFe₂O₄ has a cubic spinel structure represented as (Mg²⁺Fe³⁺)_x[Mg²⁺Fe³⁺]_{2-x}O₄ where round and square brackets denote sites of tetrahedral (A) and octahedral (B) coordination respectively and 'x' represents degree of inversion defined as fraction of the (A) sites occupied by Fe³⁺ cations.

6.2.1. Laser Raman Spectroscopic Analysis

Raman peaks observed in the region 620–720 cm^{-1} reflect the nature of the tetrahedral sites in ferrites, while those in the 450–620 cm^{-1} region reflect the octahedral sites indicating a high degree of disorder in cations distribution in the octahedral sites of MgFe_2O_4 . Figure 6.1 shows the Raman spectra recorded on the MgFe_2O_4 film deposited on $\text{CS}/\text{Fe}_3\text{O}_4$ by PLD (labeled as $\text{CS}/\text{Fe}_3\text{O}_4/\text{MgFe}_2\text{O}_4$). Raman shift values observed on $\text{CS}/\text{Fe}_3\text{O}_4/\text{MgFe}_2\text{O}_4$ (Figure 6.1a) were compared with standard MgFe_2O_4 (Figure 6.1b). The high intensity peak was observed at 671.3 cm^{-1} indicating the A_{1g} mode due to symmetric stretching of oxygen atoms along Fe-O and Mg-O bonds in the tetrahedral site. Low intensity peaks observed at 312.2 and 547.1 cm^{-1} reflect the nature of the metal oxygen bond in octahedral sites.

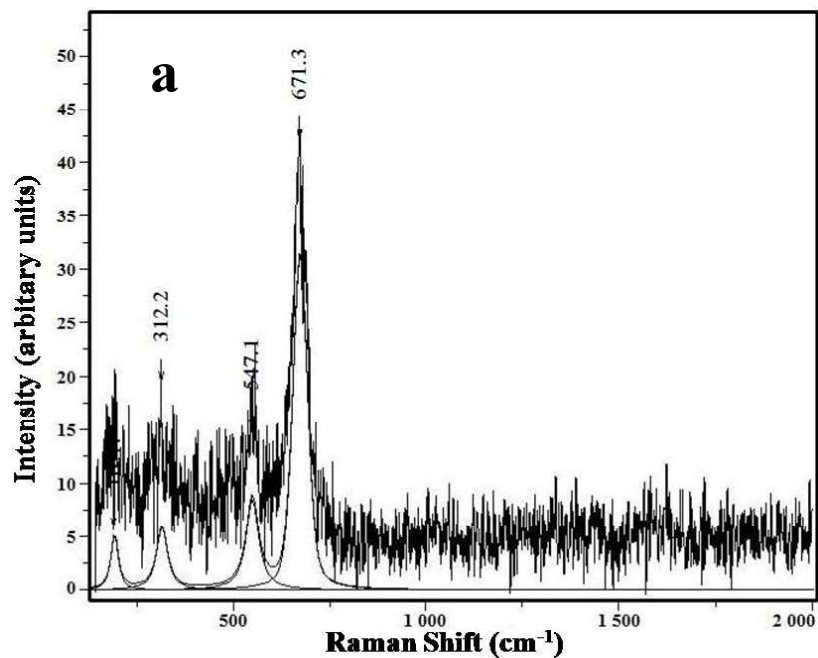


Figure 6.1(a): Raman spectrum of $\text{CS}/\text{Fe}_3\text{O}_4/\text{MgFe}_2\text{O}_4$

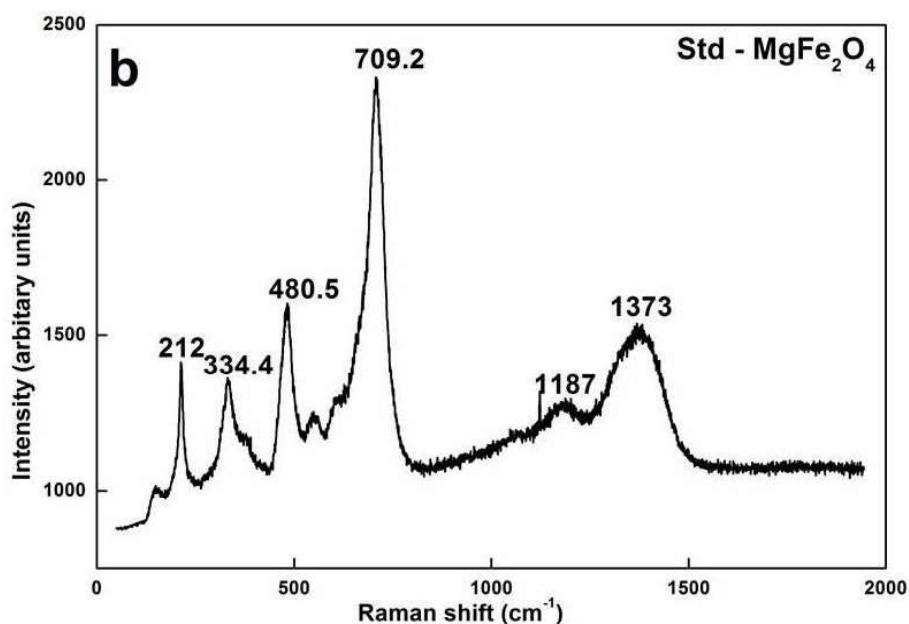


Figure 6.1(b): Raman spectrum of Standard MgFe₂O₄

6.2.2. X-Ray Diffraction Analysis

XRD pattern of synthesized MgFe₂O₄ and GI-XRD pattern of CS/Fe₃O₄/MgFe₂O₄ are shown in Figure 6.2 (a) and (b) respectively. The average crystallite size of the synthesized powder after considering all the prominent peaks were calculated to be 75 nm. An analysis of the XRD pattern revealed that the synthesized material exhibited the diffraction peaks that agreed with the international standard diffraction data card (ICDD.No.04-012-0915) and provided the evidence for MgFe₂O₄ formation. The most intense reflections observed at 2θ values are at 18.21, 29.85, 35.15, 36.8, 42.79, 53.14, 56.55, 62.08, 70.55, 73.49 and 74.55 degrees are assigned to (111), (220), (311), (222), (400), (422), (511), (440), (620), (533) and (622) planes of single phase cubic spinel structure. The findings above indicated that the synthesized material was crystalline. The calculated lattice parameter value was 8.44 which was close to the standard lattice parameter value (8.43) obtained from the

ICDD confirming that the synthesized powder was cubic in nature. No other impurity peak was observed. The space group of MgFe_2O_4 is $Fd\bar{3}m$ [144] similar to the other spinels.

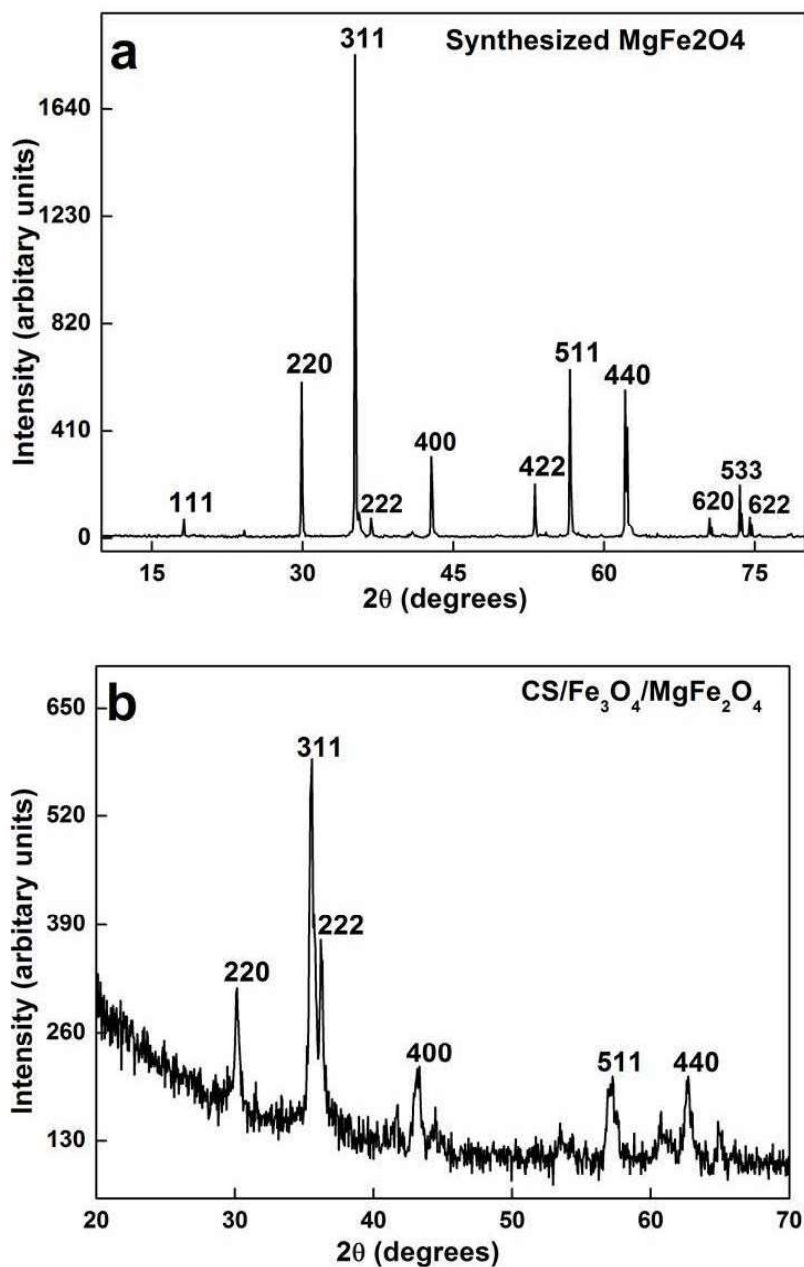


Figure 6.2: (a) XRD pattern of synthesized MgFe_2O_4 powder and (b) GI-XRD pattern of $\text{CS}/\text{Fe}_3\text{O}_4/\text{MgFe}_2\text{O}_4$

The GI-XRD pattern observed in Figure 6.2 (b) revealed well developed reflections of CS/Fe₃O₄/MgFe₂O₄. Strong Bragg reflections were seen in the XRD pattern with the characteristic peak corresponding to the (220), (311), (222), (400), (511) and (440) planes (ICDD.No.04-012-0909). It has face-centered cubic crystal structure with unit cell dimension 'a' = 8.37 Å. The average crystallite size calculated using Scherrer's formula was about 23 nm for the deposited MgFe₂O₄. Comparing the FWHM of the XRD pattern of synthesized MgFe₂O₄ and CS/Fe₃O₄/MgFe₂O₄ samples, it was apparent that deposited MgFe₂O₄ may have lower crystallite size as shown in Table 6.1. It could be seen that the values of FWHM relative to the mentioned planes for the deposited MgFe₂O₄ were greater than that for the synthesized MgFe₂O₄. This confirmed the contraction of the lattices of the deposited MgFe₂O₄ with subsequent decrease in their size.

Table 6.1: FWHM values from XRD pattern of synthesized and deposited MgFe₂O₄

Planes	FWHM	FWHM
(hkl)	Synthesized MgFe ₂ O ₄	Deposited MgFe ₂ O ₄
220	0.126	0.327
311	0.118	0.471
222	0.137	0.247
400	0.135	0.237
511	0.117	0.670
440	0.160	0.399

6.2.3. Scanning Electron Microscopic Analysis

The surface morphology of CS/Fe₃O₄/MgFe₂O₄ was studied by SEM and the micrograph is shown in Figure 6.3 (a) which showed that the coating was composed of uniform coarse structure with a well crystalline microstructure with non-porous and uniform shaped particles. The thickness measured by the cross section FE-SEM image was 1.13 μm as shown in Figure 6.3 (b). The elemental composition of the coating was investigated by EDAX as shown in Figure 6.3 (c) for CS/Fe₃O₄/MgFe₂O₄. The EDAX spectrum confirmed the presence of Mg, Fe and O in CS/Fe₃O₄/MgFe₂O₄. The atomic and weight percentages of MgFe₂O₄ are presented in Table 6.2 confirming the atomic ratio of Mg to Fe to be slightly less than 1:2.

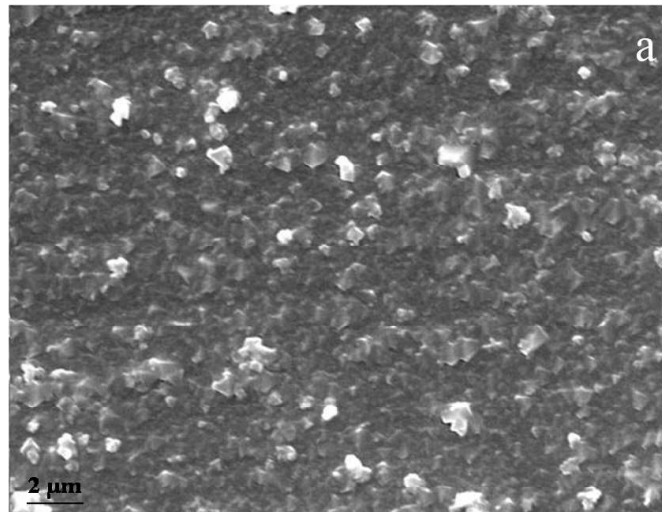


Figure 6.3: (a) SEM image of CS/Fe₃O₄/MgFe₂O₄

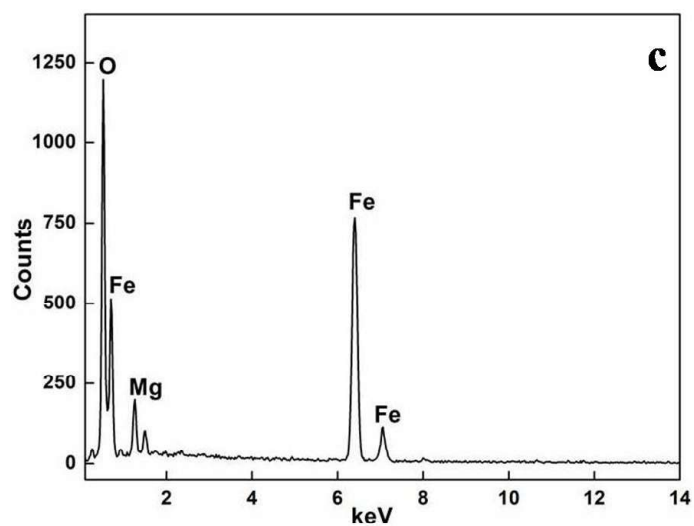
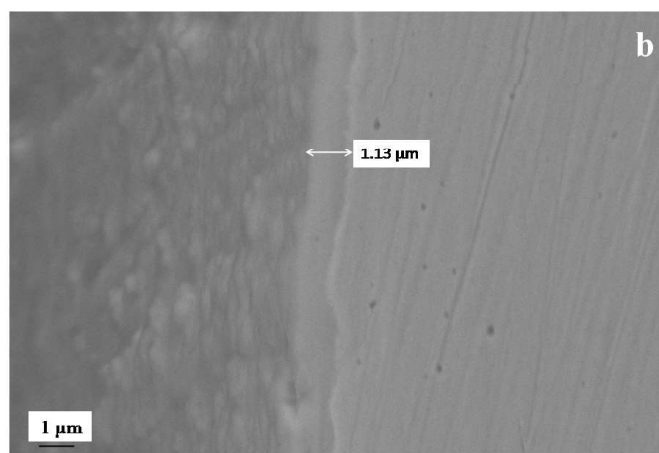


Figure 6.3: (b) Cross section FE-SEM image and (c) EDAX spectrum of CS/Fe₃O₄/MgFe₂O₄

Table 6.2: Elemental composition from EDAX analysis

Element	Series	CS/Fe ₃ O ₄ /MgFe ₂ O ₄	
		Weight %	Atomic %
Mg	K	10.54	12.21
Fe	K	57.84	29.16
O	K	31.62	58.63

6.2.4. X-Ray Photoelectron Spectroscopic Analysis

Mg 1s peak obtained from CS/Fe₃O₄/MgFe₂O₄ is shown in Figure 6.4 (a). The peak at around 1305 eV confirmed the formation of MgFe₂O₄ [145]. Mg 1s peak obtained from the MgFe₂O₄ deposited specimen was compared with the MgFe₂O₄ pellet used for the deposition process. The peak from the CS/Fe₃O₄/MgFe₂O₄ was broader compared to the MgFe₂O₄ pellet. MgFe₂O₄ has a mixed spinel structure and hence the binding energy of Mg 1s peak at around 1305 eV indicated the presence of Mg²⁺ in the octahedral site of the spinel lattice. The binding energy of Mg 1s peak associated with Mg²⁺ in tetrahedral site is around 1 eV [145] lower than that for the octahedral site. In the deposited specimen, the peak broadening was attributed to the presence of Mg²⁺ in both tetrahedral and octahedral sites of the lattice of the ferrite. Fe 2p photoelectron peaks obtained from CS/Fe₃O₄/MgFe₂O₄ are shown in Figure 6.4 (b). The binding energy values of Fe 2p_{3/2} and Fe 2p_{1/2} observed at 710.9 and 724.3 eV corresponded to Fe³⁺ state in CS/Fe₃O₄/MgFe₂O₄ specimen according to the literature [146]. Mg 2p along with Fe 3p obtained from the pellet and the deposited specimen are shown in Figure 6.4 (c). Mg 2p peak from CS/Fe₃O₄/MgFe₂O₄ was observed at 49.1 eV and Fe 3p peak at 56.1 eV respectively. These two peaks (Mg 2p and Fe 3p) are taken for finding the atomic composition of CS/Fe₃O₄/MgFe₂O₄. Relative atomic concentration of Mg and Fe in case of pellet is 31% and 69% respectively whereas in case of deposited specimen the atomic concentration of Mg and Fe was 21% and 79% respectively. The relative atomic concentration of Fe in the deposited specimen was more than the expected due to formation of Mg deficient ferrite. A single sharp peak observed for O 1s at

530.1 eV for the deposited specimen indicated that the oxygen atoms were in the O^{2-} form in the lattice as shown in Figure 6.4 (d). The concentration of oxygen present in the sample was slightly more than the expected value due to physisorbed oxygen on the sample surface.

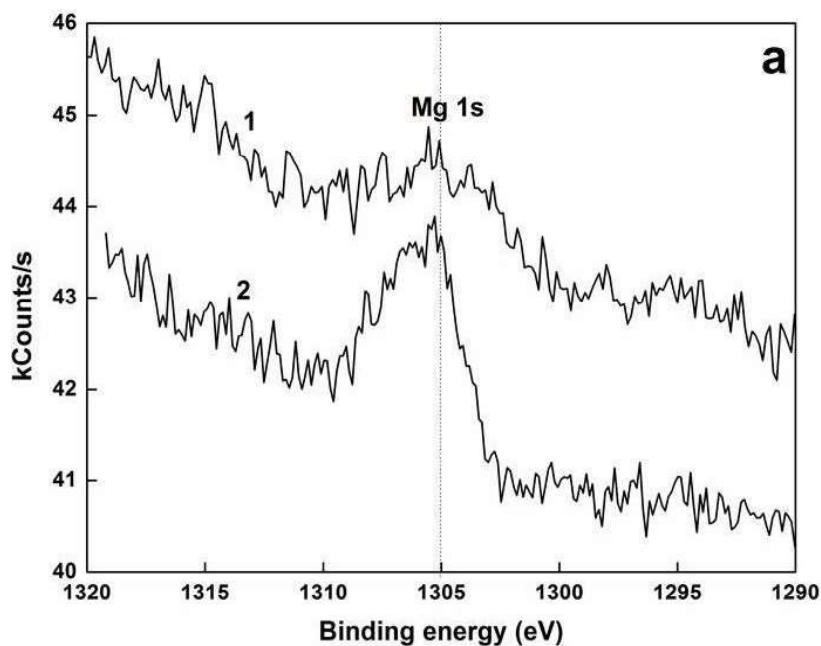


Figure 6.4 (a): XPS spectra of Mg 1s obtained from (1) CS/Fe₃O₄/MgFe₂O₄ and (2) MgFe₂O₄ pellet used for deposition

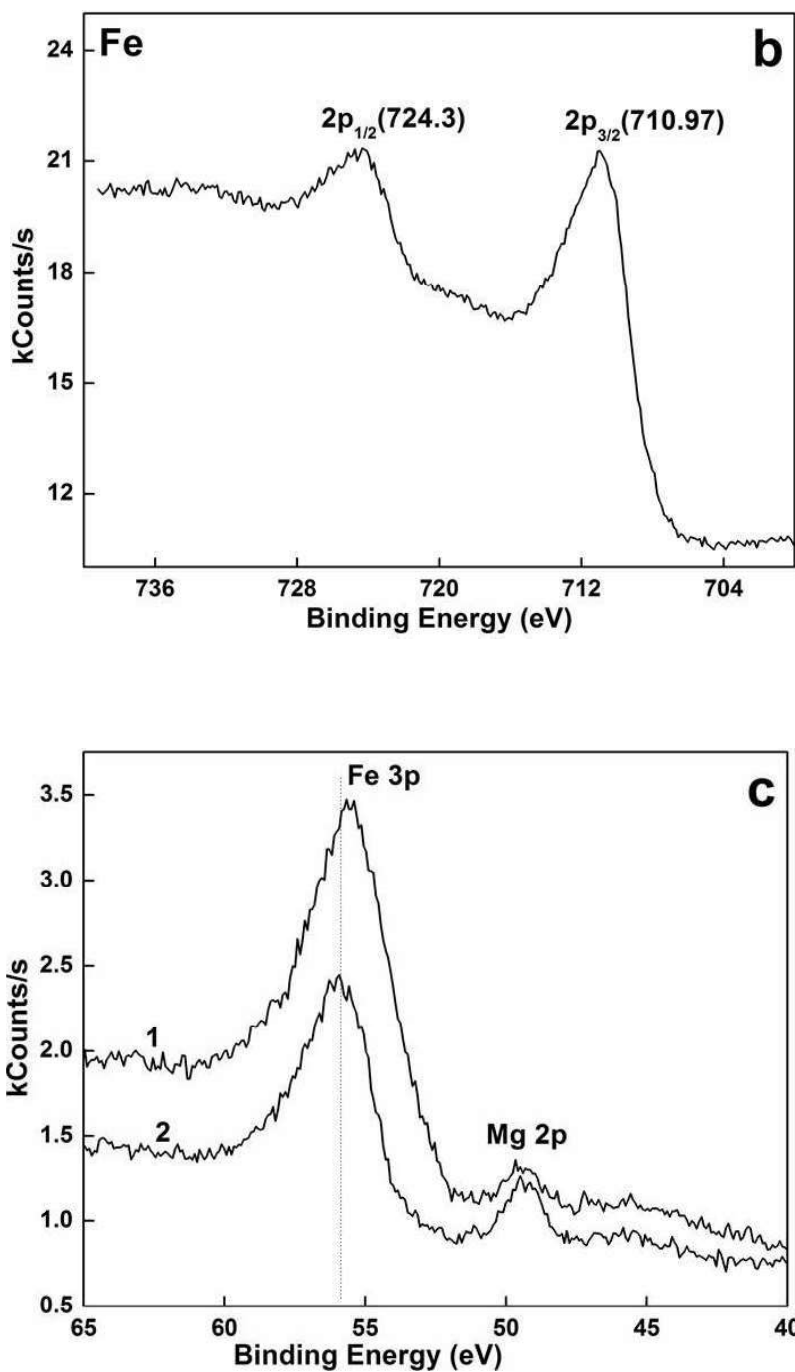


Figure 6.4: XPS spectra of (b) Fe 2p and (c) Mg 2p with Fe 3p peaks obtained from (1) CS/Fe₃O₄/MgFe₂O₄ and (2) MgFe₂O₄ pellet used for deposition

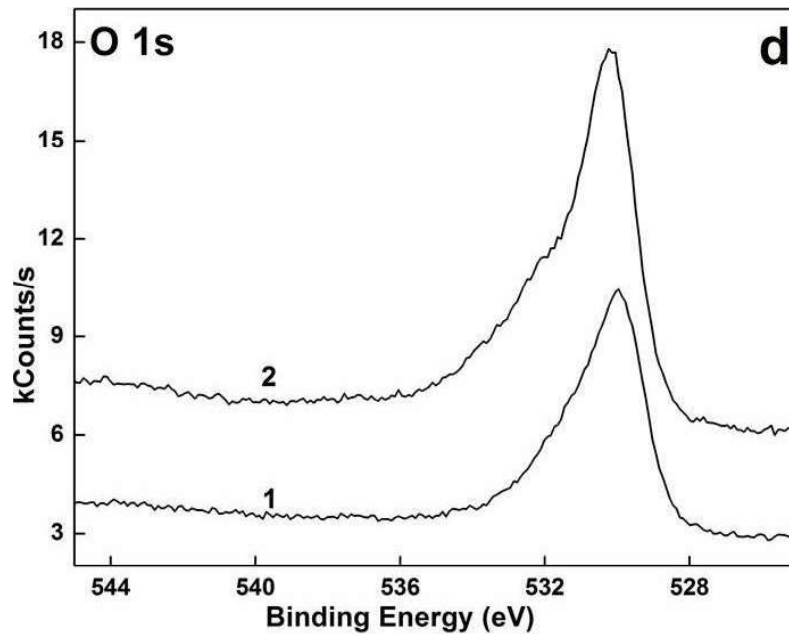


Figure 6.4 (d): XPS spectra of O 1s peaks obtained from (1) CS/Fe₃O₄/MgFe₂O₄ and (2) MgFe₂O₄ pellet used for deposition

6.2.5. Scratch Test

The friction coefficient, acoustic signal, penetration depth, normal load applied against scratch length is plotted along with SEM image of scratch performed on CS/Fe₃O₄/MgFe₂O₄ are as shown in the Figure 6.5. As the applied normal load increases during a scratch test, the coating undergoes failure resulting in the generation of elastic waves with increasing frequency and the severity of failure are detected and recorded by acoustic emission. Acoustic emission signal along with detailed SEM microscopic analysis of the coating gives information about the damage occurred on the coating. The fluctuations in the friction coefficient observed till 1 N load can be correlated with different mechanisms of energy dissipation with the change in contact conditions leading to deformation which saturated at around 0.14. A clear spallation of coatings from the surface explains that this coating is

brittle and poor in adhesion to the substrate. The first intense acoustic emission peak was observed at a load of 1.69 N and was attributed to the first critical failure of the film from the substrate. This was also confirmed by SEM analysis where adhesive failure was clearly seen at 1.69 mm of the scratch length.

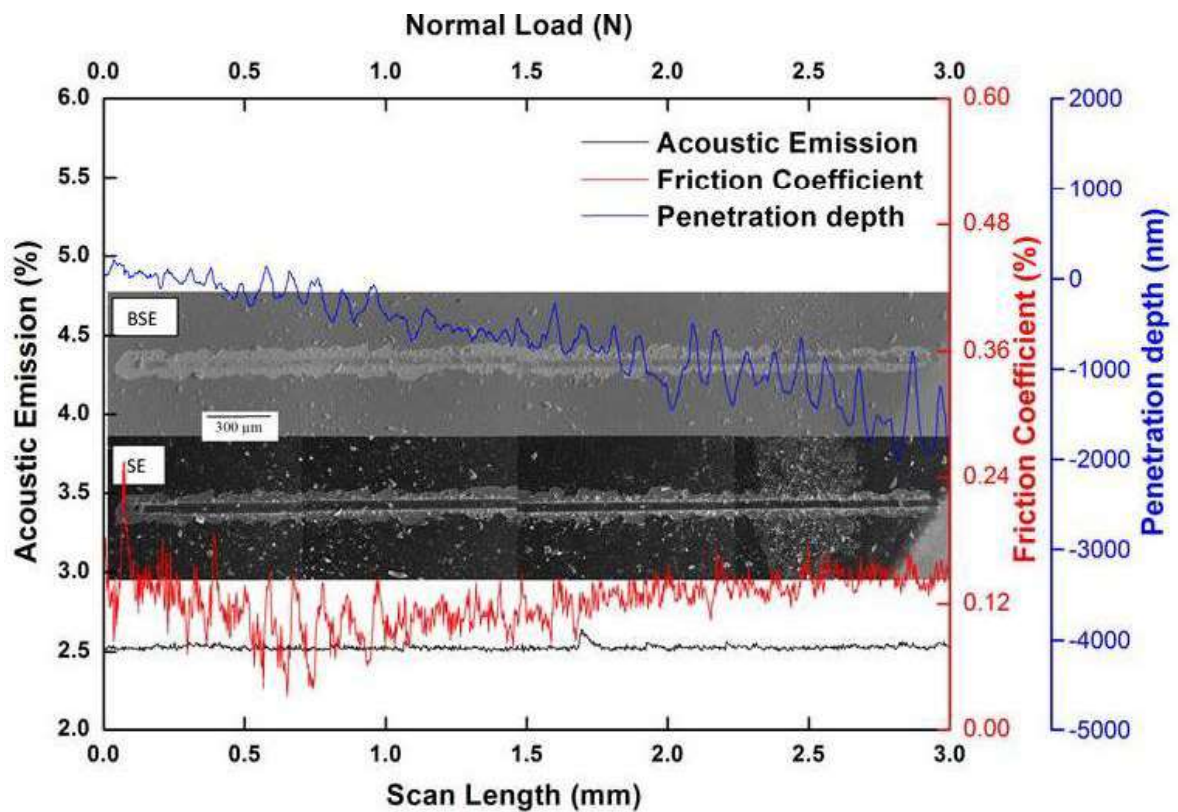


Figure 6.5: Scratch Test for CS/Fe₃O₄/MgFe₂O₄

6.2.6. Rutherford Backscattering Spectrometry

The thickness measurement for MgFe₂O₄ coating was carried out on silicon wafer by stylus profilometer. To confirm the thickness of the MgFe₂O₄ coating on CS/Fe₃O₄, RBS measurement was carried out [147]. RBS is a non-destructive and sensitive technique used to analyze the oxygen content in the coated film.

$^{16}\text{O}(\alpha,\alpha)^{16}\text{O}$ reaction with the resonant energy 3.045 MeV was used for oxygen analysis. From the RBS spectra, the signals scattered from Fe, present in the film as well as in substrate (as indicated in the spectra) and O are clearly seen. To check the oxygen content throughout the film, RBS spectra have been recorded with varying the incident alpha particle energy from 3.045 to 3.185 MeV (probing from surface to interior).

The thickness of the film was calculated as follows:

Stopping power (S) = 53.68 eV/Å (estimated from Stopping and Range of Ions in Matter (SRIM))

Thickness, $\Delta x = \Delta E/S$

$$= (573 \times 103) / 53.68 = 1067 \text{ nm}$$

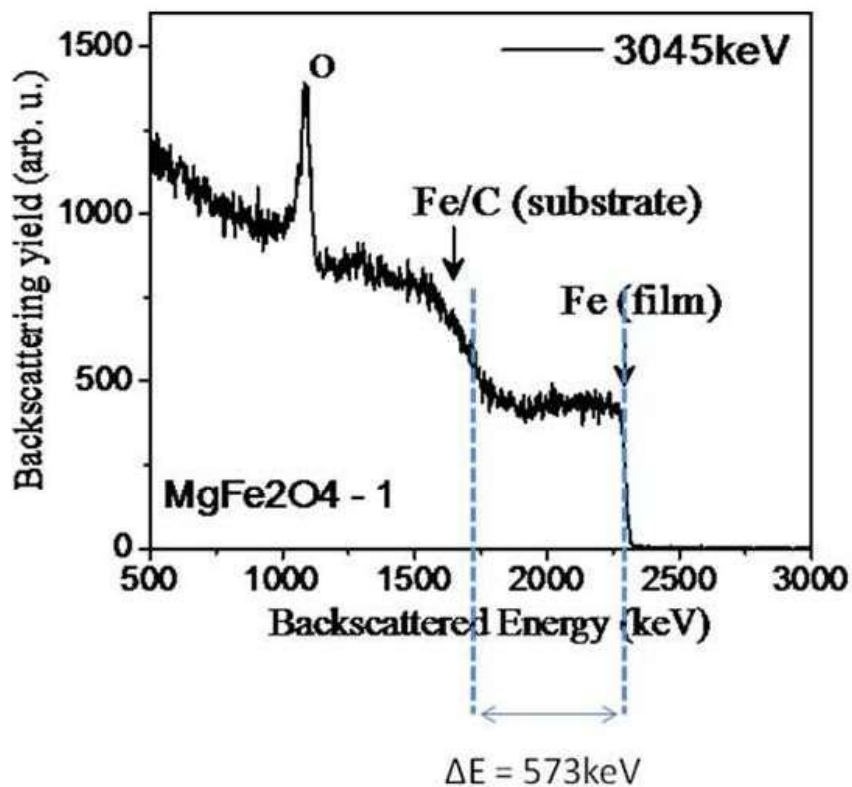


Figure 6.6: RBS spectrum for CS/Fe₃O₄/MgFe₂O₄

The calculated value 1067 nm was the thickness of the complete film over CS including Fe_3O_4 whose thickness was around 450 nm as mentioned in chapter 2 section 2.4.3 and the thickness of the MgFe_2O_4 coating was around 500 nm. Hence, the thickness of the film by PLD has been confirmed by RBS.

6.2.7. Electrochemical Characterization

6.2.7.1. *Electrochemical Impedance Spectroscopy*

The Nyquist and Bode diagrams for CS/ Fe_3O_4 / MgFe_2O_4 obtained at OCP using EIS in deaerated LiOH solutions at room temperature are shown in Figure 6.7 (a), (b) and (c) respectively. Existence of two semicircles in the Nyquist diagram (Inset Figure 6.7 (a)) indicated the formation of two time constants attributed to processes occurring near metal/film interface and film/solution interface for the uncoated CS and metal/oxide interface and oxide/solution interface for CS/ Fe_3O_4 and CS/ Fe_3O_4 / MgFe_2O_4 . The impedance parameter values obtained after the best fit are presented in Table 6.3. A high charge transfer resistance (R_2) was obtained in MgFe_2O_4 deposited on CS/ Fe_3O_4 indicating a better corrosion resistance. The resistance (R_1 and R_2) values followed the order: CS/ Fe_3O_4 / MgFe_2O_4 > CS/ Fe_3O_4 > CS and the constant phase element (Q_1 and Q_2) followed the order: CS/ Fe_3O_4 / MgFe_2O_4 < CS/ Fe_3O_4 < CS indicating that the deposited coating is protective. The Bode impedance spectra presented in Figure 6.7 (b) showed significant increase in the impedance modulus over the full frequency range, indicating an increase in corrosion resistance in case of CS/ Fe_3O_4 / MgFe_2O_4 but the

phase angle plot as shown in Figure 6.7 (c) was similar for both the coated specimens.

Table 6.3: Impedance parameters obtained from EIS analysis

Specimen	R ₁ (KΩ)	R ₂ (KΩ)	Q ₁ (μF)	n	R ₃ (KΩ)	Q ₂ (mF)	n
Uncoated CS	0.487	0.607	0.44	0.85	9.5	0.49	0.63
CS/Fe ₃ O ₄	0.543	0.801	0.97	0.79	191.2	0.19	0.85
CS/Fe ₃ O ₄ /MgFe ₂ O ₄	0.635	1.728	0.01	0.93	240.6	0.06	0.91

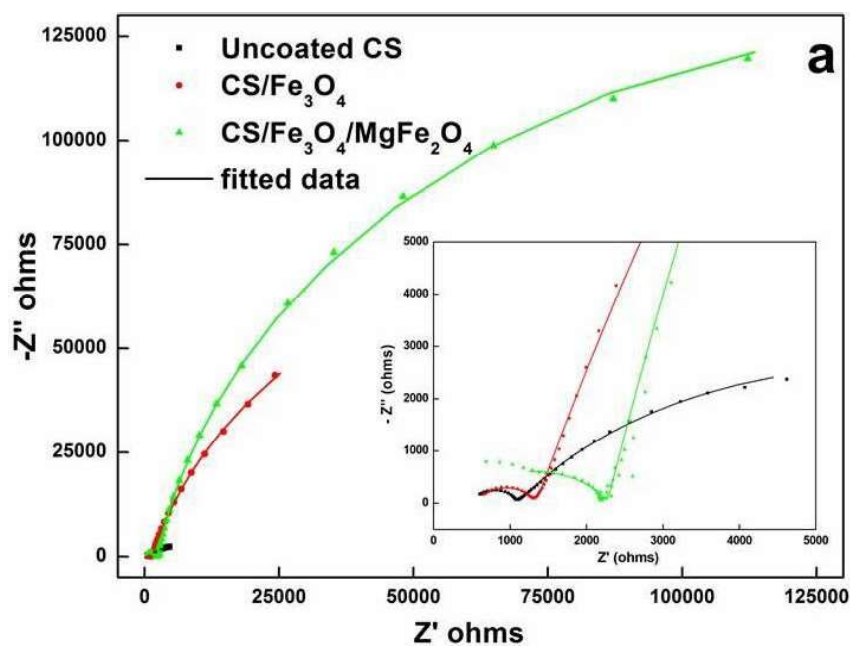


Figure 6.7 (a): Nyquist plot of uncoated CS, CS/Fe₃O₄ and CS/Fe₃O₄/MgFe₂O₄

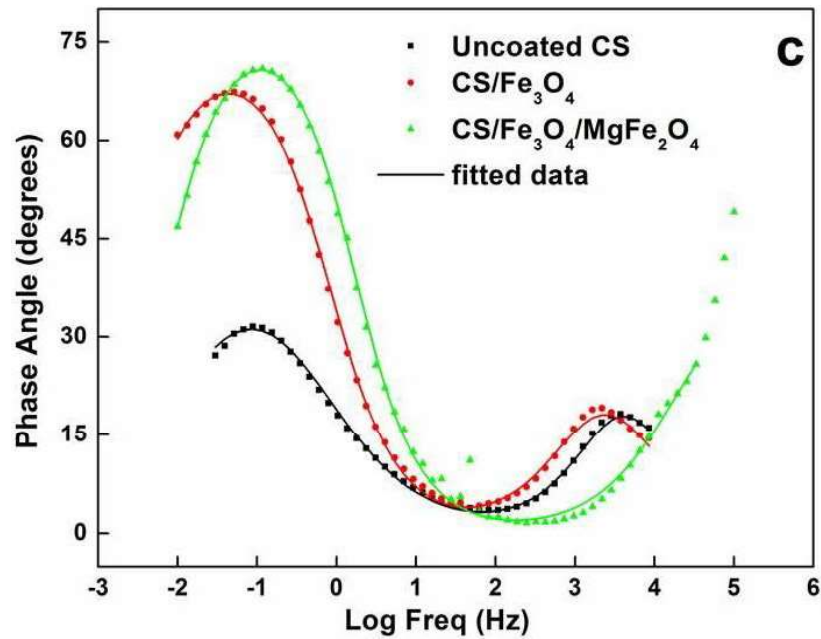
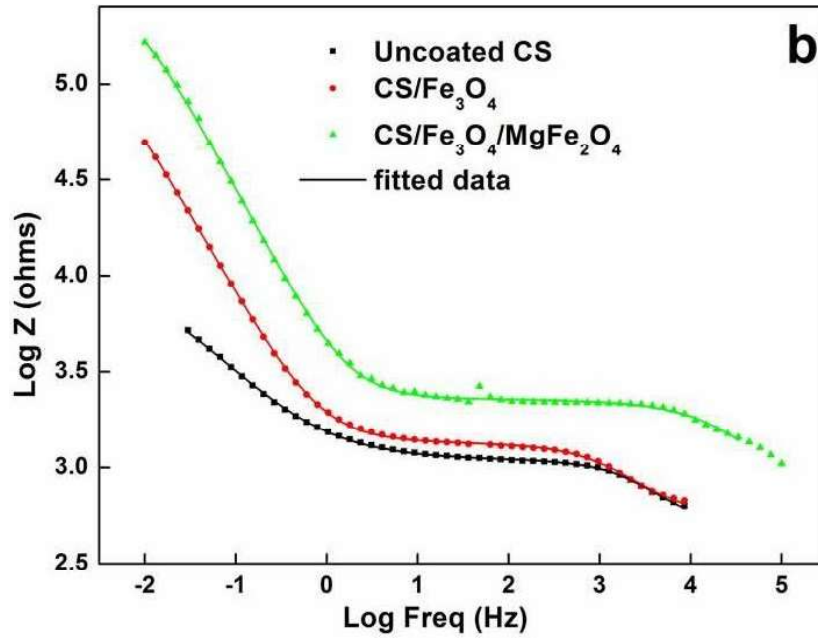


Figure 6.7: (b) Bode and (c) Phase angle plot of uncoated CS, CS/Fe₃O₄ and CS/Fe₃O₄/MgFe₂O₄

6.2.7.2. Potentiodynamic Anodic Polarization

Figure 6.8 shows the PDAP curves for CS, CS/Fe₃O₄ and CS/Fe₃O₄/MgFe₂O₄ in deaerated LiOH medium at room temperature. The corrosion parameters obtained from these measurements are given in Table 6.4. The OCP obtained for CS/Fe₃O₄/MgFe₂O₄ shifted towards the noble side (+0.197 V vs. SCE) compared to uncoated CS (-0.497 V vs. SCE) indicating the protective nature of the coating. A wider passive region was observed in the range of 0 to +0.8 V for CS/Fe₃O₄ and a narrower passive region (+0.25 to +0.5 V) for CS/Fe₃O₄/MgFe₂O₄. Based on the values of corrosion current, the corrosion resistance was found to be in the following order: CS/Fe₃O₄/MgFe₂O₄ > CS/Fe₃O₄ > CS. The corrosion rates were of same order for both the coatings but significantly lower compared to the uncoated CS. At more anodic potentials, the corrosion current was slightly higher in the case of CS/Fe₃O₄/MgFe₂O₄ when compared to CS/Fe₃O₄ which may be due to the instability of the coated magnesium ferrite. However, both the coatings provided protection for the uncoated CS specimen.

Table 6.4: Corrosion parameters obtained from PDAP analysis

Specimen	PDAP				
	b _c (V/dec)	b _a (V/dec)	OCP (V)	i _{corr} (μA/cm ²)	Corrosion Rate (mpy)
Uncoated CS	-0.236	0.283	-0.497	1.194	0.552
CS/Fe ₃ O ₄	-0.148	0.414	-0.424	0.219	0.101
CS/Fe ₃ O ₄ /MgFe ₂ O ₄	-0.202	0.307	0.197	0.137	0.060

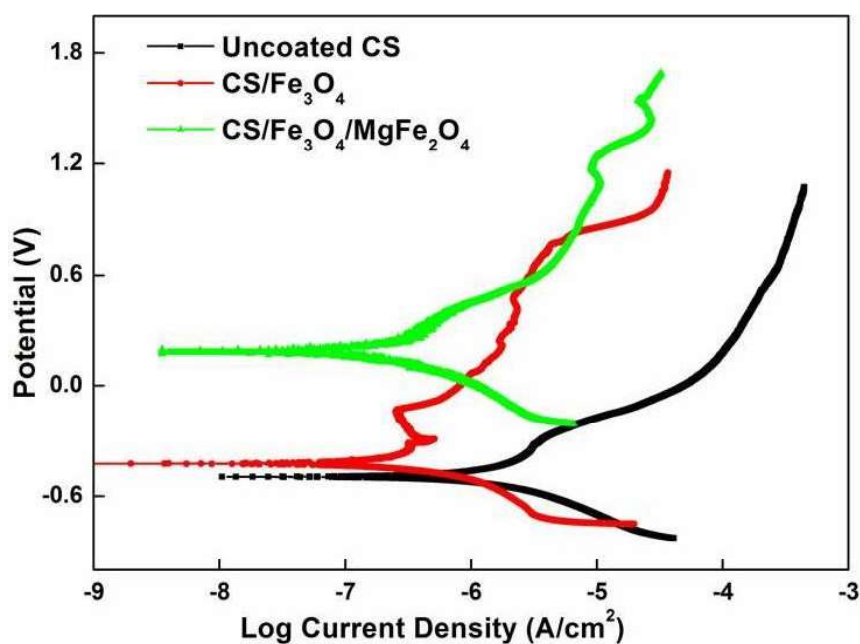


Figure 6.8: PDAP plots for uncoated CS, CS/Fe₃O₄ and CS/Fe₃O₄/MgFe₂O₄

6.2.7.3. Semiconducting properties of the oxide film

Mott-Schottky plots of the coated specimens acquired at 100Hz in 1.5 ppm LiOH solution (pH 10.2) at room temperature are shown in Figure 6.9. The oxide coated specimens were found to follow Mott-Schottky relationship at a certain potential range. The curves obtained for CS/Fe₃O₄ and CS/Fe₃O₄/MgFe₂O₄ presents a positive slope from -0.13 V_{SCE} upward to more anodic potentials. The flat band potential was ~-0.13 V for the coated specimen. This variation of the capacitance⁻² with the applied potential is typical of an n-type semiconductor and the main defects in the oxide film are cation interstitials or anion vacancies (oxygen) acting as electron donors [112].

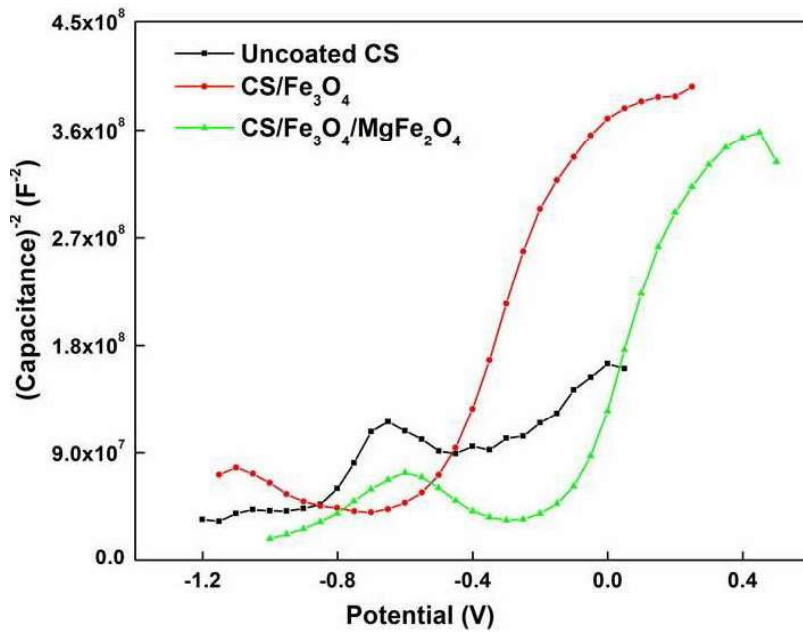


Figure 6.9: Mott-Schottky plots for CS, CS/Fe₃O₄ and CS/Fe₃O₄/MgFe₂O₄

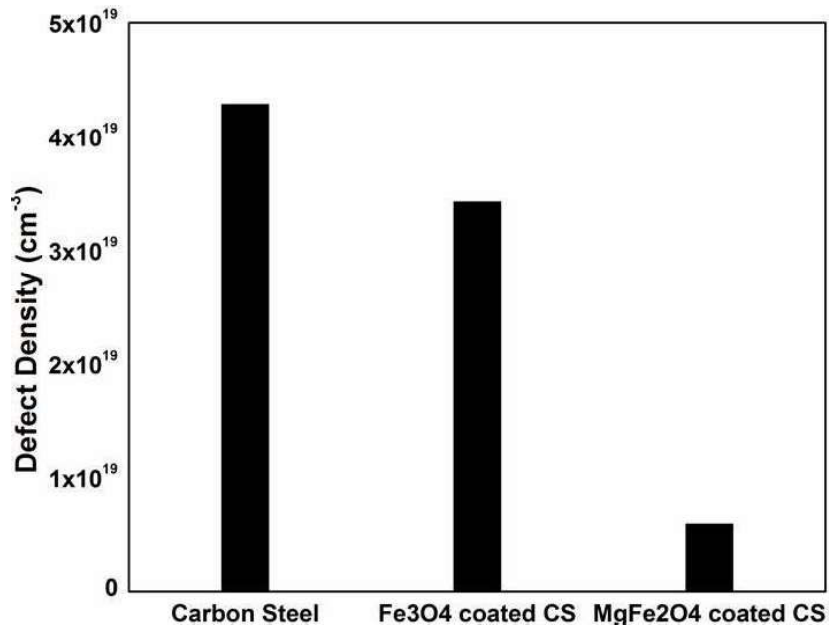


Figure 6.10: Defect Density graph for uncoated CS, CS/Fe₃O₄ and CS/Fe₃O₄/MgFe₂O₄

The defect densities were calculated from the slope of the linear portion of the Mott-Schottky plots. This concentration corresponds to the number of defects in the film.

A high doping density is typical of a defective oxide layer which, in turn, is associated with a lower corrosion resistance [85]. The charge carrier concentrations corresponding to uncoated and coated specimens are shown in Figure 6.10. The calculated defect density was similar for uncoated and CS/Fe₃O₄ and lower for CS/Fe₃O₄/MgFe₂O₄. The reduction in number of defects points to the formation of a more protective oxide layer. This result confirms the increase in corrosion resistance for MgFe₂O₄ coated on CS/Fe₃O₄ as observed from the AC and DC techniques.

6.3. Conclusion

A thin film of nano size MgFe₂O₄ developed on CS/Fe₃O₄ by PLD technique protected the base metal (CS). XRD analysis of the film confirmed the formation of spinel structure. Based on the measured relative atomic ratio of Mg and Fe on the film, XPS studies determined the chemical composition of MgFe₂O₄. The SEM micrograph of the coated film showed uniform coverage on the surface. AC impedance measurements of the coating showed increase in corrosion resistance property of MgFe₂O₄ coated on CS/Fe₃O₄ when compared to CS/Fe₃O₄ and uncoated CS. DC polarization measurements of the coating showed similarity in corrosion rate values for CS/Fe₃O₄/MgFe₂O₄ and CS/Fe₃O₄ when compared to uncoated CS. Mott-Schottky analysis showed that the defect density was less for CS/Fe₃O₄/MgFe₂O₄ indicating improvement in the corrosion resistance. Scratch test indicated that this coating was poor in adhesion with the substrate.

Part II: MgFe₂O₄ film formation by hydrothermal method

6.4. Introduction

Ferrites like magnetite and nickel ferrite dominate the corrosion product oxide inventory and play a major role in the activity transport process. To know the effect of Mg²⁺ ions during the formation of oxides on the corrosion behavior, this work was carried out. Hence, attempts were made to incorporate Mg²⁺ ions into the magnetite lattice during its formation by hydrothermal method for 24, 96 and 240 hours and the oxide formed was characterized by Raman, XRD, XPS and SEM measurements. The corrosion resistance of these oxides were studied by EIS and PDAP and the electronic properties by Mott-Schottky measurements in aqueous LiOH.

6.5. Results and Discussion

6.5.1. Cation concentration and thickness measurement

The magnesium and iron ion concentrations in the autoclave solution measured after the exposure experiments are as given in Figure 6.11 (a). 1000 ppb Mg²⁺ ion concentration was taken at the start of the experiment. The decrease in the concentration of magnesium in the autoclave solution reflects the transport of the magnesium from solution to the CS specimen. The thickness of the oxides was measured by Clarke's method and Figure 6.11 (b) shows the oxide film growth on the CS surface which followed a parabolic path.

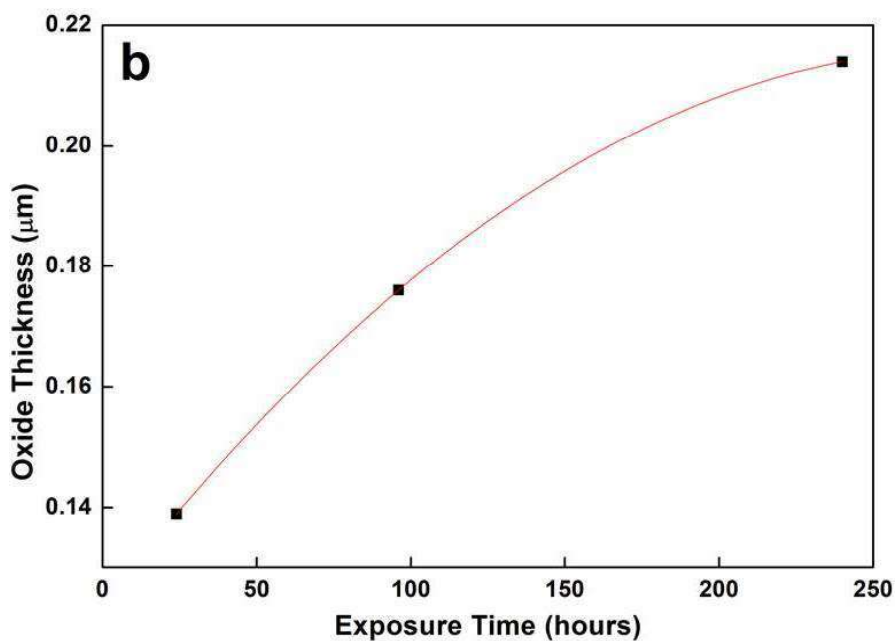
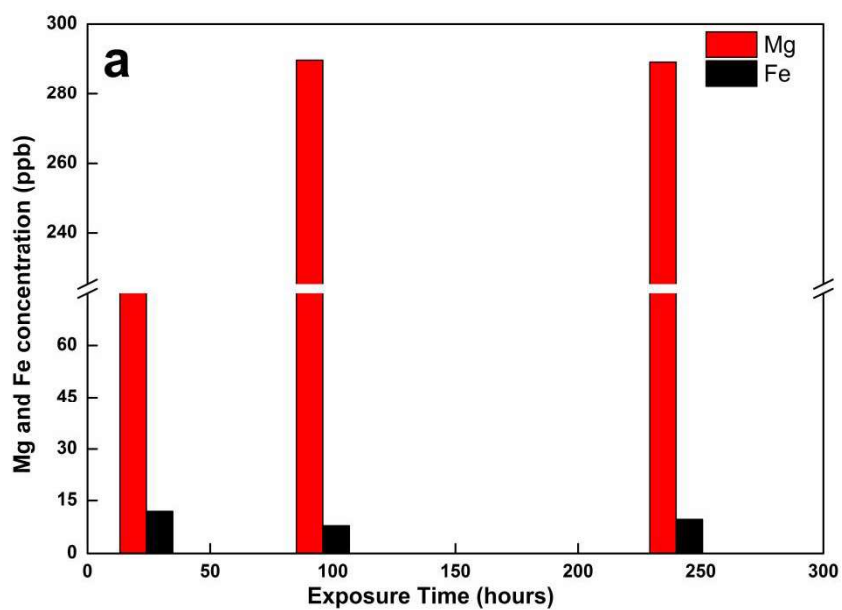


Figure 6.11: (a) Magnesium and Iron concentration and (b) oxide film thickness at the end of different exposure time

6.5.2. Surface characterization of oxides

6.5.2.1. X-Ray Diffraction Analysis

Figure 6.12 shows the GI-XRD patterns of the oxide films formed on CS exposed to LiOH and Mg^{2+} for different time duration at 250 °C. Characteristic peaks for the oxides formed in 24, 96 and 240 hours suggested the formation of spinel structure.

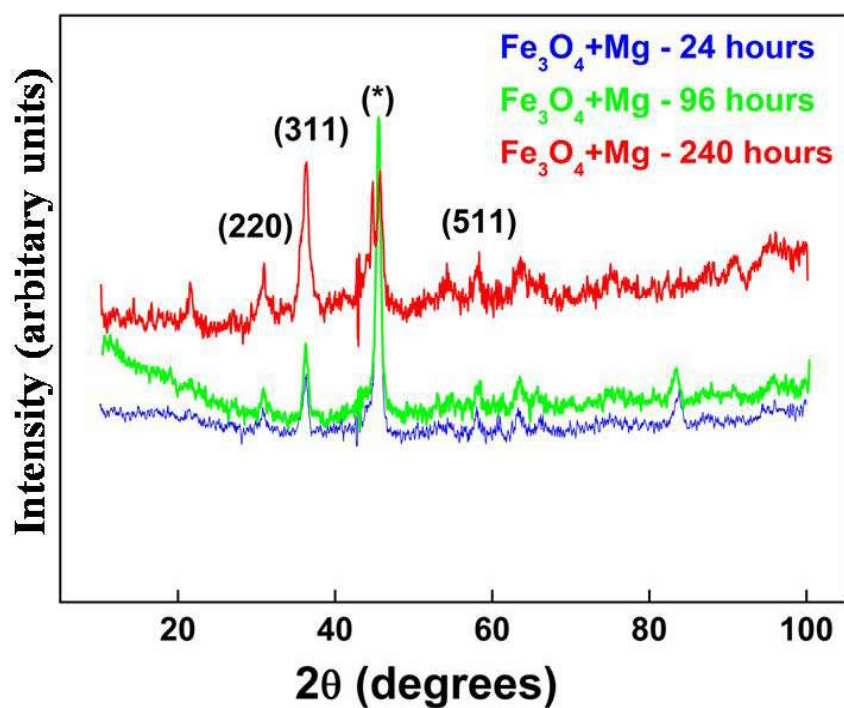


Figure 6.12: GI-XRD patterns of the oxide formed on CS exposed to 250 °C in presence of Mg^{2+} for 24, 96 and 240 hours

Table 6.5: Crystallite size and Lattice parameter obtained from GI-XRD

	Exposure Time	Crystallite size (nm)	Lattice Parameter (Å°)
$\text{Fe}_3\text{O}_4 + \text{Mg}^{2+}$	24 hours	10.2	8.586
	96 hours	11.5	8.656
	240 hours	10.8	8.614

The GI-XRD pattern showed that the formed spinel consisted entirely of crystalline MgFe_2O_4 having preferred orientation along (311) plane and its intensity increased with increase in exposure time and were compared with the standard data of cubic MgFe_2O_4 from the database (ICDD. No. 04-012-0909). Lattice parameter for the oxide films were 8.58, 8.65 and 8.61 for 24, 96 and 240 hours exposed specimens suggesting the incorporation of magnesium into the magnetite lattice. The crystallite size and the lattice parameter of all the oxides formed were estimated from the FWHM using Scherrer's equation and are given in the Table 6.5. Additional peak of base material marked as '*' was observed in the GI-XRD pattern at 45.5° . As explained in chapter 5 section 5.5.2.1, similar observations for MgFe_2O_4 with small peaks marked as '#' were seen at 21.5° , 54° , 63.57° and 83° due to the formation of $\text{FeO}(\text{OH})$ which is the intermediate layer in the Fe_3O_4 formation.

6.5.2.2. Scanning Electron Microscopic Analysis

Figure 6.13 shows the SEM morphologies of the oxide films formed on CS exposed to 250°C in LiOH and Mg^{2+} for different time duration. The surface of the specimen was covered with uniform shaped oxide particles. Crystal formation was not clear in

24 hours exposed specimen whereas in 96 and 240 hours the crystal formation was complete with different crystallite sizes.

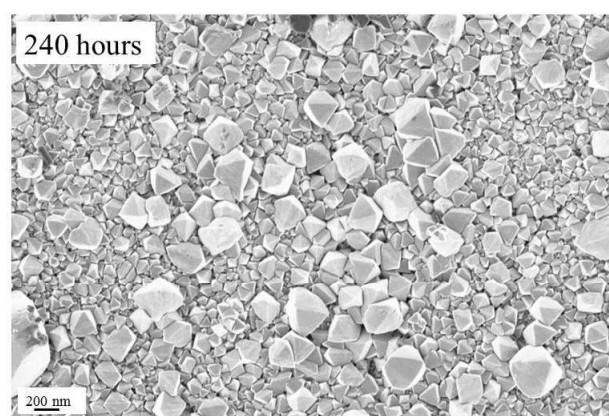
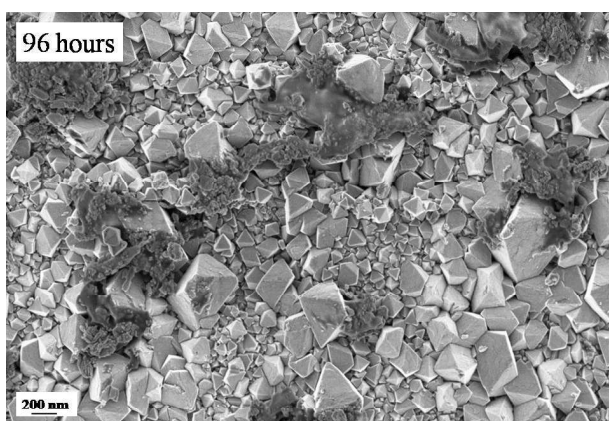
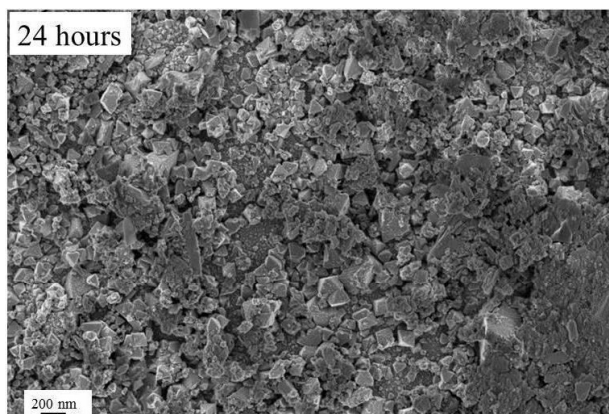


Figure 6.13: FE-SEM images of CS exposed in LiOH and Mg²⁺ ions

6.5.2.3. X-Ray Photoelectron Spectroscopic Analysis

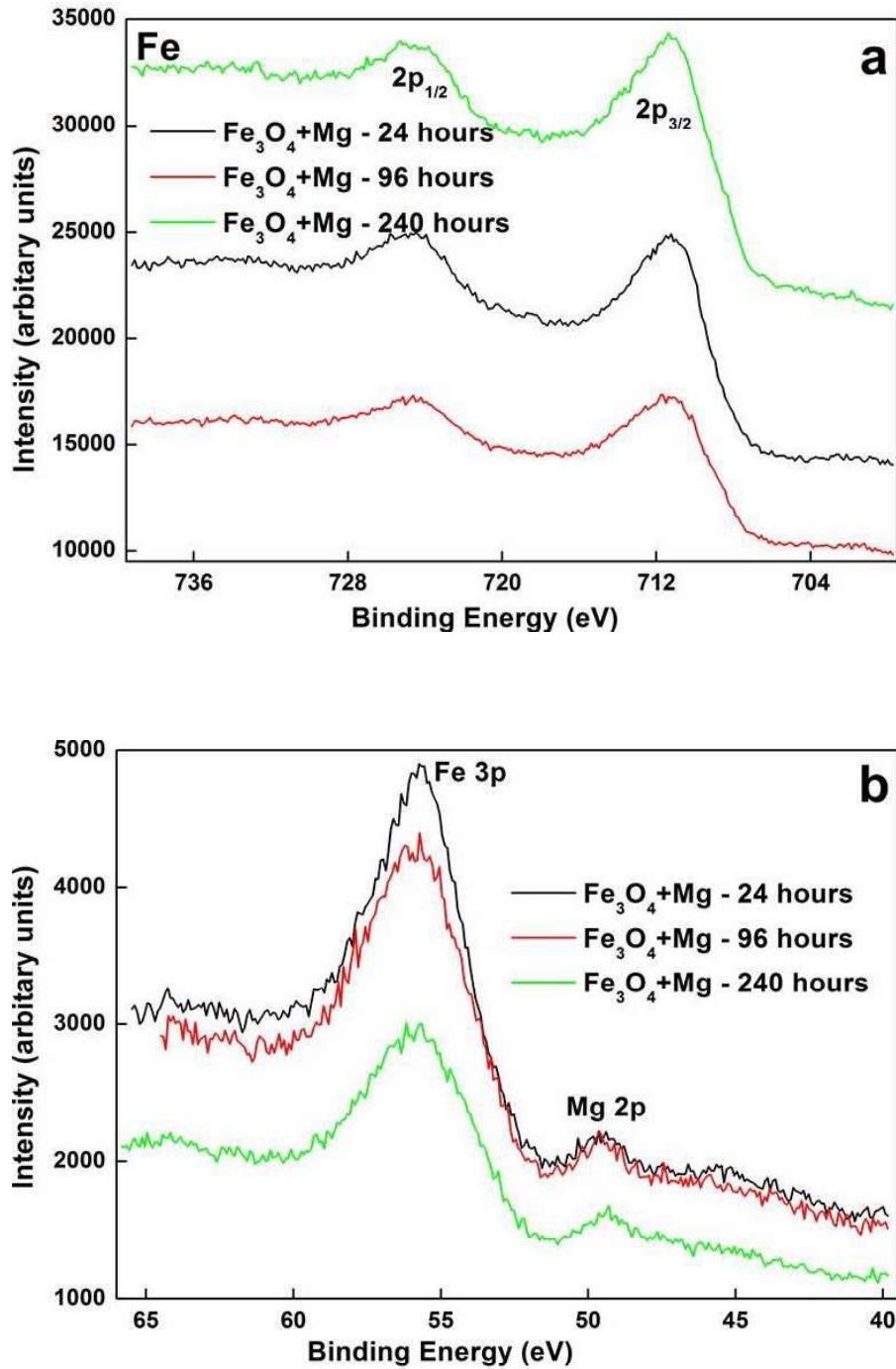


Figure 6.14: XPS spectra of (a) Fe 2p and (b) Mg 2p obtained for CS in presence of Mg²⁺ ions

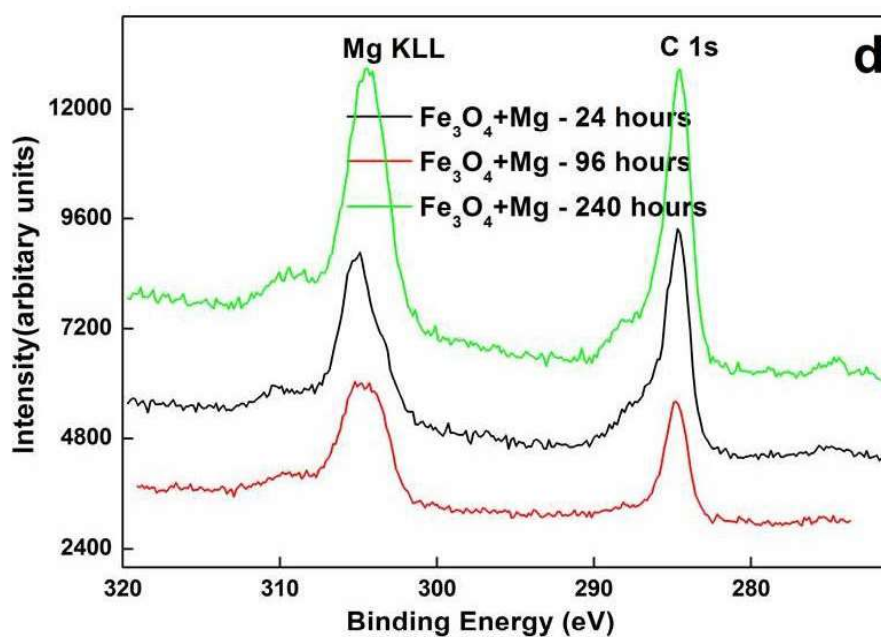
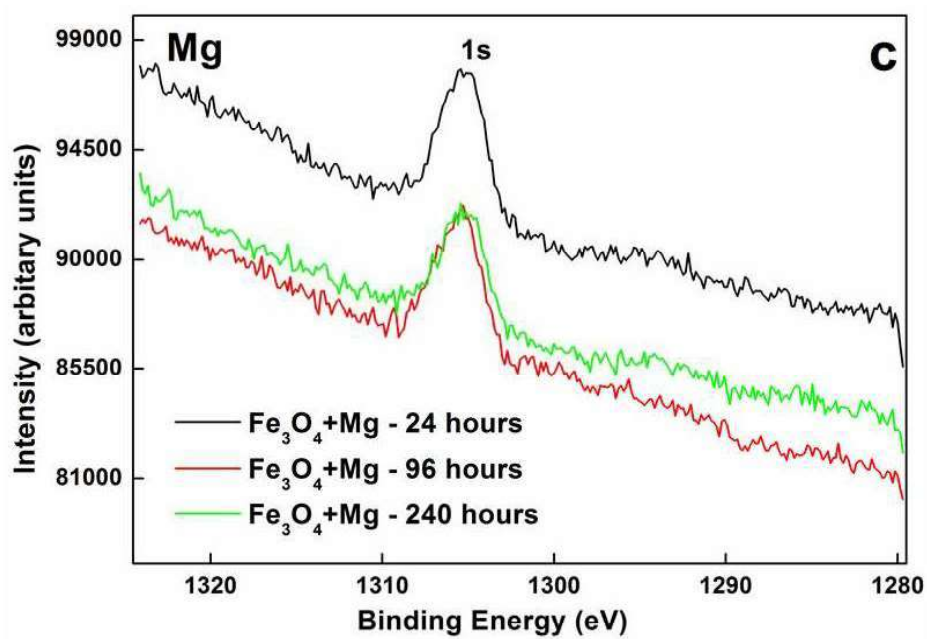


Figure 6.14: XPS spectra of (c) Mg 1s and (d) Mg KLL Auger and C peaks obtained for CS in presence of Mg^{2+} ions

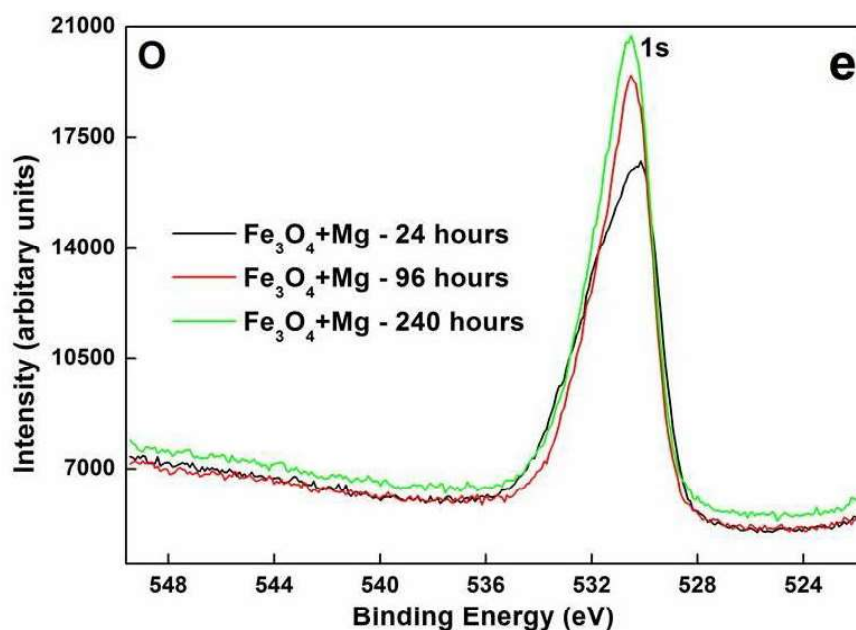


Figure 6.14 (e): XPS spectra of O 1s peaks obtained for CS in presence of Mg²⁺ ions

XPS spectra of (a) Fe 2p, (b) Mg 2p, (c) Mg 1s, (d) Mg KLL and C and (e) O 1s peaks obtained for CS in presence of Mg²⁺ ions exposed for 24, 96 and 240 hours are as shown in Fig. 6.14. Fe 2p_{3/2} and 2p_{1/2} photoelectron peaks were formed in the range 711.4-711.6 and 724.5-724.6 respectively for all the 3 oxide samples as shown in Figure 6.14 (a). Mg 2p peak from the oxide formed on CS was observed at around 49.2 eV and Mg 1s was observed at 1305.5 eV as indicated in Figure 6.14 (b) and (c) respectively. Mg KLL Auger peak along with C 1s peak is shown in Figure 6.14 (d) indicated the incorporation of significant amount Mg²⁺ into the oxide lattice. Only one peak was observed for O 1s at 530.7 eV for all the specimens indicating that the oxygen atoms are in the O²⁻ form in the lattice. From the above XRD and XPS analyses, it was clear that the oxide grown on the CS sample was composed of MgFe₂O₄ only. The binding energy values and the quantification of the oxides

formed at different exposure time are given in Table 6.6 which showed that the % of the Mg^{2+} remained same for the 96 and 240 hours. The stoichiometric ratio of Mg:Fe was observed to be 1:2 only in case of 24 hours exposed specimen.

Table 6.6: Binding Energy and Quantification of the elements by XPS

Exposure Time (hours)	Fe		Mg		O	
	Binding Energy (eV)	(%)	Binding Energy (eV)	(%)	Binding Energy (eV)	(%)
24	711.5	16	1305.5	8	530.6	76
96	711.6	17	1305.7	6	530.7	77
240	711.4	14	1305.5	6	530.7	80

6.5.2.4. Laser Raman Spectroscopic Analysis

Figure 6.15 shows the Raman spectra of the oxide films formed on CS exposed to 250 °C LiOH and 1000 ppb Mg^{2+} as function of exposure time i.e., (a) 24, (b) 96 and (c) 240 hours and the vibrational modes are as given in Table 6.7. The data fitting for the oxide formed on CS in absence and presence of magnesium showed four phonon modes. The oxide formed in presence of magnesium showed four peak maxima, with highest vibrational energy mode shift to higher wave numbers compared to the oxide formed in absence of magnesium. The mass difference between the two ions (Mg^{2+} and Fe^{3+}) shifts the A_{1g} mode of the lightest ion Mg^{2+} to higher wave number (680 - 683 cm^{-1}) and the heaviest ion Fe^{3+} to lower wave number 672 cm^{-1} . The changes in relative peak intensity and peak position in the oxides formed may be due to the incorporation of Mg^{2+} ions into the magnetite

lattice. Further, the Raman frequency depends on the Fe(Mg)-O and bond length. MgFe₂O₄ may be characterized as a mixture of normal and inverse spinel ferrite. The Raman shift for A_{1g} peak did not change significantly with exposure time in presence of magnesium ions.

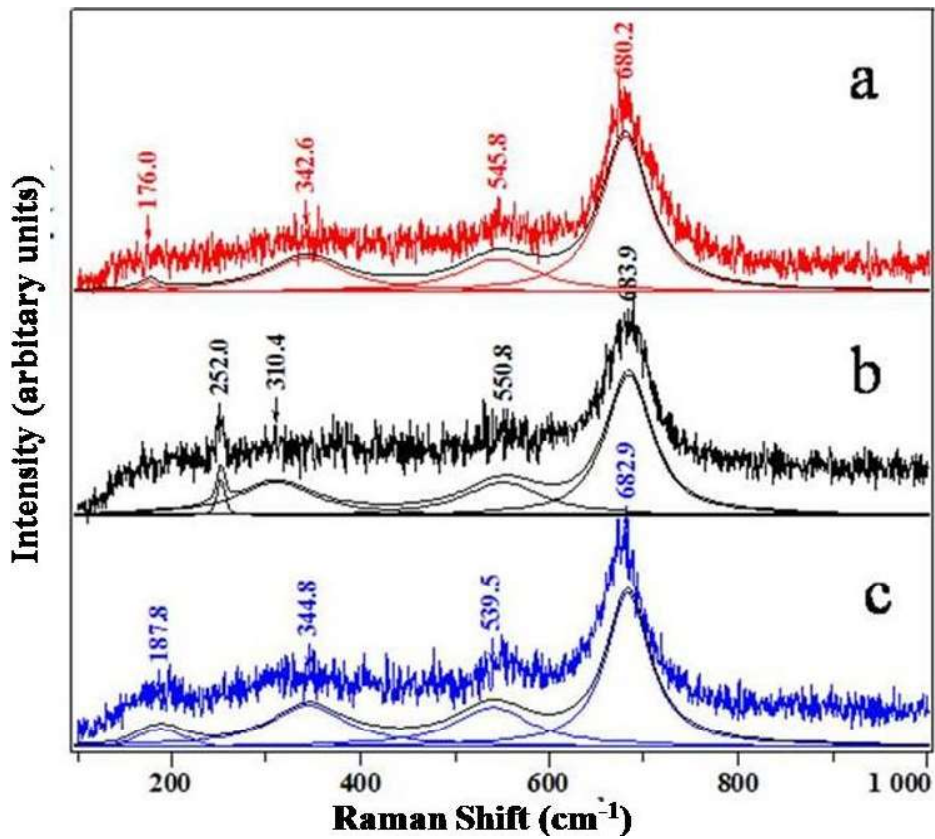


Figure 6.15 : Raman spectrum of the oxide films formed on CS at 250 °C in LiOH in presence of Mg²⁺ exposed for (a) 24, (b) 96 and (c) 240 hours

Table 6.7: Vibrational modes obtained for the oxides from Raman analysis

Raman mode	A _{1g}	T _{2g} (1)	T _{2g} (2)	E _g	T _{2g} (3)
Fe ₃ O ₄	672.6	551.2	-	323.9	187.0
MgFe ₂ O ₄ - 24 hours	680.2	545.8	-	342.6	176.0
MgFe ₂ O ₄ - 96 hours	683.9	550.8	-	310.4	252.0
MgFe ₂ O ₄ - 240 hours	682.9	539.5	-	344.8	187.8

6.5.3. Electrochemical Characterization

6.5.3.1. Potentiodynamic Anodic Polarization

Figure 6.16 shows the PDAP curve for uncoated CS and the oxides formed in presence of Mg²⁺ ions for 24, 96 and 240 hours in deaerated LiOH aqueous medium at 28 °C. The corrosion parameters obtained from these measurements are tabulated in Table 6.8.

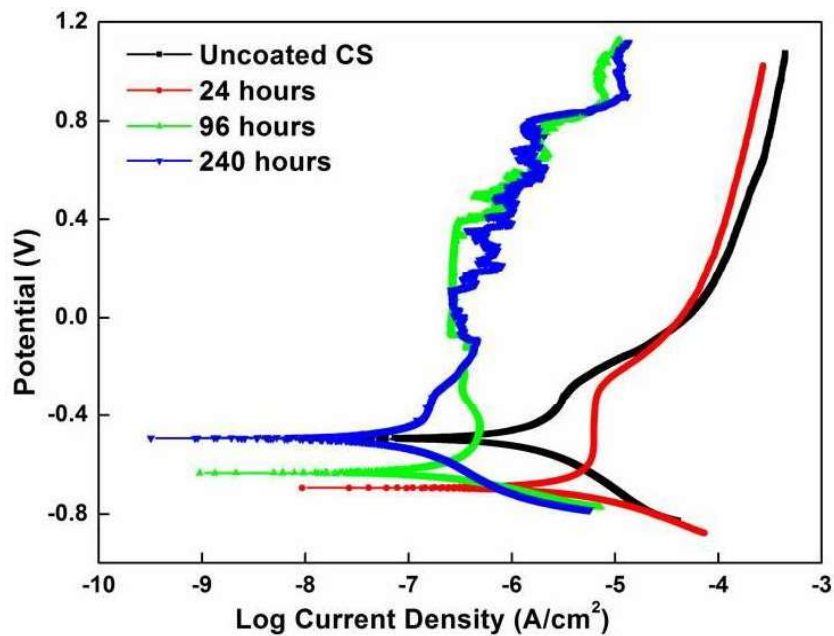


Figure 6.16: PDAP plot of CS exposed to 24, 96 and 240 hours in LiOH and

Mg²⁺

Table 6.8: Corrosion parameters for different exposure time in LiOH and Mg²⁺ ions

Specimen	PDAP				
	b _c (V/dec)	b _a (V/dec)	OCP (V)	i _{corr} (μA/cm ²)	Corrosion Rate (mpy)
Uncoated CS	-0.236	0.283	-0.497	1.194	0.552
24 hours	-0.117	0.309	-0.719	1.847	0.854
96 hours	-0.094	0.416	-0.634	0.216	0.099
240 hours	-0.198	0.312	-0.493	0.076	0.035

The OCP for the oxides in presence of Mg²⁺ ions for 24 and 96 hours duration shifted towards the active side (-0.719 V and -0.634 V respectively vs. SCE) compared to uncoated CS (-0.497 V vs. SCE) indicating that the dissolution of the base metal was more compared to the formation of the film. The OCP, in the case of 240 hours exposed CS (-0.493 V vs. SCE) was similar to the uncoated CS. The current densities for the oxides formed in 96 and 240 hours exposure were lower than that for uncoated CS. The passive region was observed in the range -0.3 to 0.8 V for 96 and 240 hours exposed CS whereas it was narrower with higher passive current density in the case of 24 hours exposed CS. Based on the values of corrosion current, the corrosion resistance was found to be in the following order: 24 hours < CS < 96 hours < 240 hours. Though the film formed in the case of 96 and 240 hours duration showed a lower passive current density compared to the uncoated CS, the passive film was not stable.

6.5.3.2. Electrochemical Impedance Spectroscopy

Figure 6.17 shows the EIS spectra for uncoated CS and the oxides formed in presence of Mg^{2+} ions for 24, 96 and 240 hours in deaerated LiOH aqueous medium at 28 °C. Oxides formed showed two time constants as observed from the Nyquist plots at different frequency ranges which may be due to the two processes taking place in the system. Oxide formed in the case of 96 and 240 hours exposure showed increased capacitive loop as observed from the Figure 6.17 (c) which could be related to increase in protectiveness of the oxide. The EIS Bode spectra (Figure 6.17 (b)) showed that magnesium ferrite formed at different exposure time behaved inhibitably. The impedance modulus at low-frequency region increased with increase in exposure time. This behavior could be attributed to the formation of a layer at the bottom of the pores on the CS surface. In order to evaluate oxide coating performance, the low-frequency impedance modulus values obtained at 0.01 Hz ($|Z|_{0.01 \text{ Hz}}$) were used to estimate the resistance of the coating [122] as given in Table 6.10. The Bode impedance values observed at low frequency region followed the order: 24 hours < CS < 96 hours < 240 hours. It was observed from Table 6.9 that the polarization resistance (R_1+R_2) increased from 13.5 k Ω to 166 k Ω and coating capacitance decreased from 1.14×10^{-3} F/cm² to 0.18×10^{-3} F/cm² with increase in the exposure time suggesting that the thickening of the oxide film improved the film passivity. Figure 6.18 gives the trend of the corrosion rate and polarization resistance in the absence and presence of magnesium ions. Ferrite formation for longer exposure times reached a saturation value.

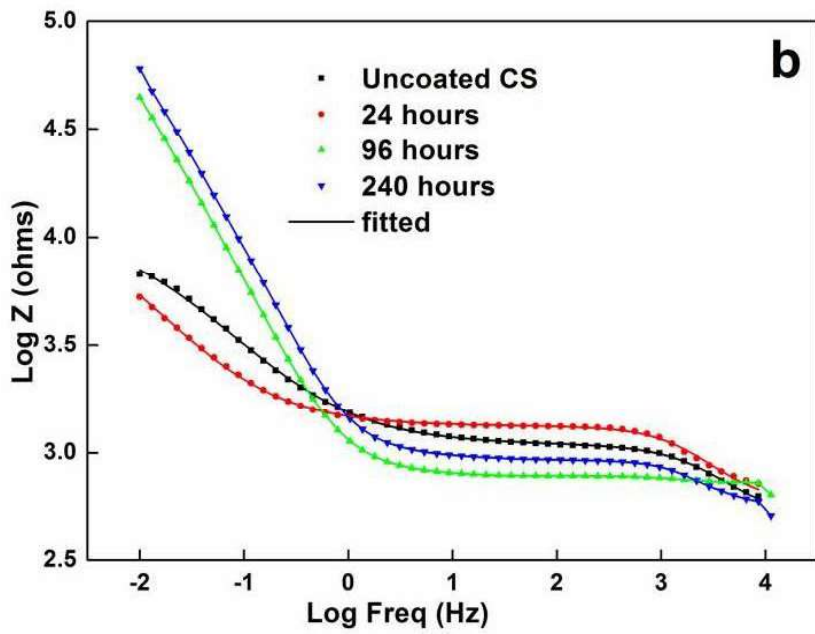
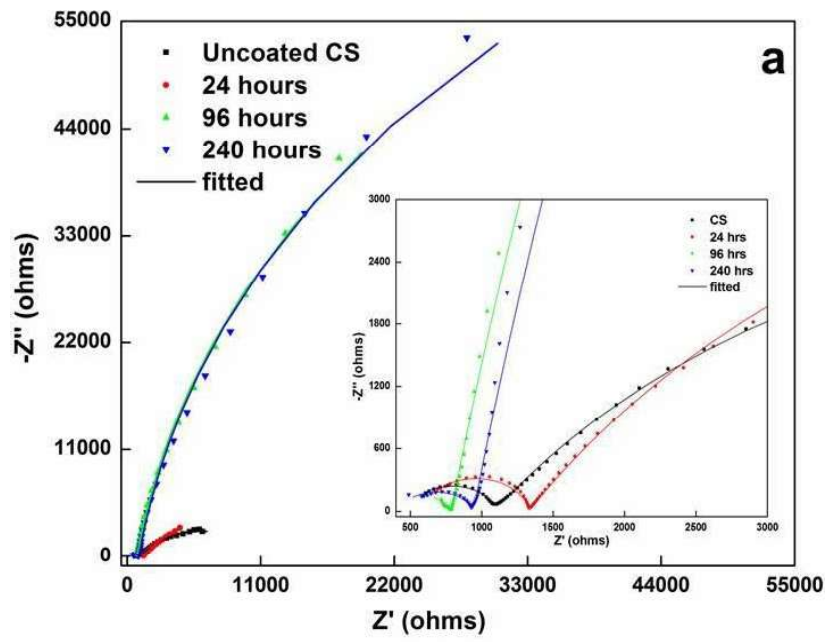


Figure 6.17: (a) Nyquist and (b) Bode plot of CS exposed to 24, 96 and 240 hours in LiOH and Mg^{2+}

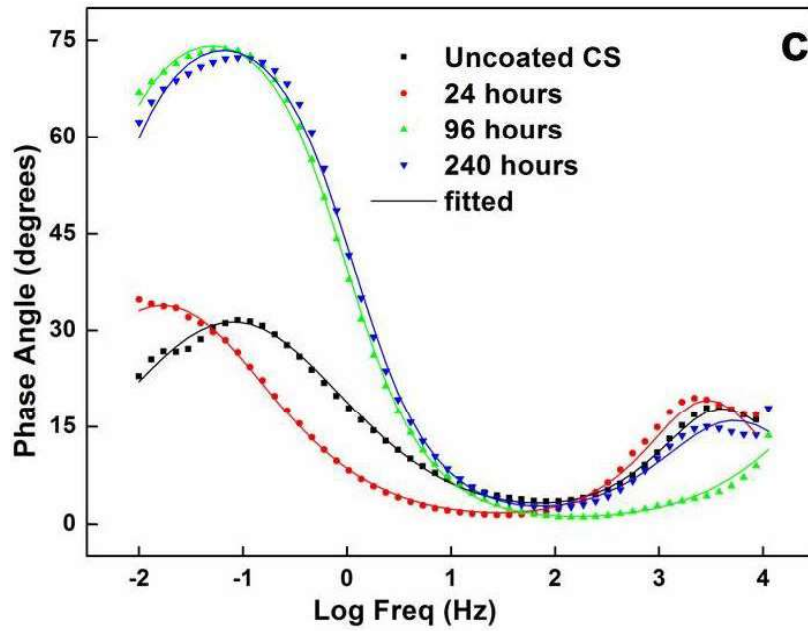


Figure 6.17 (c): Phase angle plot of CS exposed to 24, 96 and 240 hours in LiOH and Mg^{2+}

Table 6.9: Impedance parameters for different exposure time in LiOH & Mg^{2+}

Specimen	R_s (K Ω)	Q_1 (μ F)	n	Q_2 (mF)	n	R_2 (K Ω)	R_1 (K Ω)
Uncoated CS	0.487	0.44	0.85	0.49	0.63	9.5	0.607
24 hours	0.590	0.31	0.89	1.14	0.67	12.8	0.741
96 hours	0.208	0.23	0.71	0.25	0.91	164.1	0.579
240 hours	0.484	0.60	0.85	0.18	0.91	166.2	0.460

Table 6.10: $\text{Log } |Z|_{0.01 \text{ Hz}}$ for magnesium ferrite vs exposure time in LiOH

	$\text{Log } Z _{0.01 \text{ Hz}}$
Uncoated CS	3.872
24 hours	3.768
96 hours	4.648
240 hours	4.790

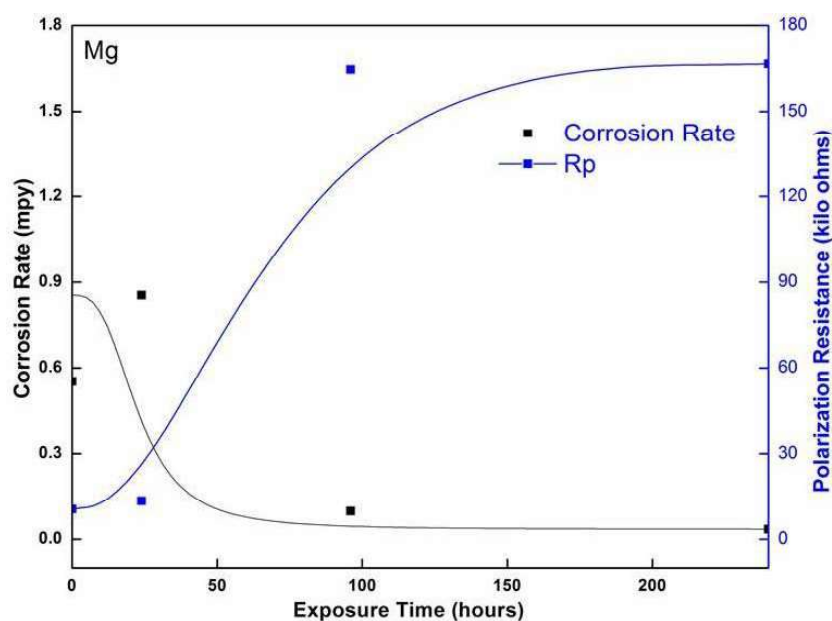


Figure 6.18: Corrosion rate and Polarization resistance comparison

6.5.3.3. Semiconducting properties of the oxide film

In the present work, the Mott–Schottky measurements for the oxides formed on CS in presence of Mg^{2+} ions for different exposure times were carried out at 1000, 100, 10 and 5 Hz in the potential range -1.2 to 1.2 V. For the calculation of N_D /or N_A , the dielectric constant 'e' was assumed as 12 for the passive films on CS. Figure 6.19 shows the C^{-2} versus potential (Mott–Schottky representation) obtained at (a) 100 Hz and (b) 10 Hz for the passive film formed anodically on CS in LiOH solution. The curves obtained for uncoated and ferrites formed on CS presents a positive slope from -0.8 V_{SCE} upward to more anodic potentials typical of an n-type semiconductor. The main defects in the oxide film are cation interstitials or anion vacancies (oxygen) acting as electron donors [99]. The oxide formed on CS showed two positive slopes in case of 100 Hz and 10 Hz frequency indicating two donor

levels. As can be observed, the Mott–Schottky plots are frequency dependent. Such behaviour is an indication of the highly disordered nature of the oxide film, which is characteristic of amorphous semiconductors. Table 6.11 gives the defect density values calculated for MS plot obtained at 100 Hz frequency, showed that the defect density reduced when compared with that of uncoated CS. Hence, magnesium ions present in the spinel structure reduced the defects and hence minimizes the corrosion rate.

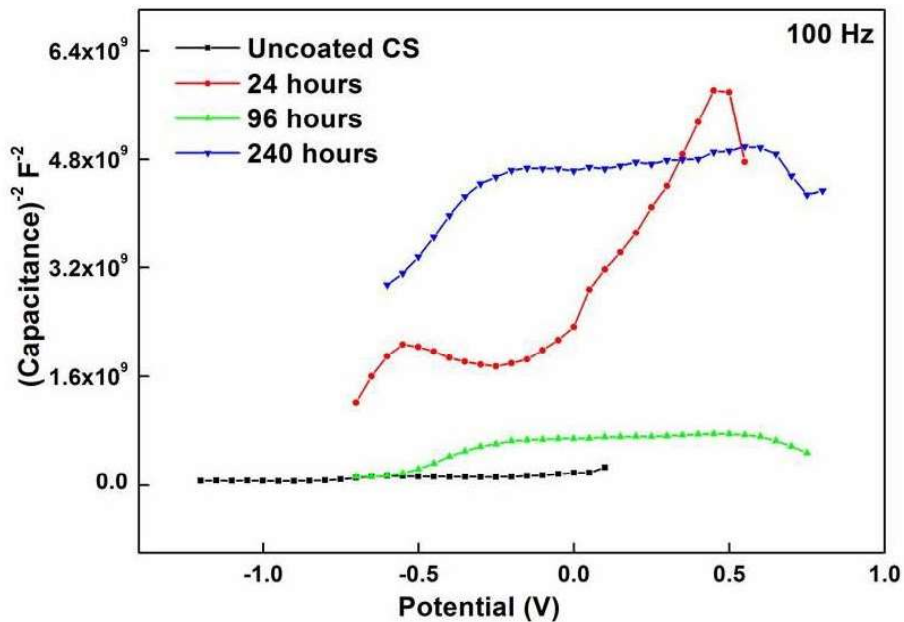


Figure 6.19 (a): Mott Schottky plot of CS exposed in LiOH and Mg²⁺

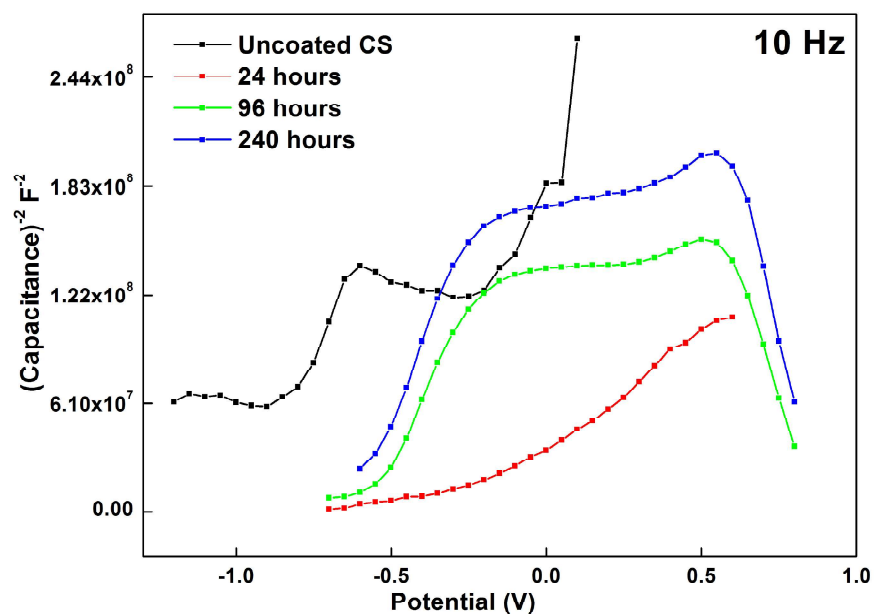


Figure 6.19 (b): Mott Schottky plot of CS exposed in LiOH and Mg^{2+}

Table 6.11: Defect density values obtained from Mott Schottky analysis

	Defect Density (cm^{-3})
Uncoated CS	4.29×10^{19}
24 hours	6.59×10^{18}
96 hours	2.39×10^{18}
240 hours	7.46×10^{18}

6.6. Conclusion

Magnesium ferrite formed on CS in presence of magnesium ions by hydrothermal method was confirmed by XRD. SEM analysis showed that the coating was uniform. The elements present in the oxides formed at different exposure time were quantified by XPS. The magnesium incorporation into the magnetite lattice remained same for 96 and 240 hours indicating that the higher exposure time does not improve the magnesium intake. Impedance and corrosion experiments showed the effectiveness of the nano sized oxides in improving the corrosion resistance of CS.

Chapter 7

Conclusions

and

Scope for Future Work

The important conclusions derived from the studies carried out on ferrites (NiFe_2O_4 , ZnFe_2O_4 and MgFe_2O_4) deposited on the $\text{CS}/\text{Fe}_3\text{O}_4$ substrate by pulsed laser deposition method and the corrosion behavior of these coatings evaluated by electrochemical methods are elucidated in this chapter. Similarly, the salient conclusions derived from the electrochemical studies of the oxide/ferrite films formed in presence of metal ions (Ni^{2+} , Zn^{2+} and Mg^{2+}) by hydrothermal method are also given in this chapter. In addition, suggestions are given for future research in this area.

7.1. Conclusions

It is well known that magnetite film formed on carbon steel provides good corrosion resistance to the base metal. In this work, nano ferrite films of type MFe_2O_4 [$\text{M} = \text{Ni}$, Zn and Mg] were developed as a coating/film on magnetite coated carbon steel ($\text{CS}/\text{Fe}_3\text{O}_4$) / carbon steel (CS) by PLD and hydrothermal methods respectively. The corrosion resistances of these ferrite coatings were evaluated by electrochemical methods and compared with the magnetite coating.

7.1.1. Pulsed laser deposition

Pulsed Laser Deposition method has the advantages of maintaining the stoichiometry of the material to be coated and the thickness of the coating can be varied in faster time duration, hence was chosen for the ex-situ deposition of ferrites. In this work, a coating thickness of 500 nm was found to be optimum to provide

significant corrosion resistance property for nickel ferrite and hence the same was fixed for the coatings of zinc and magnesium ferrites. With this thickness, the corrosion resistance of various coatings in alkaline LiOH followed the order: $\text{ZnFe}_2\text{O}_4 > \text{NiFe}_2\text{O}_4 \cong \text{MgFe}_2\text{O}_4 \cong \text{Fe}_3\text{O}_4$, which may be due to the higher stability of zinc ions in the spinel lattice compared to nickel and magnesium ions. Adhesive property was analyzed by scratch test and followed the order: $\text{ZnFe}_2\text{O}_4 > \text{NiFe}_2\text{O}_4 > \text{MgFe}_2\text{O}_4$.

7.1.2. Hydrothermal

Hydrothermal method is closer to the real systems, hence was chosen for the in-situ deposition of the ferrites on CS. Experiments with magnetite coating showed an optimum exposure time of 240 hours (corresponding to maximum corrosion resistance) for film development in lithiated high temperature (250 °C) water. At 240 hours, the corrosion protection offered by these oxide films on carbon steel followed the order: $\text{ZnFe}_2\text{O}_4 \cong \text{MgFe}_2\text{O}_4 \geq \text{NiFe}_2\text{O}_4 \cong \text{Fe}_3\text{O}_4$. In fact, from the values, only marginal benefit was observed between the films. However, the thickness of the oxide film formed in 240 hours followed the order: $\text{ZnFe}_2\text{O}_4 < \text{MgFe}_2\text{O}_4 < \text{Fe}_3\text{O}_4 < \text{NiFe}_2\text{O}_4$. The above trending between the corrosion protection and the thickness of the oxide films showed that the Zn and Mg ferrites form a more adherent and compact film compared to magnetite and nickel ferrite.

7.2. Future Scope/Directions

The trend in the corrosion resistance of oxide films formed in presence of soluble ions like Ni^{2+} , Zn^{2+} and Mg^{2+} for a longer exposure time by hydrothermal method, was evaluated based on the electrochemical results. However, the morphological studies revealed that the CS was fully covered by oxide film in 24 hours due to its corrosive nature. In this regard, studies on the nucleation process at the initial stages (exposure time less than 24 hours) of oxide growth on CS by the incorporation of the metal ions will be essential to find out the role of particle size of ferrite coatings on corrosion resistance properties. In this study, the corrosion resistance values were obtained in lithiated water of pH 10.2 at 28 °C. Since the corrosion resistance values also depend on the solubility of these ferrites which in turn depend on pH, studies on solubility at different pHs may be useful for optimising the best water chemistry conditions in the actual reactor systems. The reactors are multi-alloy systems and the presence of the mixture of ions (Ni^{2+} , Zn^{2+} and Mg^{2+}) may lead to the formation of mixed ferrites. Studies related to simultaneous addition of both zinc and nickel ions was found to be effective in suppressing the cobalt deposition onto stainless steel in oxygenated high temperature water than the addition of either zinc or nickel ions alone. Hence, studies related to mixed ferrite formation on CS by hydrothermal method will be useful. Studies related to metal ion passivation using zinc and magnesium ions as acetate salts are being carried out. In this work, soluble sulphate salts have been taken for the formation of oxides. In this regard, further studies to evaluate the role of anions in the oxide formation and subsequently its effect on the corrosion resistance properties will also be useful.

References

- [1] S. Bajaj and A.R. Gore, *Nuclear Engineering and Design*, 236 (2006) 701–722.
- [2] B. Stellwag and U. Staudt, *Power Plant Chemistry*, 7(2) (2005) 95–102.
- [3] R.L. Cowan, ‘Modern BWR Chemistry Operating Strategies’, Proc. International Conference of Water Chemistry of Nuclear Reactor Systems, San Francisco, CA, USA, October 11–14, (2004) 170-182.
- [4] S. Hettiarachchi, R.L. Cowan, R.J. Law and T.P. Diaz, ‘NobleChem™ Technology for Life Extension of BWRs – Field Experiences’, Proc. 8th International Conference on Water Chemistry of Nuclear Reactor Systems, Bournemouth, England, October 22–26, (2000).
- [5] K. Ishigure, *Nuclear Engineering and Design*, 160 (1996) 171–183.
- [6] C.C. Lin, ‘A Review of Radiation Field Buildup in BWRs’, Proc. International Conference of Water Chemistry of Nuclear Reactor Systems, San Francisco, CA, USA, October 11–14, (2004).
- [7] F. Nordmann, S. Odar, H. Venz, J. Kysela, W. Ruehle and R. Riess, ‘ANT International Chemistry Update and best Practices’. Nuclear Plant Chemistry Conference, Quebec- October 3-7, (2010).
- [8] F. Nordmann, ‘Aspects on Chemistry in French Nuclear Power Plants’, 14th International Conference on the Properties of Water and Steam (ICPWS), Kyoto, Japan, August 29 - September 3, (2004).
- [9] J.C. Killeen, F. Nordmann, J. Schunk and K. Vonkova, ‘Optimisation of water chemistry to ensure reliable water reactor fuel performance at high burnup and in ageing plant (FUWAC): An International Atomic Energy Agency coordinated research project’, Nuclear Plant Chemistry Conference, Quebec, October 3-7, (2010).
- [10] D.J. Ferrett and G.C.W. Comley, IAEA-TECDOC-356, (1985) 65.
- [11] B. Stellwag, *Corros. Sci.*, 40 (1998) 337-370.
- [12] J. Robertson, *Corros. Sci.*, 29 (1989) 1275-1291.

- [13] K.A. Burrill, 'An Activity Transport Model for CANDU Based on Iron Transport in the Primary Coolant', AECL-11805, COG-97-373-I, (1998).
- [14] D.H. Lister, Nucl. Sci. Eng., 59 (1976) 406-426.
- [15] A.B. Johnson, B.G. Jr., F.M. Kustas and R.A. Shaw, 'Nature of Deposits on BWR and PWR Primary System Surfaces-Relation to Decontamination', Water Chemistry for Nuclear Reactor System, BNES, London, 1980.
- [16] R. Vanbarabant and P. Regge, 'Characterization of the Corrosion Products in Primary Reactor Water of PWR during Normal Operation and Transient Phases', Water Chemistry for Nuclear Reactor System, BNES, London, 1980.
- [17] J. Manjanna, in., PhD thesis, Industrial Chemistry, Kuvempu University, Shimoga, Karnataka, India 2001.
- [18] M. Sherik Ajwad, H. Rasheed, A.H. Jabran and R.G. Ortiguerra, 'Adhesion and Corrosion Performance of Nanostructured Nickel and Cobalt-based Coatings', Corrosion, March New Orleans LA; Document ID 08025, (2008) 16-20.
- [19] A. Gruskeva, J. Slama, R. Dosoudil, M. Usakova, V. Jancarik and E.Usak, J. Magn. Magn. Mater., 320 (2008) 860-864.
- [20] M.I. Ivanovskaya , A.I. Tolstik and V.V. Pan'kov, Inorg. Mater., 45(11) (2009) 1309-1313.
- [21] M. George, A. Mary John, S.S. Nair, P.A. Joy, M.R. Anantharaman, J. Magn. Magn. Mater., 302 (2006) 190-195.
- [22] C. Dong-Hwang and H. Xin-Rong, Mater. Res. Bull., 36(7-8) (2001) 1369-1377.
- [23] J. Wang, Mater. Sci. Eng. B, 127 (2006) 81-84.
- [24] K. Nejati and R. Zabihi, Chem. Cent. J., 6 (2012) 23-28.
- [25] R. Saez Puche, M.J. Torralvo Fernandez, V. Blanco Gutierrez, R. Gomez, V. Marquina, M.L. Marquina, J.L. Perez Mazariago and R. Ridaura, Bol. Soc. Esp. Ceram., (47), (2008), 3, 133-137.
- [26] P. Vlazan and M. Vasile, Optoelectron. Adv. Mater. – Rapid Communications, 4 (9) (2010) 1307-1309.

- [27] N. Moumen and M.P. Pileni, *Chem. Mater.*, 8 (1996) 1128–1134.
- [28] A.A. Pandit, S.S. More, R.G. Dorik and K.M. Jadhav, *Bull. Mat. Sci.*, 26 (2003) 517-521.
- [29] B.P. Rao, A.M. Kumar, K.H. Rao, Y.L.N. Murthya, O.F. Caltunb, I. Dumitruc and I. Spinuc, *J. Optoelectron. Adv. Mater.*, 8 (2006) 1703-1705.
- [30] A.K. Giri, E.M. Kirkpatrick, P. Moongkhamklang, S.A. Majetich and V.G. Harris. *Appl. Phys. Lett.* 80 (2002) 2341-2443.
- [31] Q. Chen and Z.J. Zhang. *Appl. Phys. Lett.* 73 (1998) 3156-3158.
- [32] S.S. Yattinahalli, S.B. Kapatkar, N.H. Ayachit, and S.N. Mathad, *International J. Self Propagating High Temperature Synthesis*, 22 (3) (2013) 147–150.
- [33] C.A. Ladole, *Int. J. Chem. Sci.*, 10 (3), (2012) 1230-1234.
- [34] M. Ueda, S. Shimada and M. Inagaki, *J. Mater. Chem.*, (3) (1993) 1199-1201.
- [35] W. Kim and F. Saito. *Powder Technol.*, 114 (2001) 12-16.
- [36] J. Mayekar , V. Dhar and S. Radha, *International J. Innovative Resear. Sci. Engineering and Technol.* 5 (5) (2016) 8367-8371.
- [37] K. Maaz, S. Karim, A. Mumtaz, S.K. Hasanain, J. Liu and J.L. Duan, *J. Magn. and Magn Mater.*, 321 (2009) 1838–1842.
- [38] Seema Joshi, Manoj Kumar, Sandeep Chhoker, Geetika Srivastava, Mukesh Jewariya and V.N. Singh, *J. Molecular Struct.*, 1076 (2014) 55–62.
- [39] S.A. Popescu, P. Vlazan, P.V. Notingher, S. Novaconi, I. Grozescu, A. Bucur and P. Sfirloaga, *J. Optoelectron. Adv. Mater.*, 13 (3) (2011) 260-262.
- [40] S.K. Emdadul Islam and Pankaj Sharma, *J. nano and electronic physics*, 6 (1) (2014) 01008.
- [41] B. K. Nath, P.K. Chakrabarti, S. Das, Uday Kumar, P.K. Mukhopadhyay and D. Das, *Eur. Phys. J. B*, 39, (2004) 417–425.
- [42] J. Balavijayalakshmi, Greeshma, *J. Environ. Nanotechnol.*, 2 (2) (2013) 53-55.
- [43] J. Govha, T.B. Narasaiah, P. Kumar and Shilpa Chakra, *International J. Engineering Resear. Technol.*, 3 (8) (2014) 1420-1422.

- [44] Salma Irfan, M. Ajaz-un-Nabi, Yasir Jamil and Nasir Amin, *Mater. Sci. Engineering*, 60 (2014) 012048.
- [45] T. Ohnishi, H. Koinuma and M. Lippmaa, *Appl. Surf. Sci.*, 252 (2006) 2466–2471.
- [46] C. Belouet, *Appl. Surf. Sci.* 96-98 (1996) 630-642.
- [47] A.K. Singh, T.R.G. Kutty and Sucharita Sinha, *J. Nucl. Mater.*, 420 (2012) 374–381.
- [48] Happy, S.R. Mohanty, P. Lee, T.L. Tan , S.V. Springham, A. Patran, R.V. Ramanujan and R.S. Rawat, *Appl. Surf. Sci.*, 252 (2006) 2806–2816.
- [49] L.L. Pan, G.Y. Li, S.S. Xiao, L. Zhao and J. S. Lian, *J. Mater. Sci: Mater. Electron.*, 25 (2014) 1003–1012.
- [50] J.L. Arias, M.B. Mayor, F.J. Garcia-Sanz, J. Pou, B. Leon, M. Peirez-Amor and J.C. Knowles, *J. Mater. Sci.: Mater. Medicine*, 8 (1997) 873-876.
- [51] G. Szwachta, M. Gajewski and S. Kac, *Arch. Metall. Mater.*, 61 (2016) (2B) 1031–1038.
- [52] H. Pelletier, V. Nelea, P. Mille and D. Muller, *J. Mater. Sci.*, 39 (2004) 3605–3611.
- [53] Wenjun Kuang, Xinqiang Wu, En-Hou Han and Liqun Ruan, *Corros. Sci.*, 53 (2011) 1107–1114.
- [54] Hu Xian-jun, Zhang Bi-ming, Chen Shao-hui, Fang Feng and Jiang Jian-qing, *Jour. Iron Steel Resear.*, 20(1) (2013) 47-52.
- [55] Jerzy A. Sawicki and Heather A. Allsop, *Journal of Nuclear Materials*, 240 (1996) 22-26.
- [56] T. Osato and Y. Hemmi, ‘Corrosion and Co-uptake behavior on structural material in BWR primary coolants at Zn and Ni addition’, 7th Water chemistry of Nuclear Reactor Systems, Vol. 1, BNES, 1996, 125-127.
- [57] M. Haginuma, S.Ono, K.Takamori, K. Takeda, K. Tachibana and K. Ishigure, ‘Effect of zinc addition on cobalt ion accumulation into the corroded surface of type 304 SS in high temperature water’, 7th Water chemistry of Nuclear Reactor Systems, Vol. 1, BNES, 1996, 128-130.

- [58] J. Piippo, T. Saario, V. Tegeder and B. Stellwag, 'Influence of zinc on properties and growth of oxides layers in simulated primary coolant', 7th Water chemistry of Nuclear Reactor Systems, Vol. 1, BNES, 1996, 131-134.
- [59] V.K. Mittal, Santanu Bera, T. Saravanan, S. Sumathi, R. Krishnan, S. Rangarajan, S. Velmurugan and S.V. Narasimhan, *Thin Solid Films*, 517 (2009) 1672-1676 .
- [60] S. Velmurugan, S. Padma, S.V. Narasimhan, P.K. Mathur and P.N.Moorthy, *J. Nucl. Sci. Technol.*, 33 (1996) 641-649.
- [61] R.M.Cornell and U.Schertmann, *Iron Oxides in the Laboratory: Preparation and Characterisation* (Weinheim: VCH:1999).
- [62] F.A.Cotton and G.Wilkinson, *Advanced inorganic chemistry* (New York: Wiley Interscience: 1988).
- [63] ASTM G1-90, 'Standard Practice for Preparing, Cleaning and Evaluating Corrosion Test Specimens', ASTM International, West Conshohocken, PA, 1998.
- [64] S.G. Clarke, *Trans. Electrochem. Soc.* 69 (1936) 131-144.
- [65] B.D. Cullity, *Elements of X-ray diffraction*, 2nd ed. Addison-Wesley, 1978.
- [66] H.P. Klug and L.E. Alexander, *X-ray diffraction procedures for polycrystalline and amorphous materials*, 2nd ed. Wiley, New York, 1974.
- [67] D.M. Moore and R.C. Reynolds, *X-Ray diffraction and the identification and analysis of clay minerals*, 2nd Ed. Oxford University Press, New York, 1997.
- [68] M.M. Hluchy, *J. Geoscience Education*, 47 (1999) 236-240.
- [69] J.I. Langford and A.J.C. Wilson, *J. Appl. Crystallogr.*, 11 (2) (1978) 102–113.
- [70] C.N.J. Wagner and E.N. Aqua, *Adv. X-ray Anal.* 7 (1963) 46–65.
- [71] D. Briggs and M.P. Seah, *Practical Surface Analysis by Auger and X-ray Photoelectron Spectroscopy*, John Wiley & Sons, 1987.
- [72] D.A. Skoog, F.J. Holler and T.A. Nieman, *Principles of Instrumental Analysis*, Harcourt Asia Pvt. Ltd., 2001.
- [73] D.K. Sarkar, S. Bera, S.V. Narasimhan, S. Dhara, K.G.M. Nair and S.C. Chaudhary, *Appl. Surf. Sci.*, 120 (1997) 159-164.

- [74] Inductively Coupled Plasma Spectrometer (ICP AES / ICP OES). Available from: <http://www.labcompare.com/Spectroscopy/26-Inductively-Coupled-Plasma-Spectrometer-ICP-AES-ICP-OES/>.
- [75] Horst Czichos, Tetsuya Saito and Leslie Smith, Springer Handbook of Materials Measurement Methods, (2006) 296-299.
- [76] ASTM C1624-05, Standard Test Method for Adhesion Strength and Mechanical Failure Modes of Ceramic Coatings by Quantitative Single Point Scratch Testing, ASTM International.
- [77] ASTM standard, Standard practice for conventions applicable to electrochemical measurements in corrosion testing, G3-89(2004), West Conshohocken, PA, 2004, 10.1520/G0003 - 89R04.
- [78] ASTM standard, Standard Reference Test Method for Making Potentiostatic and Potentiodynamic Anodic Polarization Measurement, G5-94(2004), West Conshohocken, PA, 10.1520/G0005 - 94R04.
- [79] A.S. Hamdy, E. El-Shenawy and T. El-Bitar, *Int. J. Electrochem. Sci.*, 1 (2006) 171-180.
- [80] W.J. Lorenz and F. Mansfeld, *Corros. Sci.* 21(9) (1981) 647-672.
- [81] J.S. Kim, E.A. Cho and H.S. Kwan, *Corros. Sci.*, 43 (2001) 1403-1415.
- [82] T. Ohtsuka and H. Yamada, *Corros. Sci.*, 40 (1998) 1131-1138.
- [83] M.A. Amin, *Electrochim. Acta*, 50 (2005) 1265-1274.
- [84] M. Da Cunha Belo, N.E.Hakiki and M.G.S. Ferreira, *Electrochim. Acta*, 44 (1999) 2473-2481.
- [85] M.F. Montemor, A.M.P. Simões, M.G.S. Ferreira, M. Da Cunha Belo, *Corros. Sci.*, 41 (1999) 17-34.
- [86] Q.D. Zhong, C. Wang, X.G. Lu, L.Y. Shi and K.C. Chou, *The Open Corros. Jour.*, 1 (2008) 1-5.
- [87] E.M.A. Martini and I.L. Muller, *Corros. Sci.*, 42 (2000) 443-454.
- [88] Y.X. Qiao, Y.G. Zheng, W. Ke and P.C.Okafor, *Corros. Sci.*, 51 (2009) 979-986.
- [89] Y. Yang, L.J. Guo and H. Liu, *J. Power Sources*, 195 (2010) 5651-5659.

- [90] R.A. Antunes, M.C.L. De Oliveira and I. Costa, *Mater. Corros.*, 63 (2012) 586–592.
- [91] M.J. Carmezim, A.M. Simões, M.O. Figueiredo and M. Da Cunha Belo, *Corros. Sci.*, 44 (2002) 451–465.
- [92] L. Diamandescu, D. Mihaila-Tarabasanu, V. Teodorescu and N. Popescu-Pogrio, *Mater. Lett.*, 37 (1998) 340-348.
- [93] L. Freire, X.R. Novoa, M.F. Montemor and M.J. Carmezim, *Mater. Chem. Phys.*, 114 (2009) 962-972.
- [94] S. Nasrazadani, P.Vemuri and S. Burckhard, ‘Evaluation of magnetite coatings for temporary protection of carbon steels’ NACE international (2003).
- [95] H. Zhu, F. Cao, D. Zuo, L. Zhu, D. Jin and K. Yao, *Appl. Surf. Sci.*, 254 (2008) 5905–5909.
- [96] D.D. Macdonald and T.E. Rummery, *Corros. Sci.*, 15 (1975) 521-527.
- [97] Z. Ristanovic, A. Kalezic – Glisovic, N. Mitrovic, S. Dukic, D. Kosanovic, A. Maricic, *Sci. Sinter.*, 47 (2015) 3-14.
- [98] D.H. Lister and W.G. Cook, *Nuclear Plant Materials and Corrosion*, 2014, University of New Brunswick
- [99] Wagner and Traud, ‘On the Interpretation of Corrosion Processes through the Superposition of Electrochemical Partial Processes and on the Potential of Mixed Electrodes’, 144 (1938) 391-402.
- [100] E. Deiss and G. Schikorr, *J. Anorg. Allg. Chem.*, 172 (1928) 32-42.
- [101] Q.W. Chen, Y.T. Qian, Z.Y. Chen, Y. Xie, G.E. Zhou and Y.H. Zhang, *Mater. Lett.*, 24 (1995) 85-87.
- [102] J.P. Hong, S.B. Lee, Y.W. Jung, J.H. Lee, K.S. Yoon, K.W. Kim, C.H. Lee and M.H. Jung, *Appl. Phys. Lett.*, 83 (2003) 1590-1592.
- [103] S. Bera, A.A.M. Prince, S. Velmurugan, P.S. Ranganathan, R. Gopalan, G. Paneerselvam and S.V. Narasimhan, *J. Mater. Sci.*, 36 (2001) 5379–5384.
- [104] K. Azumi, T. Ohtsuka and N. Sata, *J. Electrochem. Soc.*, 134 (1987) 1352–1358.
- [105] L. Hamadou, A. Kadri and N. Benbrahim, *Corros. Sci.* 52 (2010) 859–864.

- [106] S.Ahn and H.Kwon, *J. Electroanal. Chem.*, 579 (2005) 311-319.
- [107] J.W. Verwey and E.L. Heilmann, *J. Chem. Phys.*, 15 (1947) 181–187.
- [108] W.B. White and B.A. DeAngeli, *Spectrochim Acta*. 23A (1967) 985–995.
- [109] Jitendra Pal Singh, R. C. Srivastava, H. M. Agrawal and Ravi Kumar, *J. Raman Spectrosc.*, 42 (2011) 1510–1517.
- [110] Z.Z. Lazarevic, C. Jovalekic, D. Sekulic, M. Slankamenac, M. Romcevic, A. Milutinovic and N.Z. Romcevic, *Sci. Sint.*, 44 (2012) 331-339.
- [111] P. Chandramohan, M.P. Srinivasan, S. Velmurugan and S.V. Narasimhan, *J. Solid State Chem.* 184 (2011) 89–96.
- [112] Yuqiu Qu, Haibin Yang, Nan Yang, Yuzun Fan, Hongyang Zhu and Guangtian Zou, *Mater. Lett.*, 60 (2006) 3548–3552.
- [113] A. Ahlawat and V. G. Sathe, *J. Raman Spectrosc.*, 42 (2011) 1087-1094.
- [114] R.S. Yadav, Ivo Kuřitka, Jarmila Vilcakova, Jaromir Havlica, Jiri Masilko, Lukas Kalina, Jakub Tkacz, Vojtěch Enev and Miroslava Hajdúchová, *J. Phys. Chem. Solids.*, 107 (2017) 150–161.
- [115] M. Cai and S.M. Park, *J. Electrochem. Soc.*, 143 (1996) 3895.
- [116] M. Opel, *J. Phys. D: Appl. Phys.*, 45 (2012) 033001.
- [117] C.Y. Chao, L.F. Lin and D.D. Macdonald, *J. Electrochem. Soc.*, 128 (1981) 1187.
- [118] M. Bojinov, G. Fabricius, T. Laitinen, K. Mäkelä, T. Saario, and G. Sundholm, *Electrochim. Acta.*, 45 (2000) 2029-2048.
- [119] I. Dehri and M. Erbil, *Corros. Sci.*, 42 (2000) 969-978.
- [120] C.C. Lin, *Prog. Nucl. Energy.*, 51(2) (2009) 207–224.
- [121] L.W. Niedrach and W.H. Stoddard, *Corros.*, 42 (1986) 546–549.
- [122] H. Inagaki, A. Nishikawa, Y. Sugita and T. Tsuji, *J. Nucl. Sci. Technol.*, 40 (2003) 143–152.
- [123] P.L. Andresen, G.S. Was, in: *Corrosion in the Nuclear Power Industry*, ASM Handbook, Vol. 13C, ASM International, OH, 2006, pp. 404–406.
- [124] B. Beverskog and I. Puigdomenech, *Corros.*, 55 (1999) 1077-1087.
- [125] David Jobe, ‘The calculated solubilities of hematite, magnetite and lepidocrocite in steam generator feed trains’, AECL, 1997.

- [126] Y.Qu, H.Yang, N. Yang, Y.Fan, H Zhu and G. Zou, *Mater. Lett.*, 60 (2006) 3548.
- [127] A. Miszczyk and K. Darowicki, *Anti-Corrosion Methods and Mater.*, 58(1) (2011) 13-21.
- [128] A. Di Paola, *Electrochim. Acta.*, 34 (1989) 203–210.
- [129] A.E. Chastukhin, A.D. Izotov, I.G. Gorichev and A.M. Kutepov, *Theoret. Foundat. Chem. Eng.*, 37 (2003) 4, 398-406.
- [130] C.C.Lin, F.R.Smith, Y.Uruma, T.Taneichi, N.Ichikawa, Cobalt deposition studies in GE Vallecitos test loops, JAIF International Conference on Water Chemistry in Nuclear Power Plants, Tokyo, Japan. 2 (1988) 386 - 392.
- [131] V.S.Saji, J.Thomas, *Nanomaterials for corrosion control*, *Curr. Sci. India*. 92(1) (2007) 51-55.
- [132] X.Shi, T.A.Nguyen, Z.Suo, Y.Liu, R.Avci, *Surf. Coat. Technol.* 204 (2009) 237-245.
- [133] R.S. Abdel Hameed, Abd-Alhakeem H.Abu-Nawwas and H.A.Shehata, *Adv. Appl. Sci. Res.* 4(3) (2013) 126-129.
- [134] S.Fujimoto, H.Tsuchiya, *Corros. Sci.*, 49 (2007) 195-202.
- [135] Z. Wang, D. Schiferl, Y. Zhao and H. St. C. O’Neil, *J. Phys. Chem. Solids*, 64 (2003) 2517-2523
- [136] Z.W. Wang, P. Lazor, S. K. Saxena and G. Aritoli, *J. Solid State Chem.*, 165 (2002) 165-170.
- [137] A.K.M. Akther Hossain, S.T. Mahmud, M. Seki, T. Kawai and H. Tabata, *J. Magn. Magn. Mater.* 312 (2007) 210-219.
- [138] B.D. Cullity, *Introduction to Magnetic Materials*, Addison-Wesley, MA, 1971.
- [139] P. Baghery, M. Farzam, A.B. Mousavi and M. Hosseini, *Surf. Coat. Technol.* 204 (2010) 3804–3810.
- [140] S. Ramalingam, V.S. Muralidharan and A. Subramania, *J. Solid State Electr.* 13 (2009) 1777-1783.
- [141] D.D. Macdonald, K.M. Ismail and E.Sikora, *J. Electrochem. Soc.*, 145 (1998) 3141–3149.

- [142] Z. Cvejic, S. Rakic, S. Jankov, S. Skuban and A. Kapor, *J. Alloys Compd.*, 480 (2009) 241-245.
- [143] H. Subramanian, Veena Subramanian, P. Chandramohan, M.P. Srinivasan, S. Rangarajan, S.V. Narasimhan and S. Velmurugan, *Corros. Sci.*, 70 (2013) 127–139.
- [144] J.A. Franco, F.C.e Silva, *Appl. Phys. Lett.* 96 (17) (2010) 172505.
- [145] V.K. Mittal, P. Chandramohan, Santanu Bera, M.P. Srinivasan, S. Velmurugan and S.V. Narasimhan, *Solid State Commun.*, 137 (2006) 6–10.
- [146] V.K. Mittal, Santanu Bera, R. Nithya, M.P. Srinivasan, S. Velmurugan and S.V. Narasimhan, *J. Nucl. Mater.* 335 (2004) 302–310.
- [147] A. Kitahara, S. Yasuno and K. Fujikawa, *Transactions Mater. Resear. Soc. Japan*, 34 [4] (2009) 613-615.